TECHNISCHE UNIVERSITÄT MÜNCHEN

DOCTORAL THESIS

Study of the strong interaction in p–d system and of deuteron production in pp collisions

Author:
Bhawani Singh

Supervisor:
Prof. Dr. Laura Fabbietti

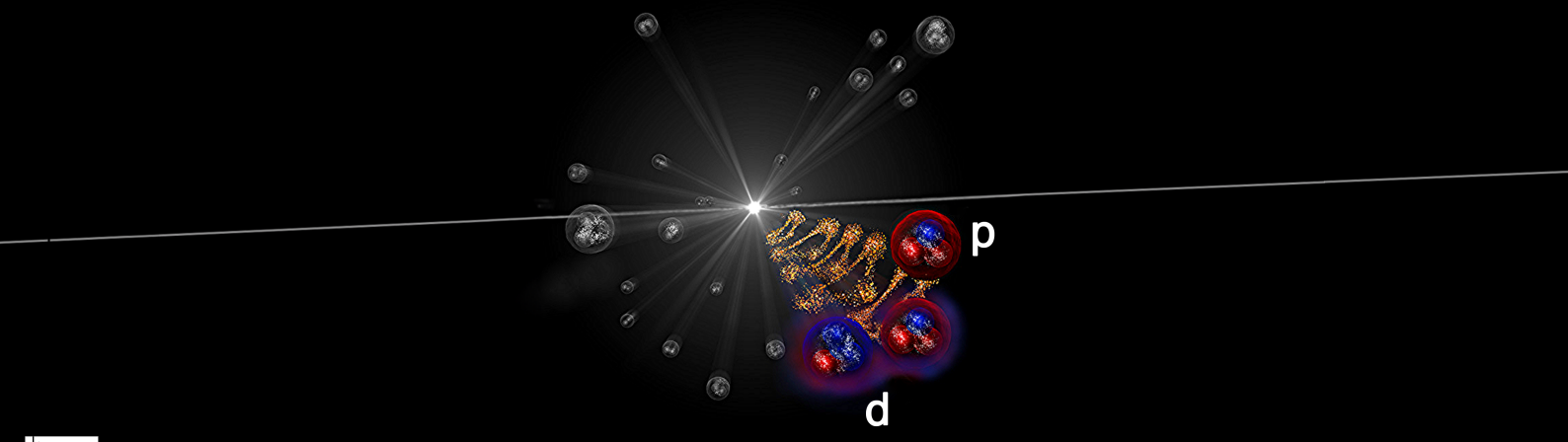

A thesis submitted in fulfillment of the requirements
for the degree of Doctor of Natural Sciences
in the
TUM School of Natural Sciences

July, 2023

Dedicated to the cherished memories of my beloved papa and brother Shaitan. Though your physical presence may be absent, your spirits live on within me, shaping my journey and fueling my relentless pursuit of knowledge.

Your determination, calm demeanor, and positive outlook during challenging moments have strengthened me. Thanks to your enduring inspiration, I am able to write this thesis today.

TUM School of Natural Sciences

Study of the strong interaction in p–d system and of deuteron production in pp collisions

Bhawani Singh

Vollständiger Abdruck der von der TUM School of Natural Sciences der Technischen Universität München zur Erlangung des akademischen Grades eines

Doktors der Naturwissenschaften

genehmigten Dissertation.

Vorsitz:	apl. Prof. Norbert Kaiser
Prüfer*innen der Dissertation:	1. Prof. Dr. Laura Fabbietti
	2. Prof. Dr. Lukas Heinrich

Die Dissertation wurde am 05.07.2023 bei der Technischen Universität München eingereicht und durch die TUM School of Natural Sciences am 10.08.2023 angenommen.

Declaration of Authorship

I, Bhawani Singh, declare that this thesis titled, "Study of the strong interaction in p–d system and of deuteron production in pp collisions" and the work presented in it are my own. I confirm that:

- This work was done wholly or mainly while in candidature for a research degree at this University.
- I have not employed the services of an organization that provides dissertation supervisors in return for payment or that fulfills, in whole or in part, the obligations incumbent on me in connection with my dissertation.
- I have not submitted the dissertation, either in the present or a similar form, as part of another examination process.
- I have not yet been awarded the desired doctoral degree nor have I failed the last possible attempt to obtain the desired degree in a previous doctoral program.
- Where I have consulted the published work of others, this is always clearly attributed.
- Where I have quoted from the work of others, the source is always given. With the exception of such quotations, this thesis is entirely my own work.
- I have acknowledged all main sources of help.
- Where the thesis is based on work done by myself jointly with others, I have made clear exactly what was done by others and what I have contributed myself.

Signed:

Date:

Abstract

Doctor of Natural Sciences

Study of the strong interaction in p–d system and of deuteron production in pp collisions

by Bhawani Singh

This thesis concentrates on two main research topics. Firstly, it explores the strong interaction within a system of three nucleons. This is done by measuring effective two-body correlations through the femtoscopy technique with proton and deuteron pairs. Secondly, it investigates the production of light nuclei in proton-proton collisions.

Two-particle momentum correlations using the femtoscopy technique have opened up new avenues for studying interactions between hadrons, including those involving strange and charm hadrons. As a natural progression, the investigation of three-body systems has emerged. The momentum correlation between protons and deuterons offers a valuable means to explore the strong interaction among three nucleons. These systems play a crucial role in nuclear physics, as their properties can help constrain nuclear interactions, leading to a deeper understanding of the nuclear structure and the equation-of-state of dense nuclear matter.

This work presents the first measurement and interpretation of the momentum space correlation between protons and deuterons (p–d) in proton-proton (pp) collisions at the LHC using ALICE. The observed signal in the correlation function cannot be adequately explained by effective two-body calculations treating protons and deuterons as point-like and distinguishable particles produced at short distances. These calculations only consider the Coulomb and strong nuclear interactions based on the measured scattering parameters from p–d scattering experiments. To properly interpret the p–d correlation, comprehensive three-body calculations were performed for the first time and applied in this analysis. These calculations appropriately account for the deuteron's internal structure, the dynamics of three nucleons when the proton and deuteron are close in phase-space, and all relevant partial waves. Additionally, the three-body calculations consider quantum statistical effects and the short-range part of the strong interaction. The fact that the measured p–d correlation can only be described by these three-body calculations suggests that nucleons explicitly play a role in the correlation between the hadron and the light nuclei at the LHC. Moreover, the measurements demonstrate the feasibility of studying interactions in a three-hadron system by investigating deuteron-hadron correlations. Such measurements will provide access to the isospin-dependent strong interaction and have the potential to explore the effects of genuine many-body interactions at the LHC in the future.

In collision experiments, the production of light (anti-)nuclei is observed. However, the microscopic understanding of their production is still intensely debated. This

is particularly true for light nuclei, which have a binding energy per nucleon of approximately 2 MeV, significantly lower than the chemical freeze-out temperature ($T_c \sim 155$ MeV). Two models, the Statistical Hadronization Model and the Coalescence Model, are commonly used to study the production yield of light nuclei. This work focuses on the latter, specifically concerning the lightest (anti-)nuclei, the (anti-)deuterons. For the first time, the calculation of the coalescence parameter $\mathcal{B}_2$, which is related to the production probability, is extended to incorporate realistic deuteron wavefunctions based on Chiral Effective Field Theory (χEFT). The study also investigates the differential behavior of $\mathcal{B}_2$ with respect to transverse momentum p_T. To predict $\mathcal{B}_2$ as a function of p_T, the calculation incorporates the femtoscopic source size of emitted nucleons, measured in pp collisions at $\sqrt{s} = 13$ TeV. The computed $\mathcal{B}_2$ successfully captures the observed slope in the measurements and is found to be sensitive to the choice of the deuteron wavefunction.

Furthermore, this work calculates the deuteron formation probability using the Wigner formalism, which is a crucial input for modeling a new coalescence afterburner for event generators. The calculation is performed for four choices of the deuteron wavefunction, each reflecting the nuclear interaction between the pair of nucleons forming the deuteron. The predicted deuteron spectra in the event generators exhibit clear sensitivity to the chosen deuteron wavefunction, with the Argonne v_{18} and χEFT wavefunctions providing the most accurate description of the deuteron yield in pp collisions at $\sqrt{s} = 13$ TeV.

Zusammenfassung

Diese Arbeit konzentriert sich auf zwei Hauptforschungsthemen. Erstens untersucht sie die starke Wechselwirkungen in einem System von drei Nukleonen. Dies wird durch die Messung effektiver Zwei-Teilchen-Korrelationen von Proton-Deuteron-Paaren mithilfe der Femtoskopietechnik erreicht. Zweitens untersucht sie die Produktion leichter Kerne in Proton-Proton-Kollisionen.

Die Untersuchung von Zwei-Teilchen-Impulskorrelationen mit Hilfe der Femtoskopietechnik hat neue Möglichkeiten eröffnet, Wechselwirkungen zwischen Hadronen zu untersuchen, einschließlich von strange und charm Hadronen. Als natürliche Weiterentwicklung ist die Untersuchung von Dreiteilchensystemen entstanden. Die Impulskorrelation zwischen Protonen und Deuteronen bietet eine besondere Möglichkeit, die starke Wechselwirkung zwischen drei Nukleonen zu erforschen. Diese Systeme spielen eine entscheidende Rolle in der Kernphysik, da ihre Eigenschaften dazu beitragen können, Kernwechselwirkungen einzuschränken und ein tieferes Verständnis der Kernstruktur sowie von der Zustandsgleichung dichter Kernmaterie zu erlangen.

Diese Arbeit präsentiert die erste Messung und Interpretation der Impulsraumkorrelation zwischen Protonen und Deuteronen (p–d) in Proton-Proton-Kollisionen (pp) am LHC unter Verwendung von ALICE. Das beobachtete Signal in der Korrelationsfunktion kann nicht angemessen durch effektive Zwei-Teilchen-Berechnungen erklärt werden. Bei diesen werden Protonen und Deuteronen als punktförmige und unterscheidbare Teilchen behandelt, welche bei kurzen Abständen erzeugt werden. Diese Berechnungen berücksichtigen nur die Coulomb- und starke Kernwechselwirkung, basierend auf den gemessenen Streuparametern aus Streuexperimenten mit p–d. Um die p–d-Korrelation angemessen zu interpretieren, wurden erstmals umfassende Dreiteilchenberechnungen durchgeführt und in dieser Analyse angewendet. Diese Berechnungen berücksichtigen angemessen die interne Struktur des Deuterons, die Dynamik der drei Nukleonen, wenn das Proton und das Deuteron im Phasenraum nahe beieinander liegen, sowie alle relevanten Partialwellen. Darüber hinaus berücksichtigen die Dreiteilchenberechnungen quantenstatistische Effekte und den kurzreichweitigen Teil der starken Wechselwirkung. Die Tatsache, dass die gemessene p–d-Korrelation nur durch diese Dreiteilchenberechnungen beschrieben werden kann, legt nahe, dass Nukleonen explizit eine Rolle in der Korrelation zwischen dem Hadron und den leichten Kernen am LHC spielen. Darüber hinaus zeigen die Messungen die Machbarkeit, mit Hilfe von Deuteron-Hadron-Korrelationen die Wechselwirkungen in einem Dreihadronensystem zu studieren. Solche Messungen ermöglichen den Zugang zur isospinabhängigen starken Wechselwirkung und haben das Potenzial, zukünftig die Auswirkungen echter Vielteilchenwechselwirkungen am LHC zu untersuchen.

In Kollisionsexperimenten wird die Produktion von leichten (Anti-)Kernen beobachtet. Jedoch wird das mikroskopische Verständnis ihrer Produktion nach wie vor intensiv diskutiert. Dies gilt insbesondere für leichte Kerne, die eine Bindungsenergie pro Nukleon von etwa 2 MeV haben, deutlich niedriger als die chemische Ausfrier-Temperatur ($T_c \sim 155$ MeV). Zwei Modelle, das statistische Hadronisierungsmodell und das Koaleszenzmodell, werden häufig verwendet, um

die Produktionsrate von leichten Kernen zu untersuchen. Diese Arbeit konzentriert sich auf letzteres, insbesondere in Bezug auf die leichtesten (Anti-)Kerne, die (Anti-)Deuteronen. Zum ersten Mal wird die Berechnung des Koaleszenzparameters $\mathcal{B}_2$, welcher mit der Produktionswahrscheinlichkeit zusammenhängt, erweitert, um realistische Deuteron-Wellenfunktionen auf der Grundlage der Chiralen Effektiven Feldtheorie (χEFT) einzubeziehen. Die Studie untersucht auch das differentielle Verhalten von $\mathcal{B}_2$ in Bezug auf den Transversalimpuls p_{T}. Um $\mathcal{B}_2$ als Funktion von p_{T} vorherzusagen, bezieht die Berechnung die femtoskopische Quellengröße der emittierten Nukleonen ein, die in pp-Kollisionen bei $\sqrt{s} = 13$ TeV gemessen wurde. Das berechnete $\mathcal{B}_2$ erfasst erfolgreich die beobachtete Steigung in den experimentellen Daten und ist empfindlich gegenüber der Wahl der Deuteron-Wellenfunktion.

Des Weiteren berechnet diese Arbeit die Deuteron-Bildungswahrscheinlichkeit unter Verwendung des Wigner-Formalismus, der eine entscheidende Zutat für die Modellierung eines neuen Koaleszenz-Nachbrenners für Ereignisgeneratoren darstellt. Die Berechnung erfolgt für vier verschiedene Möglichkeiten der Deuteron-Wellenfunktion, die jeweils die Kernwechselwirkung zwischen dem Paar von Nukleonen, welche das Deuteron bilden, widerspiegeln. Die vorhergesagten Deuteron-Spektren in den Ereignisgeneratoren zeigen eine klare Empfindlichkeit gegenüber der gewählten Deuteron-Wellenfunktion, wobei die Argonne-v18- und χEFT-Wellenfunktionen die genaueste Beschreibung des Deuteron-Ertrags in pp-Kollisionen bei $\sqrt{s} = 13$ TeV liefern.

Acknowledgements

The journey of this work would not have been possible without the support of numerous brilliant and helpful individuals.

I would like to thank the incredible research group with several people has become my second family throughout this journey.
I'm extremely grateful to Prof. Laura Fabbietti for being my supervisor. In Hindi, there's a saying that a Guru (supervisor) brings enlightenment and guides us out of the darkness. I am lucky to have received consistent guidance from Laura, which has given me the confidence to navigate this path. Despite my limited knowledge of experimental physics, she believed in me and allowed me to pursue my Ph.D. research. Thanks to her, I had the chance to work on a fascinating and challenging analysis that wouldn't have reached such heights without her support.

Valentina (Vale): you are always the most energetic person in the office. I've learned a lot of physics and Italian slang from you. Thanks for the beautiful advice and an awesome song, "S-Bhawani" though! Dimitar (Dimi): without whom, my learning in experimental physics would have been slow and incomplete. At every step of the analysis, you were there to help. Coffee breaks and discussions, besides physics, are always amazing. It's fair to say that we became friends more than colleagues over time. Rafa: a passionate physicist. Whenever I talk to you, I feel increasingly motivated to pursue physics more and more. Oh, and thanks for the number of ^{3}He candidates from p–d pairs btw;). Laura Šerkšnytė: Bonjour! we used to discuss a lot of physics but never hesitated to share memes and general discussions. Going to many conferences together are some of the best moments. Stephan K. –a colleague and a friend, it's a pleasure completing graduation at a similar time. Thank you for topics enriched with humor in our casual discussions. Among them, the topic of Poppies' secret delight seemed to be the most obvious choice;) thanks for proofreading my thesis and for providing valuable feedback. Maximilian K. –I wonder counting how many times you were called upon to assist with Aliphysics issues at the beginning of my Ph.D :D. Marcel: I must say your offer of farming together is not less exciting, though! you are the best person for having random but interesting discussions. Thanks a lot for helping with translations. Emma: forever calm and cool, never lose interest in tractors! Anton: a computer Geek with brilliance in physics in the office. Thanks for helping with Zusammenfassung! Daniel: Geek 2.0 in the office and Github savior. Good luck with the D meson analysis. Chiara: the only voice with Hallo zusammen! always cheered up the day in the office. Maxi Horst: thanks for giving me a chance to remind complex analysis! Georgios: S.S.C. Napoli fan! keep it up for a permanent position in Napoli. Thomas: I could annoy you thanks to TPC QC and gazillions of errors while compiling O2 tasks that forced us to work together. Berkin: the best teammate for Friday football. Thank you for bearing with me when I had to leave the QC task in between;) Herr Ante: thanks for approving slides and abstracts, minor but important things, and for coordinating the chess tournaments. To former members: Bernie: I'm grateful to have worked with you briefly. I learned a lot about femtoscopy. Andi: My journey started off a bit bumpy, but I managed to survive thanks to your guidance. Cindy: our conversations during coffee breaks gave me a lot of courage for my journey! Luca: the Lord, thanks for helping finalize the analysis for the preliminaries. Many thanks to Petra Z. for taking care of the documents.

I sincerely thank my collaborators Sebastian König (NC State University), Oton Vazquez Doce (INFN Frascati), and Michele Viviani, Alejandro Kievsky, and Laura Marcucci (INFN Pisa) for their acceptance of our joint venture to understand the three-body dynamics of p–d system. Working with them to unravel the theoretical description of these complex systems has been a true pleasure. I greatly appreciate their detailed responses, engaging discussions, and invaluable contributions to the p–d analysis.

I am deeply thankful to Prof. Norbert Kaiser for suggesting this Ph.D. position and for the discussion related to theoretical calculations.

Along my professional journey, Friday football has been incredibly energizing, and it has been one of those rare moments during graduate school that I have truly enjoyed a lot. Thanks to the gang: Thomas, Berkin, Laszlo, Dong-fang, and Georgios & Maxi.

My beloved family, whose support and unconditional love have played a pivotal role in my journey. My mother's (Bhausa) blessings, constant encouragement, and belief in my abilities have strengthened my determination to succeed. Growing up surrounded by my cherished siblings, cousins, nephew, and niece—Bhagwat Bhaba, Bhabhisa, Kanchan di, Dasu Bhaba, Sohan, Kiran, (Bhindo;)-looking forward to your Ph.D.), Arjun-Puran (Nagu-Koku), Kisu-Mumal (Andharo-Samiyo), Kundan, and the little ones Jitu, Tanu, and Raja (the robots with the love of the family)[1], has been an extraordinary experience filled with love and happiness. The moments I shared with them during my visits to family hold a special place in my heart and provide me with constant inspiration to continue on my journey. Their presence has constantly reminded me of the importance of family and fueled my drive to succeed in this endeavor. I am immensely grateful for their love, support, and the countless memories.

Shallu: the most important person in my life. The journey of my Ph.D. has been truly amazing, especially with our deep love. Your contribution to this thesis is immeasurable and interwoven into every aspect. Words cannot express my gratitude for your patience when I could not find time. You have supported me in every possible way. Going for long walks discussing random things, political discourse, and your favorite optimization in mathematics. I am truly happy to think about our future together.

Kaushik Da: a friend and brother, thanks for sharing your academic life experiences. Going on trips together and exploring different restaurants in Munich were some of our best experiences while you were here, Aswathi and Vishnu: you were always there as my "Bhidu" whenever I asked for help.

I'm grateful to my uncle Ganga Mamosa and cousin BhamBhaba for their support and financial assistance during my MS thesis at TUM, which played the role of a foundation for my Ph.D. I'm truly thankful to them.

[1] I may answer all questions, but there's one question I cannot answer: Kadi Avola?

Contents

List of Figures

List of Tables

List of Abbreviations

ALICE	**A** **L**arge **I**on **C**ollider **E**xperiment
CATS	**C**orrelation **A**nalysis **T**ool using the **S**chrödinger equation
CPA	**C**osine **P**ointing **A**ngle
DCA	**D**istance of **C**losest **A**pproach
EoS	**E**quation **o**f **S**tate
FSI	**F**inal **S**tate **I**nteraction
HBT	**H**anbury **B**rown and **T**wiss effect
HI	**H**eavy **I**on
HM	**H**igh **M**ultiplicity
ITS	**I**nner **T**racking **S**ystem
LHC	**L**arge **H**adron **C**ollider
MB	**M**inimum **B**ias
MC	**M**onte **C**arlo simulations
N	**N**ucleon
NS	**N**eutron **S**tar
PDG	**P**article **D**ata **G**roup
PID	**P**article **Id**entification
PV	**P**rimary **V**ertex
RHIC	**R**elativistic **H**eavy **I**on **C**ollider
RUN1	First period of LHC operation
RUN2	Second period of LHC operation
SM	**S**tandard **M**odel
SHM	**S**tatistical **H**adronization **M**odel
SV	**S**econdary **V**ertex
TOF	**T**ime **o**f **F**light detector
TPC	**T**ime **P**rojection **C**hamber
QCD	**Q**uantum **C**hromo**D**ynamics
QGP	**Q**uark **G**luon **P**lasma
χEFT	**C**hiral **E**ffective **F**ield **T**heory
LO	**L**eading **O**rder
NLO	**N**ext to **L**eading **O**rder
AV18	**A**rgonne v_{18}
UIX	**U**rbana **iX**
Y	H**y**peron

Chapter 1

Introduction

1.1 The goal of this work

This thesis aims to study the strong interaction in the system of three nucleons (protons and neutrons) in a vacuum, specifically a pair consisting of a deuteron and a nucleon. Deuterons are light nuclei composed of a neutron and a proton bound by the strong interaction. Nucleons and other hadrons in turn consist of quarks and gluons, the degrees of freedom of the strong interaction within the Standard Model of particle physics. The fundamental theory for the strong interaction is quantum chromodynamics (QCD). The gauge bosons (gluons) can interact among themselves. This occurs when a gluon emits and reabsorbs another gluon, resulting in a change in its momentum and direction. This self-interaction is responsible for rich and complex dynamics. The theory is characterized by its scale dependence, which makes it non-perturbative at low energies. Hence, obtaining reliable theoretical predictions at low energy is difficult. Typically, two approaches are employed in the low energy regime: solving QCD numerically and using effective theories of interactions. On the one hand, numerical methods (lattice) have made significant progress but can only provide reliable predictions for heavy particles. On the other hand, effective theories for the interaction of nucleons are understood by the exchange of virtual mesons. Furthermore, the strong nuclear interaction range is not short enough for quark degrees of freedom to play any significant role. Effective field theories come with free parameters that can be constrained by measurements. So far, parameters are only well-constrained by the experimental nucleon-nucleon (NN) scattering database using phase-shift analysis. Thus, only the nuclear interaction between two nucleons in a vacuum is well-understood.

However, using just the NN interaction from the current theoretical framework fails even to describe the simplest nuclear many-body systems, such as three-nucleon systems, for example, the nucleon-deuteron (N–d) scattering observables or the binding energy of triton or ^{3}He. Over the decades, while studying the three-body systems[1], it was realized that the underlying dynamical ingredients are missing in the theoretical framework, one of which is known as the three-body force. For example, including Three-Nucleon Force (3NF) in the theoretical framework better describes the experimental data of N–d elastic scattering and the binding energy spectrum of light nuclei, which will be discussed later in this chapter. The role of the three-nucleon forces can be much more relevant when there are three or

[1]There is a common misconception that three-body systems and three-body forces are the same things. However, this is incorrect as three-body systems involve the dynamics of three particles, while the underlying force may or may not act on all three particles simultaneously

more nucleons [1–3]. Furthermore, from the scattering experiment perspective, the 3NF effect can be very subtle depending on the studied phase space and thus demands high-precision data. So far, several scattering experiments on N–d have been performed to study the importance of 3NF effects. Besides the scattering, the new experimental method correlation techniques applied to particles produced at the accelerators can investigate multi-baryon systems at distances shorter than those characterizing nuclei and hypernuclei.

The main objective of this study is to analyze the momentum correlation in p–d pairs in high-multiplicity events[2] in pp collisions at 13 TeV using data collected by the ALICE experiment at the LHC. The study aims to investigate the impact of three-body dynamics on the p–d system. This will be accomplished by comparing the measured p–d correlations with a comprehensive three-body calculation that incorporates the composite nature of the deuteron and accounts for the short-range interactions of the p-(pn) system.

In addition to studying the strong interaction in three-body systems, this thesis also aims to study the production of deuterons in collision experiments. From the theoretical standpoint, the formation of light nuclei in the collision experiments is not well understood. The light nuclei, despite being shallow bound objects, with binding energies much smaller than the collision temperatures of about 156 ± 5 MeV [4] (such as deuterons are composed of a neutron and a proton bound by the strong interaction, with a binding energy of approximately 2.2 MeV) are produced in collision experiments. This is puzzling how such a shallow-bound object survives the hot and dense medium of the collisions. Hence the production mechanism of (anti)nuclei remains an open problem under intense debate within the scientific community. The production yield of deuterons and other light nuclei is compatible with statistical hadronization models [4–8] of an equilibrated system at a temperature of $T = 156 \pm 5$ MeV. An alternative theoretical framework so-called coalescence model, suggests that the nuclei are formed following the creation of protons and neutrons, where the formation of a bound object is catalyzed by pions [9–12] provide a good description of the data [12–16] as well. The aim of this is to extend the coalescence framework by using realistic deuteron wavefunction from several interaction models/theories within the coalescence framework, predicting (anti)deuteron yields, which will provide a reliable estimate of the antideuterons produced in the collisions of cosmic rays with the interstellar medium, which constitute the background for the search for dark-matter annihilation with antinuclei in the final state.

1.2 The standard model of particle physics

This section is dedicated to a brief introduction of the ***Standard Model*** (SM) of particle physics to introduce the terminology and concepts which will be used in this thesis.

The Standard Model of particle physics is a theoretical framework that describes how fundamental particles interact with each other. This theory has been widely accepted and has been tested and confirmed by numerous experiments

[2]Events with a high number of produced particles, this will be discussed more in the upcoming chapters.

over the past several decades. The underlying postulate of the theory is that all known matter and energy can be explained by classifying all particles into four different classes: quarks, leptons, gauge bosons, and the Higgs scalar boson, as summarized in Fig. 1.1 [17]. The Higgs scalar bosons are responsible for generating

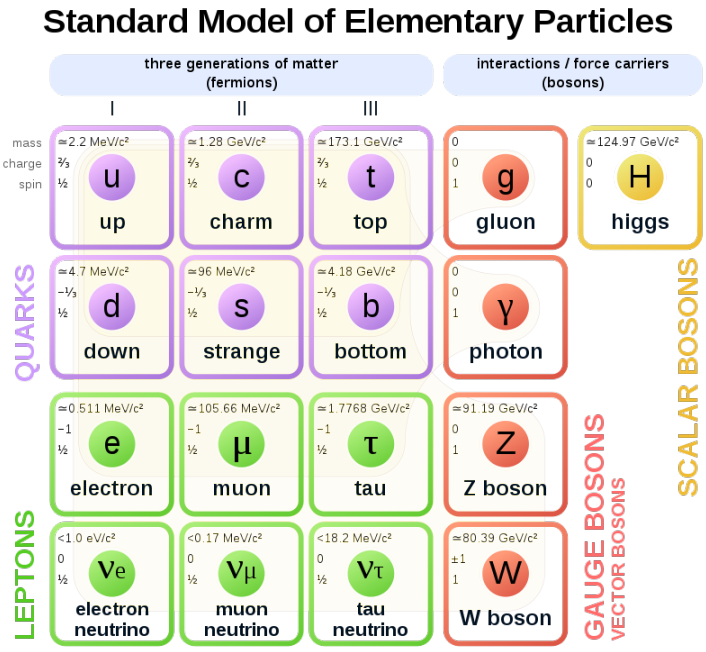

FIGURE 1.1: The elementary particles within the Standard model [18]

the mass of particles at rest. The other category of bosons, particularly the gauge bosons, serve as the carriers of the strong (gluon g), weak (Z and W bosons), and electromagnetic (photon γ) forces. The strong force, as mentioned, is described by quantum chromodynamics (QCD), while the electromagnetic force and weak force are described by quantum electrodynamics (QED) and electroweak theory (EWT), respectively. Gravity, as the fourth fundamental force of nature, completes the picture of the four fundamental forces in nature. Although the Standard Model has been incredibly successful and widely accepted as a theory for the three forces, it has not been able to incorporate gravity, which remains unexplained by the Standard Model. Moreover, phenomena such as dark matter and dark energy, which are currently not explained by the Standard Model, have led to the search for physics beyond the Standard Model (BSM).

The basic building blocks of matter within the SM are quarks and leptons, which are of six different types or flavors and are spin 1/2 fermions. They are grouped into three generations based on their mass. The leptons are further divided into two categories: charged leptons ($q = -1$), which are heavy particles (electron, muon, and tau), and neutral leptons, which are very light neutrinos (ν_e, ν_μ, ν_τ). The leptons interact can with each other particles via the weak force by exchanging W and Z bosons. These bosons are extremely massive, which means that the range of the weak force is very short, on the order of 10^{-18} meters. In addition to the weak force, charged leptons, such as electrons and muons, primarily interact with each other through electromagnetic force.

Quarks are heavier than leptons in their generation, carry electric charge, and

are the only known particles with non-integer elementary charge (q = -1/3 and 2/3). Similar to leptons, quarks can interact via the electromagnetic and weak forces. However, they also possess a color charge (red, green, or blue) mediated by gluons and responsible for the strong interaction. Additionally, gluons can interact with themselves since they also carry the color charge of the strong force. The dynamics of quarks and gluons are described by QCD, a theory of the strong interaction, which will be briefly discussed in the following section.

The three generations of quarks are split into up-like quarks with a +2/3 electric charge and down-like quarks with a -1/3 electric charge. The former consists of up, charm, and top quarks (u, c, t), and the latter consists of down, strange, and bottom quarks (d, s, b), listed in increasing order of mass. Normal nuclear matter is composed of u and d quarks, which are the lightest quarks, i.e. protons uud and neutrons udd.

All particles in the SM have corresponding antiparticles with the same mass, spin, and lifetime as their particles. However, the quantum numbers undergo inversion based on charge, parity, and time reversal (CPT) symmetry[3]. The main consequence of CPT is that antiparticles have opposite electric and color charges to their particle counterparts, leading to three additional color types (anti-red, anti-green, and anti-blue). It's important to note that quarks cannot be separated and are never found individually. As mentioned above, quarks carry a color charge, which is the charge of the strong force. The nature of the strong force does not allow isolated color charges to exist, a principle called ***color confinement***, which will be described in detail in the forthcoming sections.

Although quarks cannot be observed individually, they can form bound states that are colorless and called hadrons. The condition of no net color charge can be fulfilled by combining color with its anticolor or all three colors. Hence, basic hadrons are either composed of a quark-antiquark ($q\bar{q}$) pair or of three quarks or antiquarks (qqq or $\bar{q}\bar{q}\bar{q}$). For example, $q\bar{q}$ pairs are called mesons (pion, kaon, etc.), while the three-(anti)quark bound states are referred to as baryons (proton, neutron, etc.).

1.3 Quantum Chromodynamics

The QCD is the theory of the strong interaction [19–21]. It is a non-Abelian SU(3) gauge theory with quarks and gluons as fundamental degrees of freedom. The force mediators, the gluons exchange the color charge. The quarks are only the elementary particles subject to strong force.

As emphasized above, this work aims to investigate the interaction between hadrons by conducting correlation measurements and comparing the results with theoretical predictions. The theoretical framework utilizes either potential phenomenological models or effective field theory, which leverages the symmetries of the interaction to reduce the number of free parameters. The starting point is quarks and gluons, with the SU(3) symmetry describing the three colors of quarks ($N_c = 3$).

[3]CPT symmetry is a fundamental principle of particle physics that states that the laws of physics must be invariant under three separate transformations: charge conjugation (C), parity inversion (P), and time reversal (T). Further details are available in the university-level textbook, such as [17]

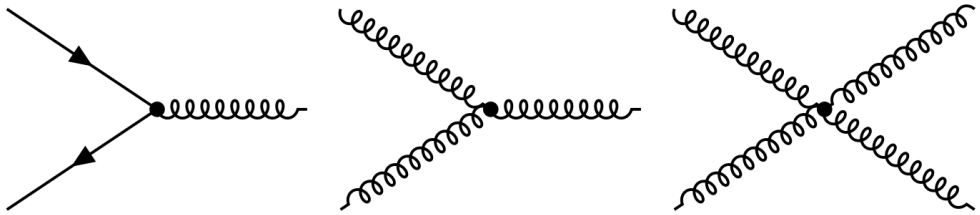

FIGURE 1.2: The basic QCD Feynman diagrams related quark-gluon (left)and gluon-gluon self(middle and right) coupling at order $\sim g$ and $\sim g^2$.

The QCD Lagrangian is given by:

$$\mathcal{L} = \bar{\psi}\left(i\gamma^{\mu} - D_{\mu} - m\right)\psi - \frac{1}{4}G^{a}_{\mu\nu}G^{\mu\nu}_{a}. \tag{1.1}$$

In this context, ψ represents the quark spinor field in six flavors and $N_c = 3$ colors. The bare quark masses are incorporated into the matrix m. The gauge covariant derivative $D_{\mu} = \partial_{\mu} - ig\mathcal{A}^{a}_{\mu}\lambda_a$ governs the quark propagation and their coupling to gluons, where λ_a are the Gell-Mann matrices that modify the color charge upon interaction with a gluon. The fields $\mathcal{A}^{a}_{\mu}$ represent the eight gluon fields with the color index a, and $g = \sqrt{4\pi\alpha_s}$ is the QCD coupling constant. The gluon tensor field $G^{a}_{\mu\nu}$ in Eq. 1.1 is defined as:

$$G^{a}_{\mu\nu} = \partial_{\mu}\mathcal{A}^{a}_{\mu} - \partial_{\nu}\mathcal{A}^{a}_{\mu} - gf^{abc}\mathcal{A}^{b}_{\mu}\mathcal{A}^{c}_{\nu}\,, \tag{1.2}$$

where f^{abc} are the structure constants of the SU(3) group. The terms $-\frac{1}{4}G^{a}_{\mu\nu}G^{\mu\nu}_{a}$ results into $-\frac{g}{2}f^{abc}\left(\partial_{\mu}A^{a}_{v} - \partial_{v}A^{a}_{\mu}\right)A^{b}_{\mu}A^{c}_{v}$ and $-\frac{g^2}{2}f^{abc}f^{cde}A_{a\mu}A_{bv}A^{\mu}_{d}A^{v}_{e}$ which gives rise to the so-called self-coupling of gluons at the order of g and g^2, as shown in Fig. 1.2. The QCD vacuum consists of virtual quark-antiquarks ($q\bar{q}$) pair, which appears as quark-loops on the propagator as shown in the upper left Fig. 1.2, which leads to a charge screening mechanism. However, due to gluon self-coupling, the vacuum is also filled with virtual gluon pairs, which results in gluon loops in the propagator, as shown in the lower left panel of Fig. 1.2. As gluons carry color charge, the effective charge increases with distance, leading to the concept of ***antiscreening*** and the development of a ***running coupling***. Calculating the propagator loop correction in QCD requires the inclusion of both quark and gluon loops. For instance, a formula for the one-loop running coupling constant in QCD is given by:

$$\alpha_s(Q^2) = \frac{\alpha_s(\Lambda^2_{\mathrm{QCD}})}{1 + \beta_0\alpha_s(\Lambda^2_{\mathrm{QCD}})\ln(Q^2/\Lambda^2_{\mathrm{QCD}})}\,. \tag{1.3}$$

The function $\beta_0 = (11N_c - 2n_f)/(12\pi)$ depends on the color charge N_c and n_f the number of flavors. Q is the momentum transfer (energy) of the interaction, and Λ_{QCD} is the QCD scale. For Q^2 values close to QCD scale ($\sim$200 MeV/c) the coupling constant becomes large and below this value, the perturbative approaches to QCD break down. The QCD coupling constant is plotted in Fig. 1.3.

At short distances (or large momentum transfers), the antiscreening effect causes the strong coupling constant to decrease, resulting in the quarks inside hadrons behaving more like free particles when probed at high energies. This phenomenon

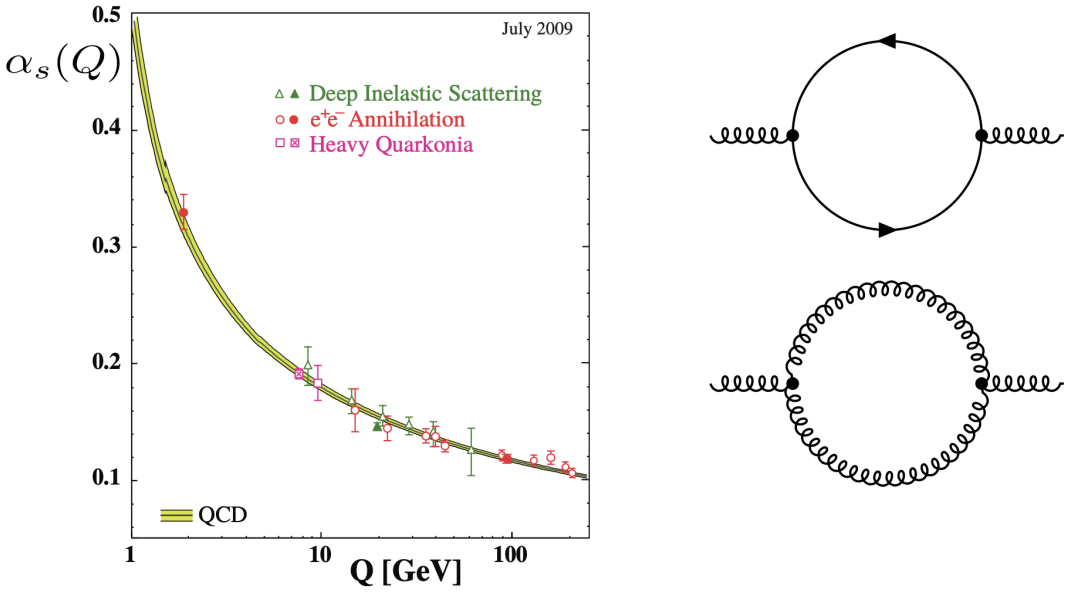

FIGURE 1.3: Left: the running coupling constant of QCD, compared to experimental constraints [22]. Right: leading order quark-gluon and gluon-gluon loop diagrams contributing to the running coupling constant.

is known as ***asymptotic freedom***[4]. As the strong coupling constant α_s is weak at high energies, QCD can be studied using perturbative methods, such as effective field theories, allowing for quantitative predictions of hard scattering cross sections in hadronic interactions.

On the other hand, at larger distances (or lower momentum transfers), the strong coupling constant α_s increases, becoming so strong that it becomes impossible to isolate a single quark from a hadron, leading to ***quark confinement***. Confinement has been confirmed by solving the QCD Lagrangian numerically using lattice QCD, but it is nonperturbative and has not yet been proven mathematically from first principles.

Although there is no analytical approach to low-energy QCD, effective field theories and numerical solutions of the QCD Lagrangian have been used to extract physics at low energies. However, many of the features of low-energy QCD remain unexplored or not firmly understood. Therefore, experimental studies of fundamental hadron properties, such as their interactions, can play a key role in advancing our understanding of the theory.

Why are hadrons massive compared to quarks?

The quark masses m in the QCD Lagrangian written in Eq. 1.1 are input parameters generated via the Higgs mechanism [23]. However, considering the masses of typical hadrons in nuclear physics, the quark masses, particularly the up, down, and strange quarks listed in Tab. 1.1, are much smaller than the scale of hadron mass. Therefore, an important question to ask is how the mass generation of

[4]The discovery of asymptotic freedom (1973) was a major breakthrough for QCD and was awarded the Nobel prize in 2004 to David Gross and Frank Wilczek, and David Politzer.

quark flavour	mass (MeV)
u	$2.16^{+0.49}_{-0.26}$
d	$4.67^{+0.48}_{-0.17}$
s	93^{+11}_{-5}

TABLE 1.1: The quark masses m for u, d, and s [24].

hadrons takes place. In the limit of vanishing quark masses, the QCD Lagrangian is invariant under a unitary transformation of left- and right-handed quark fields known as chiral transformations. This gives rise to an exact symmetry of the QCD Lagrangian, which is denoted as $\mathrm{SU(3)_R \times SU(3)_L \times U(1)_V}$. The $\mathrm{U(1)_V}$ subgroup leads to the conservation of the baryon number. The $\mathrm{SU(3)_R \times SU(3)_L}$ is the chiral symmetry of the QCD Lagrangian but not a symmetry of the ground state of the QCD Lagrangian $\langle 0|q\bar{q}|0\rangle$. This symmetry is broken in two ways: i) explicitly broken because u and d quark masses are not exactly zero, ii) spontaneously broken[5]; chiral symmetry would imply the existence of a degenerate hadron spectrum of opposite parity, but the experimental observation of the ρ-meson of negative parity ($J^P = 1^-$) and the a_1-meson of positive parity ($J^P = 1^+$), with very different masses [24], suggests that the chiral symmetry of the QCD Lagrangian is spontaneously broken. The QCD vacuum is then filled with so-called *chiral quark-antiquark condensates* with a non-zero expectation value of mass $\langle 0|q\bar{q}|0\rangle \approx (-250\ \mathrm{MeV})^3$ [25].

The quark condensate under the chiral transformation becomes $\langle 0|q_L\bar{q}_R + q_R\bar{q}_L|0\rangle$, which breaks the chiral symmetry by connecting left- and right-handed quark fields. As a result, the quark propagator (dynamics) in the QCD vacuum is dressed by its interactions, leading to an effective mass increase. Additionally, as mentioned earlier, the explicit breaking of chiral symmetry causes the mixing of left- and right-handed quark fields. However, since the quark masses are small, spontaneous chiral symmetry breaking is dominant in generating hadron masses. The chiral symmetry is restored if the vacuum temperature or density is high, where the quark condensates are expected to melt [25, 26].

1.4 The two- and three-nucleon interactions

At the collider experiments, the hadrons typically experience rather low energies compared to the QCD scales, where the QCD Lagrangian cannot be solved analytically. To explore physics at low energy, this study relies on different theoretical tools, which provide access to the rich properties of QCD. This section briefly overviews the most relevant theoretical tools used to study the NN and 3N systems in this work. This includes the Lippmann-Schwinger equation for the scattering problem and the Faddeev formalism for treating the three-nucleon problems. It is followed by a discussion of the existing, realistic NN and 3N potential models, which are key in describing the strong interaction in three-body systems.

One way to study the interaction between two hadrons is to use quantum mechanical scattering to describe the scattering cross-section of the processes. The scattering processes are directly related to the transition matrix/operator (t), which provides a relation between the free asymptotic state and the 2N scattering state.

[5] A continuous symmetry is called spontaneously broken if a symmetry of the Lagrangian is not realized in the ground state of the system.

Starting with an initial quantum state $|\phi\rangle$, which describes the free particles that come from an infinite distance in space to the potential V, due to potential V, the particles scatter and move away from V in a scattering state $|\psi\rangle$. At large distances, the final state $|\psi\rangle$ can be given as a sum of an incoming wave and an outgoing scattered wave. In order to extract $|\psi\rangle$, the Lippmann-Schwinger (LS) equation is used [27].

$$|\psi\rangle = |\phi\rangle + \frac{1}{E - H_0 + i\epsilon} V|\psi\rangle \,, \tag{1.4}$$

where E is the energy and H_0 is the Hamiltonian of the incoming particle. The LS equation is solved for the limit $\epsilon \to +0$. In terms of the transition operator t, it satisfies the relation $t = V + VG_0t$, where G_0 is the Green's operator for the non-interacting system and is given by

$$G_0 = \frac{1}{E - H_0 + i\epsilon} \,. \tag{1.5}$$

Here, t is a fundamental quantity for calculating scattering observables [27]. The LS equation is formulated for the NN scattering; however, for three-particle systems, one uses the Faddeev equation instead of the LS equation [28]. Ignoring the Coulomb interactions, the basic Faddeev equation for the three-nucleon bound-state problem can be written as

$$|\psi\rangle = G_0 t P \,|\psi\rangle \,, \tag{1.6}$$

where G_0 is the free three-nucleon Green's function, as defined in the case of LS equations. $|\psi\rangle$ is one of the three equivalent Faddeev components, t refers to the pair-wise two-nucleon T-matrix, and P is a permutation operator. Further details of the scattering state for 3N can be found in [28].

The scattering observables for NN and 3N systems can be calculated using techniques such as LS and Faddeev equations with input from NN and 3N potentials. These potentials can be calculated using various approaches such as (a) "realistic potentials," which are semi-phenomenological and based on the meson-exchange mechanism, (b) based on Chiral Effective Field Theory (χEFT), and (c) the coupled-channel approach, which includes the excitation of Δ isobars in nucleons.

1.4.1 Realistic NN potentials

The nucleon-nucleon interaction is quite well understood, as nucleons are the fundamental building blocks of stable matter and are experimentally accessible. In the past several decades, a wealth of NN scattering experiments have provided an extensive scattering database to constrain the properties of the interaction. For example, partial wave analyses of measured NN cross-sections have made it possible to determine the interaction accurately. The resulting interaction potentials are often developed without using the details of the QCD Lagrangian but using the nature of the NN interaction, which is governed by three different parts of interactions depending on the inter-nucleon distance r. The simplest part is the One-Pion-Exchange Potential (OPEP), which is often added to the other parts of the potential as a tail and is known as the long-range interaction ($r \geq 2$ fm, e.g., the Yukawa potential). The second part, intermediate-range interaction (1 fm $\leq r \leq$ 2 fm), includes various single-meson exchange terms and is mainly from the scalar-meson exchanges (two pions and heavier mesons) and is often probed in normal nuclear densities. The third and most important part, the short-range interaction

($r \leq 1$ fm), is given by exchanges of vector bosons (heavier mesons and multi-pion exchanges) responsible for the strong nuclear force at a very short range. Using the nature of the strong interaction at different ranges, several potential models have been developed to accurately describe NN interactions. The most commonly used being boson exchange models such as Nijm-I, Nijm-II [29], Charge-Dependent (CD) Bonn [30], phenomenological models such as Argonne group potentials (AV14 and AV18 [31]) and Urbana group potentials (e.g., UrbanaV14). These models have been extended to describe many Baryon-Baryon (BB) interactions such as Hyperon-Nucleon (YN) and Hyperon-Hyperon (YY) interactions. Meson exchange models are based on the interaction carried by the exchange of mesons between a pair of particles, and the range of interaction is governed by the meson's Compton wavelength, which is inversely proportional to the meson mass. Phenomenological models use symmetries such as rotation, translation, and isospin. In general, these models often have a similar spirit as EFT and have several parts consisting of combinations of central terms, spin-spin ($\vec{\sigma}_1 \cdot \vec{\sigma}_2$), spin-orbit ($\vec{L} \cdot \vec{S}$), and tensor ($S_{12}$) terms responsible for strong nuclear interaction. Each of these terms is multiplied with and without isospin-dependence ($\vec{\tau}_1 \cdot \vec{\tau}_2$) to account for the total isospin of the NN system. Most of the NN potential models have many free parameters that are fitted to high precision NN scattering databases with reduced χ^2 close to 1, but they are only suitable at energy scales below pion production.

Although some of the aforementioned phenomenological and boson-exchange potentials have a short-range interaction based on QCD, the relation to QCD is not systematic in terms of theoretical framework. Nonetheless, another set of NN potentials which are obtained from the Lagrangian exploiting the chiral symmetry of the QCD Lagrangian has been developed. The chiral potentials are obtained from the chiral Lagrangians which are written in terms of pions and nucleons and their covariant derivatives including the chiral symmetry of QCD. The effects of higher degrees of freedom are integrated out as their effects might be considered in some undetermined coefficients at higher order terms. The resulting effective Lagrangian gives rise to the NN potential, which is expanded systematically in the powers of $(Q/\Lambda_{\mathrm{QCD}})$, where Q is the momentum transferred. Thus, the resulting potential is consistent with the symmetries of QCD and provides a logical and systematic way to describe NN interaction and directly relates it to QCD. Within the expansion scheme χEFT, NN potentials have been derived up to five orders of expansions ranging from leading order (LO) to next-to-next-to-next-to-next-to-leading order ($\mathrm{N^4LO}$). These NN potentials are fitted to the available NN data below the pion-production threshold using the data up to 2016 [32]. The potential from the highest order ($\mathrm{N^4LO}$) provides the best description of the NN data with reduced χ^2 close to 1.15, which is the highest precision ever accomplished by the chiral potentials so far. In this thesis, two body potentials namely the Argonne v_{18} and chiral NN potentials at ($\mathrm{N^3LO}$) [33] and ($\mathrm{N^4LO}$) [32] expansions are used to study NN observables.

1.4.2 Realistic 3N potentials

Although NN potentials can accurately reproduce the NN scattering database and the deuteron binding energy, as well as provide high predictive power suitable for "ab initio" calculations, they are not sufficient for a comprehensive understanding of nuclear physics. This limitation arises due to the following reasons:

- The simplest three-nucleon system, the N–d scattering observable; is not reproduced by the NN interaction alone [34, 35]. Calculations of scattering cross sections using modern NN potentials are shown in blue bands in Fig. 1.4.2.
- The NN potential alone cannot describe three- and four-nucleon bound and scattering states. The ground or low-lying excited state energies of light nuclei predicted using only the NN interaction from AV18 lie much above the experimentally measured values, as shown in Fig. 1.4. Moreover, the doublet ($S = 1/2$) channel neutron-deuteron scattering length ($a^2_{\mathrm{nd}} = 1.258$ fm) is overestimated in comparison to the experimental measurement ($a^2_{\mathrm{n-d}} = 0.645 \pm 0.003 \pm 0.007$ fm) [36].
- The equilibrium density ρ_0 of Symmetric Nuclear Matter (SNM) is overestimated using only the NN potential. The green curve shows a much larger value than $\rho_0 \sim 0.16, , \mathrm{fm}^{-3}$, as shown in Fig. 1.5.

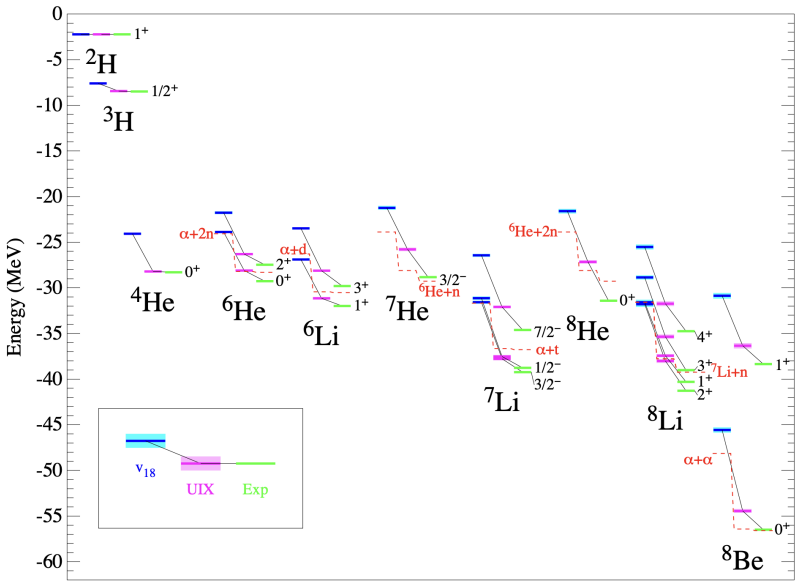

FIGURE 1.4: Figure from [37] compares the energies of ground or low-lying excited states of light nuclei calculated using the AV18 and AV18/UIX interactions with experimental measurements. The light shades represent the statistical errors obtained from Monte Carlo simulations. The dashed lines indicate the thresholds for each model or experiment against breakup.

With several limitations as mentioned above, it has been realized that the theoretical description of nuclear systems with $A \geq 3$ requires further development, namely the inclusion of three-nucleon forces (3NF) [39]. The 3NF was initially developed and described by Fujita-Miyazawa based on the two-pion exchange model in 1957 [39] 3NF term is depicted by the Feynman diagram in Fig. 1.7. The 3NF plays a key role when there are three or more nucleons, the existence of 3NF is due to the fact that the nucleons themselves are not point-like objects but have an internal structure, as they are made of up and down quarks.

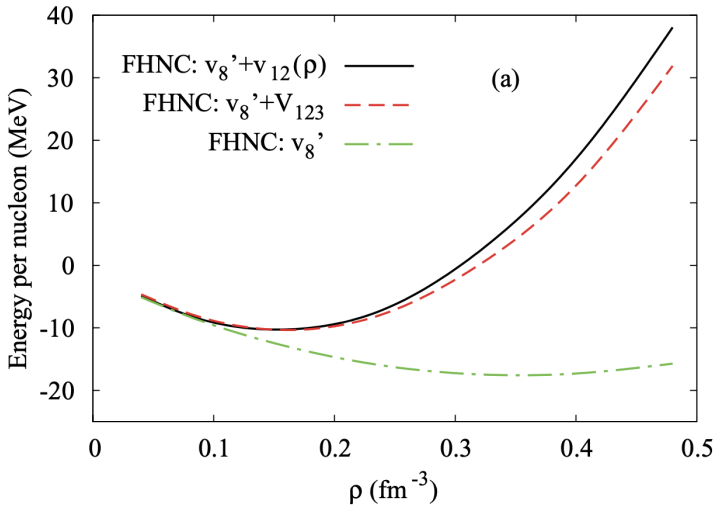

FIGURE 1.5: Figure from [38] showing the effect of the 3N interaction on the energy per particle for SNM calculations. The black line represents the results obtained using the density-dependent potential added to the Argonne v_{18} NN potentials, while the dashed red line shows the results obtained from the genuine three-body potential. The green line represents the results obtained from the two-body potentials alone.

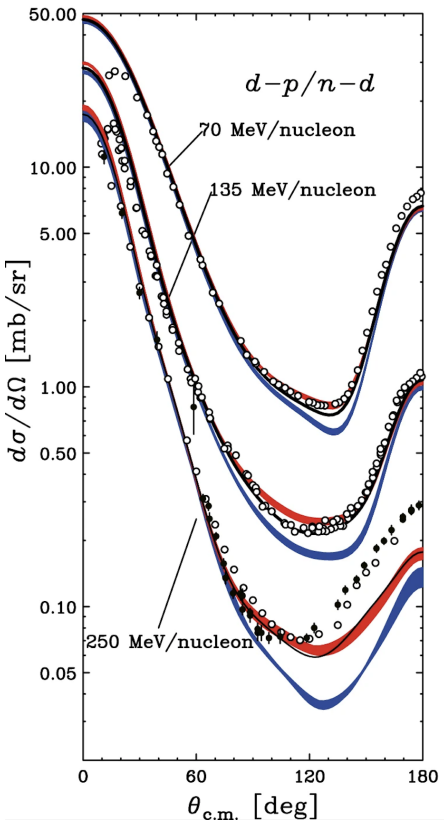

FIGURE 1.6: Figure adapted from [35] shows a comparison of measured and calculated differential cross sections for elastic N–d scattering. The open circles at 70 and 135 MeV/nucleon represent p–d scattering cross sections, while the open and solid circles at 250 MeV/nucleon are the p–d and n–d data, respectively. The red (blue) bands correspond to calculations based on modern NN potentials, namely CD Bonn, AV18, Nijmegen I, and II with (w/o) the TM99 3NF. The solid lines show calculations based on the AV18 potential with the Urbana IX 3NF.

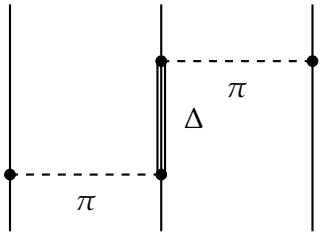

FIGURE 1.7: Feynman Diagram for three-nucleon interaction via two-pion exchange in the Fujita Miyazawa three-nucleon potential term.

UIX three-body potential

The Urbana IX (UIX) [40] is a widely used three-body potential for three-body systems. It consists of two terms: the two-pion (2π) exchange term $V^{2\pi}$ and the phenomenological core repulsive core V^{core}. The former gives rise to an attractive interaction that turns out to be useful in fixing the problem of underbinding in light nuclei, but worsens the nuclear matter-energy. Meanwhile, the latter prevents nuclear matter from being overbound at large density. The term $V^{2\pi}$ is based on the Fujita-Miyazawa approach and can be written as a sum of an anticommutator and a commutator term.

$$\hat{V}^{2\pi}(3:12) = A_{2\pi}\left\{\hat{X}_{13}, \hat{X}_{23}\right\}\left\{\tau_{13}, \tau_{23}\right\} + C_{2\pi}\left[\hat{X}_{13}, \hat{X}_{23}\right]\left[\tau_{13}, \tau_{23}\right] \tag{1.7}$$

where

$$\hat{X}_{ij} = Y\left(m_\pi r\right)\sigma_{ij} + T\left(m_\pi r\right)S_{ij}. \tag{1.8}$$

The $\xi(x)$ are short-range cutoff functions defined by

$$\xi_Y(x) = \xi_T(x) = 1 - e^{-cx^2}. \tag{1.9}$$

The parameter c is a cutoff parameter, which is kept fixed at $c = 2.1\text{fm}^{-2}$, the same value as in the case of the one-pion exchange term of the Argonne v18 two-body potential. On the other hand, the term $A_{2\pi}$ is varied to fit the observed binding energies of ^{3}H. The repulsive term V^R is spin-isospin independent and can be written in the simple form $V^R(3:12) = U_0 T^2(m_\pi r_{13}) T^2(m_\pi r_{23})$, where $T(x)$ is a tensor component. The strength U_0 is adjusted to reproduce the empirical nuclear matter saturation density. For example, with AV18, $U_0 = 0.0048$ MeV.

Adding the UIX to the AV18 calculations brings the theoretical prediction of the N–d scattering cross-section closer to the measured values, as shown by the solid black line in Fig. 1.4.2. Moreover, the theoretical expectation of the binding energies of ^{3}H are precisely reproduced, and the binding energy of ^{4}He turns out to be very close to the experimental value, as shown by the pink bands in Fig. 1.4. However, a still large underbinding is provided by the AV18+UIX for increasing A and $A - Z$, which is the subject of further discussion and irrelevant to this thesis. In addition, including UIX improves the doublet n–d scattering length close to the measurement, but it still fails to reproduce the measured values for large energies.

3NF models based on Chiral EFT

In the past decades, χEFT has been extensively employed to derive 3N potentials [41–44]. This approach offers the possibility of treating the NN and the 3N potentials

more consistently by fixing some of the low energy constants with NN and πN data, which are also used in the definition of the 3NF. In fact, an extension to the next-to-next-to-leading-order (NNLO) 3N interaction requires only two additional parameters (c_D and c_E) with respect to low energy constants in the NN interaction. These constants are typically determined by fitting low-energy 3N observable. Unfortunately, however, πN and NN data still leave some uncertainties on the c_i's that cannot be completely determined by 3N observables such as triton binding energy. In this thesis, chiral 3N potentials up to N^{2}LO and N^{3}LO, UIX, and the chiral-inspired revision of Tucson-Melbourne (TM') are combined with AV18 NN potentials or chiral NN potentials to calculate relevant observables [45].

1.5 Femtoscopy

The technique of femtoscopy has its origins in traditional intensity interferometry, which was originally used to measure the angular dimensions of stars using the Hanbury-Brown and Twiss (HBT) interferometry [46]. In particle physics, this approach is employed to measure the yield of particle pairs instead of intensities. An interference occurs due to the final state interaction (wavefunction) of the emitted particles from a source. One of the first experimental HBT measurements in 1960 was performed using pions in proton-antiproton reactions [47]. The angular distributions of like and unlike-sign combinations of pion pairs were found to be different. However, it was soon realized that this discrepancy could be explained if the Bose-Einstein statistics of identical bosons were employed [48]. The two-particle correlations not only occur due to the (anti-symmetrization) of the wavefunction but also due to the Coulomb and strong interactions between the pair of particles. Further developments in the theory and experiments have led to the refinement of the formalism where correlation measurements became the tool to study the space-time properties of the particle emitting region created in heavy-ion collisions [49]. Since the typical length of the spatial extension of the source in heavy-ion collisions is of the order of a few femtometers, this method is commonly referred to as femtoscopy.

The idea can be inverted, and femtoscopy can be applied to study the interaction of particle pairs, where the small source plays a key role in the study of strong interactions between different particle pairs at short distances. The advantage of this method is that the interaction between any detectable particle pair produced in elementary or heavy-ion collisions with known source extension can be studied. This includes the measurements of interactions that may not be accessible via scattering experiments due to the difficulties associated with the production of particles and handling beams of unstable hadrons.

1.5.1 Two-particle correlation function

In femtoscopy, the two-particle correlation function is the main observable. It is defined as the ratio of the Lorentz-invariant yield of a particle pair to the product of the single-particle yields, where $\vec{p}_i$ is the momentum of each particle [50].

$$C\left(\vec{p}_1, \vec{p}_2\right) = \frac{E_1 E_2 \, \mathrm{d}N^{12} / \left(\mathrm{d}^3 p_1 \, \mathrm{d}^3 p_2\right)}{\left(E_1 \, \mathrm{d}N^1 / \mathrm{d}^3 p_1\right)\left(E_2 \, \mathrm{d}N^2 / \mathrm{d}^3 p_2\right)} = \frac{\mathcal{P}\left(\vec{p}_1, \vec{p}_2\right)}{\mathcal{P}\left(\vec{p}_1\right)\mathcal{P}\left(\vec{p}_2\right)} \,. \tag{1.10}$$

The correlation function can also be understood as the ratio between the probabilities $\mathcal{P}(\vec{p}_1, \vec{p}_2)$, the probability of finding a pair of particles with momentum $\vec{p}_1$ and $\vec{p}_2$, and $\mathcal{P}(\vec{p}_i)$, the probability of finding each particle with momentum $\vec{p}_i$. In the absence of any correlations, the two-particle probability factorizes, $\mathcal{P}(\vec{p}_1, \vec{p}_2) = \mathcal{P}(\vec{p}_1)\mathcal{P}(\vec{p}_2)$, and the correlation function is equal to unity. In the experiment, a convenient choice of reference frame is the *pair rest frame* (PRF), where the correlation function can be redefined in terms of the particle momenta $\vec{p}_i^*$ in the PRF as

$$C\left(\vec{p}_1^*, \vec{p}_2^*\right) = C\left(k^*\right) = \zeta(k^*)\frac{N_{same}(k^*)}{N_{mixed}(k^*)} \xrightarrow{k^* \to \infty} 1\,, \tag{1.11}$$

where $k^* = 1/2|\vec{p}_1^* - \vec{p}_2^*|$ is relative momentum in PRF. $N_{same}(k^*)$ is the measured yield of the correlated pairs *signal* while $N_{mixed}(k^*)$ is the measured yield of the on correlated pair *reference* required to account for the phase-space background, the reference distribution is divided by the signal. The reference sample is obtained by building pairs from a large sample of particles in separate events so that this distribution exhibits a much smaller statistical uncertainty than $N_{same}(k^*)$. At large values of k^*, the particles are not interacting, and the final-state interaction is absent. Therefore, the $N_{same}(k^*)$ distribution is normalized using a constant $\zeta(k^*)$ chosen so that $C(k^*) = 1$ in the region (typically $k^* > 200$ MeV$/c$) where the femtoscopic signal is expected to be absent. More details on the experimental aspects of the correlation function are discussed in Chap. 4.2.3.

In the quantum mechanical description, the correlation between a pair of particles can be related to the particle emission and the interaction of the particle pair, as defined in [49].

$$C(\mathbf{P}, \mathbf{q}) = \frac{\int \mathrm{d}^4x_1\, \mathrm{d}^4x_2 s_1\left(\mathbf{p}_1, \mathbf{x}_1\right) \cdot s_2\left(\mathbf{p}_2, \mathbf{x}_2\right) \left|\psi\left(\mathbf{q}, \mathbf{r}^*\right)\right|^2}{\int \mathrm{d}^4x_1 s_1\left(\mathbf{p}_1, \mathbf{x}_1\right) \int \mathrm{d}^4x_2 s_2\left(\mathbf{p}_2, \mathbf{x}_2\right)} \tag{1.12}$$

where $\mathbf{P} = \mathbf{p}_1 + \mathbf{p}_2$ is the total momentum of the pair and $\mathbf{q}$ is the relative momentum of the pair $q^\mu = \frac{1}{2}\left[(p_1 - p_2)^\mu - \frac{1}{\mathbf{P}^2}\left(p_1 - p_2\right)_v \cdot P^v \cdot P^\mu\right]$. The function $s_i\left(\mathbf{p}_i, \mathbf{x}_i\right)$ is the emission functions for particle i which gives the probability to production of a particle i with momentum $\mathbf{p}_i = (E_i, \vec{p}_i)$ at the space-point $\mathbf{x}_i = (t_i, \vec{x}_i)$. While the Lorentz-invariant production spectra of particle i are then given by

$$E_i \frac{\mathrm{d}N^i}{\mathrm{d}^3p_i} = \int \mathrm{d}^4x_i\, s_i(\mathbf{p}_i, \mathbf{x}_i)\,, \tag{1.13}$$

and

$$E_1E_2 \frac{\mathrm{d}N^{12}}{\mathrm{d}^3p_1\, \mathrm{d}^3p_2} = \int \mathrm{d}^4x_1\, \mathrm{d}^4x_2 s_1\left(\mathbf{p}_1, \mathbf{x}_1\right) \cdot s_2\left(\mathbf{p}_2, \mathbf{x}_2\right) \left|\psi\left(\mathbf{q}, \mathbf{r}^*\right)\right|^2\,. \tag{1.14}$$

The probability weights are given by square of the Bethe-Salpeter amplitude [51] $\left|\psi\left(\mathbf{q}, \mathbf{r}^*\right)\right|^2$. Assuming that the emission time is equalised in the PRF $t_1^* - t_2^* = 0$, the time component of the $\psi\left(\mathbf{q}, \mathbf{r}^*\right)$ is dropped i.e. $\psi\left(\mathbf{q}, \mathbf{r}^*\right) \to \psi\left(\vec{q}, \vec{r}^*\right)$ [51]. However, the time dependence still remains in the source function s_i in the Eq. 1.12. Furthermore, a smoothness approximation in the emission function with $\mathbf{p}_i \to \overline{\mathbf{p}}_i = m_i/\left(m_1 + m_2\right)\mathbf{P}$ is used. Defining $\mathbf{r}^* = \mathbf{x}_1 - \mathbf{x}_2$ and $\mathbf{R} = \left(\mathbf{x}_1 + \mathbf{x}_2\right)/2$ gives the single particle source as

$$S_{\mathbf{P}}\left(\vec{r}^*\right) = \int \mathrm{d}t^* \mathcal{S}_{\mathbf{P}}\left(\mathbf{r}^*\right)\,. \tag{1.15}$$

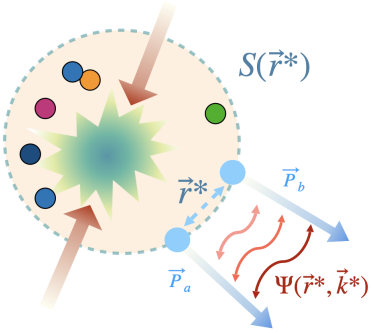

FIGURE 1.8: Illustration of the femtoscopy principle at a collider. Two beam particles (red arrows) collide to produce a group of particles (colored circles within the large dashed circle) emitted from an effective surface known as the emission source $S(\vec{r})$. A pair of particles is selected for analysis, and they may undergo final state interactions that result in a correlation in their relative momentum $\vec{k}^*$.

The momentum dependence however is removed by choosing the PRF where $\mathbf{P} = \vec{p}_1 + \vec{p}_2 = 0$, and $\vec{q} \to k^*$ becomes a scalar quantity, where $k^* = \frac{1}{2}\left|\overrightarrow{p_1}^* - \overrightarrow{p_2}^*\right|$. After employing these transformations the Eq. 1.12 is transformed in the so-called ***Koonin-Pratt relation*** [52] which is written as

$$C\left(k^*\right) = \int \mathrm{d}^3 r^* \left|\psi\left(k^*, \vec{r}^*\right)\right|^2 S\left(\vec{r}^*\right) . \tag{1.16}$$

In this relation the correlation function $C(k^*)$ depends only on two terms: the source function $S(\vec{r}^*)$, which describes the space-time configuration of the emitted particles, and $\psi(k^* \vec{r}^*)$, which accounts for the propagation of the particles in space, including any interactions they may undergo. In the early stages of femtoscopy in particle physics, the technique was used to study particle-emitting sources $S(r^*)$ in systems such as π–π or K–K correlations, where the final state interactions can be neglected [51]. In such systems, the interference occurs due to quantum statistics, also known as Bose-Einstein correlations, resulting from the symmetrization of the wavefunction. Fig. 1.8 provides an illustrative sketch of the femtoscopy principle.

1.5.2 Femtoscopic source

The source distribution plays crucial role in the femtoscopic studies aiming at investigation of the interaction between pair of particles.

The femtoscopic source $S(\vec{r}^*)$ lacks a strong theoretical framework, and to understand its physical meaning in terms of a three-dimensional spatiotemporal source distribution, it is useful to describe its size and shape using certain parameters. The simplest description assumes a Gaussian parameterization of the shape of the source distribution[6]. Additionally, time and momentum dependence in the source function is often ignored. In the case of a single particle, the Gaussian emitter

[6]It should be noted that in reality, source distributions can deviate from the Gaussian form, such as the strongly decaying short-lived resonances that may lead to non-Gaussian tails, which will be discussed later in this thesis.

is defined as follows

$$s(\mathbf{p},\mathbf{x}) = \delta\left(t^*\right)\exp\left(-\frac{x^{*2}+y^{*2}+z^{*2}}{2\left(r_{\text{Gauss}}\right)^2}\right). \tag{1.17}$$

Defining $\vec{r}^* = \vec{x}_1 - \vec{x}_2$ and $d\vec{R} = (\vec{x}_1 + \vec{x}_2)/2$ performing d^4R integral leads to Eq. 1.16 where a Gaussian distribution gives the two-particle source.

$$S\left(\vec{r}^*\right) = \frac{1}{\left(4\pi r_{\text{Gauss}}^2\right)^{3/2}}\exp\left(-\frac{|\vec{r}^*|^2}{4\left(r_{\text{Gauss}}\right)^2}\right). \tag{1.18}$$

The final source depends only on the relative distance, i.e., $r^* \equiv |\vec{r}^*|$. Although the width of single-particle source distributions may differ in spatial directions, three-dimensional source studies can investigate this using a three-dimensional measurement of the correlation function [49]. However, these kinds of analyses require significant statistics and may be impossible to perform for low-abundance particle species. Pions are abundantly produced in high-energy collision experiments, allowing for a sufficient number of same-charge π-π pairs to study three-dimensional source geometry [49, 53, 54]. Furthermore, heavy-ion collisions at relativistic energies can also produce an abundance of kaons, extending these source studies to K-K pairs [55]. In practical cases, the number of particle pairs is not sufficient due to fewer particle abundances, such as heavier particles, therefore the correlation function is typically measured in one dimension (i.e. r^*) in pp or p–Pb collisions. In this situations the source function $S(r^*)$ in Eq. 1.16 is parameterized with a Gaussian function of the one-dimensional source size r_{Gauss} also referred to as r_0.

To investigate the strong interaction in p–d system, the source size for p–d pairs is determined using the study relies on the common source for baryons in pp collisions at $\sqrt{s} = 13$ TeV, obtained by the ALLICE Collaboration [56], which is obtained using the well-known interaction between p–p pairs and the relatively well-known interaction among p–Λ pairs. More details on the estimation of the source size for p–d pairs will be discussed in Chap. 4.4.

1.5.3 Two particle wavefunction

One of the main aspects of femtoscopy is that it provides access to the interactions between given pairs of particles whose source is known. This interaction is described by the wave function $\psi(k^*,\vec{r}^*)$ in Eq. 1.16, which is a function of the relative coordinates of the particle pairs.

There are various methods to calculate the two-particle wavefunction $\psi(k^*,\vec{r}^*)$. One natural approach is to solve the Schrödinger Equation (SE) for a two-particle system with a central potential $V(r^*)$, where the potential is typically a function of only the relative distance r^*. After obtaining the solution, the wavefunction must be symmetrized or antisymmetrized depending on whether the particles obey Bose-Einstein or Fermi-Dirac statistics. In practice, solving the SE analytically can be a challenging task; hence numerical methods are typically used to obtain solutions. In this thesis, we use the numerical approach developed by Dimitar Mihaylov, which is implemented in the Correlation Analysis Tool Solving the Schrödinger Equation (CATS) framework [57]. The CATS codes are publicly available, and more

details are discussed in Dimitar's Ph.D. thesis [58].

Apart from solving the SE, there is another possibility to calculate $\psi(k^*, \vec{r}^*)$, the approach based on the formalism employing scattering parameters for the considered particle pair as known as Lednický-Lyuboshitz. This approach will be discussed in details in Chap. 1.5.4.

To begin the discussion, we first consider the simplest cases of Bose-Einstein and Fermi-Dirac statistics, where particles are non-interacting and can be identical fermions (e.g., proton-proton) or bosons (e.g., pion-pion). In these two cases, the total two-particle relative wavefunction $\psi(k^*, \vec{r}^*)$ must be (anti-)symmetric under the exchange of the particle positions for (fermions) bosons, which implies that the parity must follow $P = (-1)^{L+S+1} \stackrel{!}{=} -1$ and $P = (-1)^{L+S} \stackrel{!}{=} 1$ for fermions and bosons, respectively. The resulting correlations for these cases are shown in the left panel of Fig. 1.9. It should be noted that in the correlation functions of π–π and p–p pairs obtained without the presence of interaction, there is a non-zero signal emerging due to the (anti-)symmetrization of the total wavefunction. The strength of the signal is particularly sensitive to the size of the emission source. These effects are relevant because the colliding system's size is small and most prominently occurs with π–π and K–K pairs since the meson-meson strong interaction is less prominent compared to the baryon-baryon strong interaction.

The correlation signal can be significantly influenced by the presence of electric charge on the particles. The long-range Coulomb potential, which decreases slowly as $1/r^*$, can introduce additional correlation even at large pair separations. In the case of an attractive Coulomb interaction, the correlation signal is enhanced with $C(k^*) > 1$, while a repulsive Coulomb interaction leads to a depletion in the correlation signal with $C(k^*) < 1$, as shown in the right panel of Fig. 1.9. The most significant contribution to the correlation function arises from the strong interaction. If applicable to the particle pair under study, the effect of (anti-)symmetrization of the wavefunction as well as Coulomb interaction, can serve as a baseline for the measurement, but the primary focus of the measurements is to study the strong interaction in the particle pair being investigated. In the following, an exercise is presented to demonstrate the effect of strong interaction on $C(k^*)$ for p–p pairs. To study the strong interaction in the case of p–p pairs, the Argonne v_{18} potential [60] is utilized. The spins and angular states are denoted using spectroscopic notation ${}^{2S+1}L_J$, where S is the total spin of the pair, L is the angular momentum, and $J = L + S$ is the total angular momentum. Since p–p are fermions, the total wavefunction is antisymmetrized according to $P = (-1)^{L+S+1} \stackrel{!}{=} -1$, and states like ${}^1P_1$ are forbidden. The total correlation function is obtained by adding the so-called Clebsch Gordan coefficients, which are the spin weights for each channel and are defined as [57]

$$w_{(S,L,J)} = \frac{(2S+1)(2J+1)}{(2s_1+1)(2s_2+1)(2L+1)(2S+1)}, \tag{1.19}$$

where s_1 and s_2 are the spins of two particles. The contributions of s-, p-, and d-waves to the p–p correlation function are shown in the left panel of Fig. 1.10. The calculations assume only the Gaussian source with a source size of $r_0 = 1.26$ fm which is typically the source for p–p pairs in pp collisions. At small relative momentum ($k^* < 100$ MeV/c), the interaction is dominated by the s-wave contribution,

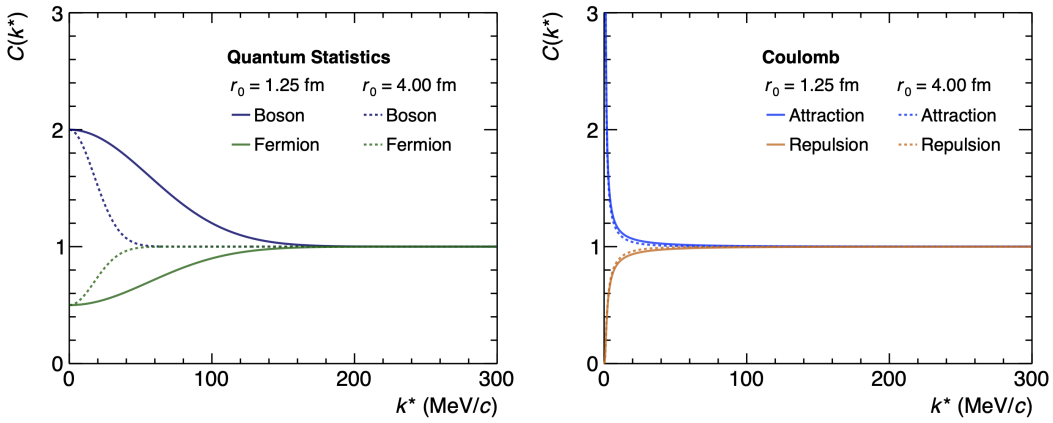

FIGURE 1.9: The figure shows the two-particle correlation signal for fermion pairs and boson pairs signal due to quantum statistics (left) and Coulomb interaction only (right), for two source sizes: $r_0 = 1.25$ fm (similar to the size of pp collision system) and $r_0 = 4.0$ fm (typical case of Pb–Pb collision system) [59].

while the contributions from the p- and d-waves become significant at larger momenta ($100 < k^* < 200$ MeV/c), and at larger momenta still ($k^* > 200$ MeV/c) the correlation is flat, indicating no interaction between particles when they are far apart. The strength of the correlation function, including all possible interactions and quantum statistics for two protons, depends on the source size. As shown in the right panel of Fig. 1.10, increasing the source size leads to a decrease in the strength of the correlation signal.

1.5.4 Lednický approach for the two-particle correlation function

One way to explore the strong interaction in a system of two particles is through scattering theory. In the Lednický [51, 61], the two-particle wave function, considering only the dominant contribution from the s-wave and the strong force, can be calculated as follows

$$\Psi\left(\vec{k}^*, \vec{r}^*\right) \approx e^{-i\vec{k}^*\vec{r}^*} + f(\theta)\frac{e^{ik^*r^*}}{r^*}, \tag{1.20}$$

where the scattering amplitude for the two charge-neutral particles is given by

$$f\left(k^*\right) \approx \left(\frac{1}{-a_0} + \frac{1}{2}d_0 k^{*2} - ik^*\right)^{-1}. \tag{1.21}$$

The scattering length a_0 and the effective range d_0 are two parameters typically determined from scattering cross-section measurements. The wavefunction from Eq. 1.20 can be substituted into Eq. 1.16, where the source distribution is assumed to be a Gaussian distribution as defined in Eq. 1.18. By subtracting the asymptotic form, which is a Bessel functions J_0 for the charge-neutral particles and performing the space integral, an analytic form is obtained as follows [61]

$$C_{\mathrm{LL}}\left(k^*\right) = 1 + \frac{1}{2}\left|\frac{f}{r_0}\right|^2 + \frac{2\mathcal{R}[f]F_1\left(2k^*r_0\right)}{\sqrt{\pi}r_0} - \frac{\mathcal{I}[f]F_2\left(2k^*r_0\right)}{r_0}. \tag{1.22}$$

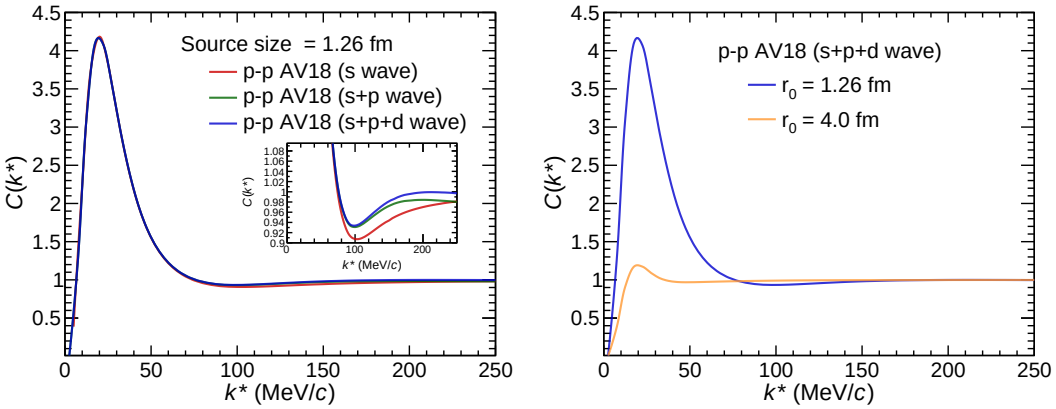

FIGURE 1.10: Two-particle correlation function for p–p pairs calculated using the CATS with the Argonne v_{18} strong interaction potential, Coulomb interaction, and Fermi-Dirac statistics. The left panel shows the contributions from s-, p-, and d-waves, as well as the sum of all partial waves, for a source size of $r_0 = 1.26$ fm. The right panel shows the correlation function, including all interactions and partial waves up to d-wave for source sizes of $r_0 = 1.26$ fm and $r_0 = 4.0$ fm.

The analytic functions $F_1(z)$ and $F_2(z)$ are defined as $F_1(z) = \frac{e^{-z^2}}{z}\int_0^z e^{x^2}dx$ and $F_2(z) = \frac{1}{z}\left(1 - e^{-z^2}\right)$ respectively. However, this simple analytic formula only works when the source size is sufficiently large, i.e., the range of the strong interaction d_0 should be larger than the source size. In most cases, d_0 is 2-3 fm, which implies that the source size should be large. In the case of pp collisions, the source size is ~ 1 fm, which is too small to use the simple analytic formula in Eq. 1.22. To account for the small source size effect, further corrections to Eq. 1.22 have been implemented by Prof. Richard Lednicky. These corrections allow the approach to be used in the case of pp collisions with a small source size, and the corrected formula is given by

$$C_{\mathrm{LL}}(k^*) = 1 + \frac{1}{2}\left|\frac{f}{r_0}\right|^2\left[1 - \frac{d_0}{2\sqrt{\pi}r_0}\right] + \frac{2\mathcal{R}[f]F_1(2k^*r_0)}{\sqrt{\pi}r_0} - \frac{\mathcal{I}[f]F_2(2k^*r_0)}{r_0}. \quad (1.23)$$

In reality, the particles can be identical, and therefore the effect of (anti-)symmetrization must be taken into account. In addition, the particles can also be charged, in which case the approximation of the Bessel function no longer can be used, and one needs to use the so-called confluent hypergeometric function for complex arguments and the regular F_0 and singular G_0 Coulomb functions for the asymptotic form. The definition of the relative s-wave function for a system of two charged point-like indistinguishable particles is given [51][7]

$$\psi_{-k^*}(r^*) = e^{i\delta_c}\sqrt{A_c(\eta)}\left[e^{-ik^*r^*}F(-i\eta, 1, i\xi) + f_C(k^*)\frac{\tilde{G}(\rho,\eta)}{r*}\right], \quad (1.24)$$

where $\eta = (k^*a_C)^{-1}$ with a_C a Bohr radius, $\xi = \rho(1 + \cos(\theta^*))$, and $\rho = k^*r^*$ are variables. The term $A_C(\eta) = 2\pi\eta[\exp(2\pi\eta) - 1]^{-1}$ is a Coulomb penetration factor, also known as Gamow factor and provides the threshold of the Coulomb barrier for

[7] This wavefunction is not (anti-)symmetrized. One needs to implement it when computing correlation for two identical particles.

the nuclear interactions. As aforementioned the asymptotic form for Coulomb interaction in the wavefunction is described by the term $e^{-ik^*r^*}F(\alpha,1,z)$ together with $\widetilde{G}(\rho,\eta)$, where $F(\alpha,1,z) = 1 + \frac{\alpha z}{!2} + + \frac{\alpha(\alpha+1)z^2}{!2^2} + \cdots$ is confluent hypergeometeric function and $\widetilde{G}(\rho,\eta) = \sqrt{Ac}\,(G_0 + iF_0)$. The strong nuclear interaction is calculated using the Coulomb corrected scattering amplitude f_C defined as

$$f_C\,(k^*) = \left[\frac{1}{-a_0} + \frac{d_0 k^{*2}}{2} - ik^* A_C\,(k^*) - \frac{2h(\eta)}{a_C}\right]^{-1}.$$

More details on this approach are discussed in Chap. 3.

1.6 Production of matter in the early Universe

This section provides a brief introduction to the production of matter in the universe and its connection to the production of light (anti-)nuclei in collision experiments. According to the Big Bang model, the universe originated from an extremely small region characterized by infinite energy density and temperature. It was once very hot and dense, and has subsequently expanded and cooled to its present state [62, 63]. In the microseconds following the Big Bang, the temperature was high enough that quarks could not bind together to form hadrons[8]. Therefore, the quarks and gluons could freely move in a phase of strongly-interacting plasma matter referred to as the *Quark-Gluon Plasma* (QGP) [64]. As the temperature and energy densities of the universe decreased, the QGP phase changed to the confined matter such as hadrons, and the phase transition took place around a critical temperature $T_C \sim 150$ MeV. This process is known as hadronization.

The high temperature at the early stage of the universe allowed for electroweak processes that converted neutrons to protons: $n + e^+ \leftrightarrow \bar{\nu}_e + p$, $n + \nu_e \leftrightarrow e^- + p$, and $n \leftrightarrow e^- + \bar{\nu}e + p$. Thus, the weak interactions were in thermal equilibrium, fixing the ratio of the neutron and proton number densities to be $n_n/n_p = e^{-Q/T}$, where $Q = 1.293$ MeV is the neutron-proton mass difference. This equilibrium state remained unchanged as long as the inter-conversion rate was faster than the universe's expansion. At a temperature of ~ 1 MeV, which corresponds to an age of the universe of ~ 1 s, the reaction equilibrium broke, and the n_n/n_p ratio froze out. Afterward, the neutrons slowly decayed into protons with a half-life of $T_{1/2} = 614$ s [65], further decreasing the neutron-to-proton number ratio n_n/n_p. At this stage of the universe, the temperature was below the deuteron (lightest nuclei) binding energy ($E_B = 2.2$ MeV), and the creation ($\mathrm{p} + \mathrm{n} \rightarrow \mathrm{d} + \gamma$) and destruction ($\mathrm{d} + \gamma \rightarrow \mathrm{p} + \mathrm{n}$) of the deuteron were possible. However, nuclei could not form stably due to the presence of high-energy photons, which were responsible for the large photo-destruction rate compared to the production rate. As the universe cooled further, when the temperature dropped below 100 keV, even the photons at the high-energy tail of the Planck distribution had smaller energy than the deuteron binding energy. Thus, the destruction of the deuteron by photons could not occur anymore. The light nuclei, mainly hydrogen and helium nuclei, formed through successive nuclear reactions. This process is known as primordial *nucleosynthesis* [66].

The universe was still ionized during the stage of primordial nucleosynthesis,

[8] According to the asymptotic freedom of QCD, at large energies, quarks and gluons tend to be free.

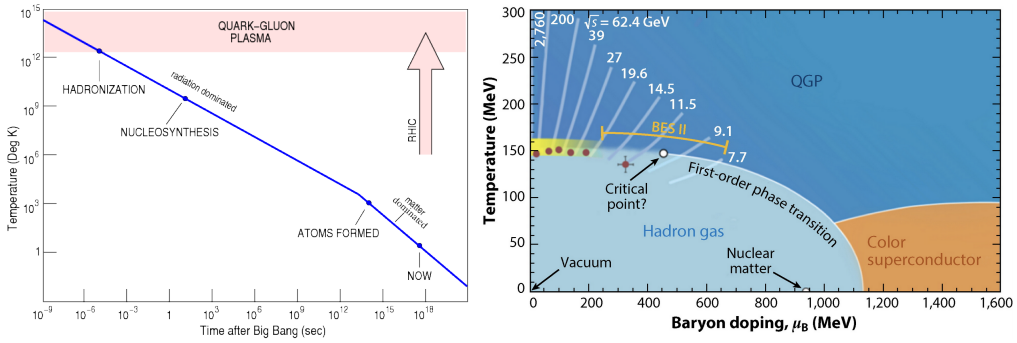

FIGURE 1.11: Temperature history of the universe [69] (left) and the QCD phase diagram [70] (right).

making it opaque to electromagnetic (EM) radiation. However, when the temperature reached around 3000 K, the first atoms began to form, and the EM radiation decoupled from matter. As a result, the Universe's expansion led to redshifts in EM radiation, which now has wavelengths in the microwave range and a temperature of approximately 2.2 K, creating what is known as the Cosmic Microwave Background (CMB) [67]. Due to gravity, matter distribution continued to develop anisotropically, forming structures such as galaxies and stars that exist in the Universe today. The anisotropies in matter distribution are evident in the CMB temperature measurements [68]. The left side of Fig. 1.11 summarizes the temperature vs. time of the Universe from the event of the Big Bang. Before the decoupling of radiation from matter, the universe was opaque. Therefore, we cannot study that time in the current Universe through the CMB[9]. In particular, the transition between the quark-gluon plasma and the hadronic phase cannot be investigated. Nevertheless, one way to recreate those conditions is through collider experiments. In these experiments, temperatures and densities comparable to those in the early Universe can be achieved.

The physics of very high temperatures or net baryon densities can be explored using the running coupling of QCD, which gives rise to the QCD phase diagram shown in the right panel of Fig. 1.11. The QCD phase diagram postulates a phase transition of hadronic matter to a deconfined state of quarks and gluons. This transition is a rather smooth crossover at low densities and high temperatures and of finite order at larger densities and smaller temperatures [70], as illustrated on the right of Fig. 1.11. The former corresponds to the conditions at the beginning of the Universe, as hypothesized by the Big Bang model. Such conditions can be partially recreated at high-energy collider experiments by considering a system characterized by extreme energy density. Present-day experiments such as the Large Hadron Collider (LHC) and the Relativistic Heavy Ion Collider (RHIC) can create such a system. On the other hand, the large density and low-temperature part of the diagram relates to the conditions for matter in neutron stars, which can be probed by low-energy experiments, such as the High Acceptance Di-Electron Spectrometer (HADES).

[9] In theory, right after the Big Bang, although the universe was an ionized medium, however, it was transparent to gravitational waves. Therefore, any primordial gravitational waves would still carry information about the universe's early moments when they reach us. However, we can unlikely detect such waves with current instruments.

1.7 Production of matter at the collider experiments

The era of heavy-ion-collision (HIC) experiments began with fixed target configurations, such as the Alternate Gradient Synchrotron (AGS) at the Brookhaven National Laboratory and the Super Proton Synchrotron (SPS) at CERN, with rather small center-of-mass (CM) energies ranging from 2 A GeV to 18 A GeV, where A is the mass number of the nuclei. Further development in the collider experiments was based on ion-beam collisions. Currently, HIC physics programs are conducted at the RHIC at the Brookhaven National Laboratories (BNL) and the LHC at CERN. The former can provide CM energy up to 200 A GeV while the latter can reach up to 5.02 TeV. At the LHC, Pb–Pb collisions at the CM energy of 2.76 A TeV led to the measurement of an energy density of 15 GeV fm^{-3}, which is well above the critical energy density of 1 GeV fm^{-3}.

The space-time evolution of the collision and the early Universe are quite similar. In both scenarios, the initial state quantum fluctuations ultimately give rise to macroscopic anisotropies in the final state. Thus, in both cosmology and the physics of HIC, the goal is to learn about the early state of matter from the final-state observations. In the space-time evolution of the collisions of two ultra-relativistic nuclei, the first initial state of a long-lived strongly interacting system is created. The subject of interest for HIC experiments is to study how the systems evolve. Although this thesis aims to study the production of light nuclei in pp collisions, it is interesting to briefly discuss the stages of heavy-ion collisions since they are closely related to pp collisions. In particular, the system's evolution is similar to that of a Pb–Pb collision. However, there is less production of quarks and gluons in the initial stages, leading to a qualitatively different final state. The HIC consists of several stages of evolution. After the nuclear collisions happen, there are states, namely:

1. **Pre-equilibrium stage**: The first instants of the collision, where hard processes occur and are characterized by a high momentum transfer between colliding partons.
2. **Thermal equilibrium**: The system results in a hot and dense interacting medium, which is the Quark-Gluon Plasma (QGP). After some strong parton scatterings, the QGP droplet attains equilibrium.
3. **Phase transition**: The expansion of the QGP droplet due to thermal pressure gradient leads to the system's cooling, which gives rise to the phase boundary between deconfined and confined strongly interacting matter. Moreover, at the critical temperature T_c between the two phases, hadronization occurs, and the system gradually evolves into an interacting hadron resonance gas.
4. **Chemical freeze-out**: At this stage, all inelastic interactions among hadrons halt due to insufficient momentum transfer between hadrons, and the abundances of the particle species are fixed.
5. **Kinetic freeze-out**: Further system's expansion leads to cooling, where the hadrons stop interaction with the medium, and the kinematics of the particles are fixed.

As mentioned earlier, for small collision systems, such as pp collisions, the system's evolution is similar to that of a Pb–Pb collision. The observable related to the

evolution of the collisions can be studied directly or indirectly in the case of intermediate stages. These observable can be broadly divided into hard, electroweak, and soft probes. The hard probes are related to the initial stages of the collisions. High-transferred momenta govern physical processes at these stages. In particular, either quarks and gluons with large momenta or heavy-flavored quarks such as charm and beauty are created. Hence, the perturbative approach to QCD can be used to study their production rates. Hard probes are created at the initial stages and can survive through all the subsequent stages of evolution. Therefore, such probes are good candidates to study the underlying mechanisms for the parton propagation and their energy loss in the QGP. In addition, the hadronization of the heavy quarks and gluons in the early stage of the collisions gives rise to the open heavy-flavored particles (hadrons composed of a heavy quark (c or b) and light quarks (d, u or s), e.g., D and B mesons), quarkonia (hadrons formed by a quark and an anti-quark with the same flavor such as the J/Ψ ($c\ \bar{c}$)), and Jets. Jets are narrow collimated bundles of hadrons with large transverse momentum consisting of multiple correlated hadrons. They are created possibly due to the confinement principle where high energies $q\bar{q}$ pairs start to separate until they split into further $q\bar{q}$ pairs, subsequently causing an avalanche process until the energy of the quarks is low enough to form a bundle of hadrons. In the presence of QGP, the jets would lose energy while traversing through the medium, changing their kinematic properties. This effect can be investigated by observing the nuclear modification factor R_{AA}, which allows quantification of the change in jet properties in HICs compared to pp collisions, where QGP is expected to be absent due to possibly insufficient energy density of quarks and gluons.

Electroweak probes refer to particles, namely leptons, photons, Z and $W^{\pm}$ bosons, or processes that involve the weak force and electromagnetic force. Since these processes are color-blind, the extremely high energy density of HICs means that only strong interactions are dominant and electroweak interactions can be neglected. Thus, the electroweak probes do not interact with the medium and therefore carry information about the initial stages of the collisions, which are extremely hot and dense conditions similar to those believed to have existed in the early universe shortly after the Big Bang.

Soft probes, on the other hand, refer to particles or processes that involve low-momentum or low-energy particles produced in the aftermath of the collision. These primarily include the production spectra of low-momentum hadrons, which represent the majority of particles produced in a collision, as well as elliptic flow and HBT correlations between particles emitted from the collision, providing information about the size, shape, and duration of the QGP, and fluctuations in the distributions of emitted particles, such as event-by-event fluctuations in particle multiplicities or transverse momenta. While modern HBT interferometry/femtoscopy, as discussed in Sec. 1.5, can be used to access strong interactions between particles, the production of hadrons and light nuclei, on the other hand, also provides an important aspect of understanding the dynamics and properties of the QGP, as it provides information about the thermalization, hadronization, and freeze-out processes of the strongly interacting matter created in these collisions. Experimental measurements of the momentum spectra, particle ratios, and correlations, are compared with theoretical models and simulations to extract information about the properties of the QGP, such as its temperature, pressure, and transport properties, as well as the dynamics of the hadronization process.

Up until now, the focus of discussions on QGP (Quark-Gluon Plasma) and hydrodynamics has primarily revolved around HICs, where the energy density is sufficient to generate a medium resembling QGP. However, recent investigations into small collision systems, particularly p–Pb and even pp collisions, have revealed certain phenomena that can be explained by considering hydrodynamic evolution and thermalization. These findings have sparked significant interest, as they suggest the possibility of creating small droplets of QGP in pp collisions or propose alternative mechanisms that produce effects resembling those observed in HICs. Although these questions remain unanswered, pp collisions offer opportunities to explore strong interactions through femtoscopic correlations and the yield of particle production. In this thesis, the strong interaction can be probed by examining the femtoscopic correlation of the proton-deuteron system. This becomes particularly intriguing because the deuteron, a light nucleus with minimal binding energy, is produced in a highly energetic excited state within the system. This aspect has generated considerable debate within the scientific community. Consequently, the thesis also focuses on studying the production spectra of light (anti-)nuclei as a secondary objective. A quick introduction to the production of light (anti-)nuclei is provided in the following section.

1.8 Production light (anti-)nuclei in collision experiment

Over the past few decades, high-energy hadronic and ultra-relativistic heavy-ion collision experiments have been used to study the production of light (anti-)nuclei and more complex multibaryon bound states [71, 72]. This has been achieved through precise measurements of differential cross-sections [73–79], flow observables [80–82], and event-by-event fluctuations [83]. Although light (anti-)nuclei are abundantly produced at the LHC, the production mechanism from a theoretical standpoint is still under intense debate. This is because nucleons are bound together in very shallow bound states with a binding energy of the order of $\sim$1 MeV/nucleon [84, 85], which is extremely small compared to the chemical freeze-out temperature of a Pb–Pb collision ($T_{\mathrm{ch}} \sim 150$ MeV). The observation of light (anti-)nuclei in collision experiments is therefore surprising and has been famously referred to as 'snowballs in hell' [86].

The production of light (anti-)nuclei can currently be described theoretically using two different phenomenological models: Statistical hadronization Models (SHMs) and models based on the coalescence of baryons.

1.8.1 Statistical Hadronization Model

In the Statistical Hadronization Model (SHM), the theoretical framework assumes that all the particles originating from an excited region occupy all available states in the phase space uniformly. This framework is commonly referred to as the Thermal Model, and the final state comprises all possible particle states that satisfy the conservation laws imposed by the Standard Model [87]. The complete occupation of the phase space at chemical freeze-out, with a freeze-out temperature T_c, allows for the determination of relative particle abundances [4–8, 88, 89]. As discussed earlier, the sizes of the systems differ in heavy-ion and pp collisions, and thus, two different approaches within the SHM framework are employed. On the one hand, systems

characterized by large volumes, such as Pb–Pb collisions, use a grand canonical approach. On the other hand, for small systems, a canonical approach is required to conserve charge locally[10]. These two approaches are briefly discussed in the following sections.

SHM approach: from large to small systems

As mentioned earlier, the grand canonical approach is appropriate to describe systems with sufficiently large volumes where the local conservation of charge is not required [90]. The system is in contact with an energy and charge reservoir. In large systems, generally, the region of interest could be a small sub-region of the whole phase space which is constantly in contact with the bigger systems. Therefore, on average, the energy and charges are conserved, and their values can be determined by the temperature and the chemical potentials associated with each charge. The system at thermal equilibrium can be described by the grand canonical partition function Z, defined as

$$Z(T,V,\mu) = \mathrm{Tr}\left[\exp\left(-\frac{H+\sum_i \mu_i Q_i}{T}\right)\right], \quad \text{with } \mu = \sum_i \mu_i Q_i\,, \tag{1.25}$$

where T, V, and μ are temperature, volume, and the chemical potentials of the system respectively. H is H is the Hamiltonian of the system which accounts for dynamics as well as the interaction of the particles within the strongly interacting medium in the system. The parameters Q_i and μ_i are the conserved charges and their respective chemical potentials. Theoretically, the Hamiltonian can be obtained from Lattice QCD approaches over a wide range of temperature values before the transition to a deconfined state. The conserved charges associated with the system are the electric charge Q, the strangeness S and the baryon number B. The total partition function of the system is a product of all single particle partition functions Z_i and $\log Z(T,V,\mu) = \sum_i \log Z_i\,(T,V,\mu_i)$ where the single particle partition function $\log Z_i\,(T,V,\mu_i)$ depending upon bosons (+) or fermions (−) is given by

$$\log Z_i\,(T,V,\mu_i) = \frac{V g_i}{2\pi}\int_0^\infty \pm p^2\,\mathrm{d}p \log\left(1 \pm \lambda_i\,(T,\mu_i)\,e^{-\epsilon_i/T}\right). \tag{1.26}$$

In order to account for spin statistics, the factor g_i is used and the energy of the particles is given by $\epsilon_i = \sqrt{m_i^2+p^2}$ with momentum p and mass m_i. Individual chemical potentials as included via the so-called fugacity parameter $\lambda_i\,(T,\mu_i) = e^{\left(B_i\mu_B + S_i\mu_S + Q_i\mu_Q\right)/T} = e^{\mu/T}$. The average number of particles (yields) are obtained from the partition function of particle species i.

$$\langle N_i\rangle\,(T,V,\mu) = T\frac{\partial}{\partial\mu_i}\log Z_i\,(T,V,\mu_i) = \frac{VTg_i}{2\pi^2}\sum_{k=1}^{\infty}\frac{(\pm 1)^{k+1}}{k}\lambda_i^k m_i^2 K_2\left(\frac{km_i}{T}\right). \tag{1.27}$$

This expression only gives the yield of the primordial particles. However, the measurements also contain contributions from the resonance decay. The latter are included in the yield for each resonance branching ratioΓ_j to species i

$$\langle N_i\rangle^{tot}\,(T,V,\mu) = \langle N_i\rangle\,(T,V,\mu) + \sum_j \Gamma_{j\to i}\,\langle N_j\rangle\,(T,V,\mu)\,. \tag{1.28}$$

[10]In the context of statistical mechanics, charge implies conserved quantities of the system.

This expression is quite general and assumes a Hamiltonian of the particle gas containing non-interacting hadrons and resonances. More sophisticated implementation for particle interaction is a matter of study and further development.

The total yield of the particles depends on the five input parameters, temperature T, volume V, and three chemical potentials $\mu(\mu_S, \mu_B, \mu_Q)$. Among these $\mu_S = 0$ and μ_Q are fixed due to net strangeness and isospin symmetry in the initial conditions, respectively. Only μ_B depends on the production of baryon and therefore depends on the energy of the collisions. The volume can be canceled out by considering the ratio of the particle yields. Only the temperature T remains as a free parameter which can be fixed either using the fit to the particle yield spectra or can be constrained from the Lattice QCD calculations.

In Fig. 1.12, the thermal model is used to fit all the light-flavored hadrons up to hypertriton ${}^{3}_{\Lambda}\mathrm{H}$ measured in central (0-10%) Pb–Pb collisions at $\sqrt{s} = 2.76$ TeV [91]. The yield of ${}^{3}\mathrm{He}$ and ${}^{4}\mathrm{He}$ has been predicted using the parameters (T, V), which are extracted from fits performed using different implementations of the SHM model. The model versions differ based on the resonance contributions included in the Hamiltonian. A common fit to the hadron yields provides a chemical freeze-out temperature of $T_{\mathrm{chem}} = 156$ MeV [91]. The predicted yields of ${}^{3}\mathrm{He}$ and ${}^{4}\mathrm{He}$ agree with measurements within the uncertainties for temperatures between 137 MeV and 177 MeV.

Summary: What do we learn?

- Light nuclei from (anti-)deuterons to (anti-)${}^{4}\mathrm{He}$ are produced at statistical equilibrium at the same temperature as the other hadrons.
- It would not be expected to see any light nuclei in heavy-ion collisions since the chemical freeze-out temperature is much higher than their binding energy. Surprisingly, a significant yield of light nuclei is observed.
- The thermal model is not sensitive to the internal structure of hadrons, and the yield of light (anti-)nuclei is the result of their distribution in phase space.

So far, the discussion has only focused on large systems, but canonical statistical models (CSMs) can also be applied to smaller systems, such as pp collisions. In small systems, the conditions of the grand canonical ensemble are not satisfied since the number of particles with a conserved charge is of the order of unity or smaller and thus fixed. Therefore, the local conservation of all charges is required, i.e., they cannot fluctuate as they can in the grand canonical approach [92]. This results in a suppression of the yields of particles carrying conserved charges. This effect is called *canonical suppression*. The canonical approach has been successfully used to describe hadron yields measured in small systems, such as $e^{+}e^{-}$ collisions [93] and pp collisions [94].

1.8.2 Coalescence model

Coalescence models are another class of models used to describe the production yields based on the hypothesis that hadrons close to each other in phase space after chemical freeze-out can bind together and form nuclei via coalescence. Similar to SHMs, current coalescence models also do not provide details on how nuclear

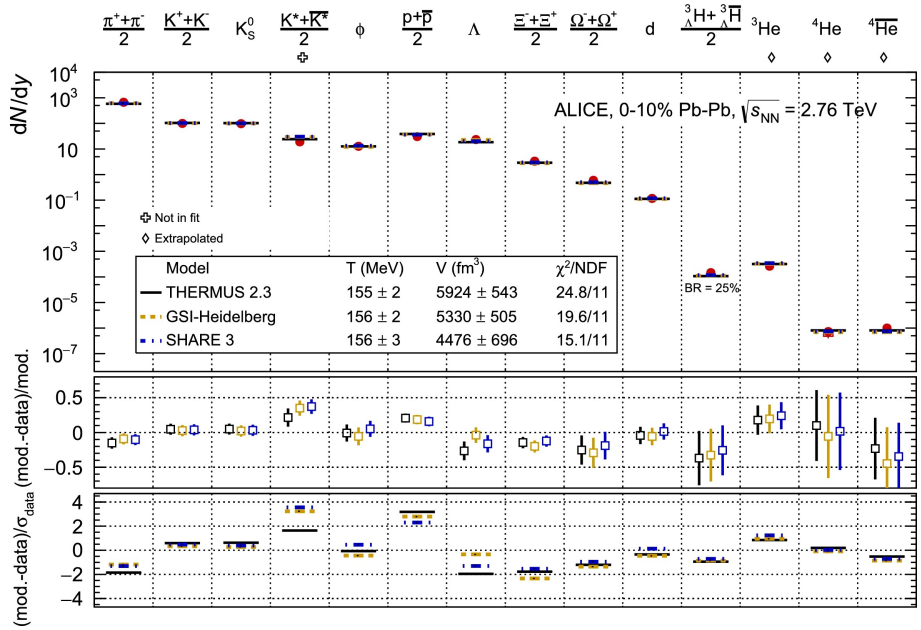

FIGURE 1.12: Figure shows the thermal model fits to the light-flavored hadron yields in central Pb–Pb collisions at $\sqrt{s} = 2.76$ TeV, with three different SHM implementations: THERMUS (black line), GSI-Heidelberg (yellow line), and SHARE (blue line) respectively. The figure is taken from Ref. [91]

.

interactions can play a role in the formation of nuclei.

The idea of coalescence originated in the early 1960s with the work of Butler and Pearson on proton-nucleus collisions, which suggested that deuterons could form from neutrons and protons that originate from the cascade of nucleons developed in the presence of the target nuclear optical potential [10]. The theoretical framework of coalescence models describes the formation of nuclear clusters from nucleons (protons and neutrons) during collision reactions. It explains the production of light nuclei, such as deuterons, helium (alpha particles), and other light (anti-)nuclei.

The key observable of the coalescence model is the ratio (B_A) of the invariant yield of nuclei with A nucleons $E_A \frac{\mathrm{d}^3 N_A}{\mathrm{d}p_A^3}$ divided by the invariant yields $\left(E_\mathrm{p} \frac{\mathrm{d}^3 N_\mathrm{p}}{\mathrm{d}p_\mathrm{p}^3}\right)^A$ of A protons. Although proton and neutron spectra are considered separately, they belong to the same isospin multiplet, and the isospin chemical potential is expected to be zero at LHC energies. Additionally, neutron measurements are difficult in collisions.

$$B_A\left(p_\mathrm{T}^p\right) = E_A \frac{\mathrm{d}^3 N_A}{\mathrm{d}p_A^3} \Big/ \left(E_\mathrm{p} \frac{\mathrm{d}^3 N_\mathrm{p}}{\mathrm{d}p_\mathrm{p}^3}\right)^A = \frac{1}{2\pi p_\mathrm{T}^A} \frac{\mathrm{d}^2 N_A}{\mathrm{d}y\, \mathrm{d}p_\mathrm{T}^A} \Big/ \left(\frac{1}{2\pi p_\mathrm{T}^\mathrm{p}} \frac{\mathrm{d}^2 N_\mathrm{p}}{\mathrm{d}y\, \mathrm{d}p_\mathrm{T}^\mathrm{p}}\right)^A . \quad (1.29)$$

where p_T is transverse momentum of the particles, and y is so-called rapidity defined as $y = \frac{1}{2} \ln \frac{E+p_z}{E-p_z}$ with E and p_z being the energy and longitudinal momentum of the particle. To evaluate the proton invariant spectrum, p_T^p is calculated as $p_\mathrm{T}^\mathrm{A}/A$, as the nucleus momentum is the sum of A nucleon's momenta.

A very simple approach to the coalescence model relies solely on momentum-space correlations, ignoring space-time correlations. [11] With these simplifications, two nucleons that are close in momentum-space are expected to coalesce into a deuteron, regardless of how far apart they are in position-space. The validity of this assumption is questionable. However, the distances between nucleons are small in small systems, and simple coalescence can be a plausible assumption. In large systems, such as Pb–Pb collisions, the system size is larger than the size of light nuclei, and the spatial distance between the produced nucleons can be very large. Therefore, even if their momenta are similar, they cannot coalesce into a nucleus. A simple formula for B_A can be obtained by considering the maximum momentum difference p_0 between nucleons, neglecting nucleon isospin.

$$B_{\mathrm{A}} = \left(\frac{4\pi}{3} p_0^3\right)^{\mathrm{A}-1} \frac{m_{\mathrm{A}}}{m_{\mathrm{p}}^{\mathrm{A}}}\,. \tag{1.30}$$

According to this simple approach for coalescence, B_A should not depend on the size of the system. However, the measured B_2 for deuteron as shown in the right panel of Fig. 1.13 shows a system dependence of p_{T} going from pp to Pb–Pb system. The simple approach also fails to explain the multiplicity dependence (number of

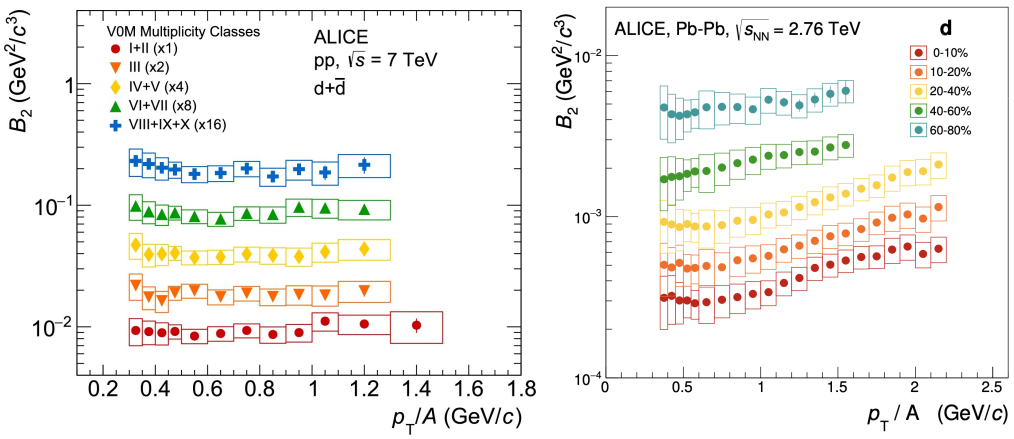

FIGURE 1.13: Measured B_2 for deuteron as function of p_{T} (a) in pp $\sqrt{s} = 7$ TeV [95] and (b) in Pb–Pb at $\sqrt{s} = 2.76$ TeV [77].

charged particles per collision) of B_2 observed in the data [76]. These limitations in the simple approach invite further development in the approach to coalescence, namely the inclusion of system size dependence by considering the overlap between the phase-space distributions of the nucleons and the phase space of the nucleus. In the quantum-mechanical treatment of coalescence, the phase space of the nucleus is replaced by its Wigner function, which is obtained via the Wigner transform of its wavefunction. Further details are discussed in Chap. 5.

Chapter 2

ALICE - A Large Ion Collider Experiment

The Large Hadron Collider (LHC) is the world's largest particle accelerator of its kind as of 2023. It was constructed to collide protons and/or heavy ions at total collision energies of up to 14 TeV [96]. The LHC is located near Geneva at the Organisation Conseil Européen pour la Recherche Nucléaire (CERN) complex. It is installed in an underground circular tunnel 175 m deep and circumference $\sim$26.7 km beneath the France-Switzerland border near Geneva. The main objective for designing such a colossal accelerator is to reach collision energies of the order TeVs essential for studying some of the open fundamental questions in particle physics. In particular, the questions related to the standard model and theories beyond. The data produced from the high-energy particle collider experiments situated at the LHC play a crucial role in understanding the current theoretical development and verifying which versions of current models based on the theoretical development of the particle physics are possibly correct and to validate their predictions and allow further theoretical development.

The accelerator facility comprises eight straight sections, each 528 m long, where the experimental setup is located. There are eight arcs where the beams are deflected using the superconducting dipole magnets with a magnetic field strength of up to 8.33 T. The accelerated particles are always of the same charge. Therefore the twin-bore magnet design configuration is used to deflect the counter-rotating beams. Moreover, the accelerator also includes quadrupole, sextupole, octupole and decapole magnets configurations which are used to focus the beams. The beam focus is used to make discrete packets of particles, each containing $\sim 1.15 \times 10^{11}$ protons, and are so-called *bunches*. Each beam can store up to 2808 bunches with a bunch spacing of 25 ns.

At the CERN accelerator complex, the hadrons are accelerated to the injection energy of the LHC, where the LHC is linked with the injector chain via two transfer tunnels, as shown in Fig. 2.1. In the chain of accelerating protons, at the first step, the protons are accelerated in a linear accelerator (Linac 2) with energies up to 50 MeV. Further acceleration is achieved up to 1.4 GeV in the Proton Synchrotron Booster (PSB) and 25 GeV in the Proton Synchrotron (PS). The accelerated protons are brought to an energy of 450 GeV in the Super Proton Synchrotron (SPS). Eventually, protons in the SPS are injected into the LHC. There are four interaction points (IP) at the LHC, which are instrumented with experiments. At IP 1 and IP 5, high luminosity spectrometers ATLAS (A Toroidal LHC Apparatus) [98]

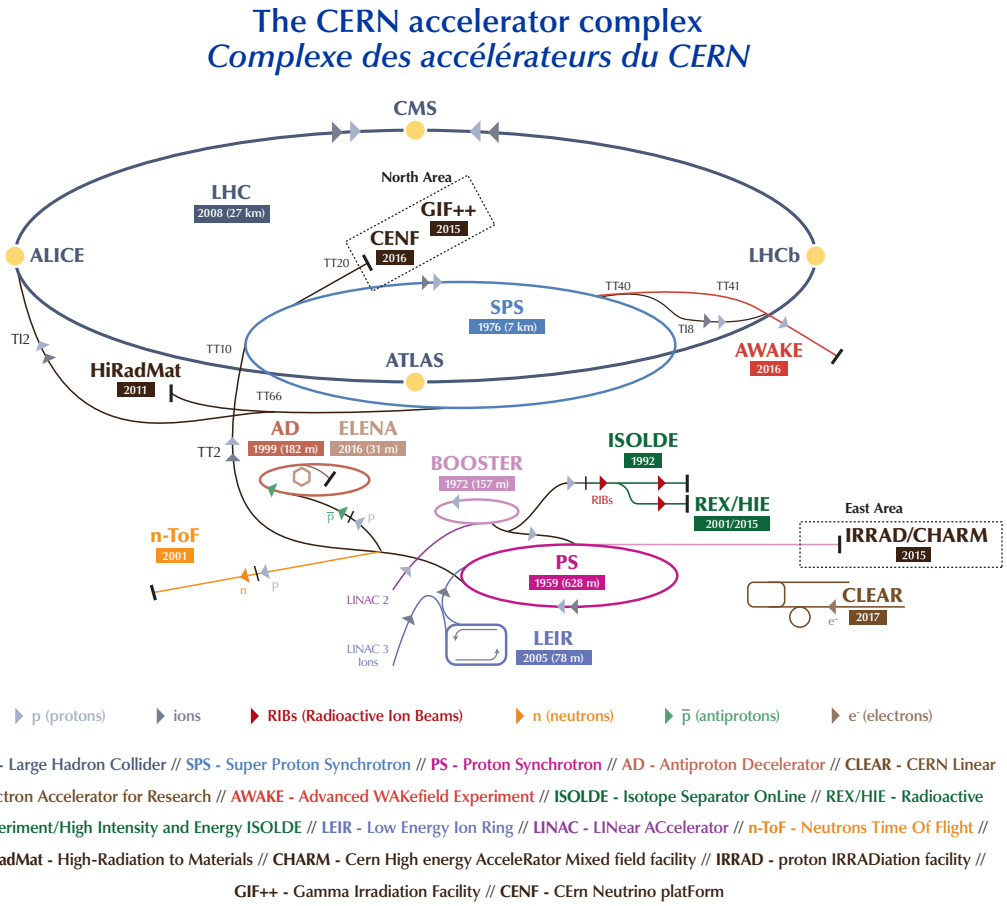

FIGURE 2.1: Schematic overview of the CERN accelerator complex [97]. The LHC is located at the last in the complex injector chain of the CERN accelerators. See text for details.

and CMS (Compact Muon Solenoid) [99]. Both the experimental apparatuses have similar designs and are devised for the study of the Standard Model Higgs boson. The physics studies include precision measurements of Standard Model parameters looking for new physics beyond the Standard Model. Both experiments are relatively general-purpose detectors that can record data at a high rate. At IP 8, there is another experiment LHCb (Large Hadron Collider beauty). This experiment aims to search for indirect evidence of charge conjugation symmetry and parity symmetry violating physics beyond the Standard Model in decays of beauty and charm hadrons. The detector system at LHCb is a single-arm spectrometer with a forward angular coverage to benefit from the Lorentz-boost the charm and beauty mesons experience when emitted in a forward direction [100]. The fourth large LHC experiment ALICE is located at the IP2 and is discussed in detail in the next Section. Apart from the large experiments, the LHC has smaller experimental facilities that provide complementary studies in the LHC physics program. These smaller experiments are designed to perform more specialized measurements or test specific particle physics aspects and are typically located along the LHC ring. For example, the TOTEM (TOTal cross-section, Elastic scattering, and diffraction dissociation Measurement), which is focused on measuring the properties of the proton and studying the mechanisms of proton-proton scattering at the LHC [101].

2.1 ALICE

This section highlights the main features of the ALICE detector, the methods for particle identifications using the relevant sub-detector systems and the data reconstruction used for femtoscopic analysis.

2.1.1 Overview

A Large Ion Collider Experiment (ALICE) is among the four major experiments installed at the LHC. ALICE is categorized as particle spectrometer [102–104] and is situated at the IP2 of the LHC. The primary purpose of building ALICE is to study the state of matter at extreme temperatures, mainly where quark-gluon plasma (QGP), a hot and dense phase of strongly interacting matter, is created in ultra-relativistic heavy-ion collisions [105]. The ALICE apparatus has the dimensions $16 \times 16 \times 26$ m^3 and weighs about 10000 t. The experimental apparatus consists of 19 sub-detector systems. The Time Projection Chamber (TPC) at the central barrel provides accurate tracking among all sub-detectors. Furthermore, because of the low magnetic field (0.5 T) inside the detector, it is capable of performing an excellent particle identification down to very low *transverse momentum*[1](p_{T} = 0.2 GeV/c). Although the excellent particle tracking in the TPC makes ALICE a unique experiment at the LHC, it has data read-out rate of $\sim$ 1 kHz which is around 100 times slower than that of other experiments at the LHC. The slow read-out is due to the dead time of the TPC read-out with multi-wire proportional chamber reading only one event in $\sim$ 1 μs time span. This was the situation in RUN 1 and RUN 2 of LHC. However, the upgrade in the ALICE hardware system mainly and software in the RUN 3 makes it possible to perform continuous read-outs. Nevertheless, In this work, the femtoscopic analysis is based on the data collected during Run 2 and hence the thesis focuses on the status of the ALICE detector for RUN 2. The ALICE detector and it's performance is described in details in Refs. [102–104, 106].

The following sections summarise the most relevant parts of the ALICE detector setup, which are essential for the studies in femtoscopy. In Sec. 2.1.2, the triggering system required for the read-out sequence in case an event of interest occurs is discussed. Next, the sub-detectors for the tracking and particle identification are discussed in sections 2.1.3, 2.1.4, and 2.1.5. The central part of the ALICE detector has three cylindrical shaped sub-detectors, which are oriented parallel to the beam pipe, and are mainly used to perform tracking and particle identifications(PID) in full azimuthal coverage as shown in Fig. 2.2. The acceptance in the polar angle is measured in units of pseudorapidity $\eta(\theta) = -\ln[\tan(\theta/2)]$, where θ is the angle between the particle three-momentum $\vec{p}$ and the positive direction of the beam axis. The pseudorapidity is used to describe the geometry of the detector. Furthermore, it is antisymmetric around the direction perpendicular to the beam axis, i.e. $\eta(\pi/2+\theta) = -\eta(\pi/2-\theta)$. Depending upon the values of η, the detector space is divided into three regions; the *mid-rapidity* region is defined for the values of η close or equal to zero, represents particle emitted in the transverse direction of the beam axis($\theta \approx \pi/2$), *forward-rapidity* and *backward-rapidity* regions are described for ($\eta > 0$), ($\eta < 0$) and $|\eta| \geq 1$ where the particles emitted fly in or opposite to the beam direction. A schematic representation of the ALICE detector for RUN 2 is shown in Fig. 2.2.

[1]The transverse momentum p_{T} is momentum component in the direction perpendicular to the beam axis

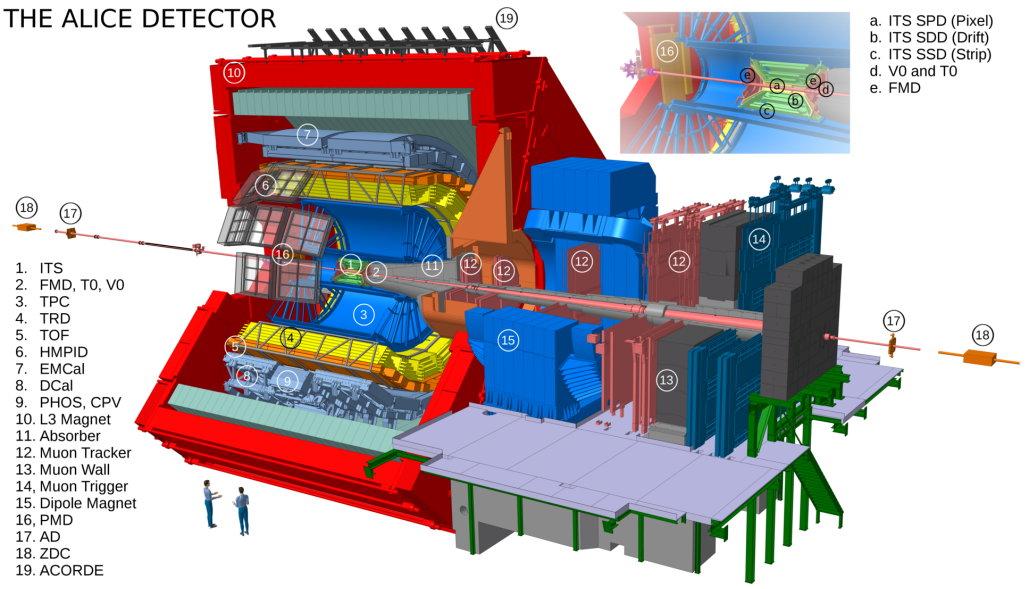

FIGURE 2.2: Schematic overview of the ALICE experimental apparatus and the sub detectors [107]. The inset shows a zoomed view of the components directly surrounding the nominal interaction point. The list on the left shows the ordered marking of the detector components.

2.1.2 Event trigger system

In order to perform a selection of an event of interest, the triggering systems are used to activate the read-out sequences. The triggers select the events based on the desired physics [104]. In Run 2, there are two main conditions for triggers: minimum-bias (MB) triggers and rare categories of triggers. The former is used when the biases related to physics selection towards an event are minimal. It is used to activate read-out sequences in the presence of any collision between the beams. The latter is used to have more specific physics-driven cases. Such triggers are used to enhance the statistics of certain types of events. In particular, the high-multiplicity (HM) trigger plays a key role in the femtoscopic analyses in pp collisions to enhance the total amount of reconstructed particle pairs. The HM trigger selects the events in which, on average, 30-40 charged particles are present per unit of rapidity. This selection helps to increase combinatorial possibilities to build the particle pairs of interest.

The event triggering uses the ALICE's V0 and TO detectors sub-system. For example, signals to measure the centrality in p–Pb and Pb–Pb collisions. The V0 detectors are placed on the A and C sides of the interaction point and are composed of two plastic scintillator arrays. Based on the names of the sides, the V0s are named as V0A detector, which is located at $z = 3.4$ m from the interaction point, covering the pseudorapidity range of $2.8 < \eta < 5.1$, on the C side the V0C detector is placed at $z = -0.9$ m, covering $-3.7 < \eta < -1.7$. The final signal is the sum of the measured signal amplitudes from both detectors. Since the scintillation signal scales with the number of charged particles in the forward and backward region, it is used as a proxy for the multiplicity at mid-rapidity. A 'V0AND' trigger is activated if the hits in the V0s produced by charged particles are present in both the V0A and V0C scintillators and are synchronous with the LHC bunch crossing time. Hence

the MB trigger allows reading out all inelastic pp collisions without introducing a significant selection bias. Subsequently, the MB events are then selected. The MB trigger is often labeled as 'kINT7' in the Software. The HM trigger events can be selected via the V0 system if the amount of hits in both the V0A and V0C satisfies the set bare minimum, typically a multiple of the average value in the case of minimum bias, i.e., $5 \cdot \langle \mathrm{V0M} \rangle$. In the present studies, the analysis has been performed using events with the HM trigger condition. A total of 1.04×10^9 events were collected in which the threshold for hits in both the V0s detectors was tuned such that 0.17% of the highest multiplicity events contain at least one measured charged particle within $|\eta| < 1$. This approach results in events with an average number of charged particles $\langle \mathrm{d}N_{\mathrm{ch}}/\mathrm{d}\eta \rangle_{\mathrm{avg}} \sim 30$.

2.1.3 Inner Tracking System

The ***Inner Tracking System*** (ITS) is primarily used to measure the precise localization of the interaction vertex, charged particle tracks with low p_{T}, and the reconstruction of secondary vertices that are associated with the decay of short-lived hyperons, and charm and beauty mesons. The ITS consists of six coaxial cylindrical layers surrounding the 800 μm thin Beryllium beam pipe whose outer radius is 3 cm. Each layer is made of a different type of lightweight silicon detector. All six layers make up three lightweight silicon-based detector sub-systems located at radii ranging from 3.9 cm to 43.0 cm, namely Silicon Pixel Detector (SPD), Silicon Strip Detector (SSD), and Silicon Drift Detector (SDD), providing the total coverage in pseudorapidity is $|\eta| < 0.9$. However, the SPD can detect particles up to $|\eta| = 1.95$. Fig. 2.3 shows a schematics view of the ITS detector system. As aforementioned, the ITS system is capable of reconstructing the particle trajectories with high resolution, which allows locating the interaction point of the colliding beam particles (***Primary Vertex (PV)***) with a precision of less than 100 µm. Such a precise determination of PV is essential to constrain the direction of the emitted charged particles' momentum and the production vertex's position. Furthermore, high resolution in the determination of primary vertex allows rejecting possible ***pile-up*** events[2]. Among all the detectors in the ALICE, the ITS is the only detector that can measure the transverse momentum of tracks down to 100 MeV/c.

2.1.4 Time Projection Chamber

The ***Time Projection Chamber*** (TPC) is one of the main components for tracking and particle identification in the ALICE detector system [109]. It is located after the ITS and is a cylindrical-shaped volume extending from 85 to 247 cm from the interaction point. The large size of the TPC covers the pseudorapidity range of $|\eta| < 0.9$ for particle identification. The schematic view of the TPC detector is shown in Fig. 2.4. The total volume of the detector is 90 m^3 and is filled with gas. It has an active detection medium such as $\mathrm{Ar} - \mathrm{CO_2}$ (88-12) or $\mathrm{Ne} - \mathrm{CO_2} - \mathrm{N_2}$ (90-10-5), and is divided into two drift regions by the central cathode with an electric field of ∼400 V/cm as depicted in the left panel of Fig. 2.4. The charged particles traversing in the field cage of the detector ionize the gas, and free charges are liberated in the form of electrons-ions pairs. The electrons drift under the action of the electric field towards the cathode and the ions drift to the anode plates of the detector, where the signal due to the drift of electrons is amplified and read out.

[2]A pile-up event contains possible tracks that stem from different collisions, those tracks were wrongly reconstructed in the same event

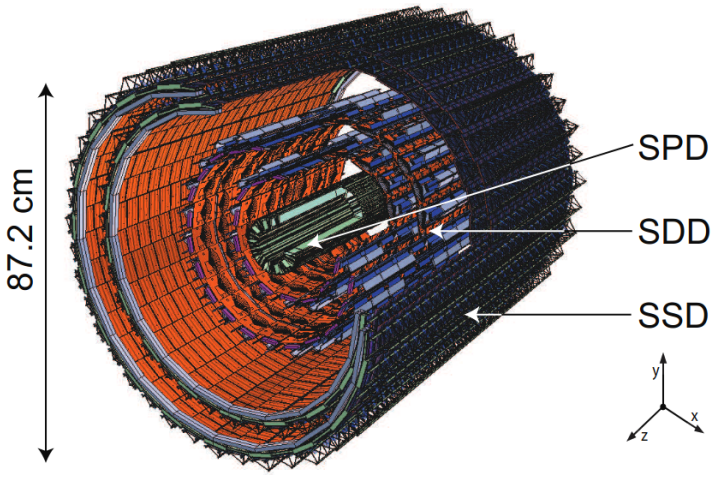

FIGURE 2.3: Schematic representation of The Inner Tracking System at ALICE experiment [108].

Depending on the composition of the gaseous mixture, the maximal drift time of the electrons defines the integration time of the detector of about 100 µs. The amplification of the charge deposited on the endplates is necessary because the total yield of ionization electrons is typical of the order of 30-40 e^-/cm per minimum ionizing particle (MIP), which is insufficient to provide a detectable signal at the read-outs. The signal amplitude can be used to calculate the energy loss of the traversing particle, which is then used for the PID. The endplates are segmented into 18 sectors in azimuthal angle ϕ. The read-out at each sector is organized in 159 pad rows and for the whole detector amounts to 557, 568 channels covering a total area of about 32.4 m^2. A single charged particle colliding with the gas constituents can cause up to 159 charge clusters. The charge clusters are interpreted as individual spatial points (hits) of the particle's trajectory (track). The position of each hit on the xy plane is determined by the location of the read charge cluster in the endplate, and the z position is determined from the time offset between the initial event collision time and the time at which the electrons reached the endplate as depicted in the right panel of Fig. 2.4. The average drift velocity of the electrons is 2.7 cm/μs which leads to a maximum drift time of 92 μs. A gating grid is opened for every collision and thus transparent for incoming ionization electrons from the drift volume. To electrically separate the amplification region from the drift volume, the getting grid is closed after one full drift time of 100 μs. The dead time is sufficient to neutralize all ions that would drift back into the TPC barrel and distort the electric field lines at the amplification stage. A closure time of about 200 μs reduces the overall ion leakage to the active detector volume. However, this procedure limits the data read rates; the total time of about 300 μs restricts the read-out rate to a few kHz for the TPC with the Run 2 read-out system. Despite the limited data collection rate of ALICE in Run 2, the TPC is the best device for providing tracking and PID performance. The device in Run 2 made it possible to simultaneously reconstruct up to 10000 charged particles per event [110], which is the case in the most central Pb–Pb collisions. In recent years, advances in the research and development of the TPC detector technologies, primarily the upgrade of TPC read-out based on Gas Electron Multiplier (GEM) foils, enable continuous operation while retaining the excellent PID, have led to the possibility of upgrading the device to record the data at a rate of 50 kHz in Run 3 campaign of the data taking. Such an upgrade has improved the detector's performance significantly in the data-taking periods that started in 2022. To per-

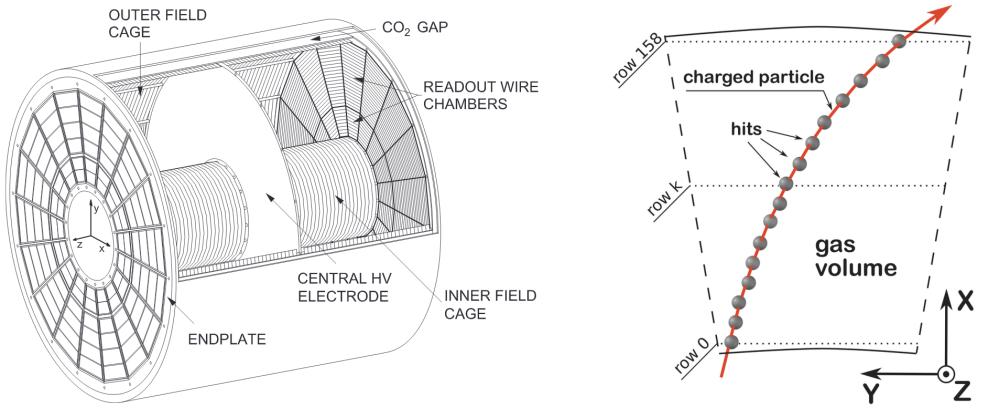

FIGURE 2.4: The Time Projection Chamber at ALICE. The left panel represents a schematic view of TPC central barrel [109], while the right panel shows a sketch of a track reconstruction mechanism [111].

form particle identification, the tracks are reconstructed using spatial coordinates of the hits as depicted in the right of 2.4 and the specific energy loss dE/dx which can be related to $\beta\gamma$ based on the amount of charge collected during the readout. The particle momentum is reconstructed by measuring the bending radius of the track, which is related to the applied magnetic field and the ratio of momentum over the charge of the particle. The identification of specific particles is performed using the Bethe-Bloch equation [112].

$$\left\langle \frac{dE}{dx} \right\rangle = A_1 \cdot \frac{z^2}{\beta^2} \left[\ln \left(A_2 \cdot \frac{\beta^2}{1-\beta^2} \right) - \beta^2 \right], \tag{2.1}$$

where $\langle dE/dx \rangle$ is specific energy loss by the charged particles, $A_{1,2}$ are constants determined by the characteristics of the material (gaseous medium), and z and β are charge number and velocity of the particle respectively. The particles of interest are relativistic, therefore the particles' momentum and mass are related by following relation

$$p = \frac{m\beta}{\sqrt{1-\beta^2}}. \tag{2.2}$$

Substituting β in terms of p and m in Eq. 2.1 one obtains

$$\left\langle \frac{dE}{dx} \right\rangle = A_1 \cdot z^2 \cdot \frac{m^2+p^2}{p^2} \left[\ln \left(A_2 \cdot \frac{p^2}{m^2} \right) - \frac{p^2}{m^2+p^2} \right]. \tag{2.3}$$

Finally, the specific energy loss of the particle $\langle dE/dx \rangle$ is then measured as a function of the particle momentum p. Depending on the particle's mass, the function has different shapes, as shown in the ALICE performance plot for the TPC in Fig. 2.5. The black lines correspond to the theoretical predictions for $\langle dE/dx \rangle (p)$ evaluated assuming the masses of the electrons, pions, kaons, protons, and deuterons. The colored bands on the plot correspond to the measured amount of tracks (increasing from blue to red) with a specific $\langle dE/dx \rangle (p)$. Depending upon the particle's charge polarities, the measured bands are segregated in the negative and positive axis of p/z. As deduced from Eq. 2.3, the particle identification is performed by identifying the bands in the measured yield of particles where each band follows the black line obtained from the theoretical prediction of a specific mass hypothesis. In addition, the width of each band is related to the resolution of the TPC. To

obtain the best mass hypothesis in this work, each particle is assigned a nσ where n is the multiplicative factor, nσ parameter measures the discrepancy in a number of σ (resolution) between the theoretical expectation. Typically, for standard particle identification, the bandwidth is 3σ. The $\langle dE/dx \rangle\,(p)$ band for individual particles are well separated for small momenta as shown in Fig. 2.5. However, the bands merge at larger momenta; hence TPC alone is insufficient for particle identifications in that region. This issue can be solved to an extent by using another (sub)detector system that provides complementary information, such as the Time-Of-Flight. Combining the information of TPC with the Time of Flight (TOF) can help obtain better resolution at large momenta. However, combining multiple detector systems can reduce tracking efficiency and acceptance, as discussed in Sec. 2.1.5.

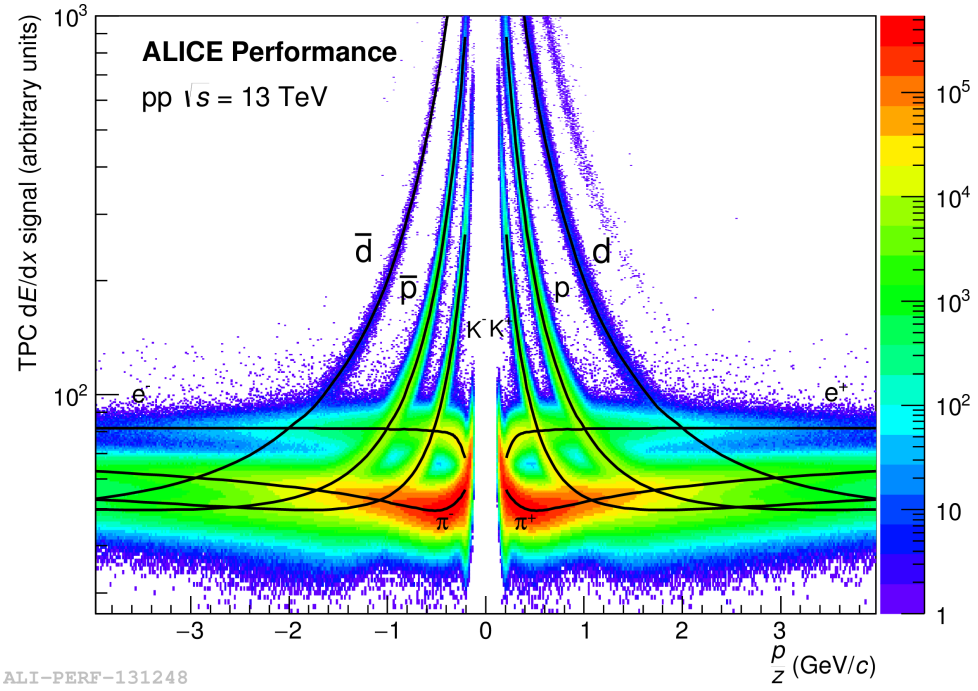

FIGURE 2.5: Specific energy loss as a function of momentum over the charge, as measured by the ALICE TPC for pp collisions at 13 TeV.

2.1.5 Time of Flight Detector

In Sec. 2.1.4, it is evident that the particle identification cannot be performed for the large momentum using the TPC detector because the specific energy loss bands $\langle dE/dx \rangle\,(p)$ as a function of momentum for each particle the start to merge relatively early at the low momenta. In order to identify particles with large momenta, it is crucial to exploit another detector facility. For the charged particles, it is convenient to measure The Time of Flight (TOF) as a complementary technique for measuring the specific ionization energy loss in ITS and TPC. It is accomplished by using the detector sitting just outside the central barrel is referred to as ***Time Of Flight sub-system*** (TOF) detector [113]. It is situated outside the TPC, at a radial distance of 370 to 399 cm from the interaction point, and provides the same angular coverage in pseudorapidity as the TPC ($|\eta < 0.9$). The detector system consists of 1593 Multi-gap Resistive Plate Chambers (MRPC), each providing an active area of 7.4×120 cm^2. The MRPC technology uses a parallel-plate chamber design where the drift gap is subdivided by resistive plates which are electrically floating. A high voltage across the drift gaps

generates a uniform electric field. The traversing charged particles in the field lead to the ionization charge in the medium, which is amplified at later stages. The insertion of the resistive plates restricts the charge drift in the intermediate gaps, thus significantly reducing the time jitter and improving the detector's resolution. The time resolution of the TOF detector is about 80 ps [104]. The TOF detector facilitates the measurement of the particles' arrival time in conjunction with the time of the initial collision, which allows one to calculate the time of flight; consequently, the velocity of the particles β is determined. The TOF velocity β for different particles as a function of momentum over charge p is shown in Fig. 2.6. The measurement of TOF β shows the capability of the TOF detector to provide the separation power among different particle species at intermediate momenta. By combining the β with

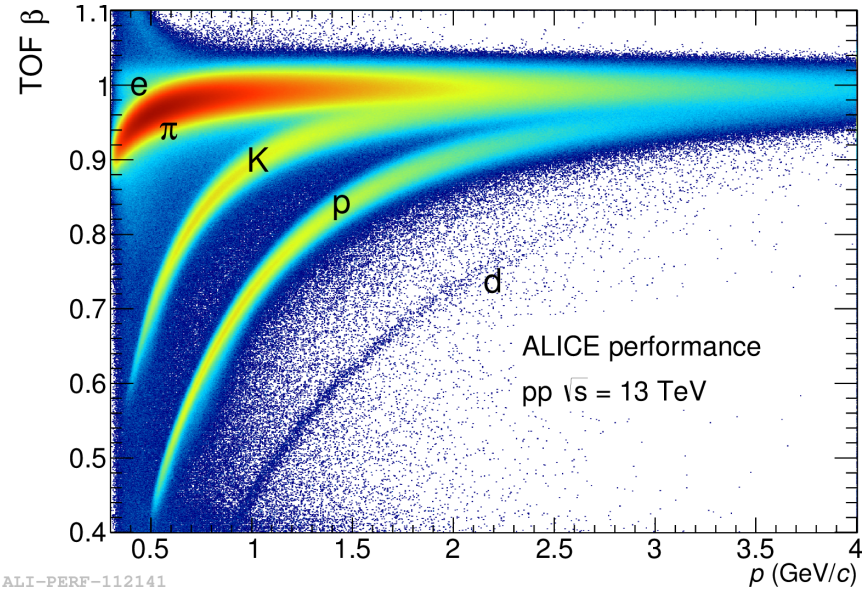

FIGURE 2.6: Particle identification using the Time-Of-Flight detector.

the momentum measurement, the mass can be evaluated using

$$m = p\sqrt{\beta^{-2} - 1}\,. \tag{2.4}$$

In this work, the mass hypothesis of the particles has been determined based on the nσ parameter measuring the discrepancy in the number of σ (resolution) between the measured value and the expected value of $\beta(p)$ for a given particle. Though the TOF detector improves the particle PID for large momenta, it suffers from low reconstruction efficiency since it is located further away from the interaction point. There is an increased probability for particle absorption before the latter reaches the detector. Moreover, a reduced acceptance for low momentum particles since particles with low momenta can be curled back into the TPC by the magnetic field. In addition, the mismatch of the tracks while reconstruction of particles using both the TPC and the TOF leads to further inefficiencies since the track hits in both detectors need to be matched. To minimize the effect of low efficiencies and resolutions, particle identification is carried out independently in the two momentum regions. In low momentum (e.g., for protons $p \leq 0.75\text{GeV}/c$), the TPC detector provides excellent resolution, and therefore the TPC detector is used. In the intermediate momentum region (e.g., for protons $0.75 \leq p \leq 4\text{GeV}/c$), the TPC and TOF information is combined to obtain enough resolution of the PID with minimal inefficiencies. In

this work, the combined information of TOF and TPC is used from the following relations

$$n_\sigma = \begin{cases} n_{\sigma,\,\mathrm{TPC}} & \text{using TPC only} \\ \sqrt{n^2_{\sigma,\mathrm{TPC}} + n^2_{\sigma,\mathrm{TOF}}} & \text{using TPC and TOF} \end{cases} \tag{2.5}$$

The momentum threshold for $\sqrt{n^2_{\sigma,\mathrm{TPC}} + n^2_{\sigma,\mathrm{TOF}}}$ is chosen based on the particles, in particular, for protons and deuterons the values of the threshold is chosen to be 0.75 and 1.4 GeV/c respectively. Further details on the particle identifications for protons and deuterons are discussed in Sec. 4.2.

2.1.6 Data from LHC Run 2

In this work, the analyzed data were collected during the Run 2 of the LHC. In Run 2, the data-taking campaign started after the long shutdown one (LS1), during which significant consolidation works on the accelerator were conducted. With this upgrade, it was possible to increase the center-of-mass energy for p–p collisions from $\sqrt{s} = 7$ TeV in Run 1 (2009-2013) to $\sqrt{s} = 13$ TeV with a bunch spacing of 25 ns, which led to the increased instantaneous luminosity of up to $L = 2 \times 10^{34}$ cm^{-2} s^{-1}. At the same time, the ALICE apparatus also underwent an upgrade during the transition from Run 1 to Run 2. In particular, the remaining five super modules of the transition radiation detector were installed, and the calorimeter's geometric acceptance was extended.

In the first year of data taking with p–p collisions, the LHC operated with relatively low interaction rates of 10 kHz, resulting in a lower yield of the charged particles; therefore, this data set was not used in the femtoscopic analysis in this work. Instead, in this work, the p–p collision data collected during the years 2016-2018 were used for the analysis since the beam conditions typically resulted in interaction rates up to 250 kHz.

Data reconstruction

Once the data taking of each run is completed, the raw data are compressed and shipped to permanent storage. The compressed data are further processed in an asynchronous method that uses an offline framework *AliRoot* based on ROOT software [114]. Aliroot is responsible for handling all relevant tasks for processing the data required for the analysis, such as simulation, reconstruction, calibration, alignment, and visualization. At first, the particle reconstruction is performed using the raw data during the LHC beam times. The data are taken for each run which are the time segments in which the LHC beam operates, and each typically lasts from several minutes to a few hours. During each run, the detector configuration of all ALICE sub-detectors is fixed. In the control room, basic quality assurance tests are conducted to monitor the beam operations and the performance of the detector system. At this stage, the information on the run conditions is stored, which is required to calibrate the data.

The data reconstruction process is divided into multiple steps starting with the initial analysis of finding digits in time and space, known as clusters, estimation of the interaction point of the collision using the SPD track information, reconstruction of the charged particles tracks using a Kalman filter [115]. In the process of track reconstruction using the TPC space points, the track finding starts in the outermost

pad row of the TPC in the inward direction and is performed in two different ways, with and without a constraint to the primary vertex. These reconstructed tracks are known as ***TPC-only*** tracks. The tracks which are propagated to the inner tracking systems and also refitted outwards using the information of detectors outside the TPC, particularly the TRD and the TOF detectors, are so-called ***global*** tracks.

Furthermore, the primary vertex is determined using the global tracks as well. The p_{T}-resolution with vertex constraining on TPC-only tracks is compatible with the constraints on global tracks up to $p_{\mathrm{T}} \sim 10$ GeV/c [104]. Once the track reconstruction is performed, the secondary vertices originating from the weak decays are searched [102–104]. In addition to the primary and secondary vertices, the tracks' topological selections are imposed to eliminate the combinatorial background. Apart from the particle tracks from primary collisions, the secondary tracks, possibly stemming from the secondary decays, are reconstructed. To suppress the contributions from primary tracks, a minimal Distance of Closest approach (DCA) to the primary interaction vertex 0.5 mm (1 mm) in p–p and (Pb–Pb) is applied [104]. The tracks with unlike-sign combinations are constructed from the sample of tracks with no primary tracks used to construct the mother tracks, known as V0 candidates (representing K^0s and Λs). Finally, the cascades, such as Ξ^- and Ω^- particles decay into the V0s and charged particles, are reconstructed. The tracking and PIDs require a calibration process to correct the data for the detector effects further. The calibration process can be divided into several stages, among which the first two stages (CPass0 and CPass1) are automated immediately after the data taking. In addition, follow-up re-calibrations are also performed in case any problem in the data reconstruction is observed. However, re-calibrations can be performed manually only at a later stage. Eventually, all the information of reconstruction is stored in so-called ***Event Summary Data*** (ESD) files on the CERN computing grid.

Data for analysis

In most cases, the ESD files for individual runs are too large, and performing analyses directly from the ESDs is thus resource expensive. Alternatively, the ESDs can be filtered into other data files known as ***Analysis Object Data*** (AOD) files, which store only the information that is most relevant to the physics analysis under consideration. In other words, the AODs store the observables relevant to the physics studies, such as track momentum, charge, and the topological properties of the tracks (e.g. closest distance to the primary vertex). Moreover, the AOD files also contain the basic properties of the underlying event, such as the multiplicity, event sphericity and spherocity relevant to the event shapes. The tracks in each event can be reconstructed using different criteria, resulting in different tracks in the final event. In addition to event characteristics, a filter-bit (FB) bit-masking approach for each track is introduced in the AOD files. FB stores whether the track satisfies a certain set of quality criteria in the combinations of bits. In Run 2 data taking, the most commonly used filter bits in AOD files are 96 and 128, where the former represents the global tracks and the latter the TPC-only tracks. As mentioned above, the global tracks are reconstructed using the combined information of TPC and ITS detectors, where the first hit in the ITS must be with the SPD or SDD layers. On the other hand, the TPC-only tracks are constrained to the SPD vertex, while the tracking and momentum determination is based only on the information from the TPC. In addition, the global and the TPC-only tracks, also so-called ***hybrid*** tracks passing standard

TPC+ITS cuts, SPD hit request, and golden χ^2 cut are stored as the filter-bit 256 tracks. In this work, the protons (anti-) are selected using the TPC-only tracks. For the selection of deuterons (anti-), hybrid tracks are used to enhance the primary candidates and to have a better constraint on the primary vertex via the ITS hits request. More details are discussed in Sec. 4.2.

Simulations

During the analysis in femtoscopy, at several places, the simulation of the collision system is required in an event-by-event process. The full-scale simulations are filtered through the detector and the reconstruction algorithms. The current ALICE detector framework makes it possible to employ various event generators, for example, different versions of PYTHIA [116–119] for pp, DPMJET [120] for p–Pb and HIJING [121] for Pb–Pb collisions. The event generators EPOS can be used for all systems [122–124]. With the event generators as aforementioned, it is possible to simulate the particle collision and extract the kinematic information of the outgoing particles. The detector response is included by passing the information of the outgoing particles to the transport codes such as GEANT3 [125] or GEANT4 [126], which simulate the energy deposit of the traversing particles in the individual detectors, the so-called hits. In AliRoot, the signal formation and processing in the corresponding sub-systems are simulated. This signal creates digits that are equivalent to the output of the detector's front-end electronics. In the end, the output of the front-end electronics, which is similar to the data, the simulated data is processed and reconstructed in the same way as actual raw data. This work uses a full-scale simulation based on Pythia 8 [116], while the transport through the detector is modelled with GEANT 3 [127] are used to study the response of the detector. Mainly the simulations are used to study the resolution effects of the detector (Sec. 4.2.3), to determine the fraction of secondary feed-down particles (Sec. 4.2.1 and 4.2.2) and the background in the femtoscopic signal Sec. 4.2.3, these all steps play a crucial role and are essential in performing a comparison between theoretical predictions and the experimentally measured correlation function.

None of the above-mentioned event generators handle the production of nuclei and therefore no primary production of nuclei are present in the simulations. In order to estimate fraction of secondary deuterons, Pythia 8 simulations as full ALICE Monte Carlo simulations have been used, it provides an estimate on the deuterons produced during spallation processes. As a proxy, the distribution of DCA of antideuterons from the data have been used in replacement of primary deuterons since the production antideutron from spallations is expected to be absent.

Chapter 3

The theoretical p–d correlation

3.1 Overview

This chapter aims to study proton-deuteron correlation function theoretically. The starting point is the two-body calculation, where the deuteron is assumed to have no internal structure. However, such a simple approach is not sufficient to describe the measured p–d correlation function, as it is discussed in Chap. 4. The incapability of the two-body approach demands calculations treating p–d as a three-body system.

3.2 p–d as effective two-body system

In the effective two-body approach, the internal structure of deuteron is ignored[1]. The concept here is that deuterons arise from collisions, and in the initial stages of these collisions, they may not be fully formed. As a result, their internal structure, which consists of a proton and neutron, may not be present. Instead, it is postulated that there could be six quarks, and consequently, the deuteron could be regarded as a spin-1 particle.

The two-particle wavefunction for assuming deuteron and proton as point-like distinguishable particles can be calculated using the Lednický approach as introduced in Chap. 1. This method has been first applied to p–p and p–K^+. The two-body correlation function is calculated using the Koonin Pratt relation Eq. 1.16 where a Gaussian source distribution and wavefunction from the Lednický approach from Eq. 1.24 are used. The total correlation is added using Clebsch Gordan coefficients w_i defined in Eq. 1.19, which are required for the weights for the contribution from different spin channels.

p–p and p–K^+ correlation

The two-particle wavefunction- assuming that strong interaction is dominant only in s-wave and neglecting contributions from higher partial waves can be calculated using the definition provided in Eq. 1.24.

In the case of the p–p pairs, the particles are identical. Therefore, the total p–p wavefunction is required to be antisymmetrized. However, physically only the

[1]Formal understanding in nuclear physics suggests that deuteron is light nuclei composed of two nucleons; however, for femtoscopic studies, one can assume that in the early stage of formation of the deuteron, it is something similar to hexaquark state where the external nucleon would not see the structure of deuteron.

spin singlet ($^1S_0$) channel contributes to the strong interaction, and spin-triplet ($^3S_1$) is forbidden in the s-wave. The p–K^+ correlation system has only a spin doublet channel ($S = 1/2$), and it is a mix of bosons and fermions; therefore does not require antisymmetrization of the total wave function.

For both p–p and p–K^+ systems, the theoretical correlation functions are obtained using the scattering lengths mentioned in Tab. 3.1. The correlation function is computed by considering the Coulomb interaction via the Gamow factor and the Coulomb-corrected scattering amplitude f_c defined in Eq. 1.5.4.[2]. The resulting

System	a_0(fm)	d_0(fm)	References
p–p (S=0)	-7.806	2.788	R. Wiringa et al. [60]
p–K^+ (S=1/2)	-0.316	0.373	M. Hoffmann et al. [128]

TABLE 3.1: Scattering lengths a_0 and effective ranges d_0 for p–p and p–K^+ s-wave states with total S = 0 or 1/2, respectively. For p–K^+ (meson-baryon system), the negative scattering length values refer to a repulsive interaction. For p–p (baryon-baryon) system, the negative and positive values of a_0 refer to attractive and repulsive interactions.

p–p correlation function from the Lednický approach has been compared with the one calculated using the AV18 potential [60] and considering only the s-wave contribution by solving the Schrödinger Equation for the p–p system in CATS [57]. These are shown by the dashed and solid red lines in Fig. 3.1 respectively. For the p–K^+ case, the Lednický correlation function is compared to the one obtained with the full p–K^+ wave function from the Jülich meson exchange model [129] represented by the solid green line in Fig. 3.1. A Gaussian parameterization was used to describe the particle source function $S(r^*)$ with a width of 1.26 fm for all the calculations. The value of Gaussian source size was extracted in a data-driven approach and validated against the measurement of p–p pairs in proton-proton collisions at a center-of-mass energy of $\sqrt{s} = 13$ TeV, as reported in the study by Ref. [130].

While the Lednický formalism reasonably describes the strength and sign of the pp interaction, it does not capture the peak of the correlation function. The deviation in the region of k^* between 20 and 100 MeV/c can be attributed to the repulsive core of the s-wave interaction which is approximated in the Lednický model. The Lednický model only captures the asymptotic form of the interaction and does not account for the short-range behavior of the interaction.

In the case of p–K^+, the Lednický approximation agrees with the meson exchange model as both the Coulomb and strong interactions are repulsive for all distances, without any features of the interaction showing up only at short distances. Thus, the asymptotic Lednický formula provides a good description of the system in this case. The measured correlation functions for p–K^+ and p–p have been successfully described by the AV18 and Jülich models, as reported in several studies [56, 130, 131].

[2]It is important to notice that the asymptotic form of the wavefunction for charged particles is always a combination of regular and singular Coulomb functions, in the case of charged neutral particles, a combination of Bessel functions are used to describe the asymptotic solution.

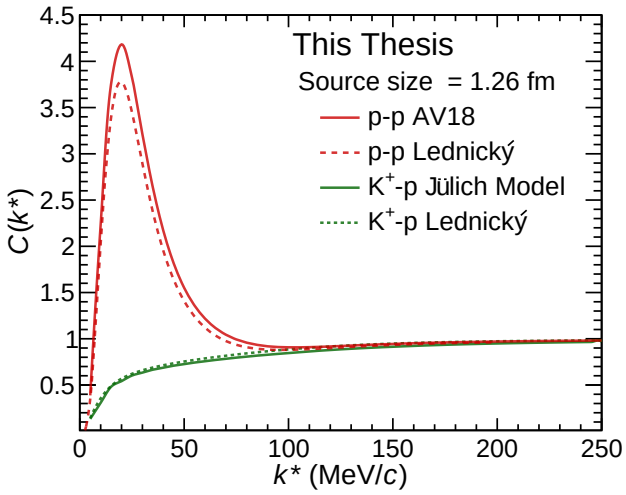

FIGURE 3.1: The theoretical correlation functions for p–p and p–K^+ were obtained using the Lednický approximation and are represented by the red and green dashed lines, respectively. The solid red line corresponds to the correlation function for p–p obtained using the AV18 interaction [60], while the solid green line represents the correlation function for p–K^+ obtained using the Julich meson exchange model [128].

Given that the Lednický approach described the p–p and p–K^+ systems reasonably well, a natural question to ask is why not to test this approach in rather complicated systems, namely K^+–d and p–d. Indeed, this approach can be extended to the p–d system where similar to pp and p–K^+ also, in the case of p–d, there are several scattering experiments have already been performed and the scattering parameters have been extracted using the partial wave analysis [132–135].

Contrary to the case of p–d, there are only a few K^+–d scattering cross-section measurements available so far [136]. The K^+–d scattering parameters may not be measured by the scattering experiments due to several limitations associated with the experimental setups. The latter is associated with detecting the scattered kaons and the deuterons. Detecting kaons is challenging because they have a short lifetime and decay quickly into other particles. Moreover, they have a small production cross-section and interact weakly with matter, which makes their detection even more difficult. On the other hand, detecting deuterons is also challenging because they are heavy and require special detection techniques. The deuteron breakup process can complicate the measurement, and identifying the scattered deuterons is also difficult due to their small cross-section. These difficulties make the measurement of K^+–d scattering parameters a challenging task. At collider experiments, one can use femtoscopy to measure the K^+–d interaction, provided that the source size of the system is known. Currently, the ALICE experiment at the LHC is carrying out a study to measure the femtoscopic correlation of K^+–d and K^-–d pairs in Pb–Pb collisions at $\sqrt{s_{\rm NN}} = 5.02$ TeV, which holds promise for constraining the K^+–d and K^-–d interaction and potentially providing the scattering parameters in these two systems. However, these results are still preliminary and cannot be used in this thesis. For the current study, the K^+–d scattering parameters are obtained from theoretical calculations, and the details of these calculations will be discussed in the next section.

p–d and K^+–d correlations

Before delving into the complete case of Coulomb and strong interactions in the K^+–d and p–d systems, it is important to examine the behavior of the correlation function when considering only the two-body Coulomb interaction in these two systems. In this case, the correlation functions are obtained by considering Coulomb potentials in the Schrödinger equation and assuming an effective two-body Coulomb interaction between the proton or K^+ and the deuteron, with different source sizes of $r_0 = 1.08$ fm and 5 fm. These correlation functions are depicted by the red and blue lines in solid (for p–d) and dashed (for K^+–d) in Fig. 3.2. As it can be observed, kaons are lighter than protons and therefore move faster relative to the deuteron, resulting in less Coulomb repulsion and slightly higher correlation values compared to the case of p–d correlation function. However, at this point, one needs to consider the fact that protons are identical particles, which imposes additional restrictions due to Pauli blocking. This Pauli blocking effect is absent in the two-body formalism and needs to be taken into account when considering the full three-body system.

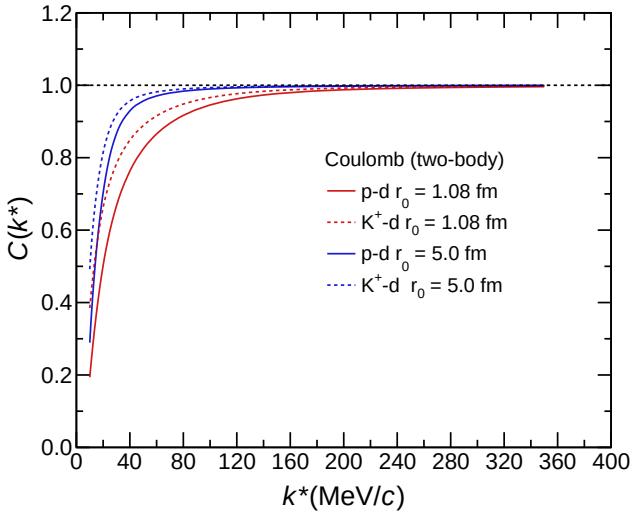

FIGURE 3.2: The solid lines represent the p–d correlation functions, while the dashed lines represent the K^+–d correlation functions. These correlation functions are obtained by solving the two-body Coulomb potential for source sizes of $r_0 = 1.08$ fm and 5.0 fm, considering the proton, kaon, and deuteron as point-like particles.

Since both p–d and K^+–d systems also have strong interaction present, and to account for the strong interaction together with the Coulomb interaction, the Lednický approach can be used to calculate the K^+–d and p–d correlation functions, assuming that these systems are effective two-body systems.

In this thesis, several scattering parameters for p–d spin doublet (S= 1/2) and quartet (S= 3/2) channel, which are obtained by different models [132–135, 137] that analyzed scattering data [138–142] have been considered to calculate the theoretical p–d correlation function. For the K^+–d system, direct measurements of the scattering parameters are scarce, the spin-averaged scattering parameters are anchored to the well-known Kaon-Nucleon (K–N) interactions [143, 144], and K^+–d scattering results are available [145]. The K^+–d scattering parameters used in this thesis rely on two calculations performed by **Prof. Tetsuo Hyodo** and **Prof.**

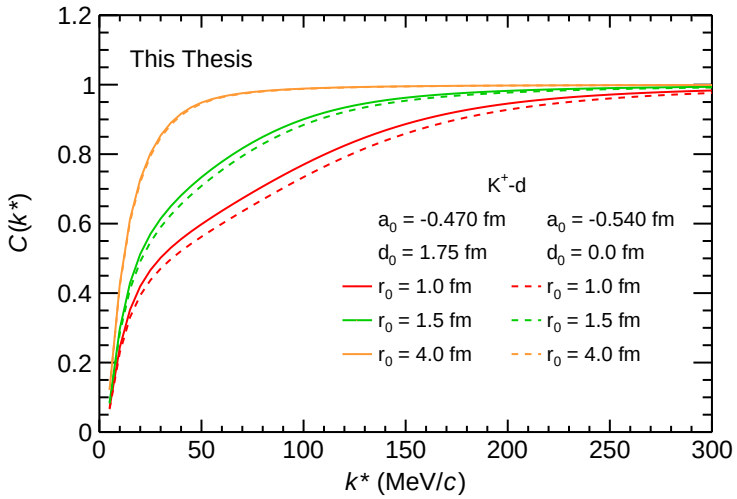

FIGURE 3.3: Theoretical correlation function K^+–d for scattering parameter from Prof. Haidenbauer (solid) and Prof. Hyodo (dashed) considering three different source size $r_0 = 1.0$, 1.5 and 4.0 fm in red green and orange colored lines respectively.

Johann Haidenbauer, and the values of the scattering parameters have been provided through private communication with them. The K^+–d scattering parameters calculated by Prof. Haidenbauer are based on the effective range formula fitted to the elastic scattering cross-section data [146]. Note that in a realistic scenario, deuteron breakup occurs around the center-of-mass energy of $\sim$ 50 MeV/c, and the inelastic part needs to be added to consider the effect of deuteron breakup. On the hand, the calculation of K^+–d scattering parameters by Prof. Hyodo relies on so-called fixed-center approximation approach [147] and uses K–N scattering parameters.

The scattering parameters of p–d and K^+–d are listed in Tab. 3.2. The calcu-

System	Spin avg.		$S = 1/2$		$S = 3/2$		Ref.
	a_0(fm)	d_0(fm)	a_0(fm)	d_0(fm)	a_0(fm)	d_0(fm)	
p–d			$1.30^{+0.20}_{-0.20}$	—	$11.40^{+1.80}_{-1.20}$	$2.05^{+0.25}_{-0.25}$	[137]
			$2.73^{+0.10}_{-0.10}$	$2.27^{+0.12}_{-0.12}$	$11.88^{-0.10}_{+0.40}$	$2.63^{+0.01}_{-0.02}$	[133]
			4.0	—	11.1	—	[134]
			0.024	—	13.8	—	[135]
			$-0.13^{+0.04}_{-0.04}$	—	$14.70^{+2.30}_{-2.30}$	—	[132]
K^+–d	−0.470	1.75					[148]
	−0.540	0.0					[149]

TABLE 3.2: Scattering lengths a_0 and effective ranges d_0 for the p–d and K^+–d s-wave states (meson-baryon convention). For the p–d system, the two different spin states (doublet and quartet) are reported. Negative and positive values of a_0 refer to attractive and repulsive interactions (for cases where the potential does not support two-body bound states), respectively.

lated K^+–d correlation functions for two different sets of scattering parameters and source size values $r_0 = 1.0$, 1.2 and 2.0 fm are shown in Fig. 3.3. For the p–d system the correlation function is calculated separately for doublet ($S = 1/2$) and quartet

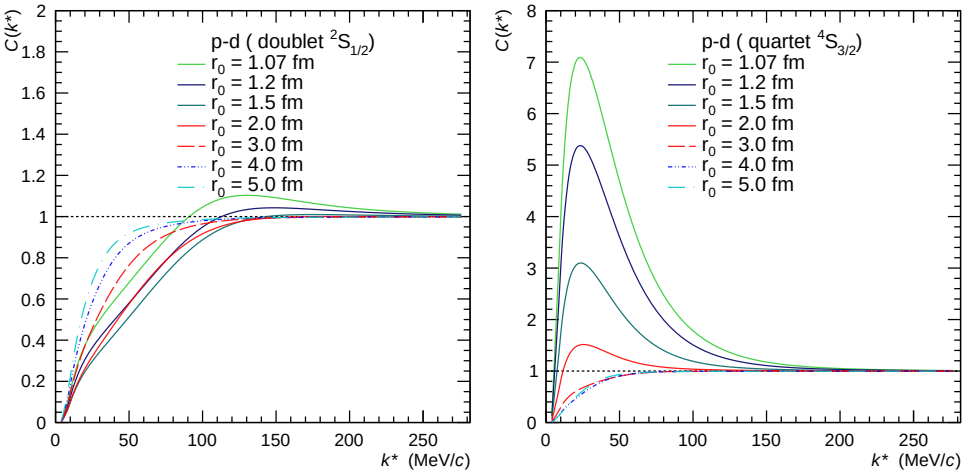

FIGURE 3.4: Theoretical correlation function for p–d doublet ($S = 1/2$) and quartet ($S = 3/2$) channels in the s-wave considering the scattering parameters from Arviuex et al. [133] for several source size $r_0 \in [1.07, 5.0]$ fm shown in the left and right panels.

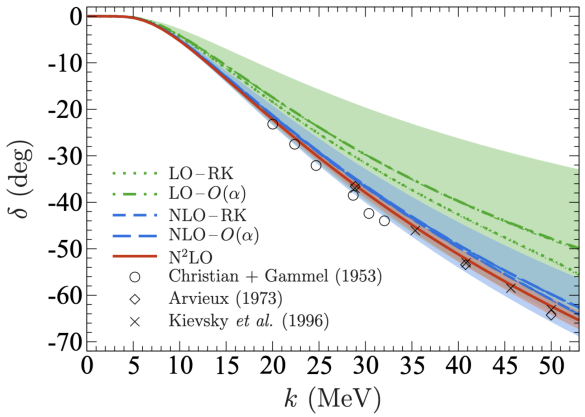

FIGURE 3.5: s-wave p–d quartet channel scattering phase shifts as functions of the center-of-mass momentum k. Figure and caption are taken from [152].

($S = 3/2$) in the s-wave. In the case of the quartet channel, the scattering length is very large, with a positive sign reflecting the repulsive interaction. While in the case of the doublet channel, the scattering length is relatively small and has a bound state of ^{3}He. The calculated correlation function for the doublet and quartet channels are shown in the left and the right panel of Fig. 3.4. It should be noted that in the doublet channel, the scattering parameters show the repulsive interaction in the low k^* region. At the same time, in the intermediate range of k^* region there is an attraction in the doublet channel which vanishes when the source size is increased. On the contrary, the quartet channel correlations show a large peak-like structure indicating an attractive interaction. The peak decreases with increasing source size. This particular feature of the correlation function is quite contradicting to the nature of the quartet channel where only the repulsion is expected from the phase-shift analysis. The theoretical values and experimental p–d phase-shift data shown as the diamonds [133] and circles [150], the crosses are the results from the AV18 potential-model calculation reported in Ref. [151] as shown in Fig. 3.5. The p–d

quartet channel phase shift shows clear repulsion when increasing k^*. Moreover, in the quartet channel, all three nucleons are in a spin aligned state, which maximizes the Pauli-blocking; thus, the effect of the strong interaction becomes negligible. However, in the Lednický approach, since the wavefunction is calculated assuming p–d an effective two-body, there is no possible way to provide antisymmetrization of the wave function w.r.t to the proton sitting inside the deuteron and the proton outside. Therefore, it already suggests that any effective two-body approach is bound to fail in capturing the effect of antisymmetrization in the p–d system. A similar approach to calculate the p–d correlation function has been performed in Ref. [153]. However, in Ref. [153], the asymptotic form of the p–d wavefunction is given by the Bessel function J_0 and the effective range of expansion formula is used for charge-neutral particles, which is disputable since the p–d system has Coulomb interaction due to the positive charge of proton and deuteron. The total p–d correlation function is given by the sum of the contributions from the doublet and the quartet channel in the following

$$C^{\mathrm{p-d}}(k^*) = \frac{1}{3}C^{\mathrm{doublet}}(k^*) + \frac{2}{3}C^{\mathrm{quartet}}(k^*)\,, \tag{3.1}$$

where 1/3 and 2/3 are Clebsch–Gordan coefficients for the doublet and quartet channels and are required to account for the spin-statistics.
The total p–d correlation function is obtained for several source sizes and shown in Fig. 3.6. From Fig. 3.6 it can be seen that at large k^* the correlation is $\sim$1 however, at $k^* \sim 20$ MeV/c there is a large peak showing attraction. This peak decreases when increasing the source size, and for sufficiently large source size $r_0 \sim 3$ fm their correlation function shows total repulsion which is possibly just the Coulomb interaction. Several scattering parameters obtained from scattering experiments are listed in Table 3.2 for p–d. The total theoretical correlation functions for all sets of scattering parameters are shown in Fig. 3.7. The predicted p–d correlation functions for $r_0 = 1.08$ fm exhibit a peak, reflecting attractive interaction in all cases of scattering parameters

As already pointed out in Ref. [51], the two-body wavefunction for two charged particles in Eq. 1.24 accounts for the asymptotic strong interaction only. Therefore, it is worth considering other two-body approaches, such as Gaussian potentials, for p–d interactions.

Gaussian potential approach for p–d

The idea is to perform a study of the p–d correlation function using Gaussian potentials in the Schrödinger equation and obtain an effective two-body wave function for the p–d system. The Gaussian potentials are defined as follows:

$$V(r) = d_1 e^{-\mu_1^2 * r^2} + d_2 e^{-\mu_2^2 * r^2}\,, \tag{3.2}$$

where d_1, d_2, μ_1, and μ_2 are the potential parameters. These potentials are tuned to reproduce the scattering parameters listed in Tab. 3.2 for both the doublet and quartet channels. The corresponding potential parameters are provided in Tab. 3.3. The theoretical correlation functions obtained from the Gaussian potentials, with potential parameters as listed in Tab. 3.3 and a source size for the Gaussian source of $r_0 = 1.0$ fm, are shown in Fig. 3.8. In all cases of the scattering parameters, the interaction model using the Gaussian potentials exhibits a strong peak resembling an

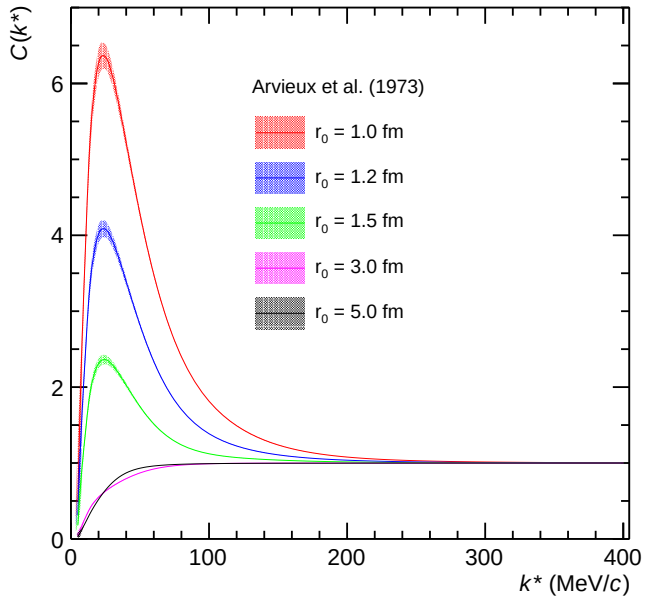

FIGURE 3.6: Theoretical p–d correlation function obtained using doublet and quartet scattering parameters from [133] showing the total contribution for different source size values r_0 = 1.0, 1.2 , 1.5 , 3.0 , and 0.5 fm. Shaded bands show the error from the scattering parameters, while central values show correlations with mean values of scattering parameters.

attractive-type interaction in p–d, which is a further reassurance of what has been obtained using the Lednický approach in Fig. 3.7, where the theoretical correlation functions show a strong peak around $k^* \sim 20$ MeV/c. The fact that both the approach based on the effective two-body potential for p–d and the Lednický approach yields a strong peak in the predicted correlation function, despite the overall repulsive nature of the strong interaction in the quartet channel, is very interesting and raises the following points for discussion:

- Can the Lednicky-Lyuboshits (LL) [61] and Lednický [51] approaches, which are based on the asymptotic form of the strong interaction, be applied to systems where the scattering length is large and the effective range of expansion is small compared to the source size? Indeed, the LL formula possesses the crucial feature of being (roughly) model-independent. It enables a direct connection between two observables: the two-body scattering amplitude (or cross-section) and the correlation function. However, it is important to acknowledge that the LL formula has a limited range of validity. As discussed earlier and extensively explained in the respective literature of the Λ–Λ and Lednický approach, it applies only when the interaction range is significantly smaller than the source size. When this condition is not satisfied, model independence is compromised, and the cross-section and correlation function become effectively independent quantities. In modern terms, one can describe it as the source and the interaction operating on the same scale, thereby breaking the scale separation.

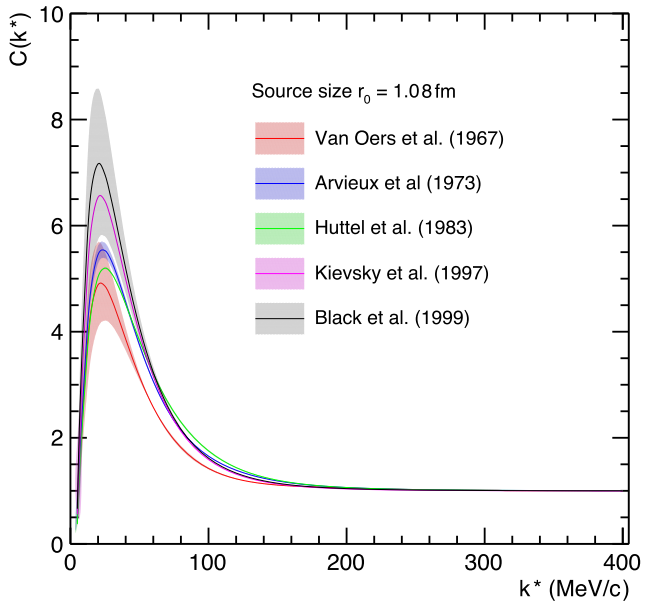

FIGURE 3.7: Theoretical p–d correlation function obtained using doublet and quartet scattering parameters from Tab. 3.2 showing the total contribution for different source size values $r_0 = 1.08$ fm. Shaded bands show the error from the scattering parameters, while central values show correlations with mean values of scattering parameters.

- Can an effective two-body potential support a shallow bound state that produces an attractive peak, even though the overall interaction is repulsive? It is conceivable that the potential in the quartet channel may have the capability to support a shallow bound state with a small binding momentum of approximately 40-50 MeV, considering an effective range of $d \approx 2$ fm based on the Coulomb-modified Effective Range Expansion (ERE) relation from Ref. [154]. Interestingly, the presence of a p–d bound state (virtual) and ERE parameters satisfying this relation suggests that any short-range potential, when combined with the Coulomb interaction, would reproduce the quartet-channel p–d ERE parameters and simultaneously support this universal bound state. However, such a bound state in the quartet channel is not observed in nature due to the Pauli exclusion principle (as a proton with the same spin as the incoming/outgoing proton already occupies the state). Consequently, there is no actual bound state, indicating a breakdown of the effective two-body picture. Fortunately, such complications do not arise in the cases of K^+–d or other hadron-deuteron systems where Pauli blocking does not take place.
- Can an effective two-body potential be constructed for the p–d system that yields an overall repulsive interaction? Constructing an effective and meaningful two-body potential for p–d presents a delicate challenge. For instance, in the quartet state, a bound state is prohibited by the Pauli exclusion principle. However, it raises questions about its manifestation in the wave function and more specifically how the Koonin-Pratt formula captures this effect. The Pauli exclusion must be considered at the potential level when constructing the effective two-body potential. By incorporating it at this stage, it will be reflected in the wavefunction and subsequently in the Koonin-Pratt equation. However,

Ref.		$d_1 \times 10^2$ fm^{-1}	$d_2 \times 10^2$ fm^{-1}	$\mu_1 \times 10^{-2}$ MeV	$\mu_2 \times 10^{-2}$ MeV
[137]	doublet	−1.360094	76.53426	64.34147	6.934830
	quartet	3.977925	−4.980722	115.6718	110.3321
[133]	doublet	−0.1991391	−1.304032	134.5703	46.95568
	quartet	−1.392660	−1.138655	26.32242	79.30126
[134]	doublet	4.329849	−5.014949	117.8091	115.2404
	quartet	3.976208	−4.982211	115.5627	110.1896
[135]	doublet	−12.67767	81.54914	22.49449	0.4028239
	quartet	38.49480	−7.050797	17.65305	44.46987
[132]	doublet	−12.70824	−17.99458	43.61619	27.26117
	quartet	3.974149	−4.980150	115.8149	110.5299

TABLE 3.3: Gaussian potential parameters obtained from the mean values of Scattering lengths a_0 and effective ranges d_0 errors on the scattering parameters from Tab. 3.2 are omitted.

at the moment such a model is not available.

- Personal comment: Although one expects the p–d system to behave similarly in both scattering experiments and Femtoscopy, this assumption may not always hold true. It is crucial to acknowledge that deuterons can exhibit different interaction dynamics in Femtoscopy compared to scattering processes. Specifically, deuterons demonstrate varying interactions within different scattering processes, particularly below and above the breakup energies. Furthermore, the possibility of rearrangements involving the nucleons leads to the formation and reformation of the deuteron over a considerable distance during the scattering process. In the case of K^+–d scattering, it becomes evident that the interaction between the K^+ particle and the deuteron is primarily confined to the surface of the latter.

Despite all the caveats associated with the effective two-body approach, it is interesting to compare it with the measured p–d and K^+–d correlation functions. In Chapter 4, we will observe that while the measured K^+–d correlation function can be adequately described by the effective two-body approach for a source size of $r_0 \sim 1.4$ fm, the same approach fails to explain the measured p–d correlation function. The measured correlation function demonstrates a repulsive interaction and the absence of an attractive peak at $k^* \sim 20$ MeV/c. The fact that the effective two-body approach for the p–d system does not work necessitates the calculation of the p–d correlation function by considering the p–d system as an ensemble of p–(p–n), which will be discussed in the next section.

3.3 Three-body treatment of p–d system

The main objective of calculating the p–d correlation function starting from the three-nucleons dynamics and interaction is to offer an accurate description of the precise measurement of the p–d correlation in momentum space, which is obtained in proton-proton (pp) collisions at the LHC, which will be discussed in detail in Chap. 4 of this thesis. The theoretical framework for this calculation encompasses all pertinent complexities necessary for accurately describing the system, including considerations for antisymmetrization effects. Additionally, the theoretical development of the Koonin-Pratt relation, which is typically used to describe the two-body

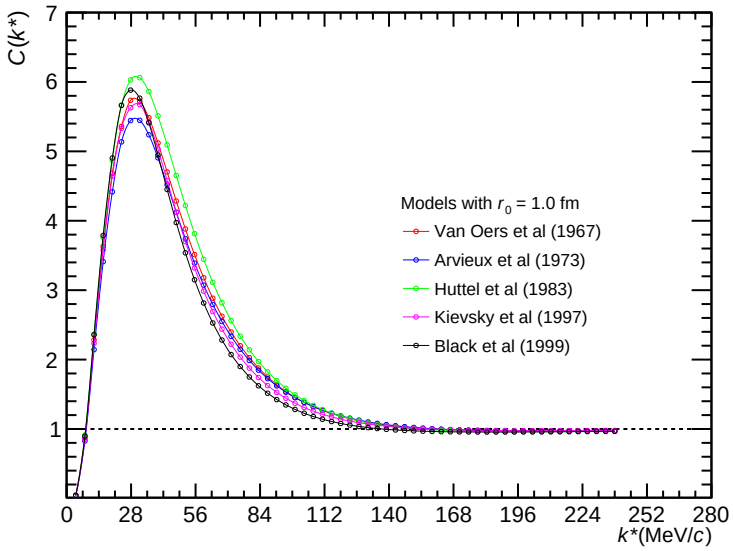

FIGURE 3.8: Theoretical p–d correlation function obtained by solving the Schrödinger equation in CATS framework for effective two-body Gaussian potentials in the p–d system, with a Gaussian source size of $r_0 = 1$ fm. The Gaussian potentials are tuned to doublet and quartet scattering parameters. The total contribution for each set of scattering parameters from Tab. 3.2 is shown in different colored curves in the figure.

correlation function related to the emission of two particles and can be precisely characterized [56], needs to be extended to account for the case of three emitted nucleons, where two of them form a deuteron.

The work presented in this section is a collaborative effort involving theorists from INFN PISA, including Michele Viviani, Alejandro Kievsky, and Laura Marcucci, as well as Sebastian König from NC State University, Oton Vazquez Doce from INFN Frascati, and myself. The corresponding work has been summarized in the manuscript [155].

The foundation of this calculation lies in the transition from the two-body definition of the Koonin-Pratt relation to a correlation function involving three particles. Within the framework of quantum mechanics, the correlation between a pair of particles (with spins s_1 and s_2 respectively) can be linked to the particle emission and subsequent interaction of the particle pair, as discussed in Ref. [156], as

$$C\left(\boldsymbol{p}_1, \boldsymbol{p}_2\right) = \frac{1}{(2s_1+1)(2s_2+1)} \sum_{m_1,m_2} \int d^3r_1\, d^3r_2 S_1\left(r_1\right) S_1\left(r_2\right) \left|\Psi_{m_1,m_2}(\boldsymbol{p}_1, \boldsymbol{p}_2, \boldsymbol{r}_1, \boldsymbol{r}_2)\right|^2 . \tag{3.3}$$

Here bold $\boldsymbol{x}$ and italic x symbols represent vector and length of x. The term $\Psi_{m_1,m_2}(\boldsymbol{p}_1, \boldsymbol{p}_2, \boldsymbol{r}_1, \boldsymbol{r}_2)$ represents the two-particle scattering wave function, which asymptotically characterizes the behavior of particle 1(2) with momentum $\boldsymbol{p}_1$ ($\boldsymbol{p}_2$) and spin projection m_1 (m_2). In Eq. 3.3, $S_1(r)$ describes the spatial profile of the emission source for a single particle. $S_1(r)$ can be approximated as a Gaussian probability

distribution with a width R_M, which is defined as follows:

$$S_1(r) = \frac{1}{(2\pi R_M^2)^{\frac{3}{2}}} e^{-r^2/2R_M^2} \,. \tag{3.4}$$

The width R_M, also referred to as the source size for single-particle emission, characterizes the size of the source. In the wave function given by Eq. 3.3, where the dependence is solely on the center-of-mass coordinates, it becomes apparent that the overall center-of-mass (CM) coordinate can be easily separated or factored out, leading to a simplification of the equation. Using the CM coordinate $\boldsymbol{R} \equiv \frac{M_1 \boldsymbol{r}_1 + M_2 \boldsymbol{r}_2}{M_1 + M_2}$, where M_1 and M_2 are the masses of the two particles, the relative distance $\boldsymbol{r} \equiv \boldsymbol{r}_1 - \boldsymbol{r}_2$, and rewriting the two-particle wave function as $\Psi_{m_1,m_2}(\boldsymbol{p}_1, \boldsymbol{p}_2, \boldsymbol{r}_1, \boldsymbol{r}_2) = e^{-i\boldsymbol{R}\cdot\boldsymbol{P}} \psi_{m_1,m_2,k}(\boldsymbol{r})$ leads to the Koonin-Pratt relation for two-particle correlation as discussed in Chap. 1 and alternatively defined as

$$C(k) = \frac{1}{(2s_1+1)(2s_2+1)} \sum_{m_1,m_2} \int d^3r \, S(r) \, |\psi_{m_1,m_2,\boldsymbol{k}}(\boldsymbol{r})|^2 \,. \tag{3.5}$$

Important Note: Throughout this calculation, $\mathbf{k}$ is a vector, and k represents the magnitude of the vector $\mathbf{k}$. The asterisk $(*)$ over k^* is dropped, indicating that $k^* \equiv k$ wherever necessary.

In general, the Koonin-Pratt relation represents a spin-averaged correlation function. However, in this specific definition of the correlation function, a deliberate inclusion of a sum over spin projections is made. This choice is motivated by the fact that when considering three-particle correlation, it is more convenient to construct the three-particle wave function by accounting for different spin projections and different partial waves and aggregating all the correlations to obtain the final result. In Eq. 3.5, where $\psi_{m_1,m_2,\boldsymbol{k}}(\boldsymbol{r})$ represents the two-particle relative wave function with $\boldsymbol{k} = \boldsymbol{p}_1 - \boldsymbol{p}_2$, and $S(r)$ denotes the two-particle emission source which is written as

$$S(r) = \left(\frac{1}{4\pi R_{\mathrm{M}}^2}\right)^{3/2} e^{-\frac{r^2}{4R_{\mathrm{M}}^2}} \,. \tag{3.6}$$

In this expression the parameters R_M is the source size of pair of particles. This formalism can be extended to the three-body case. However, it is significantly more challenging due to the construction of three-body wave functions. A generic three-particle correlation function is defined in Ref. [157, 158]

$$\begin{aligned} C_3(\boldsymbol{p}_1, \boldsymbol{p}_2, \boldsymbol{p}_3) = & \frac{1}{(2s_1+1)(2s_2+1)(2s_3+1)} \sum_{m_1,m_2,m_3} \int d^3 r_1 \, d^3 r_2 \, d^3 r_3 \\ & \times S_3(\boldsymbol{r}_1, \boldsymbol{r}_2, \boldsymbol{r}_3) \, |\Psi_{m_1,m_2,m_3}(\boldsymbol{p}_1, \boldsymbol{p}_2, \boldsymbol{p}_3, \boldsymbol{r}_1, \boldsymbol{r}_2, \boldsymbol{r}_3)|^2 \,, \end{aligned} \tag{3.7}$$

where $\boldsymbol{r}_i$, $\boldsymbol{p}_i$, and m_i for $i \in [1,3]$ represent the coordinates, momenta, and spin projections of the three particles. $S_3(\boldsymbol{r}_1, \boldsymbol{r}_2, \boldsymbol{r}_3)$ is the three-body source function, which is normalized to unity. $\Psi_{m_1,m_2,m_3}(\boldsymbol{p}_1, \boldsymbol{p}_2, \boldsymbol{p}_3, \boldsymbol{r}_1, \boldsymbol{r}_2, \boldsymbol{r}_3)$ represents the wave function of the three-body system in the position coordinates representation.

Similar to the two-particle case, the source for the emission of three particles can be assumed to factorize in terms of single-particle sources

$$S_3(\boldsymbol{r}_1, \boldsymbol{r}_2, \boldsymbol{r}_3) = S_1(\boldsymbol{r}_1) \, S_1(\boldsymbol{r}_2) \, S_1(\boldsymbol{r}_3) \,. \tag{3.8}$$

More details on the theoretical description of the three-particle correlation function, specifically when all three particles are unbound, including the case of three protons or proton-proton-Lambda, can be found in the Ph.D. Thesis of Laura Šerkšnytė [159].

In the case of p–d, the starting point is the same as defined in Eq. 3.7. Furthermore, the theoretical framework for p–d correlations is also built upon the approach proposed by Mrowczynski, which has previously been utilized to study the coalescence of proton-neutron pairs into a deuteron using hadron-deuteron correlations [156]. The correlation function for p–d is defined as follows:

$$A_d C_{pd}(k) = \frac{1}{6} \sum_{m_2,m_1} \int d^3r_1 d^3r_2 d^3r_3 \; S_1(r_1) S_1(r_2) S_1(r_3) \left|\Psi_{k;m_2,m_1}\right|^2 . \tag{3.9}$$

The p–d correlation function involves the three-particle p–(p–n) wavefunction, denoted as $\Psi_{k;m_2,m_1}$, which described the p–d asyptotic. The details of this wavefunction will be discussed in the upcoming text. Here, m_1, m_2, and $\boldsymbol{k}$ represent the angular momentum components and the relative p–d momentum respectively. The given equation includes an explicit summation over the angular momentum components m_1 and m_2 for the wavefunction. However, whether or not these components appear explicitly in practical calculations depends on the specific method used to calculate $\Psi_{k;m_2,m_1}$. The prefactor A_d represents the probability of deuteron formation and is defined as follows:

$$A_d = \frac{1}{3} \sum_{m_2} \int d^3r_1 d^3r_2 \; S_1(r_1) S_1(r_2) \left|\varphi_{d,m_2}\right|^2 , \tag{3.10}$$

where φ_d denotes the deuteron bound-state wave function. The primary motivation for reweighting the p–(p–n) correlation function with A_d arises from the deuteron formation process. It is assumed that deuteron formation occurs through coalescence, implying that there is a probability for the p–n pair to combine and form a deuteron. The probability of d formation denoted as A_d, needs to be considered when calculating the p–d correlation function. Similarly, this argument applies to any nuclei-nuclei or nuclei-hadron correlation function, where the probability of formation of the desired composite particle must be taken into account.

The equation 3.9 can be simplified by introducing the CM and relative coordinates. To evaluate A_d, the integration variables are changed by introducing a coordinate transformation $\boldsymbol{r} = \boldsymbol{r}_1 - \boldsymbol{r}_2$, which represents the relative distance between the proton-neutron (p–n) pair, and $\boldsymbol{R} = \frac{1}{2}(\boldsymbol{r}_1 + \boldsymbol{r}_2)$, which represents the coordinate for the deuteron. By expressing the product $S_1(r_1)S_1(r_2)$ in terms of r and R, and then integrating over $\boldsymbol{R}$, gives rise to the following simple expression:

$$A_d = \frac{1}{3} \sum_{m_2} \int d^3r \; \frac{e^{-r^2/4R_M^2}}{(4\pi R_M^2)^{\frac{3}{2}}} \left|\varphi_{m_2}\right|^2 . \tag{3.11}$$

Furthermore, Eq. 3.9 can be simplified by introducing the following relative coordinates

$$\boldsymbol{x} = \boldsymbol{r}_1 - \boldsymbol{r}_2 , \qquad \boldsymbol{y} = \boldsymbol{r}_3 - \frac{\boldsymbol{r}_1 + \boldsymbol{r}_2}{2} , \qquad \boldsymbol{R}_3 = \frac{1}{3}(\boldsymbol{r}_1 + \boldsymbol{r}_2 + \boldsymbol{r}_3) , \tag{3.12}$$

where x,y, and R_3 are distance between p–n pair that form d, distance between CM of p–n and the proton, and coordinate of CM of p–d as depicted in the Fig. 3.9 (a). With these substitutions into the $S_1(r_1)\, S_1(r_2)\, S_1(r_3)$ gives the following expression

for the source

$$S_3\left(r_1, r_2, r_3\right) = \frac{e^{-\left(3R_3^2+\frac{2}{3}y^2+\frac{1}{2}x^2\right)/2R_M^2}}{\left(2\pi R_M^2\right)^{\frac{9}{2}}}\,. \tag{3.13}$$

By substituting $\mathrm{d}^3r_1\,\mathrm{d}^3r_2\,\mathrm{d}^3r_3 = \mathrm{d}^3R_3\,\mathrm{d}^3x\,\mathrm{d}^3y$ and $S_1\left(r_2\right)S_1\left(r_3\right)$ in Eq. 3.10, and integrating over $\int \mathrm{d}^3R_3$ where the wavefunction $\Psi_{k;m_2,m_1}$ is independent of R_3, results into a simpler expression

$$A_d C_{pd}(k) = \frac{1}{6}\sum_{m_2,m_1}\int d^3x\, d^3y\, \frac{e^{-(\frac{4}{3}y^2+x^2)/4R_M^2}}{(3\pi R_M^2)^{\frac{3}{2}}(4\pi R_M^2)^{\frac{3}{2}}}\left|\Psi_{k;m_2,m_1}\right|^2\,. \tag{3.14}$$

The source function is then given by the following expression

$$S_3\left(x, y\right) = \frac{e^{-(\frac{4}{3}y^2+x^2)/4R_M^2}}{(3\pi R_M^2)^{\frac{3}{2}}(4\pi R_M^2)^{\frac{3}{2}}}\,. \tag{3.15}$$

It is advantageous to introduce Jacobi coordinates while dealing with the three-body problem. Jacobi coordinates allow us to leverage the symmetries of the system, which can be very useful in simplifying the problem mathematically [160, 161]. A generalized form of Jacobi coordinates for a system of A particles with masses $m_1, \ldots, m_A$ and spatial coordinates $\boldsymbol{r}_1, \ldots, \boldsymbol{r}_A$, can be written by separating the internal and C.M. motion. The coordinate for C.M is given by

$$\boldsymbol{\xi}_{cm} = \frac{1}{M}\sum_{i=1}^{A} m_i \boldsymbol{r}_i \tag{3.16}$$

where $M = \sum_{i=1}^{A} m_i$ is the system's total mass. The $N = A - 1$ internal Jacobi coordinates $\boldsymbol{\xi}_1, \ldots, \boldsymbol{\xi}_N$ are determined by the spatial coordinate of A particles. There are different ways to define the Jacobi coordinates. One of the ways used in this calculation is

$$\boldsymbol{\xi}_{N-j+1} = \sqrt{\frac{2m_{j+1}M_j}{M_{j+1}m}}\left(\boldsymbol{r}_{j+1} - \frac{1}{M_j}\sum_{i=1}^{j} m_i \boldsymbol{r}_i\right)\,, \text{for } j = 1, \ldots, N \tag{3.17}$$

where m is a reference mass, $M_j = \sum_{i=1}^{j} m_i$. A schematic representation of Jacobi coordinates for $A = 3$ is shown in Fig. 3.9 (b). For a system of A particles with the same masses m, Eq. 3.17 reduces to:

$$\boldsymbol{\xi}_{N-j+1} = \sqrt{\frac{2j}{j+1}}\left(\boldsymbol{r}_{j+1} - \frac{1}{j}\sum_{i=1}^{j} \boldsymbol{r}_i\right)\,. \tag{3.18}$$

Using the Jacobi vectors, one can introduce hyperspherical coordinates (ρ, Ω_N), where the hyperradius ρ and the set of hyperangular coordinates Ω_N are defined by:

$$\rho = \sqrt{\sum_{i=1}^{N}\xi_i^2} \text{ and } \Omega_N = \left\{\hat{\boldsymbol{\xi}}_1, \ldots, \hat{\boldsymbol{\xi}}_N, \varphi_2, \ldots, \varphi_N\right\}\,, \tag{3.19}$$

The modulus of the Jacobi vector $\boldsymbol{\xi}_i$ is denoted by ξ_i. The hyperradius ρ is symmetric with respect to particle exchanges and does not depend on the particular choice of

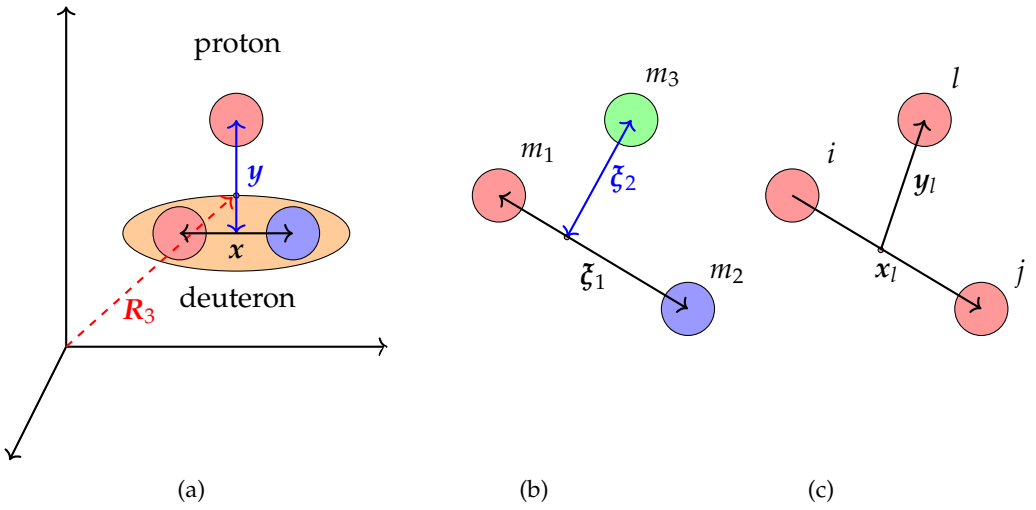

FIGURE 3.9: (a) Sketch representing the coordinates for the p–d system. (b) Sketch illustrating the Jacobi coordinates for a three-particle system with masses m_1, m_2, and m_3. (c) Sketch for the Jacobi coordinates of three nucleons.

Jacobi coordinates. The angular parts $\hat{\xi}_i = (\theta_i, \phi_i)$ represent the spherical components of the Jacobi vectors $\boldsymbol{\xi}_i$, where $i = 1, \ldots N$. Additionally, the hyperangles φ_j are defined by $\cos\varphi_j = \frac{x_j}{\sqrt{x_1^2+\ldots+x_j^2}}$ with $0 < \varphi_i < \pi/2$ and $j = 2, \ldots, N$.

In the case of p–d system, neglecting the difference in proton and neutron mass ($m_p \approx m_n$), the Jacobi vectors are then obtained as

$$\boldsymbol{\xi}_1 = \sqrt{\frac{4}{3}}\boldsymbol{y} \quad \text{and} \quad \boldsymbol{\xi}_2 = \boldsymbol{x}\,, \tag{3.20}$$

where the internal coordinates $\boldsymbol{x}$ and $\boldsymbol{y}$ are defined in Eq. 3.12. and the hyperradius, see Eq. 3.19, is $\rho = \sqrt{\xi_1^2 + \xi_2^2}$, and $d^3\xi_1 d^3\xi_2 = \rho^5 d\rho d\Omega$. Finally, one obtains

$$A_d C_{pd}(k) = \frac{1}{6}\sum_{m_2,m_1}\int \rho^5 d\rho d\Omega\, \frac{e^{-\rho^2/4R_M^2}}{(4\pi R_M^2)^3}\,|\Psi_{k;m_2,m_1}|^2\ . \tag{3.21}$$

The variable R_M represents the Gaussian source size for the pairwise interaction between two nucleons participating in the formation of the p–d system. It is estimated in the analysis of p–d correlation measurements, which will be discussed in Chap. 4.2. However, a crucial missing component is a three-particle wavefunction $\Psi_{k;m_2,m_1}$ which is the proton-deuteron scattering wave function. This wavefunction needs to be calculated in order to study the p–d correlation.

Two different methods are used to compute the wavefunction: the Hyperspherical Harmonics (HH) approach [161] and the Faddeev equations in momentum space. In the (HH) approach, the explicit sums over m_2 and m_1 are performed for the angular-momentum components of the wave function as indicated in the above equations. On the other hand, the Faddeev equations in momentum space implicitly incorporate these sums through the choice of basis. Detailed descriptions of the methods will be given in the forthcoming sections.

3.3.1 Hyperspherical harmonics method for p–d

In the Hyperspherical harmonics formalism, the p–d system is treated as a system of three particles with full dynamics. The particle distances are represented by Jacobi coordinates $\boldsymbol{x}_\ell$ and $\boldsymbol{y}_\ell$ for a particular configuration ℓ, as shown in Fig. 3.9 (c). Since the particles are identical in this scenario, it is necessary to account for the wave-function's antisymmetrization (Pauli-blocking effect). To achieve this, $\boldsymbol{x}_\ell$ and $\boldsymbol{y}_\ell$ are defined for a given permutation $ij\ell$ of the three nucleons in the following way:

$$\boldsymbol{x}_\ell = \boldsymbol{r}_j - \boldsymbol{r}_i, \quad \boldsymbol{y}_\ell = \boldsymbol{r}_\ell - \frac{\boldsymbol{r}_i + \boldsymbol{r}_j}{2}\,. \tag{3.22}$$

In order to construct an antisymmetric wavefunction it is sufficient to consider the three even permutations of the three particles, namely ijl = 123, 231 and 312. The nuclear Hamiltonian for p–d in this approach is written as

$$H = T + V = T_{CM} - \frac{h^2}{2m}\left(\nabla^2_{x_\ell} + \nabla^2_{y_\ell}\right) + \sum_{j>i=1}^{3} V_{ij}^{NN} + \sum_{\ell>j>i=1}^{3} V_{ij\ell}^{NNN}\,, \tag{3.23}$$

where T_{CM} is the kinetic energy of the center of mass of the p–d system while $\frac{h^2}{2m}\left(\nabla^2_{x_\ell} + \nabla^2_{y_\ell}\right)$ is the kinetic energy of the deuteron and proton due to internal motion. The terms V_{ij}^{NN} and $V_{ij\ell}^{NNN}$ represent the two-nucleon (NN) and three-nucleon (NNN) potentials, respectively. In this method two different cases for the potentials are considered: the AV18 potential supplemented by the Urbana IX (UIX) three-nucleon force [162], and a two- and three-nucleon potential model derived from χEFT, specifically the Norfolk interactions [163], referred to as NVIa+3N in Ref. [164].

The internal kinetic energy term in Eq. 3.23 can be written using the hyperspherical coordinates and can be decomposed as

$$T = -\frac{h^2}{2m}\left(\nabla^2_{x_\ell} + \nabla^2_{y_\ell}\right) = -\frac{\hbar^2}{m}\left(\frac{\partial^2}{\partial\rho^2} + \frac{3N-1}{\rho}\frac{\partial}{\partial\rho} - \frac{\Lambda^2_N(\Omega_N)}{\rho^2}\right)\,. \tag{3.24}$$

where the operator $\Lambda^2_N(\Omega_N)$ is the so-called grand-angular momentum operator [161]. The exact form of $\Lambda^2_N(\Omega_N)$ is not important but can be found in Red. [160]. However what is more important are the eigenfunctions of the grand-angular momentum $\Lambda^2_N(\Omega_N)$, the so-called hyperspherical harmonics $\mathcal{Y}^{KLM_L}_{[K]}(\Omega_N)$, details of which are defined in [160, 161].

In order to obtain the wavefunction for a three-particle system, the Schrödinger Equation $H\Psi = (T+V)\Psi = E\Psi$ needs to be solved. Various methods exist to solve this equation, including the Faddeev equations (FE) technique [165, 166]. These equations can be solved in either configuration space or momentum space [167–169]. Alternatively, variational principles can be used. For instance, the Rayleigh-Ritz variational principle is employed to study bound states, while the Kohn variational principle [170] and quantum Monte Carlo variational methods have been applied in different ways [171, 172]. These methods utilize sophisticated algorithms to evaluate appropriate path integrals and obtain the properties of bound states of the Hamiltonian.

To obtain p–d three-particle wavefunction, the HH method is employed using the hyperangular coordinates. The hyperradius ρ and hyperangles φ_ℓ are defined in terms of the moduli of the Jacobi vectors

$$\rho = \sqrt{x_\ell^2 + \frac{4}{3} y_\ell^2}\,, \qquad \tan\varphi_\ell = \sqrt{\frac{4}{3}}\frac{y_\ell}{x_\ell}\,. \tag{3.25}$$

The hyperradius ρ is independent of the permutation ℓ. In fact, it can be shown that $\rho^2 = \frac{2}{3}(r_{12}^2 + r_{13}^2 + r_{23}^2)$, where r_{ij} is the distance between particles i and j. The set of hyperangular and angular variables is denoted with Ω_ℓ, namely

$$\Omega_\ell \equiv \{\varphi_\ell, \hat{\boldsymbol{x}}_\ell, \hat{\boldsymbol{y}}_\ell\}\,. \tag{3.26}$$

The symbols $\hat{\boldsymbol{x}}_\ell$ and $\hat{\boldsymbol{y}}_\ell$ represent the polar angles of the vectors $\boldsymbol{x}_\ell$ and $\boldsymbol{y}_\ell$, respectively. If the permutation index is not specified, the default ordering of particles is assumed to be $ij\ell = 123$. The wave function of the p–d system, which is characterized by the total angular momentum J, the z-component of angular momentum J_z, and the parity π, is calculated in two distinct cases: 1. The free case, where only the Coulomb interaction is taken into account, and 2. The full interaction case.

Coulomb interaction in p–d

The simple case in the HH method is to first consider a free p–d system, where the only distortion in the plane wave arises from the presence of the Coulomb interaction. In this case, the wave function is given by:

$$\Psi^{(\text{free})}_{m_2,m_1} = \frac{1}{\sqrt{3}} \sum_{\ell}^{\text{even perm.}} \phi_{m_2}(ij)\chi_{m_1}(\ell)\Phi_c(\boldsymbol{k}, \boldsymbol{y}_\ell)\,, \tag{3.27}$$

The factor $1/\sqrt{3}$ is necessary for normalization due to antisymmetrization. The wavefunction $\phi_{m_2}(ij)$ represents the deuteron wavefunction with spin projection m_2. $\boldsymbol{k}$ denotes the relative momentum between the proton and deuteron, $\chi_{m_1}(\ell)$ is a spinor describing the proton, and $\Phi_c(\boldsymbol{k}, \boldsymbol{y}_\ell)$ represents a Coulomb-distorted plane wave. The Coulomb-distorted plane wave has the following partial-wave expansion:

$$\Phi_c(\boldsymbol{k}, \boldsymbol{y}) = \sum_{LM} 4\pi\, i^L\, Y^*_{LM}(\hat{\boldsymbol{k}}) Y_{LM}(\hat{\boldsymbol{y}}) e^{i\sigma_L} \frac{F_L(\eta, ky)}{ky}\,. \tag{3.28}$$

Here $Y_{LM}(\hat{\boldsymbol{y}})$ represents the standard spherical harmonic function [160], $F_L(\eta, ky)$ denotes the regular Coulomb function, and σ_L represents the Coulomb phase shift. It should be noted that the deuteron wavefunction is obtained using either the AV18 potential or from χEFT, both of which are two-nucleon potentials for the strong interaction.

Finally, the Coulomb distorted plane wave from Eq 3.28 is plugged in the Eq. 3.27 and expanded as a sum of terms with definite total angular momentum J. Using one of the possible choices of the recoupling order, the Eq. 3.27 reads as

$$\begin{aligned}\Psi^{(\text{free})}_{m_2,m_1} = &\sum_{LSJ} \sqrt{4\pi} i^L \sqrt{2L+1} e^{i\sigma_L} (1 m_2 \frac{1}{2} m_1 \mid S J_z)(L0 S J_z \mid J J_z) \\ &\times \frac{1}{\sqrt{3}} \sum_{\ell}^{\text{even perm.}} \left\{ Y_L(\hat{\boldsymbol{y}}_\ell) \left[\phi_{m_2}(ij)\chi_{m_1}(\ell)\right]_S \right\}_{JJ_z} \frac{F_L(\eta, k y_\ell)}{k y_\ell}\,.\end{aligned} \tag{3.29}$$

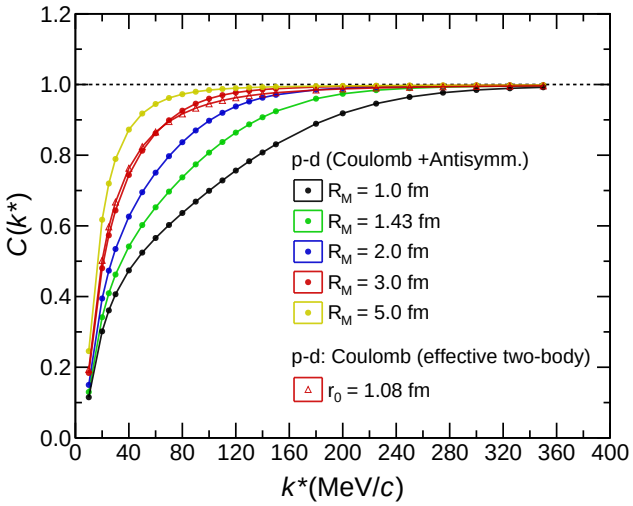

FIGURE 3.10: The p–d correlation is studied using three-body dynamics with Coulomb interaction. The nucleon-nucleon pair source sizes considered are $R_M = 1.0, 1.43, 2.0, 3.0$, and 5.0 fm. The $R_M = 1.43$ fm corresponds to the source size of the nucleon-nucleon pair constrained by the p–d analysis. Additionally, for comparison, the two-body correlation function is calculated using only the Coulomb interaction and the p–d source size $r_0 = 1.08$ fm, represented by the magenta line.

In order to account for the total spins and angular momenta of the system, different coupling coefficients $\sum_{LSJ} \sqrt{4\pi} i^L \sqrt{2L+1} e^{i\sigma_L} (1 m_2 \tfrac{1}{2} m_1 \mid SJ_z)(L0SJ_z \mid JJ_z)$ with $J_z = m_1 + m_2$, are used. The coefficients are required for various recouplings such as $Y_{LM}\chi_{SS_z} = \sum_{J,J_z}(L, M, S, S_z|J, J_z)[Y_L\chi_S]J, J_z$ from Ref. [160], are denoted as $[Y_L\chi_S]_{J,J_z} = \sum_{M',S'_z}(L, M', S, S'_z|J, J_z)Y_{LM'}\chi_{SS'_z}$ in this calculation. The Clebsch-Gordan coefficients $(L0SJ_z|JJ_z)$ are given in a short form for $(L, 0, J, J_z|J, J_z)$. Additionally, it is assumed that $\hat{\boldsymbol{k}}||\hat{\boldsymbol{z}}$ are parallel, hence $Y_{LM}(\hat{\boldsymbol{k}}) = \frac{\sqrt{2L+1}}{\sqrt{4\pi}}\delta_{M,0}$.

The correlation function for p–d, considering the Coulomb interaction and all possible antisymmetrization effects, is calculated using Equation 3.21 and the wavefunction $\Psi^{(\text{free})}_{m_2,m_1}$. The calculated correlation function is shown in Fig. 3.10 with solid markers for source sizes $R_M = 1.0, 1.43, 2.0, 3.0$, and 5.0 fm. The same figure also includes a comparison with the two-body Coulomb case for the p–d source size $r_0 = 1.08$ fm (represented by red triangles), which corresponds to the NN source size $R_M = 1.41$ fm (represented by a green solid marker). It should be noted that the p–d correlation function exhibits a significant effect due to Pauli blocking, resulting in increased repulsion compared to the effective two-body calculations that consider only Coulomb interaction without accounting for Pauli blocking.

Coulomb and strong interaction in p–d

In practice, the p–d system consists of three nucleons that interact strongly. Therefore, a theoretical description of the p–d system requires the explicit inclusion of the strong interaction. This is achieved by using the V_{ij}^{NN} and $V_{ij\ell}^{NNN}$ potentials in Equation 3.23. The solution to the Schrödinger equation is then given by the wave function Ψ_{LSJJ_z}. The total wave function, which considers all possible spin, isospin,

and angular states, is defined as

$$\Psi^{pd}_{m_2,m_1,k} = \sum_{LSJ} \sqrt{4\pi} i^L \sqrt{2L+1} e^{i\sigma_L} (1 m_2 \tfrac{1}{2} m_1 \mid SJ_z)(L0SJ_z \mid JJ_z) \Psi_{LSJJ_z} , \tag{3.30}$$

The term $(1m_2\frac{1}{2}m_1 \mid SJ_z)(L0SJ_z \mid JJ_z)$ represents the Clebsch-Gordan coefficients for the coupling of spin, isospin, and angular momentum states. The wavefunctions Ψ_{LSJJ_z} are three-body wavefunctions that satisfy $(H-E)\Psi_{LSJJ_z} = 0$, where H is the Hamiltonian. The total energy of the system is given by $E = \frac{4}{3}\frac{k^2}{M_N} - B_d$, where k is the relative momentum between the nucleons and B_d is the binding energy of the deuteron. The parameter M_N represents the nucleon mass.

To compute the wavefunctions Ψ_{LSJJ_z}, the HH approach developed in Refs. [160, 161] is used. This method allows the bound state wavefunction of a system of three particles, characterized by total angular momentum J, J_z, parity π, and third component of the total isospin M_T, to be decomposed as a sum of Faddeev-like amplitudes. The final form of Ψ_{LSJJ_z} is given as a sum of three terms

$$\begin{aligned}\Psi_{LSJJ_z} = &\sum_{n,\alpha} \frac{u_{n,\alpha}(\rho)}{\rho^{5/2}} \mathcal{Y}_{n,\alpha}(\Omega) + \frac{1}{\sqrt{3}} \sum_{\ell}^{\text{even perm.}} \left\{ Y_L(\hat{\boldsymbol{y}}_\ell) \left[\varphi^d(i,j)\chi(\ell) \right]_S \right\}_{JJ_z} \frac{F_L(\eta, ky_\ell)}{ky_\ell} \\ &+ \sum_{L'S'} T^J_{LS,L'S'} \frac{1}{\sqrt{3}} \sum_{\ell}^{\text{even perm.}} \left\{ Y_{L'}(\hat{\boldsymbol{y}}_\ell) \left[\varphi^d(i,j)\chi(\ell) \right]_{S'} \right\}_{JJ_z} \\ &\times \frac{\overline{G}_{L'}(\eta, ky_\ell) + iF_{L'}(\eta, ky_\ell)}{ky_\ell} .\end{aligned} \tag{3.31}$$

Where $\mathcal{Y}_{n,\alpha}(\Omega)$ represents the set of eigenfunctions of the grand-angular momentum operator $\Lambda^2_N(\Omega_N)$. These eigenfunctions form a complete basis in the Ω Hilbert space and are constructed using hyperspherical harmonic (HH) functions.

The HH functions are combined with appropriate combinations of spin-isospin states of the three particles to construct completely antisymmetric basis functions. These basis functions, denoted as $\mathcal{Y}_{n,\alpha}(\Omega)$, are defined as follows:

$$\begin{aligned}\mathcal{Y}_{n,\alpha}(\Omega) = &\sum_{\ell}^{\text{even perm.}} f_\alpha(x_\ell) \mathcal{N}_\alpha (\sin\phi_\ell)^{L_y} (\cos\phi_\ell)^{L_x} P_n^{L_y+\frac{1}{2}, L_x+\frac{1}{2}}(\cos 2\phi_\ell) \\ &\times \left\{ \left[Y_{L_y}(\hat{y}_\ell) Y_{L_x}(\hat{x}_\ell) \right]_\Lambda \left[(s_i s_j)_{S_2} s_\ell \right]_\Sigma \right\}_{JJ_z} \left[(t_i t_j)_{T_2} t_\ell \right]_{T,T_z} ,\end{aligned} \tag{3.32}$$

The set of quantum numbers $\alpha \equiv L_x, L_y, \Lambda, S_2, \Sigma, T_2, T$ specifies the hyperspherical harmonic (HH) functions used in the construction of the basis functions. These basis functions are multiplied by Jacobi polynomials $P_n^{a,b}$ of degree n, and appropriate normalization factors $\mathcal{N}$.

In order to enhance the convergence of the expansion in terms of n, correlation factors $f_\alpha(x_\ell)$ are introduced. These factors are chosen to capture the behavior of the wave function when the particles i and j are in close proximity, corresponding to small distances x_ℓ. The correlation factors incorporate the two-body correlations of the wave functions and depend on the spin, isospin, and angular state of the pair, represented by the quantum numbers α. This expansion scheme is referred to as the

Pair-Correlated HH (PHH) expansion [160].

For a detailed discussion on the selection of the functions f_α and a comprehensive review of the properties of HH and PHH states, refer to references such as Kievsky et al. [160] and Marcucci et al. [161]. Further details on the calculations are described in Ref. [155]. However, it is important to understand the physical significance of the different terms in Eq. 3.31. The expansion in the first row of Eq. 3.31 captures the behavior of the system when the three nucleons are in close proximity to each other. The hyperradial functions $u_{n,\alpha}(\rho)$ is obtained by solving a set of coupled differential equations is solved using the Kohn variational principle [173, 174]. These functions approach zero asymptotically for energies below the deuteron breakup threshold where three nucleons are sufficiently far apart and asymptotic behavior of $u_{n,\alpha}(\rho) \to A_\alpha e^{iQ\rho}$ is obtained for $\rho \to \infty$.

The second term in Eq. 3.31 corresponds to the configuration where the proton and deuteron are sufficiently far apart from each other, rendering the strong nuclear interaction negligible. In this case, only the Coulomb interaction contributes. This term, denoted as Eq. 3.29, represents the asymptotic form of Ψ_{LSJJ_z} given by:

$$\Psi_{LSJJ_z} \to \frac{1}{\sqrt{3}} \sum_{\ell}^{\text{even perm.}} \left\{ Y_L(\hat{\boldsymbol{y}}_\ell) \Big[\varphi^d(i,j)\chi(\ell) \Big]_S \right\}_{JJ_z} \frac{F_L(\eta, ky_\ell)}{ky_\ell} \,. \tag{3.33}$$

In this scenario, where the strong nuclear interaction is absent, the hyper-radial functions $u_\alpha = T^J_{LS,L'S'}$ become zero, and $\Psi^{pd}_{m_2,m_1,\boldsymbol{k}}$ simplifies to $\Psi^{pd,(\text{free})}_{m_2,m_1,\boldsymbol{k}}$. It is important to note that the term multiplying the T-matrix in Eq. 3.33 exhibits an outgoing wave behavior, as characterized by the sum of regular and irregular Coulomb functions $G_{L'}(\eta, ky_\ell) + iF_{L'}(\eta, ky_\ell)$ resembling e^{iky_ℓ} in the asymptotic region.

The third term in Eq. (3.31) incorporates the T-matrix elements $T^J_{LS,L'S'}$, which characterize the p–d scattering observables. These elements are obtained through the Kohn variational principle. Furthermore, the factor

$$\overline{G}_{L'}(\eta, ky) = G_{L'}(\eta, ky)\Big(1 - e^{-\beta y}\Big)^{(2L'+1)} \,, \tag{3.34}$$

is required for the Coulomb behaviour in the scattering state, where $G_{L'}$ represents the irregular Coulomb function. By defining $\overline{G}_{L'}(\eta, ky)$ in this manner, it is ensured that $\overline{G}_{L'}(\eta, ky)$ remains well-behaved for all values of y, and for $y \gg \beta^{-1}$, it converges to the irregular Coulomb function. Typically, a regularization scale of $\beta = 0.25$ fm^{-1} is employed. In Eq. 3.31, the combinations of $L'S'$ encompass all possible combinations for a given J and parity $(-1)^L$.

Finally, when considering the nuclear interaction, it is important to limit the contributions up to a certain value of $\overline{J}$. For $J > \overline{J}$, the centrifugal barrier prevents the three particles from being close to each other. In such cases, the free wave function described by Eq. 3.33 describe the dynamics of p–d system. Therefore, it is beneficial to separate the asymptotic ("free") part from the wave function expressed in Eq. 3.31. The total wave function $\Psi^{pd}_{m_2,m_1,\boldsymbol{k}}$ for the p–d system, including the effects

of nuclear interactions up to a specified $\bar{J}$, is then written as:

$$\Psi^{pd}_{m_2,m_1,\boldsymbol{k}} = \Psi^{pd,(\text{free})}_{m_2,m_1,\boldsymbol{k}} + \sum_{LSJ}^{J\leq\bar{J}} \sqrt{4\pi} i^L \sqrt{2L+1} e^{i\sigma_L} (1 m_2 \frac{1}{2} m_1 \mid S J_z)(L0 S J_z \mid J J_z) \widetilde{\Psi}_{LSJJ_z} \,. \tag{3.35}$$

The quantity $\widetilde{\Psi}_{LSJJ_z}$ represents the sum of all terms proportional to $F_L(\eta, ky_\ell)$, with the free part subtracted from Eq. 3.31. It can be expressed as:

$$\begin{aligned} \widetilde{\Psi}_{LSJJ_z} = & \sum_\alpha \frac{u_\alpha(\rho)}{\rho^{5/2}} \mathcal{Y}_\alpha(\Omega) \\ & + \sum_{L'S'} T^J_{LS,L'S'} \frac{1}{\sqrt{3}} \sum_{\ell}^{\text{even perm.}} \left\{ Y_{L'}(\hat{\boldsymbol{y}}_\ell) \left[\varphi^d(i,j) \chi(\ell) \right]_{S'} \right\}_{JJ_z} \\ & \times \frac{\overline{G}_{L'}(\eta, ky_\ell) + i F_{L'}(\eta, ky_\ell)}{ky_\ell} \,, \end{aligned} \tag{3.36}$$

More details regarding the wavefunction $\Psi^{pd}_{m_2,m_1,\boldsymbol{k}}$ can be found in Ref. [155]. It represents the three-nucleon wavefunction, as defined in Eq. 3.35, which asymptotically behaves as a distorted *pd* plane-wave, with the proton (deuteron) in the spin state m_1 (m_2). The components $\widetilde{\Psi}_{LSJJ_z}$ describe configurations where the three particles are close to each other, and the choice of $\bar{J}$ allows for the control of waves where the strong interaction is taken into account.

Careful attention should be given to include a sufficient number of Pair-Correlated HH (PHH) states $\mathcal{Y}_{n,\alpha}(\Omega)$, especially in terms of the number of channels α in Eq. 3.36. This is crucial for accurately describing configurations where the three particles are in close proximity. The convergence of this expansion is particularly critical for partial waves with low orbital angular momentum L and specific values of J^π, such as $1/2^+$, $3/2^+$, $1/2^-$, $3/2^-$, and $5/2^-$. For instance, in the $J^\pi = 1/2^+$ case, where the ^{3}He bound state is formed, it is necessary to construct the scattering wavefunction orthogonal to it. Additionally, for states with relative orbital angular momentum $L = 1$, the interaction among the three particles is highly attractive, necessitating a large number of terms in the sum over α in Eq. 3.36.

The final correlation function is obtained by substituting the wavefunction defined in Eq. 3.35 into Eq. 3.21 and simplifying it with a summation over m_2 and m_1. Additionally, it is recognized that the integral $\int d\Omega \, \Psi^\dagger_{L'S'J'J'_z} \Psi_{LSJJ_z}$ is non-zero only when $J = J'$ and $J_z = J'_z$.

$$C_{pd}(k) = \frac{1}{A_d} \frac{1}{6} 4\pi \sum_{JLS} (2J+1) \int \rho^5 d\rho d\Omega \, \frac{e^{-\rho^2/4R_M^2}}{(4\pi R_M^2)^3} \, |\Psi_{LSJJ_z}|^2 \equiv \sum_{JLS} C^{LSJ}_{pd}(k) \,. \tag{3.37}$$

where $\pi = \pm$ corresponds to parity of the wavefunction. Each component of the wave function Ψ_{LSJJ_z}, characterized by L and S, contributes individually to the correlation function. These contributions are defined as $C^{J^\pi}_{pd}(k) = \sum_{LS} C^{LSJ}_{pd}(k)$, where $C^{LSJ}_{pd}(k)$ represents the contribution of a specific LS component to the total correlation function $C_{pd}(k)$.

The calculations are performed using the AV18 potential for the two-body interaction, the UIX potential for the three-body interaction, and a NN source size of

$R_M = 1.5$ fm. The calculation focuses specifically on partial waves up to $J^\pi = 7/2^-$ which gives non-negligible contributions. For $J^\pi = 7/2^+$ and higher angular momenta, the nuclear interaction has a negligible contribution, and therefore, the correlation function is computed considering only the Coulomb force, which is labeled as "Rest". Further technical details regarding the summation of all contributions can be found in Ref. [155]. The curves presented in Fig. 3.11 display both the total correlation function and the individual contributions from different partial waves.

It is important to note that the dominant contribution at low k values arises from the s-wave interaction ($J^\pi = 1/2^+$), where low values of k correspond to small values of the *pd* relative kinetic energy T_{pd} (for example, k = 10 MeV/c corresponds to $T_{pd} = 79$ keV). As k approaches zero, the Coulomb repulsion becomes the dominant factor, causing the correlation function to rapidly decrease towards zero. In this region, the largest contribution comes from the *pd* waves with $L = 0$, particularly the $L = 0$, $S = J = 1/2$ wave, where the spins of the proton and deuteron are aligned in opposite directions. However, the s-wave quartet channel with $L = 0$, $S = J = 3/2$ wave is suppressed at short inter-particle distances due to the Pauli exclusion principle (with all three nucleons having aligned spins for $S = 3/2$).

Between $k = 60$ and 160 MeV/c, the $L = 1$, $S = 3/2$ components of p-waves with total angular momentum and parity $J^\pi = 1/2^-$, $3/2^-$, and $5/2^-$ start to significantly contribute, exhibiting resonance-like behavior. In these waves, the effective *pd* interaction is attractive, and the corresponding phase shifts increase rapidly with energy [175]. Additionally, below $k = 200$ MeV/c, there is a moderate splitting of the quartet $L = 1$ phases [173], and their relative contributions are nearly proportional to $(2J + 1)$, as described in Eq. 3.37. This leads to the appearance of a wide bump in the total correlation function, with a maximum located approximately at k = 120 MeV/c. At higher values of k, higher partial waves begin to contribute, and the correlation function tends to approach unity. The total correlation function exhibits a depletion at low k, reflecting an overall repulsive interaction in p–d. This behavior is consistent with the phase-shift measurement in the quartet channel which is shown in Fig. 3.5.

The effect of the source size on the calculation is explored by performing a variation of the source size R_M across different values. The results are depicted in Fig. 3.12. It is observed that the dependence of the C_{pd}(k) on R_M is weak at low k^*. However, for values ranging between 150 MeV/c and 400 MeV/c, the dip increases as the source size is reduced. This indicates that the short-range interaction becomes more significant at intermediate relative momenta. The AV18 and UIX potentials are considered realistic potentials, but their derivation is not directly based on the properties of QCD. Hence, it is crucial to investigate how predictions may change by employing more recent potentials derived from χEFT. In order to expand this study, NVIa+3N interaction potentials are used in a similar manner as in the AV18+UIX case. The resulting correlation function is indicated by red square markers in Fig. 3.13. Remarkably, the correlation function calculated using NVIa+3N shows excellent agreement with that obtained using AV18+UIX potentials. This outcome is anticipated since both potentials accurately describe the NN and 3N interactions. A final fitting of the measured p–d correlation function using both potentials is presented in Chap. 4.

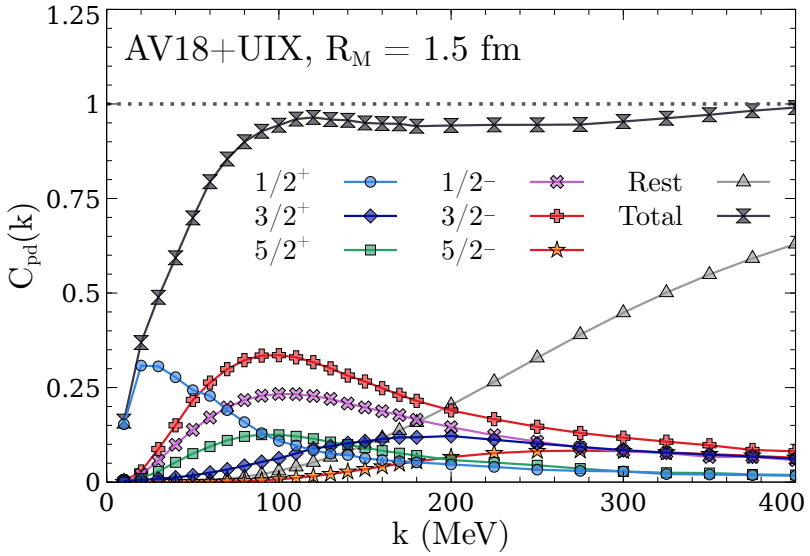

FIGURE 3.11: The figure and caption are taken from Ref. [155]. The figure displays the p–d correlation function $C_{pd}(\mathrm{k})$ along with its various contributions $C_{pd}^{J^\pi}(\mathrm{k})$. These calculations were performed using the AV18+UIX interaction and the PHH method. The "Rest" curve specifically represents the contribution of $J^\pi = 7/2^+$ and $J > 7/2$ states, which are taken into account through the $\Psi^{\mathrm{free}}_{m_2,m_1}$ term in Eq. 3.31. The calculations utilize a source size of $R_M = 1.5$ fm.

Furthermore, in order to investigate the impact of 3N interactions, the correlation function is calculated using the AV18 potential while disabling the 3N interactions in the interaction Hamiltonian. The resulting correlation function, obtained solely from the AV18 potential NN interaction, is represented by the blue diamonds in Fig. 3.13. It is observed that for a source size of $R_M = 1.5$ fm, the predictions closely approximate the full case but still the difference between AV18+UIX curve and the one labeled "AV18" (blue diamonds) highlights the importance of including the nuclear interaction between the two clusters. To examine how this effect changes for smaller source sizes where the distances are smaller, a ratio is plotted for various source sizes in Fig. 3.14. The figure demonstrates that for smaller source sizes, the effect of 3N interactions is approximately 5%.

An intriguing aspect of the p–d system as a three-body system is to examine how the correlation function changes when interactions occur only asymptotically. This scenario could potentially arise when the deuteron is in a hexaquark state until it is fully formed in collision experiments. During the formation of the deuteron, the interaction between the proton and deuteron is assumed to be absent.

To study this aspect, the so-called Born approximation is employed, which assumes that the interaction potential between the proton and deuteron in p–d is weak enough to neglect higher-order effects. This approximation provides a reasonable estimate when the interaction strength is small compared to the kinetic energy of the nucleons.

In this case, the Born approximation is applied to the p–d wavefunction defined in Eq. 3.36 by neglecting the first term in the full expression of the wave

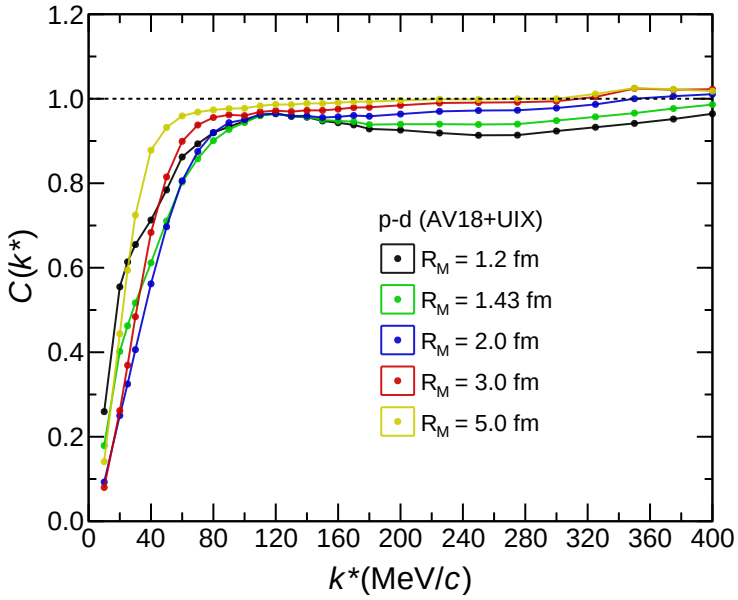

FIGURE 3.12: The figure displays a source size R_M variations for the p–d correlation function $C_{pd}(k^*)$ using the AV18+UIX interaction with all partial wave contribution up to $J^\pi = 7/2^-$ and $J^\pi \geq 7/2^+$ states.

function. However, the antisymmetrization of the wavefunction is still performed due to the identical protons, making it referred to as the "optimized Born" approximation. The wave function is approximated using asymptotic terms, and the T-matrix elements are determined using the Kohn variational principle with this wave function as the trial input. This approximation works well for high partial waves where the centrifugal barrier suppresses the effects of the interaction. However, for S and P waves, this approximation yields different results compared to using the full wave function. The difference between the curves obtained with the full wave function and the one labeled "optimized Born" demonstrates the significance of considering the "distortion" of the deuteron in the process. In other words, the p–d wavefunction at short distances cannot be simply obtained by multiplying the deuteron wave function with the spin state of the third particle. A comprehensive treatment of the three-body dynamics is necessary. It should be noted that, for momenta $k < 60$ MeV/c, the "optimized Born" approximation produces a completely incorrect correlation function. Therefore, values of the correlation function for $k < 60$ MeV/c are excluded from the figure.

Furthermore, for comparative purposes, the correlation function is calculated by considering only the Coulomb force, as indicated by the "Coulomb only" label in Fig. 3.13. It is worth noting that the curves obtained from the full interaction significantly differ from the Coulomb-only case. This stark difference highlights the significant role of strong nuclear interaction in the p–d system.

3.3.2 p–d correlation from the Pionless Effective field Theory

Pionless Effective Field Theory (EFT) is a framework within nuclear physics that aims to describe low-energy dynamics and interactions in few-nucleon systems without explicitly including pions as degrees of freedom. The theory exploits a

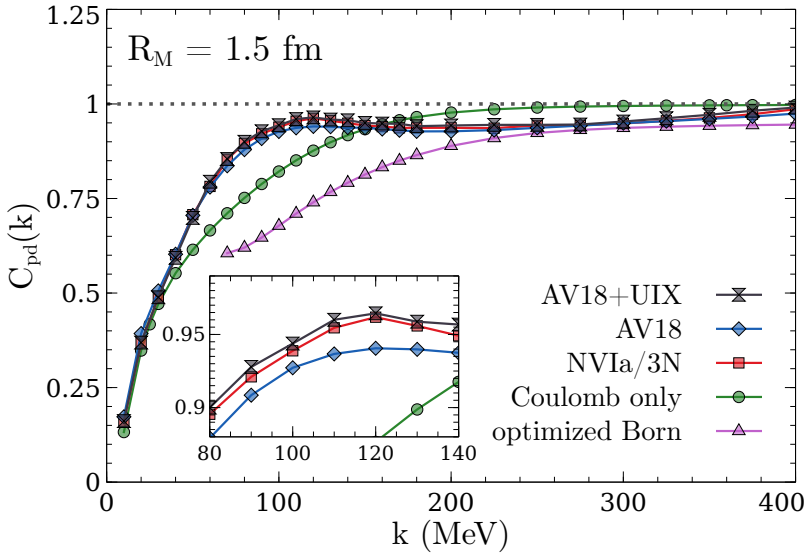

FIGURE 3.13: The figure taken from [155]. The figure presents the proton-deuteron correlation function $C_{pd}(k)$, which is calculated using various interactions and approximations of the wave function through the PHH method. The calculations are conducted with a source size of $R_M = 1.5$ fm. For further information and specific details, please refer to the main text.

systematic expansion of the nuclear Lagrangian in terms of a small parameter related to the pion mass, enabling a systematic and model-independent approach to studying nuclear systems at low energies. It is specifically tailored for situations where the nucleon-nucleon S-wave scattering lengths are much larger than the typical range of the nuclear interaction, which is characterized by the inverse pion mass, approximately 1.4 fm ($M_\pi^{-1} \sim 1.4$ fm.). Within its applicable range, governed by the EFT breakdown scale of approximately M_π, Pionless EFT provides a comprehensive parametrization of the nuclear force [176].

Within the framework of this theory, the strong nuclear interaction is described by a series of contact interactions (terms with vanishing range of interaction) with increasing numbers of derivatives, in subsequent higher orders of the EFT expansion scheme. In the two-nucleon sector, this series reproduces the well-known effective range expansion [177] and extends it to describe both few- and many-nucleon systems accurately. Notably, Pionless EFT captures the universal aspects stemming from the proximity of low-energy nuclear systems to the unitarity limit, leading to a remarkable inclusion of a three-nucleon contact interaction at leading order [178, 179].

To evaluate the p–d correlation function, the definition of the CF from Eq. 3.14 is derived in momentum space. The relevant equations are obtained directly from the so-called 'diagrammatic approach', and the p–d wavefunction is obtained by summing over all the relevant Feynman diagrams. More details on this calculation can be found in [155].

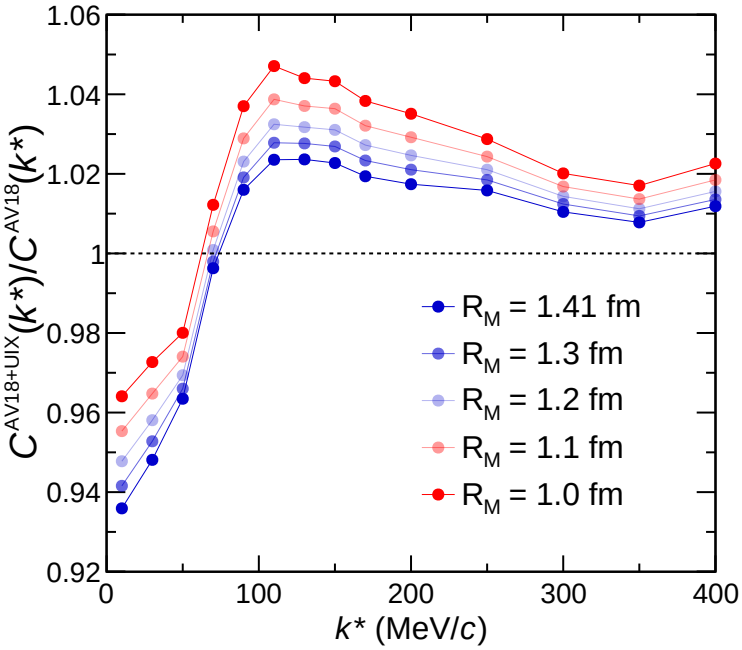

FIGURE 3.14: The figure displays the ratio of the theoretical p–d correlation functions obtained from full three-body calculations (AV18+UIX) to those obtained using AV18 for the NN interaction only. The ratios are presented for various values of the effective radius of the two nucleons, denoted as R_M.

p–d scattering in Pionless EFT

The inclusion of Coulomb effects in p–d scattering is crucial, especially in the very-low-energy regime, where it becomes necessary to treat them non-perturbatively. This non-perturbative treatment leads to an isospin-breaking correction to the leading-order (LO) three-nucleon force at the next-to-leading order (NLO) in the EFT power counting [180].

In order to compute the p–d scattering wavefunction, the non-perturbative treatment of Coulomb effects is employed to describe p–d scattering from zero energy up to the breakdown scale of the theory, $M_\pi \sim 140$ MeV, in a single unified formulation. The complete details on the Pionless EFT Lagrangian are given in [155, 181], nevertheless the most important ingredient to compute p–d scattering wavefunction in this theory is the diagram equation shown in Fig. 3.15. The p–d scattering process in the spin-doublet channel ($J = 1/2$) is described by the diagram equation. This diagram represents the contribution to the amplitude $\mathcal{T}$, indicated by the hatched shading within the blob. It involves two coupled channels due to the possible presence of spin-triplet and spin-singlet two-nucleon states in intermediate configurations, which are represented by double lines and thick lines, respectively. In the spin-quartet channel ($J = 3/2$), all nucleon spins are aligned, which means that intermediate spin-singlet states are prohibited by the Pauli principle. Consequently, the scattering amplitude in this channel is exclusively determined by the first row in Fig. 3.15. To implement the integral equation numerically for either channel, projection of specific spin channel, characterized by the quantum numbers s_d introduced in the previous section. Furthermore, all the momentum integrals occurring due to the loops in the diagrams are evaluated. During the computation

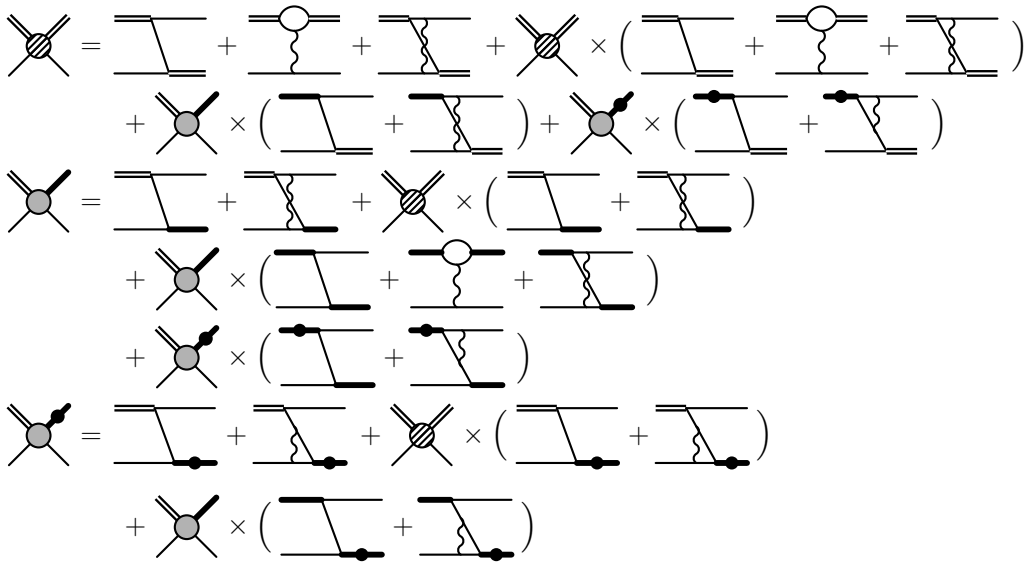

FIGURE 3.15: Figure and caption from Ref. [155] represents coupled-channel integral equation for the full (*i.e.*, strong + Coulomb) proton-deuteron scattering amplitude in the $J = 1/2$ channel. The diagrams representing the three-nucleon force have been omitted. Notation as in Ref. [181].

of momentum loop integrals, a regulator scale (cutoff) called $\Lambda = 800$ MeV is employed. This cutoff acts as an upper limit on the loop momenta, providing a sharp upper bound on momentum integrals at the three-nucleon level. On the other hand, the two-nucleon subsector is treated using dimensional regularization. As an effective field theory, the Pionless EFT exhibits residual cutoff dependence, which should diminish as higher-order calculations are performed. The fact that results for observables level off at large cutoffs indicates proper renormalization. It is expected that the magnitude of residual cutoff dependence decreases with increasing orders of calculation.

The evaluation of the p–d correlation function is performed in momentum space[3]. In order to work in the momentum space first the source function is redefined in the momentum space. The source function $S(r)$ in the coordinate space can be written as an operator $\hat{S}$ which is given by

$$\langle \boldsymbol{r}|\hat{S}|\boldsymbol{r}'\rangle = \frac{\exp\left(-r^2/R^2\right)}{(4\pi R)^{3/2}}\delta^{(3)}(\boldsymbol{r}-\boldsymbol{r}')\ . \tag{3.38}$$

The operator $\hat{S}$ then translates to a non-local representation that can be written in closed form [182]:

$$\langle q,\ell|\,\hat{S}\,|q',\ell'\rangle = \exp\left(-R^2(q^2+q'^2)\right)\ i_\ell\left(2Rqq'\right)\,\delta_{\ell\ell'}\,, \tag{3.39}$$

where ℓ denotes the orbital angular momentum of a particular partial wave, and i_ℓ is a modified spherical Bessel function. The scale R is related to the source radius

[3]One can transform back to coordinate space using Fourier transformation, but here the correlation function is defined and utilized directly in momentum space instead, which computationally easy.

via $R = \sqrt{3/4}R_M$. Finally the Eqs. 3.9 and 3.10 can be written as

$$A_d\, C_{pd}(k) = \sum_{s_d} \alpha(s_d)\ \langle \Psi_k; s_d |\, \hat{S}\, | \Psi_k; s_d \rangle\ , \tag{3.40}$$

The factor $\alpha(s_d)$ is used for different spin state and defined as

$$\alpha(s_d) = \frac{1}{3}\frac{2J+1}{2\times 3}\ , \tag{3.41}$$

the factor of $1/3$ in the front is due to the antisymmetrization in the total p–d wavefunction. The remaining terms account for the spin weights of each individual contribution to the correlation function. The factors of 2 and 3 in the denominator correspond to the spin $1/2$ of the proton and the spin 1 of the deuteron, respectively.

Finally, the amplitude $\mathcal{T}$ is used to relate the scattering amplitude $\tilde{T}$ via the following relation:

$$\tilde{T}(u_1, u_2) = g(u_1)\tau(M_N E - \tfrac{3}{4}u_2^2) G_0(E; u_1, u_2)\tilde{\mathcal{T}}(u_2)\,, \tag{3.42}$$

where u_1 and u_2 are the conjugate Jacobi momenta of x and y respectively. The function $g(u)$ is used as an ultraviolet cutoff for a given regularization scheme in Pionless EFT. G_0 denotes the free three-nucleon Green's function and τ expresses the energy dependence of the separable two-nucleon T-matrix:

$$t(E; u, u') = g(u)\tau(M_N E) g(u')\,. \tag{3.43}$$

There is a simple relation between $\tilde{\mathcal{T}}$ and $\mathcal{T}$, given by a factor:

$$\tilde{\mathcal{T}} = -\frac{M_N}{4\pi}\mathcal{T}\,, \tag{3.44}$$

For a special case of a separable two-body interaction between nucleons, $V(u, u') = C_0 g(u) g(u')$ for momenta u and u', the T-matrix for each two-nucleon channel can be obtained by algebraically solving the Lippmann-Schwinger equation for the separable potential V [183], or equivalently, by solving an equation that is derived from a diagrammatic representation of the "dibaryon propagators" that appear as intermediate states (double and thick lines) in Fig. 3.15 [180, 184].
The scattering amplitude $\tilde{T}$ is then used in the following equation to compute a Fadeev component:

$$\langle \varphi_d u_2; s'_d | \psi_k; s_{nd} \rangle = \frac{\delta(u_2 - k)}{k^2} + \langle \varphi_d u_2; s'_d | \tilde{T} | \varphi_d k; s_d \rangle\ ,, \tag{3.45}$$

where $\langle \phi' | = \langle \varphi_d u_2; s'_d |$, with an arbitrary momentum u_2 and $\langle s'_d |$ chosen such that $l'_2 = l_2$ and $s'_2 = s_2$. The deuteron wavefunction amplitude $|\varphi_d\rangle$ is assumed to be properly normalized to unity. It is worth noting that the discussion so far is solely based on the single Faddeev component $|\psi_k; s_d\rangle$ and its corresponding amplitude $\tilde{T}$. However, to calculate the full scattering wavefunction, one needs to solve the following equation for $|\psi_k; s_d\rangle$

$$|\Psi_k; s_d\rangle = (1 + P)\, |\psi_k; s_d\rangle\ . \tag{3.46}$$

where s_d is a set of all quantum numbers for the scattering process.

The correlation function at leading order is computed using a source size of R_M fm and the state $|\Psi_k; s_d\rangle$ from Eq. 3.40. This calculation takes into account the nuclear interaction in *pd* *S*- and *P*-waves, which are degenerate in terms of the total spin J at this order. Additionally, it incorporates pure Coulomb contributions on top of the interacting waves, considering a maximum total angular momentum of $\ell_{\max} = 15$.

To obtain the final values of the correlation function at leading order, two different EFT cutoff values, $\Lambda = 400$ and 800 MeV, are employed (represented by yellow and green respectively). The source sizes R_M used are 1.35, 1.43, 1.51, 1.59, and 1.67 fm, each represented by different line styles. These results are depicted in Fig. 3.16. The correlation function is plotted only up to $k = 120\text{MeV}/c$ since higher values are restricted by the theory's breakdown scale, which is pion mass $M_\pi \sim 140$ MeV. The obtained correlation function shows depletion at low k^*, which is observed in the case of AV18+UIX and NVIa+3N potentials.

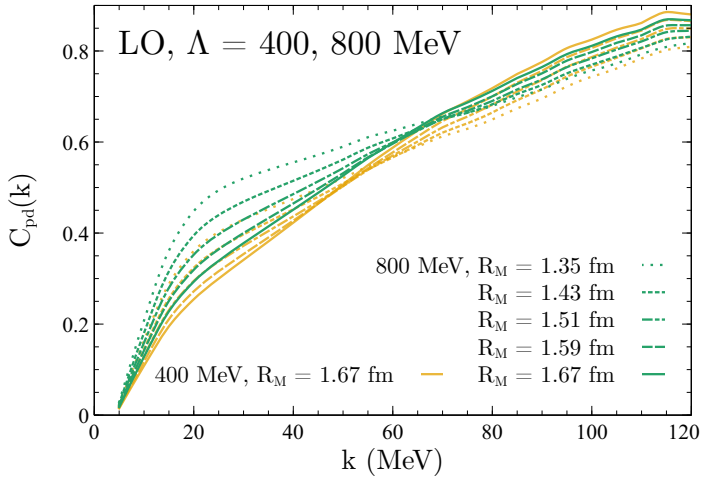

FIGURE 3.16: The p–d correlation function $C_{pd}(k)$ calculated in Pionless EFT at LO for different EFT cutoffs Λ and source radii R_M [155].

The Pionless EFT at LO approach introduces additional theoretical uncertainty due to the variation of input parameters, specifically the two-nucleon interaction in the ${}^3S_1$ channel and the three-nucleon contact interaction. In order to estimate this uncertainty, the parameters relevant to the leading-order (LO) calculation are varied. At LO, it is equivalent from the EFT perspective to fit $C_0(\Lambda)$ to reproduce either the exact binding energy of the deuteron or the experimental value of the scattering length in the ${}^3S_1$ channel. Fitting the scattering length results in a slightly underbound deuteron with a binding energy of approximately 1.4 MeV. However, by including perturbative next-to-leading-order (NLO) corrections, the binding energy is brought closer to the experimental value. Similarly, the three-body interaction can be fitted to reproduce either the experimental binding energy of the triton or the *nd* scattering length. The prediction of the energy splitting between ^{3}H and ^{3}He binding energies at this order has been extensively studied and reported in the literature, specifically in Refs. [155, 180, 184–188].

The final uncertainty band is determined by taking the maximum variation minus the minimum variation, resulting in the final band representation. The final

theoretical correlation function at LO is represented by the green band in Fig. 3.17. In the framework of the EFT expansion scheme, higher-order terms can be included

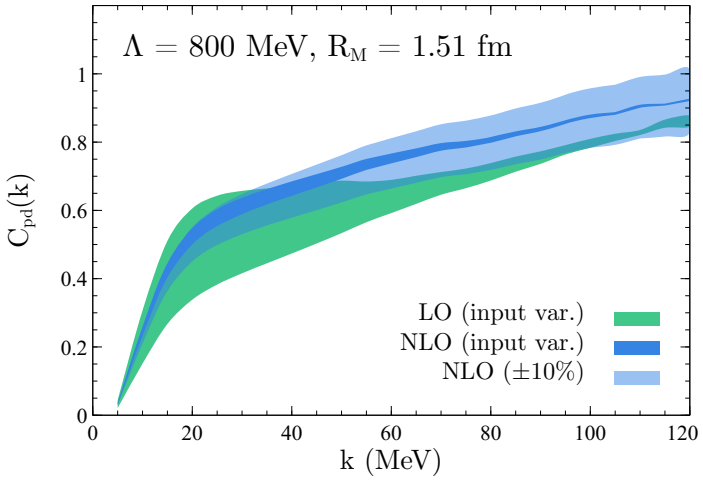

FIGURE 3.17: Figure from [155], the p–d correlation function calculated in Pionless EFT for a source radius $R_M = 1.51$ fm. The shaded bands represent the theoretical uncertainty from the EFT expansion. At LO, the uncertainty is estimated by varying the EFT input parameters for both the $^3S_1$ two-body interaction and the three-nucleon force (see text for details). At NLO, due to technical restrictions, only the input for the three-nucleon force is varied, while the $^3S_1$ two-nucleon interaction remains fixed to reproduce the deuteron at its physical binding energy. To provide a rough estimate of the NLO uncertainty, an additional lighter band is included, representing a 10% variation as *a priori*.

to incorporate further corrections to the observables. In the perturbative expansion, the p–d correlation function is expressed as follows:

$$C_{pd}(k) = C_{pd}^{(0)}(k) + C_{pd}^{(1)}(k) + \cdots , \tag{3.47}$$

Here, $C_{pd}^{(0)}(k)$ represents the leading-order (LO) result, $C_{pd}^{(1)}(k)$ corresponds to the next-to-leading-order (NLO) correction, and the ellipses denote higher-order corrections that are not considered in this study. Instead, for the higher-order corrections, a 10% uncertainty range is assigned to the final correlation. More details regarding the perturbative setup to obtain $C_{pd}^{(0)}(k)$ and $C_{pd}^{(1)}(k)$ can be found in [155]. However, it should be noted that in order to expand $C_{pd}(k)$, the source operator $\hat{S}$ is assumed to have no expansions itself. The key aspect lies in how the p–d wavefunction is treated within the perturbative setup, which is generated by the EFT expansion of the scattering wave function. This expansion can be expressed as a series in Eq. 3.47.

$$|\Psi_k\rangle = |\Psi_k^{(0)}\rangle + |\Psi_k^{(1)}\rangle + \cdots . \tag{3.48}$$

This expansion arises from the expansions of the amplitude $\tilde{\mathcal{T}}$ and τ, where the diagrams occur in an order-by-order manner within the expansion scheme, as seen in Eq. 3.44. In addition to the p–d wavefunction, A_d includes the deuteron wavefunction ϕ_d, which is also expanded analogously, as written below

$$|\varphi_d\rangle = |\varphi_d^{(0)}\rangle + |\varphi_d^{(1)}\rangle + \cdots , \tag{3.49}$$

consequently the deuteron formation probability A_d together with p–d wavefunction leads to the following term at LO

$$A_d^{(0)} C_{pd}^{(0)}(k) = \langle \Psi_k^{(0)} | \hat{S} | \Psi_k^{(0)} \rangle \,. \tag{3.50}$$

At NLO, the relation between expansion of A_d, $C_{pd}^{(0)}(k)$ and $C_{pd}^{(1)}(k)$ is obtained

$$A_d^{(0)} C_{pd}^{(1)}(k) + A_d^{(1)} C_{pd}^{(0)}(k) = 2\mathrm{Re}\, \langle \Psi_k^{(0)} | \hat{S} | \Psi_k^{(0)} \rangle \,, \tag{3.51}$$

where $C_{pd}^{(1)}(k)$ can be extracted by independently calculating $A_d^{(1)} = 2\mathrm{Re}\, \langle \varphi_d^{(0)} | \hat{S} | \varphi_d^{(1)} \rangle$ and from the LO calculation, $C_{pd}^{(0)}(k)$ is already known. Hence,

$$C_{pd}^{(1)}(k) = \frac{1}{A_d^{(0)}} 2\mathrm{Re}\, \langle \Psi_k^{(0)} | \hat{S} | \Psi_k^{(0)} \rangle - \frac{A_d^{(1)}}{A_d^{(0)}} C_{pd}^{(0)}(k) \,. \tag{3.52}$$

Finally, p–d correlation function from pionless EFT at NLO is obtained using Eq. 3.47 and shown in Fig. 3.18 Similarly to the LO case, the NLO calculation

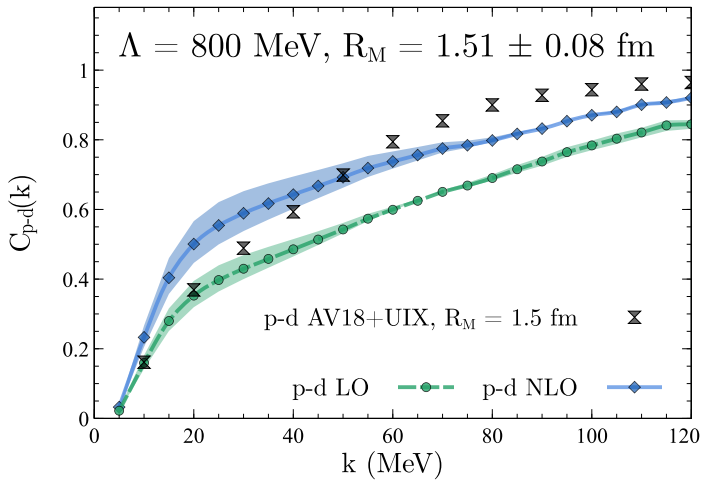

FIGURE 3.18: The proton-deuteron correlation function calculated in Pionless EFT with $\Lambda = 800$ MeV. The central curves show results for a source radius $R_M = 1.51$ fm, while shaded bands here indicate the result of varying the source radius by ± 0.08 fm. Double triangle show *pd* AV18+UIX results calculated at $R_M = 1.5$ fm for comparison [155].

involves input parameters, and their variation allows us to estimate uncertainties in the calculated *pd* correlation. However, as discussed in [155], there are conceptual constraints that currently prevent us from performing an NLO calculation with the ${}^3S_1$ input fixed to the scattering length. This is because the range correction would shift the deuteron binding energy. Therefore, further theoretical development is required to create a perturbative nucleon-deuteron scattering formalism capable of handling the moving threshold resulting from the expansion in the two-nucleon sector.

As a result, only the three-nucleon interaction is varied, following the procedure described for the LO calculation. The final *pd* correlation with uncertainties arising from the variation of the three-nucleon interaction is represented by the

blue bands in Fig. 3.17. The darker region within the bands corresponds to the variation of the input parameters for the three-nucleon interaction. Additionally, in a conservative approach, a 10% uncertainty blanket is assigned to account for possible uncertainties related to the truncation of the EFT expansion at NLO.

It is important to note that while this approach provides an *a priori* estimate of the Pionless EFT uncertainty at NLO, it does not take into account the constraint that the correlation function should approach unity as $k \to \infty$. Therefore, in the final comparison with the experimental *pd* correlation function, this 10% uncertainty blanket will be omitted, as shown in Chap. 4.

As a comparison between the p–d correlation functions obtained from the PHH method employing the AV18+UIX potential and from the Pionless EFT (with input parameters fixed, where the $^3S_1$ channel is fixed to reproduce the deuteron binding energy and the three-nucleon force is fit to the *nd* scattering length), it is observed that the Pionless EFT provides a very good agreement. At LO and NLO, the Pionless EFT results agree well with the AV18+UIX potential for low momenta ($k < 30$ MeV). However, for larger momenta ($k > 30$ MeV), there are significant differences at LO, while the NLO results still show a decent comparison. It is important to note that the uncertainties at LO and NLO, as shown in Fig. 3.18, also need to be taken into account. Overall, these results indicate that both calculations are in reasonable agreement.

3.4 Summary and Discussion

In this chapter, the key point to be learned is how the dynamics of nucleons in the deuteron contribute to the determination of the theoretical p–d correlation function. It is demonstrated above that the effective two-body models for the hadron-deuteron system work qualitatively for the K^+–d case. However, in the case of the p–d system, an attractive peak-like structure around $k^* \sim 20$ MeV/c is observed in the correlation function when considering the two-body results based on Lednický or Gaussian potentials that reproduce p–d scattering lengths. However, such a peak is absent in the correlation function when the p–d system is considered as a three-body system and the correlation function is computed using the PHH method with AV18+UIX and NVIa+3N chiral potentials, as well as within the Pionless EFT. This suggests that the approximation of the p–d system as an effective two-body system does not work. This observation becomes even more evident when the measured p–d correlation function in pp collisions is compared, which will be discussed in great detail in the next chapter.

Additionally, it is interesting to note that the PHH method is an extremely powerful approach that can be used to solve three-body problems for given potentials such as AV18+UIX and NVIa+3N. Since the uncertainties on these potentials are $\leq 1\%$, the calculated correlation function using the PHH method is very precise without any additional uncertainties. One key point to be observed in this study is the role of the three-nucleon (3N) interaction in the p–d correlation function. As shown in Fig. 3.14, for a source size of $R_M = 1.5$ fm, the effect of the 3N interaction on the correlation function is at most 3%, and for smaller source sizes, the effect increases up to 5%. Another key point to stress here is that the results from the Pionless EFT calculation and the comparison with potential models show reasonable agreement.

For k $>$ 40 MeV, deviations can be observed between AV18+UIX calculations and those based on Pionless EFT at the NLO level with fixed input parameters, as depicted in Figure 3.18. However, by including uncertainty bands associated with EFT expansions and input parameters, the agreement between AV18+UIX and Pionless EFT NLO calculations is expected to improve. Additionally, it is observed that there is a significant improvement in the obtained correlation function when going from LO to NLO. Based on these observations, it is believed that an N2LO calculation, which would include NN P-wave interactions as well as effects from the $^3S_1$-$^3D_1$ mixing induced by the nuclear tensor force, is likely to narrow the discrepancy between the different interactions. This suggests that further refinement of the theoretical framework, including higher-order contributions, is necessary to improve the agreement between the EFT and potential model results.

In summary, two key conclusions can be drawn from this study. First, the correlation function is significantly influenced by the proton-deuteron scattering wave function, which takes into account the three-body dynamics and introduces a complex dynamical behavior through the interplay between different partial waves, particularly the S- and P-waves. This highlights the importance of the nucleon-deuteron interaction. Second, the correlation function demonstrates sensitivity to various aspects of the nuclear interaction, encompassing both two- and three-nucleon contributions in this study. This indicates that the correlation function can provide valuable insights into the properties of light nuclear systems dominated by the strong interaction. In light of these findings, ongoing experimental efforts devoted to measuring the correlation function in such systems are supported, as they can provide important information about the underlying nuclear dynamics.

Chapter 4

Unraveling the p-d interaction: Insights from Femtoscopy

4.1 Introduction and physics motivation

The p–d systems have drawn the attention of modern nuclear physicists, particularly due to two main aspects.

The first aspect of the p–d system is the strong interaction among nucleons that form the p–d system. Understanding the strong interaction in three-body systems is essential for studying the structure of nuclear-bound states [189] and the equation of state of dense nuclear matter [190]. The current theoretical framework of Effective Field Theories (EFTs), such as χEFT and Pionless EFT, which incorporate many-body forces. These calculations are anchored to scattering data [31, 191] and provide a proper description of nuclear binding energies [192, 193]. At the nuclear saturation density $\rho_0 = 0.17$ fm^{-3}, the binding energy per nucleon in atomic nuclei is closely linked to the nature of the nuclear force. In the EFTs, the 3N force occurs at the subleading order compared to the two 2N interactions. However, 3N interactions play a crucial role in achieving accurate theoretical predictions for nuclear observables, including the binding energies of nuclei. In many-body calculations of ground-state energies for $A \leq 12$ nuclei using NN and 3N potentials derived from χEFT, contributions from genuine three-nucleon forces have been found to be around 10% [194]. The significance of many-body forces can become even more prominent at internuclear distances smaller than those characterizing nuclei and hypernuclei, particularly in the creation of dense matter [1]. Conventional nuclear binding measurement techniques are insufficient to investigate the interaction of multiple baryons at distances shorter than those observed in nuclei and hypernuclei. New experimental techniques are required. Analyzing the femtoscopic correlation of the p–d pairs produced at small distances in collision experiments could shed light on the dynamics of systems composed of three nucleons.

The second aspect of the p–d system is that the deuteron is a light nucleus. Over the past few decades, high-energy hadronic and ultra-relativistic heavy-ion collision experiments have been dedicated to investigating the production of light (anti-)nuclei and more complex multibaryon bound states [71, 72]. These studies involve precise measurements of differential cross-sections [73–75, 77–79, 195], flow observables [80–82], and event-by-event fluctuations [83]. As discussed in Chap. 1, the production mechanism of light (anti-)nuclei remains an open question and subject to considerable debate. Two different approaches based on phenomenological

models, namely the Statistical Hadronization Model (SHM) and the Coalescence model, are commonly employed to predict the production of these multibaryon-bound states. In the SHM, canonical and grand canonical ensemble approaches are used to study the yields of particles and nuclei at fixed chemical freeze-out temperatures in both small and large collision systems. The predicted yields of nuclei are consistent with experimental measurements. However, the observation of deuteron and other light nuclei production is intriguing since the system temperature is significantly higher than their binding energies, for example, $B_d \sim 2.2$ MeV. On the other hand, the Coalescence model involves the initial production of nucleons followed by the formation of a bound object, catalyzed, for instance, by pions, as discussed in Chap. 1. Coalescence models have shown success in describing the data [12–16]. However, even the Coalescence model lacks a comprehensive understanding of the microscopic mechanisms responsible for the production of light nuclei. A femtoscopic correlation study involving deuteron-deuteron (d–d) and deuteron with other hadrons provides a valuable opportunity to investigate the final-state interaction of the many-body system and understand the production mechanisms of deuterons [153].

In 1985, the first experimental measurement of the p–d correlation was conducted at the Holifield Heavy-Ion Research Facility [196] using O+Au collisions at E/A = 25 MeV. A year later, in 1986, another experiment at the Laboratoire Grand Accelerateur National d'Ions Lourds (GANIL) in Caen reported the p–d correlation using ^{40}Ar-induced reactions on ^{40}Au at E/A = 60 MeV [197, 198]. The results of both p–d correlation measurements are illustrated in Figs. 4.1 and 4.2. The data show a clear signature of the strong final-state interaction among light nuclei and nucleons. In 2007, another experiment was conducted at GANIL, using

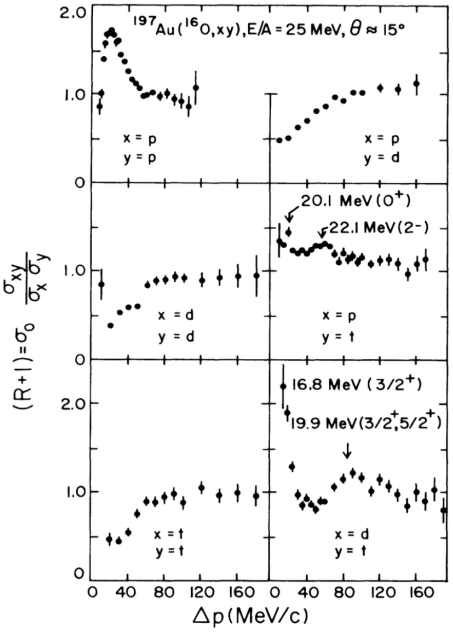

FIGURE 4.1: The measured pp and p–d correlations are shown in the top left and top right panels, respectively. The deuteron-deuteron and proton-triton correlations are shown in the middle left and middle right panels, respectively [196].

collisions between Argon and Nickel nuclei at a kinetic energy of 77 MeV/u [199].

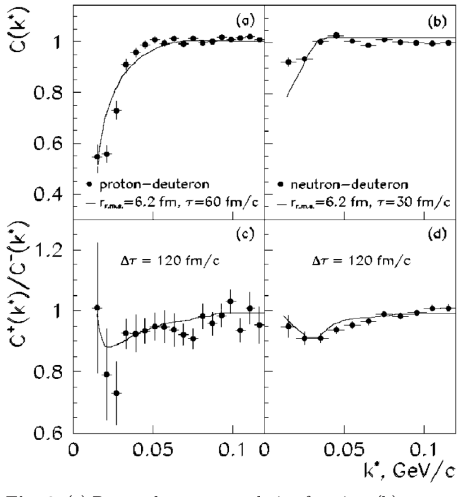

FIGURE 4.2: Results from [199], the upper panel shows the measured p–d and n–d correlations using ^{40}Ar–^{58}Ni reactions at 77 MeV/u, together with prediction using Lednický approach.

In this experiment, the measured n–d and p–d correlations also exhibit a signature of final-state interaction, as shown in Fig. 4.2. The comparison of the measured p–d correlation function with a simple theoretical model (black line in Fig. 4.2), which treats the deuteron and proton as point-like particles and assumes their distinguishability (referred to as the Lednický-Lyuboshitz formula [51]). The model qualitatively reproduces the data by employing the scattering parameters of p–d. It is important to note that these measurements show a clear signature of strong final-state interaction among light nuclei and nucleons. However, at the time of these analyses, theoretical calculations describing the process from a many-body perspective and precise knowledge of the source were not available. Therefore, the interpretation of the observed signal in these measurements could not be established conclusively.

This chapter presents a new measurement of the p–d correlation function in pp collisions at a center-of-mass energy of $\sqrt{s} = 13$ TeV, performed by the ALICE Collaboration. The aim is to analyze the p–d correlation in the pp collision system, which is a smaller collision system, thereby enabling the observation of the femtoscopic signal in the p–d correlation. The observed signal in the p–d correlation function is compared using the complete many-body calculations accounting for the three-nucleon dynamics from Chap. 3.

4.2 Analysis techniques

In this study, the p–d correlation function is measured using data obtained from Run 2 of pp collisions at a center-of-mass energy of $\sqrt{s} = 13$ TeV at the ALICE detector. During Run 2 of pp collisions at $\sqrt{s} = 13$TeV, the data set collected by the ALICE detector was obtained using a high-multiplicity trigger (*kHighMultV0*). As discussed in Chap. 2, this trigger requires the summed signal amplitudes in both V0 (V0M) detectors to exceed a threshold set as a multiple of the average value for minimum bias events, typically around 5. Various event selection criteria are applied to ensure the quality of the collected data, as outlined in Tab. 4.1. The events originating from

interactions of beam particles with residual gas in the beam line or mechanical structures are suppressed using timing measurements with the V0 detectors. The inelastic pp interactions occurring within a single bunch crossing are rejected by evaluating the presence of additional event vertices [104], with a maximum allowed contamination of 1.4% for residual pile-up. As discussed in Sec. 2.1.6, the primary vertex (PV) is reconstructed using two different methods: the SPD standalone and the combined global track information. If both methods provide a vertex candidate with sufficient tracks pointing to it, the difference in z-coordinates between them must be smaller than 0.5 cm. The tracks with poorly reconstructed SPD vertices are discarded by demanding a resolution obtained from the covariance matrix. To ensure uniform detector coverage, the maximum deviation between the reconstructed PV and the nominal interaction point at the center of the detector is restricted to be smaller than 10 cm. After applying these selection criteria, a total of 1.0×10^9 high-multiplicity events are used for the analysis.

Selection criterion	Value
z vertex offset	$\lvert vtx_z \rvert < 10\,\text{cm}$
Contributors to track vertex	$N_{\text{contrib,track}} > 1$
Contributors to SPD vertex	$N_{\text{contrib,SPD}} > 0$
Distance between track and SPD vertex	$d_{\text{vtx,track}-\text{SPD}} < 0.5\,\text{cm}$
SPD vertex z resolution	$\sigma_{\text{SPD},z} < 0.25\,\text{cm}$

TABLE 4.1: Event selection criteria for pp 13 TeV.

4.2.1 Reconstruction of protons

Track reconstruction

The reconstruction of protons is crucial for studying the p–d interaction. Since protons are charged and stable particles, they can be directly measured using ALICE's PID capabilities. To ensure the reliability of the reconstructed proton candidates in the sample, poorly reconstructed particle tracks and reconstruction artifacts (referred to as "fakes") must be removed. The selection criteria for protons are identical to those used in previous analyses [56, 130, 200] and are also applied to antiproton candidates. Therefore, the term "proton" refers to both protons and antiprotons unless specifically stated otherwise.

To ensure the selection of primary protons and minimize the contribution of candidates originating from feed-down decays, strict topological cuts are applied based on the distance of the closest approach (DCA) to the primary vertex (d_{PV}). Additionally, in the low transverse momentum (p_{T}) region, there is an increased probability of particles originating from interactions with the detector material. Therefore, only tracks with $p_{\text{T}} > 0.5$ GeV/c are accepted [201]. The PID is performed using the energy loss information from the TPC for particles with momentum p below 0.75 GeV/c. The TOF information is utilized for higher momentum tracks to evaluate the number of standard deviations (n_σ) related to the PID hypothesis, as discussed in Chap. 2. The PID information from the TPC and TOF is combined, and a circular selection $\sqrt{(n_{\sigma,\text{TPC}})^2 + (n_{\sigma,\text{TOF}})^2} < 3$ is applied. At high momenta, the TOF β does not provide sufficient separation power for unique identification, leading to contamination in the sample. To ensure a high-purity sample (approximately 80%) across the entire p_{T} range, only proton candidates with

Selection criterion	Value
Pseudorapidity	$\lvert\eta\rvert<0.8$
FilterBit	128
Transverse momentum	$0.5 < p_{\mathrm{T}} < 4.05\ \mathrm{GeV}/c$
TPC cluster	$n_{\mathrm{TPC}}>80$
Crossed TPC pad rows	$n_{\mathrm{crossed}}>70$ (out of 159)
Findable TPC clusters	$n_{\mathrm{crossed}}/n_{\mathrm{findable}}>0.83$
Tracks with shared TPC clusters	rejected
DCA to PV in xy	$\lvert d_{\mathrm{PV},xy}\rvert<0.1\,\mathrm{cm}$
DCA to PV in z	$\lvert d_{\mathrm{PV},z}\rvert<0.2\,\mathrm{cm}$
Particle identification	$\lvert n_\sigma\rvert<3$

TABLE 4.2: Track selection criteria used for proton reconstruction.

$p_{\mathrm{T}} < 4.05\ \mathrm{GeV}/c$ are considered. The n_σ distributions for TPC and TOF for protons are shown in the left and right panels of Fig. 4.3. The proton selection criteria are summarized in Tab. 4.2. After applying the selection of protons on all tracks, the resulting distribution for p_{T} of the protons is obtained as shown in the left panel of Fig. 4.4.

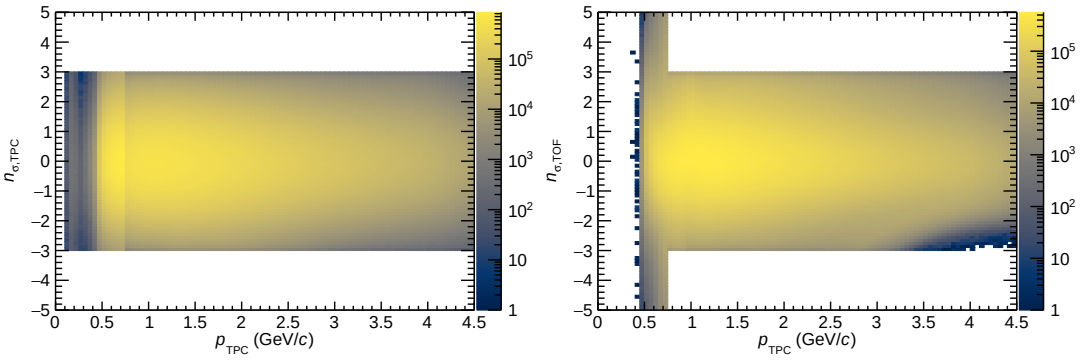

FIGURE 4.3: Distributions of n_σ from TPC (left) and TOF (right) for protons.

Purity and primary fractions

The purity of the selected protons is estimated using simulations using the PYTHIA 8.2 event generator [119]. These simulations are processed through the ALICE detector [126] using the reconstruction algorithm [106], as discussed in Chap. 2. The right panel of Fig. 4.4 shows that the p_{T}-weighted purity exceeds 99% and decreases towards the upper p_{T} threshold applied in the analysis. In addition to proton purity, the measured correlation is significantly influenced by feed-down contributions originating from weak decays, particle misidentifications, and particles produced through the spallation of the beam pipe material. To isolate the genuine correlation originating from particles produced in the collision, the feed-down contributions from weak decays and spallation for protons are estimated using a template fit of the DCA_{xy} distributions. This approach is more sensitive to individual distributions and has been successfully demonstrated in previous studies [131].

Primary protons, originating close to the interaction points, are expected to

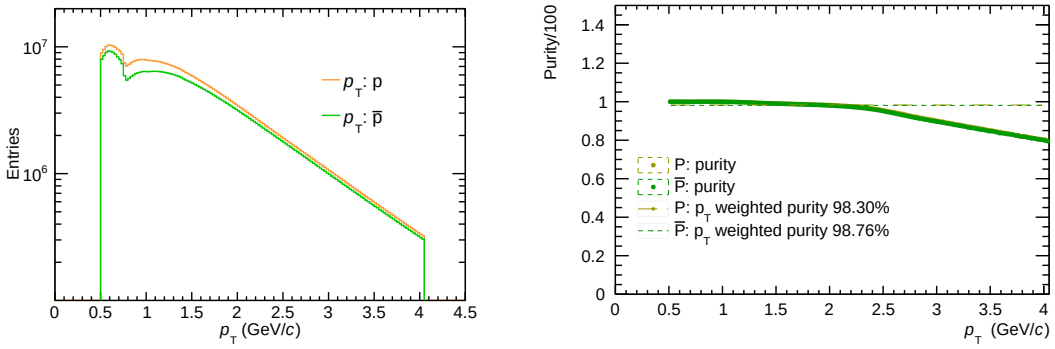

FIGURE 4.4: The p_T distributions (left) and purity (right) of (anti) protons.

have small values of DCAxy. Therefore, their distribution should be narrower than secondary protons, which arise from the decay of Λ and Σ^+ particles. On the other hand, the DCAxy distribution for protons produced in the detector material is generally flat. The individual contributions from these sources can be quantified by performing a template fit of the experimental distribution. An example of such template fits for protons and antiprotons is shown in the left panel of Figs. 4.5 and 4.6 for the p_T bin $(1.03 < p_T < 1.21)$ GeV/c. The resulting fractions are displayed as functions of p_T in the right panel. The primary fractions for protons and antiprotons are very similar, with average values of approximately 85%. However, in the case of antiprotons, the material contribution is negligible since they cannot be produced from the beam-pipe material. The DCA fits for protons and antiprotons for all p_T bins can be found in Appendix B. The primary fraction of protons, weighted by p_T,

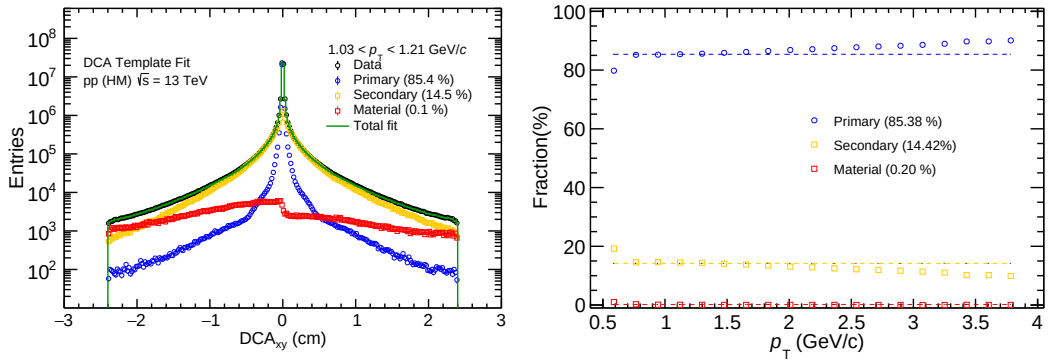

FIGURE 4.5: An example of a template fit for the DCA$_{xy}$ distribution (left) and the corresponding fractions of protons as a function of p_T (right). The dashed lines represent the p_T-weighted averages of the fractions.

is found to be 85%, while the remaining fraction is associated with weak decays of Λ and Σ^+ particles in a ratio of 70%/30%. Additionally, the contribution of protons from the detector material is found to be negligible. To further enhance the purity of the proton sample, n_σ is calculated assuming different particle hypotheses (kaons, electrons, and pions). If the corresponding hypothesis is found to be more favorable, i.e., if the n_σ value is smaller, the track is rejected. Applying all the aforementioned track quality and PID selection criteria, approximately 516×10^6 (449×10^6) proton

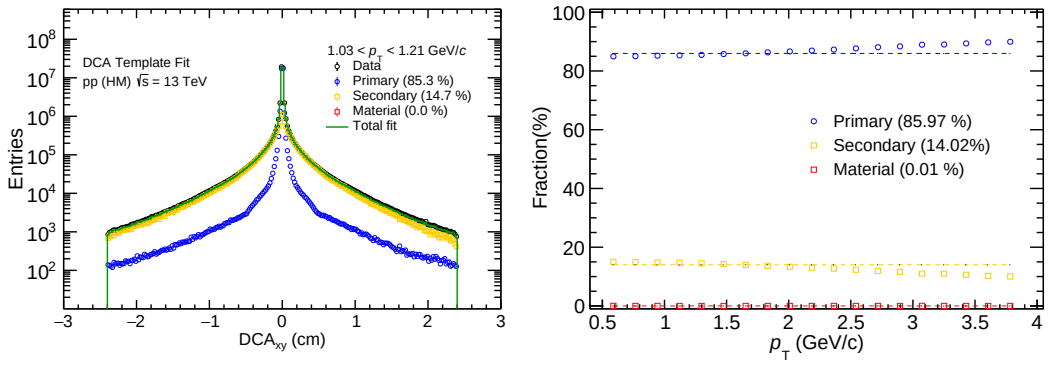

FIGURE 4.6: An example of a template fit for the DCA$_{xy}$ distribution (left) and the corresponding fractions of antiprotons as a function of p_{T} (right). The dashed lines represent the p_{T}-weighted averages of the fractions.

(antiproton) candidates with a purity larger than 99% are obtained for the p–d analysis.

4.2.2 Reconstruction of deuterons

Track reconstruction

The selection of deuteron tracks is very similar to the selection of proton tracks, with the difference being the use of FilterBit (FB) 256 instead of FB128. FB256 requires at least two ITS clusters, with at least one cluster required in the SPD, which helps ensure the quality of individual primary deuteron tracks.

Deuteron particle identification is performed using only the energy loss information from the TPC for particles with momentum p below 1.4 GeV/c. For tracks with higher momentum, particle identification also requires the TOF information to evaluate the n_σ related to the PID hypothesis. More details can be found in Sec. 2.1.5, along with Figs. 2.6, 2.5, and Eq. 2.3.

Similarly to the selection of protons, deuterons with $p_{\mathrm{T}} > 1.4$ GeV/c are identified using the combined PID information of TPC and TOF, with a circular selection $\sqrt{(n_{\sigma,\mathrm{TPC}})^2 + (n_{\sigma,\mathrm{TOF}})^2} < 3$. However, this approach is used only to assess the purity of the deuteron sample. From Fig. 2.6, it can be observed that the TOF β does not provide sufficient separation power for momenta above $p > 2.0$ GeV/c, which is necessary for unique identification. Consequently, including deuteron candidates with $p > 2.0$ GeV/c introduces significant contamination into the sample. A lower $p_{\mathrm{T}} > 0.5$ GeV/c threshold is applied to avoid large contamination of secondaries due to material loss. Furthermore, in contrast to the proton track selection, there is a notable difference in the (anti-)deuteron track selection criteria. An upper limit of $p_{\mathrm{T}} < 1.4$ GeV/c is set for (anti-)deuterons, ensuring a 100% pure sample since the (anti-)deuteron purity significantly decreases with increasing p_{T}, as discussed in Sec. 4.2.2. For the high-p_{T} range of deuterons, a special correction procedure has been attempted to account for contamination from fake-deuteron correlations, which will be described in Sec. 4.2.3. Only the high purity range of deuterons with $0.5 < p_{\mathrm{T}} < 1.4$ GeV/c is used for the final results. All the deuteron selection criteria are summarized in Tab. 4.3.

Selection criterion	Value
Pseudorapidity	$\|\eta\|<0.8$
FilterBit	256
Transverse momentum	$0.5 < p_{\mathrm{T}} < 1.4$ GeV/c
TPC cluster	$n_{\mathrm{TPC}}>80$
Crossed TPC pad rows	$n_{\mathrm{crossed}}>70$ (out of 159)
Findable TPC clusters	$n_{\mathrm{crossed}}/n_{\mathrm{findable}}>0.83$
Tracks with shared TPC clusters	rejected
DCA to PV in xy	$\|d_{\mathrm{PV},xy}\|<0.1$ cm
DCA to PV in z	$\|d_{\mathrm{PV},z}\|<0.2$ cm
Particle identification	$\|n_{\sigma}\|<3$

TABLE 4.3: Track selection criteria used for (anti-)deuteron reconstruction. The systematic variations are given in Tab. 4.5.

Purity and primary fractions

Due to the absence of primary light (anti-)nuclei production in PYTHIA 8.2, the purities of (anti-)deuterons cannot be directly evaluated from the MC simulation. To address this issue, two different approaches are used. For $p_{\mathrm{T}} < 1.4$ GeV/c, (anti-)deuterons can be clearly separated from other particle species, resulting in 100% purity, as shown in Fig. 2.5. This particular transverse momentum interval is called the *high-purity sample*, which is used for the final results. For $p_{\mathrm{T}} > 1.4$ GeV/c, (anti-)deuterons are identified using the TOF detector. Specifically, the extraction of the signal with the TOF detector is based on measuring the squared mass m^2 of the particle associated with the track, as described in the following equation.

$$m^2 = \frac{p^2}{c^2}\left(\frac{1}{\beta^2} - 1\right), \tag{4.1}$$

where p is the track momentum and β is the velocity of the particle divided by the speed of light c. The TOF β is calculated using the length L and the time of flight t_{TOF} of the tracks, as described in Chap. 2. The obtained TOF mass squared distributions are fitted with a signal and background fit function. The signal function is modeled using a mathematical function which is written as

$$sig(x; N_{sig}, \mu, \sigma, \alpha,) \propto N_{sig} \begin{cases} \exp[-\frac{1}{2}\left(\frac{x-\mu}{\sigma}\right)^2] & \text{for } x \leq \mu + \alpha\sigma \\ \exp[-\alpha\left(\frac{x-\mu}{\sigma} - \frac{\alpha}{2}\right)] & \text{for } x > \mu + \alpha\sigma \end{cases} \tag{4.2}$$

The presence of an exponential tail is a known effect of TOF PID. The background is modeled using an exponential function. An example of such a fit is shown in Fig. 4.7, and the remaining fits for the TOF mass of deuterons and antideuterons can be found in Appendix B.

The purity of the signal is defined as the ratio of the integral of the signal to the integral of the total fit within 3σ of the signal distribution. The purity values are shown as a function of p_{T} in Fig. 4.8 for deuterons (left) and antideuterons (right). At very low momenta ($p \approx 0.9$ GeV/c), deuteron candidates barely reach the TOF detector, resulting in a lack of statistics for the fit. Therefore, the fit cannot be performed, but deuterons are known to be 100% pure below $p_{\mathrm{T}} < 1.4$ GeV/c, as

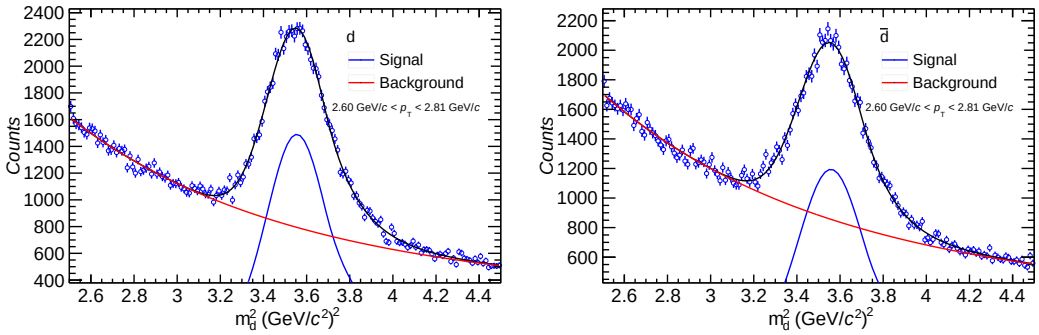

FIGURE 4.7: Exemplary fit to the TOF m^2 distribution of deuterons (left) and antideuterons (right) in the p_T range $2.6 < p_T < 2.8$ GeV/c, used to determine the purity.

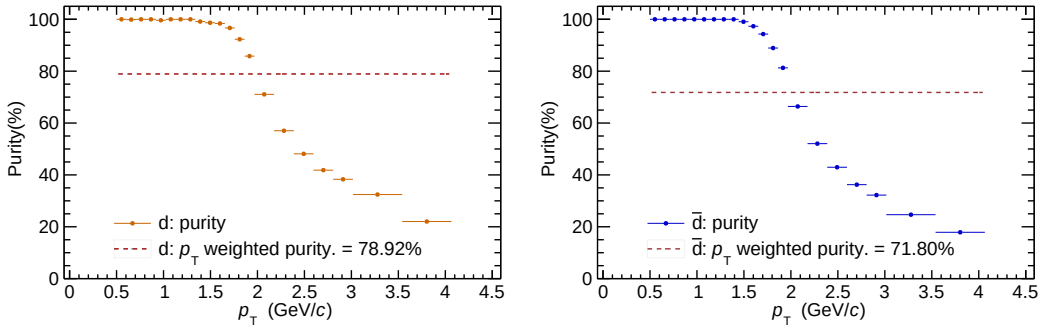

FIGURE 4.8: Purity as a function of transverse momentum for deuterons (left) and antideuterons (right). The dashed lines represent the p_T-weighted average values, which are 78.97% for deuterons and 71.90% for antideuterons. At very low momenta ($p \approx 0.9$ GeV/c), where deuteron candidates have limited statistics in the TOF detector, the purity is set to 100% based on the TPC dEdx band of (anti-)deuteron candidates shown in Fig. 2.5.

shown in the TPC dEdx band of the (anti-)deuteron candidates in Fig. 2.5. Hence, the purity is set to 100% in this momentum range. The p_T-weighted average values are represented by dashed lines and are 78.97% for deuterons and 71.90% for antideuterons. As with protons, the fraction of primary deuterons is determined by performing a template fit to the DCA_{xy} distribution. In the case of secondary deuterons, a fraction of the candidates originate from the interaction of primary particles with the detector material, known as a material knock-out. However, antideuterons cannot be produced through material knock-out due to the conservation of baryon number. Additionally, deuterons are less likely to be produced from weak decays. The only possible source of deuteron decay is through the three-body decay channel of the hypertriton ${}^{\Lambda}_{3}\mathrm{H} \rightarrow \mathrm{d} + \mathrm{p} + \pi^-$, and its charge conjugate ${}^{\Lambda}_{3}\bar{\mathrm{H}} \rightarrow \bar{\mathrm{d}} + \bar{\mathrm{p}} + \pi^+$ for anti-hypertriton. The production of (anti-)hypertriton in pp collisions has not been observed yet, and its production yield is expected to be lower than that of ^{3}He. Moreover, the production of ^{3}He is suppressed by a factor of one-thousandth compared to deuteron production [202], making the yield of secondary (anti-)deuterons from (anti-)hypertriton decays in pp collisions negligible compared to (anti-)deuteron production. Primary deuterons are not produced in the PYTHIA simulations. Therefore, the DCA distributions of antideuterons are

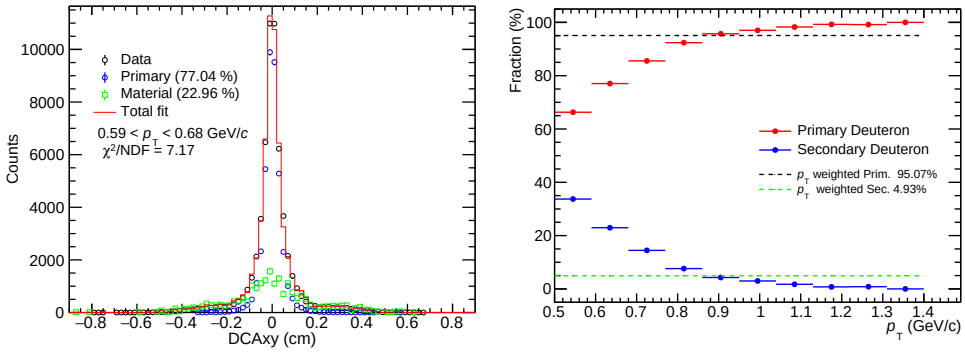

FIGURE 4.9: An exemplary plot for the template fit to the DCA_{xy} distribution for deuterons in the momentum range $0.59 < p_{\mathrm{T}} < 0.68$ GeV/c (left). On the right, the distributions of fractions for primary and secondary deuterons as a function of p_{T}. The dashed lines indicate the average values.

used as the templates for the DCA distributions of primary deuterons, as there are negligible contributions from secondaries for antideuterons. On the other hand, material knock-outs for deuterons are simulated in PYTHIA and GEANT, and these simulated events are used as MC templates for the secondary deuterons.

Finally, the DCA template fits to the data are performed using the primary and secondary templates. An example of a template fit is shown in the left panel of Fig. 4.9, and the fraction of primary and secondary deuterons as a function of transverse momentum is displayed in the right panel of Fig. 4.9. The dashed line represents the p_{T}-weighted average values of the primary and secondary fractions of deuterons, which are 95.07% and 4.93%, respectively. After applying all PID selection criteria, a total of 371×10^3 (490×10^3) (anti-)deuterons are selected in the final sample.

4.2.3 The experimental p–d correlation

After the final selection of candidates, proton-deuteron (p–d) pairs are formed by pairing candidates from the same collisions, referred to as the *Same Event* distribution. Additionally, a reference distribution of uncorrelated p–d pairs is constructed using particles from events that do not contain any two particles from the same physical event. This reference sample, known as the *Mixed Event*, ensures that the individual particles in the reference distribution have correct kinematic properties but do not exhibit any final-state interactions. Pair mixing is achieved by considering all possible permutations of particles from different physical events.

The correlation between the proton and deuteron is obtained by calculating the ratio of the same-event distribution to the mixed-event distribution. Both distributions are obtained as functions of the relative momentum k^* for each p–d pair. The relative momentum of the pair is defined as $k^* = \frac{1}{2} \cdot |\mathbf{p}_1^* - \mathbf{p}_2^*|$, where $\mathbf{p}_1^*$ and $\mathbf{p}_2^*$ are the momenta of the two particles in the rest frame of the pair. The correlation function is then defined as

$$C_{\mathrm{exp}}(k^*) = \zeta(k^*) \frac{N_{same}(k^*)}{N_{mixed}(k^*)} \xrightarrow{k^* \to \infty} 1\,, \tag{4.3}$$

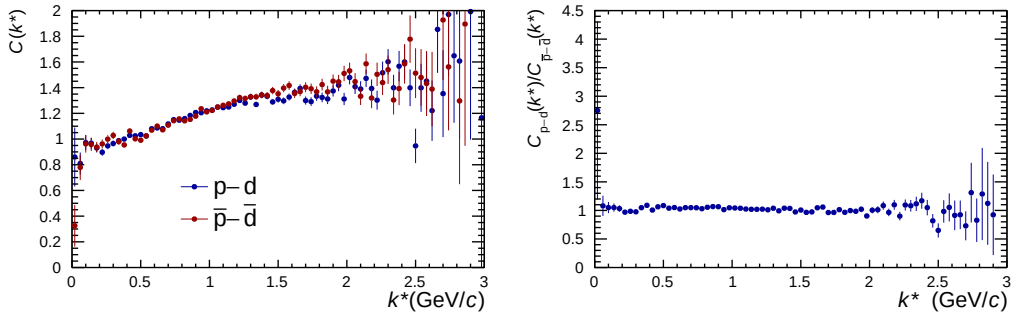

FIGURE 4.10: Measured correlation functions for p–d and for $\overline{\text{p}}$–$\overline{\text{d}}$ are shown in the left panel, and the corresponding ratio is shown in the right panel.

where, $N_{\text{same}}(k^*)$ and $N_{\text{mixed}}(k^*)$ refer to the measured yield of the correlated *signal* pair sample and the *reference* pair sample without correlated p–d respectively. The reference sample is expected to have very high statistics since the mixing is performed among 10^9 events, while the number of p–d pairs in each event is rarely greater than 3. Therefore, the pair statistics in the mixed event are much higher than those in the same event.

To comply with the theoretical definition of the correlation function, a normalization factor, denoted as $\zeta(k^*)$, is applied in the experimental correlation function. In heavy-ion collisions, the correlation function typically flattens outside the region of final-state interaction, usually for k^* values above 200-300 MeV/c. However, in small collision systems like pp, the presence of a stronger femtoscopic signal often leads to a complete absence of convergence towards a flat correlation, making it impossible to normalize the raw correlation function at large k^* values.

In the case of the experimental p–d correlation, the normalization is chosen in the region of k^* where the effect of the final-state interaction is negligible, and the correlation function is relatively flat, typically within the range of $k^* \in [0.2, 0.5]$ GeV/c. In addition to the normalization of the raw correlation, the measured correlation is affected by the deterioration of the reference sample due to the acceptance effects of the detector system. To mitigate this effect, the mixing procedure is carried out only between particle pairs arising from events with a similar z-position of the primary vertex and similar multiplicities. The z-vertex position is binned with a width of 2 cm, and the multiplicity is grouped into classes such as $[1-4], [5-8], ..., [93-96], [97-100], [> 101]$. The particle multiplicities are estimated using the reference multiplicity, RefMult08, which counts the number of charged particles N_{ch} within $|\eta| \leq 0.8$. Furthermore, the mixed event distributions $N_{\text{mixed}}(k^*)$ are reweighted to match the corresponding multiplicity distribution of the same event. The raw correlation functions for the p–d and $\overline{\text{p}}$–$\overline{\text{d}}$ pairs are shown in Fig. 4.10. Both correlation functions exhibit a flat behavior in the intermediate k^* region. However, for large k^*, both distributions have an increasing tail, which may be attributed to energy-momentum conservation effects. A depletion at very low k^* indicates a repulsive interaction in the p–d and $\overline{\text{p}}$–$\overline{\text{d}}$ pairs. The ratio between the two correlation functions remains flat, indicating agreement between the two correlations.

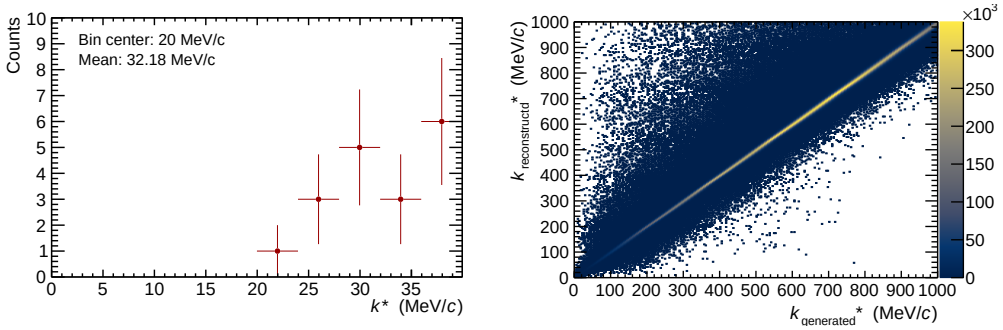

FIGURE 4.11: Distribution of k^* within the bin $0 < k^* < 40$ MeV/c (left) and momentum resolution matrix for p–d pairs obtained from the Minimum Bias LHC18a2 simulation (right).

Addition of the correlations

In the raw measured correlations of p–d and $\overline{\text{p}}$–$\overline{\text{d}}$, a total of 2,318 (p–d) pairs and 1,533 ($\overline{\text{p}}$–$\overline{\text{d}}$) antipairs contribute to the correlation function in the region $k^* < 200$ MeV/c. According to charge-parity conservation, the correlations for pair and antipair are expected to be identical. Consistent with this expectation, the measured p–d and $\overline{\text{p}}$–$\overline{\text{d}}$ correlations exhibit strong similarity. As aforementioned, the ratio between them remains close to 1 across the entire k^* range, as shown in Fig. 4.10. The correlations from pairs and antipairs are added in order to increase statistical precision. The final measured correlation function is obtained by adding the same-event distributions of pairs and antipairs and the separately added mixed-event distributions. The procedure for combining correlations in the case of low-statistics analysis has been extensively discussed in Dimitar's Ph.D. thesis [58]. The formula for combining correlations from pairs and antipairs is given as follows:

$$C_{\text{exp}}^{Tot}(k^*) = \zeta(k^*)\frac{N_{same}^{pair}(k^*) + N_{same}^{antipair}(k^*)}{N_{mixed}^{pair}(k^*) + N_{mixed}^{antipair}(k^*)} \xrightarrow{k^* \to \infty} 1\,. \tag{4.4}$$

Thus, the combined correlation of p–d and $\overline{\text{p}}$–$\overline{\text{d}}$ is denoted as p–d. However, even after combining the pair and antipair correlations, the p–d correlation suffers from low statistics. To observe the physical signal in the correlation, a bin width of 40 MeV/c in k^* is chosen as optimal for this study. However, the wide bin width introduces a complication for the bin centers. The data points of the experimental correlation function are shifted to the center of gravity of the bins. This adjustment is necessary because the shape of the k^* distribution can cause the mean k^* within a bin to differ from the bin center. Since the theoretical models exhibit a significant dependence on the relative momentum (as discussed in Chap. 3), the consistency between the data and theoretical predictions is evaluated at the corresponding mean k^* value rather than at the bin center. The average k^* is obtained by dividing each original bin into narrower bins of width 4 MeV/c and calculating the mean value within those narrower bins. An example of this procedure is illustrated in Fig. 4.11 for the first bin ($0 < k^* < 40$ MeV/c). The difference between the two values becomes more significant at low k^* due to the limited statistics.

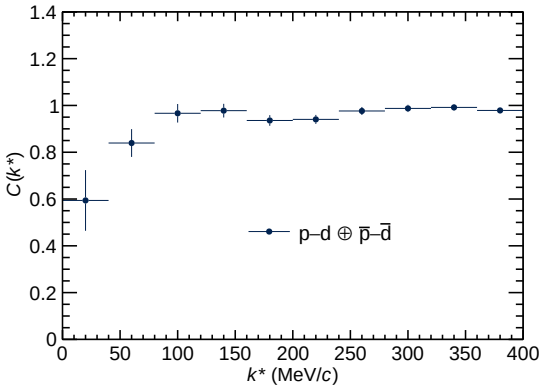

(a) The measured p–d $\oplus$ $\overline{\text{p}}$–$\overline{\text{d}}$ correlation from the data.

FIGURE 4.12: The measured p–d $\oplus$ $\overline{\text{p}}$–$\overline{\text{d}}$ correlation from the data.

Detector effects

The finite momentum resolution of the detector affects the experimentally determined correlation function, which must be accounted for when comparing the theoretical correlation function with the experimental data. The measured p–d correlation is corrected for this kinematic effect using Monte Carlo simulation, as described in [59, 131, 203]. To perform the correction, a map from generated to reconstructed k^* is obtained from the k^* resolution matrix, as shown in the right panel of Fig. 4.11. Directly evaluating k^* for p–d pairs from the Monte Carlo simulation of pp is not possible due to the limitations of PYTHIA 8.2 in handling the production of light (anti-)nuclei. Therefore, a resolution map is obtained using Minimum Bias data from p-p simulations (LHC18a2) where deuterons are injected using afterburner techniques. Since the resolution matrix requires particle kinematics and does not involve final-state interaction, the resolution for p–d is expected to be similar to p–p (Λ-p) as the single-track resolution is comparable for protons and deuterons. Further details on the procedure for correcting the measured correlation for finite momentum resolution are discussed in Sec. 4.2.3.

In addition to the finite momentum resolution, another correction is necessary for cases where the trajectories of particles in a low- k^* pair are nearly co-linear. This situation can occur at low k^* when the particle momenta are very similar. In such cases, the spectrometer's spatial resolution and the tracking algorithm's precision can introduce detector effects [204]. Specifically, track splitting occurs when one track is incorrectly reconstructed as two, while track merging happens when two tracks are reconstructed as one. This can artificially enhance or deplete pair statistics at a particular value of k^*. To evaluate this effect, the angular difference between two tracks is studied in a Monte Carlo event where no correlations between the particles are expected. This study was conducted to measure the p–p correlation [130]. To reject track pairs originating from track splitting or merging, a circular rejection condition of $\sqrt{\Delta\varphi^2 + \Delta\eta^2} \leq 0.17$ is applied. Here, $\eta_{1,2}$ represents the pseudorapidity, and $\varphi^*_{1,2}$ denotes the azimuthal angle evaluated at a given TPC radius. After applying this correction, the measured correlation function is presented in Fig. 4.12.

Momentum smearing

Often, researchers outside of the ALICE collaboration use the data from femtoscopic analyses. One of the main challenges in comparing data with theoretical predictions is accounting for detector effects, especially the resolution in the estimation of k^* by the detector. As discussed, a resolution matrix is required for each measured correlation and the additional complexity of applying the correction procedure to the measured data. In the p–d analysis, an effort is made to simplify the presentation of results by correcting the measured correlation function for resolution effects. This correction procedure is similar to the analysis of p–Λ [205]. The smeared correlation function can be obtained by utilizing the experimental resolution matrix defined in the following expression.

$$C_{\text{smear}}(k^*) = \mathcal{M}_{k^*\,k^{*\prime}} C_{\text{theory}}(k^{*'}), \tag{4.5}$$

where $C_{\text{smear}}(k^*)$ represents the correlation function affected by the detector, $k^{*\prime}$ denotes the true relative momentum, and k^* represents the measured relative momentum. To extract the measured correlation with the true values of k^*, the inverse $\overline{\mathcal{M}}_{k^*,k^{*\prime}}$ of the matrix $\mathcal{M}_{k^*,k^{*\prime}}$ is required. However, obtaining $\overline{\mathcal{M}}_{k^*,k^{*\prime}}$ experimentally is challenging due to statistical uncertainties and non-zero entries limitations, making it difficult to obtain an accurate inverse. Alternatively, instead of seeking $\overline{\mathcal{M}}_{k^*,k^{*\prime}}$, a Monte Carlo method is used to iteratively compare the unfolded correlation $C_{\text{unfold}}(k^{*\prime})$, which is an initial guess, with the smeared experimental correlation $C_{\text{smear}}(k^*)$. The deviation between the obtained $C_{\text{smear}}(k^{*\prime})$ and the original $C_{\text{original}}(k^{*\prime})$ is evaluated to determine the precision of the procedure. The iteration is repeated until the desired precision is reached. A maximum deviation $\chi^2 < 10^{-3}$ is considered acceptable given the uncertainties of the current data. In the case of p–d, separate unfolding is performed for the same event (SE) and mixed event (ME) distributions, as shown in Fig. 4.13. The correction for momentum resolution is ex-

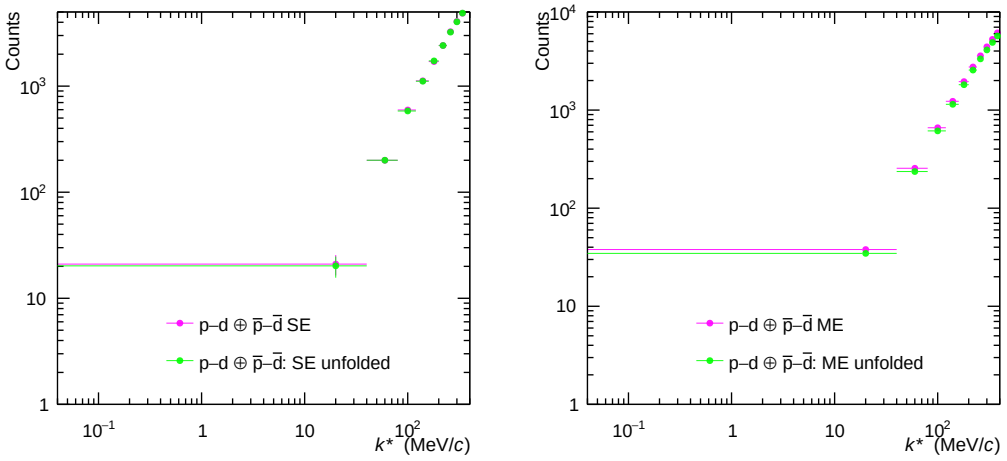

FIGURE 4.13: Comparison of raw and unfolded same-event distributions (left) and mixed-event distributions (right) for p–d ⊕ p̄–d̄.

pected to significantly impact small relative momenta. However, since the bin width of the SE and ME distributions for p–d is relatively large (40 MeV/c), the effect is negligible. The final correlation function is obtained by combining the unfolded SE

and ME events and is presented in Fig. 4.14. The effect of unfolding on the final correlation function is negligible.

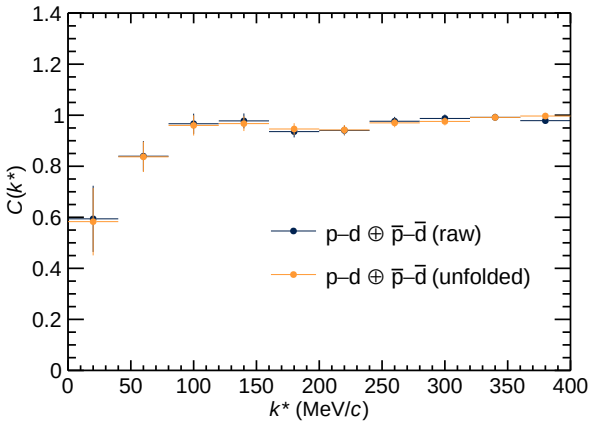

FIGURE 4.14: The measured and unfolded correlation function p–d $\oplus$ $\overline{\text{p}}$–$\overline{\text{d}}$.

Impact of (anti-)deuteron purity

(Anti-)Deuteron purities play a crucial role in the measured p–d correlation. As depicted in Fig. 4.8, the purities of (anti-)deuterons exhibit a significant decrease as a function of p_{T}. The selection of (anti)deuterons within the transverse momentum ranges $0.5 < p_{\mathrm{T}} < 4.05$ GeV/c results in substantial contamination, primarily originating from the measurement of energy loss (dE/dx) in the TPC detector for $p/z > 1.4$ GeV/c, where the energy loss bands of e^+ (e^-), π^+ (π^-), K^+ (K^-), and p ($\overline{\text{p}}$) begin to overlap with the deuteron ($\overline{\text{d}}$) energy loss band, as illustrated in Fig. 2.5 and the mismatching of the deuterons tracks in the TOF to TPC. Additionally, the TOF β band for deuteron ($\overline{\text{d}}$) exhibits a significant background for $p/z > 2.0$ GeV/c, leading to further contamination in the sample. This contamination manifests as a non-physical signal in the p–d correlation within the range $80 < k^* < 120$ MeV/c. The measured p–d $\oplus$ $\overline{\text{p}}$–$\overline{\text{d}}$ correlations, obtained from full p_{T} (anti-)deuteron and (anti-)deuteron PID restricted to $p_{\mathrm{T}} < 1.4$ GeV/c, are displayed in the left panel of Fig. 4.15.

In order to investigate the source of the unphysical signal in the measured p–d correlation function, high-multiplicity pp MC simulations were utilized as a proxy. The MC sample was chosen due to the absence of primary d($\overline{\text{d}}$) and minimal secondary deuterons, making it suitable for studying any spurious correlations arising from the pair of proton and fake candidate. Additionally, the MC sample contains no antideuterons, including secondary ones. Therefore, any pairing of antiprotons $\bar{x} - \overline{\text{p}}$ would result in fake $\overline{\text{p}}$–$\overline{\text{d}}$ pairs. Interestingly, the presence of a peak in the p–d $\oplus$ $\overline{\text{p}}$–$\overline{\text{d}}$ correlation obtained from the MC simulations closely resembles the peak observed in the measured p–d $\oplus$ $\overline{\text{p}}$–$\overline{\text{d}}$ correlation, strongly suggesting contamination in the measured p–d $\oplus$ $\overline{\text{p}}$–$\overline{\text{d}}$ correlation leading to the spurious peak. To further investigate the correlation of fakes with antiprotons, all $\overline{\text{p}}$–$\overline{\text{d}}$ fake pairs (excluding anti-deuterons from material spallation) below $k^* < 400$ MeV/c were stored and subjected to a PDG (Particle Data Group) ID check. The PDG check scheme is illustrated in Fig. 4.16. It turns out that a total of 2557 $\bar{x} - \overline{\text{p}}$ pairs are misidentified as e^-, π^-, K^-, and $\overline{\text{p}}$. While the $\overline{\text{p}}$ candidates have a purity

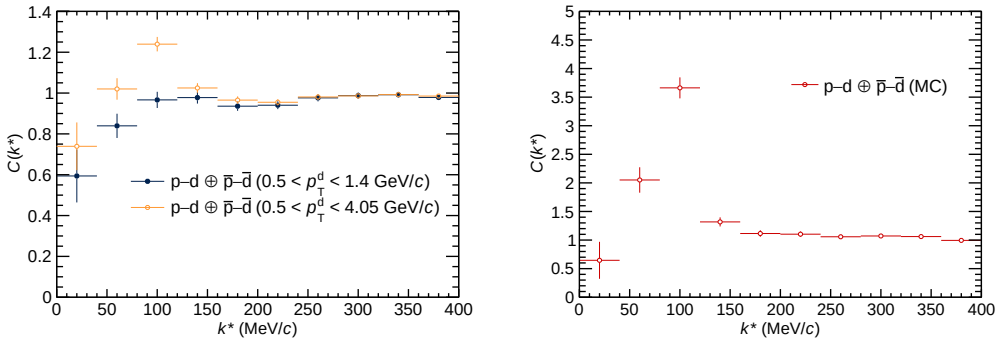

FIGURE 4.15: The left panel shows the measured p–d $\oplus$ $\overline{\text{p}}$–$\overline{\text{d}}$ correlation function using d($\overline{\text{d}}$) transverse momentum ranges $0.5 < p_{\text{T}}^{d} < 1.4$ GeV/c and $0.5 < p_{\text{T}}^{d} < 4.05$. The right panel displays the measured p–d $\oplus$ $\overline{\text{p}}$–$\overline{\text{d}}$ correlation function simulations using transverse momentum $0.5 < p_{\text{T}}^{d} < 4.05$ GeV/c.

of 97.1% in this sample, all the $\overline{\text{d}}$ candidates are fake. Specifically, there are 1525 $\overline{\text{p}} - \pi^{-}$ pairs, 541 $\overline{\text{p}} - \overline{\text{p}}$ pairs, and 385 $\overline{\text{p}} - \text{K}^{-}$ pairs. In conclusion, the non-physical peak-like signal around $80 < k^{*} < 120$ MeV/c in the p–d correlation is a result of the fake d($\overline{\text{d}}$) candidates, particularly those reconstructed with $p_{\text{T}} > 1.4$ GeV/c. At this point, there are two options: either restrict the (anti-)deuteron identification to (anti-)deuteron momenta $p_{\text{T}} < 1.4$ GeV/c, or apply a correction to remove the contamination effect caused by the background of d($\overline{\text{d}}$) candidates by utilizing a sideband correction procedure, as discussed in Sec. 4.2.3.

Sideband correction studies

One of the main objectives of any analysis is to maximize candidate statistics without introducing bias into the final results from the low-purity region. In this analysis, the idea is to include all deuteron candidates within the maximum p_{T} range. However, as discussed in Sec. 4.2.2, the purity of (anti-)deuterons decreases significantly for $p_{\text{T}} > 1.4$ GeV/c. Therefore, the sample is divided into two parts. In the first sample, a hard cut on the transverse momentum of d($\overline{\text{d}}$) ($p_{\text{T}} < 1.4$ GeV/c) is applied to ensure 100% pure d($\overline{\text{d}}$) candidates in the sample. In the second sample, deuteron candidates with $1.4 > p_{\text{T}} > 1.4$ GeV/c are considered, where a background in signal due to misidentified deuterons arises, but the signal is corrected for the misidentified d($\overline{\text{d}}$). This section will discuss the second approach.

The purity is evaluated by fitting the TOF m^2 distribution (Fig. 4.7) in specific intervals of p_{T}. Therefore, in the full-p_{T} analysis, it is necessary to assess the contribution of background (resulting from misidentifications of deuterons) to the correlation function. This contribution is determined from the sideband region of the TOF m^2 distribution. To define the sideband region, it is first necessary to study the dependence of the TOF m^2 on p_{T}. As discussed in Sec. 4.2.2, deuteron tracks that contribute to the TOF m^2 distribution are pre-selected using a cut on the $n\sigma$ of the TPC ($|n\sigma_{TPC}| < 3$), which reduces the background. For each p_{T} bin, the TOF m^2 distribution is fitted with a function that models the sum of signal and background. As mentioned earlier, the signal is modeled as a Gaussian with a right exponential tail for deuterons and antideuterons, as described in Eq. 4.1. From the fits of the TOF m^2 distribution, the parameters μ and σ, associated with the mean

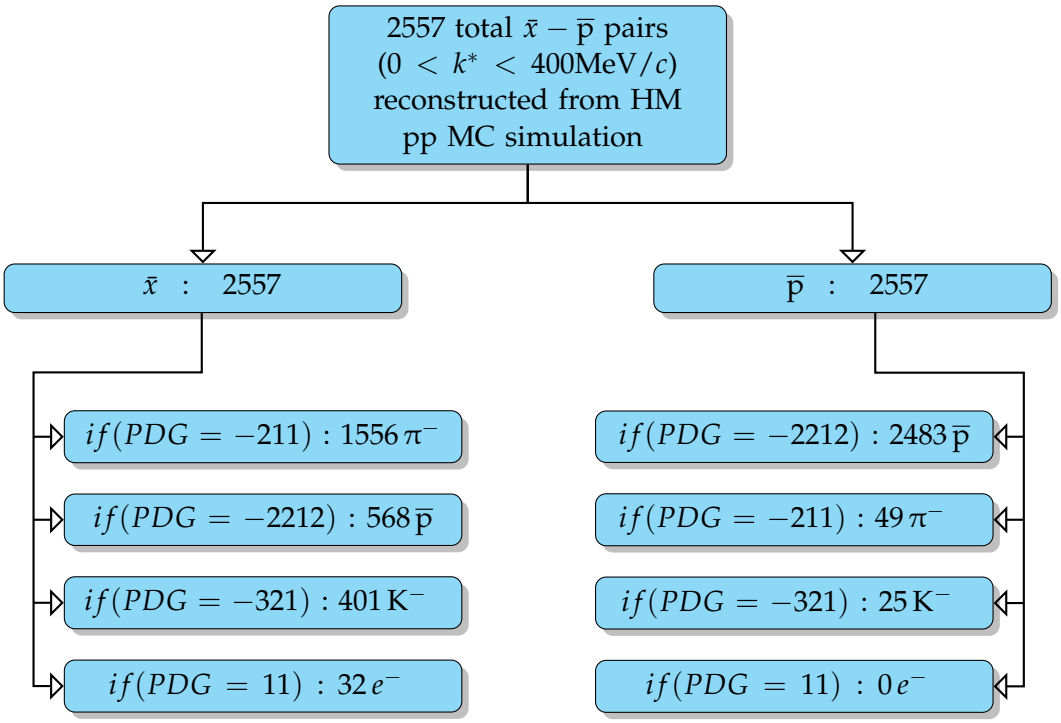

FIGURE 4.16: Sketch for fake pairs $\overline{\mathrm{p}}$–$\overline{\mathrm{d}}$ sorted according to the identifications of the MC PDG code of e^-, π^-, K^-, and $\overline{\mathrm{p}}$.

and spread of the distributions, are determined for each p_T bin. The extracted values of μ and σ from the TOF m^2 distribution are then fitted with appropriate functions to extract parameters for the fit functions in Eqs. 4.7 and 4.8. The fits are shown in Fig. 4.17, and the corresponding fit parameters are reported in Tab. 4.4. With μ and σ determined for each p_T, the signal region is defined to contain 99.75% (corresponding to 3 σ) of the candidates with respect to the circular $n\sigma_\mathrm{com}$ cuts described in Tab. 4.3. The edges of the signal region are determined by the functions mentioned below.

$$\mu(p_\mathrm{T}) - 3.5\,\sigma(p_\mathrm{T}) < m^2_\mathrm{TOF}(p_\mathrm{T}) < \mu(p_\mathrm{T}) + 3.0\,\sigma(p_\mathrm{T})\,, \tag{4.6}$$

$$\mu(p_\mathrm{T}) = p_0 + \exp\left[p_1 \cdot p_\mathrm{T} + p_2 \cdot p_\mathrm{T}^2 + p_3 \cdot p_\mathrm{T}^3 + p_4 \cdot p_\mathrm{T}^4\right], \tag{4.7}$$

and σ with the function

$$\sigma(p_\mathrm{T}) = p_0 + p_1 \cdot p_\mathrm{T} + p_2 \cdot p_\mathrm{T}^2 + p_3 \cdot p_\mathrm{T}^3 + p_4 \cdot p_\mathrm{T}^4 + p_5 \cdot p_\mathrm{T}^5. \tag{4.8}$$

For the sideband regions, the selection criterion is defined as

$$(\mu - 7.4\,\sigma \leq m^2_\mathrm{TOF} \leq \mu - 4.1\,\sigma) \cup (\mu + 3.6\,\sigma \leq m^2_\mathrm{TOF} \leq \mu + 6.5\,\sigma)\,. \tag{4.9}$$

The regions for the sidebands are selected to ensure adequate statistics while also maintaining similar underlying kinematics to the signal. Fig. 4.18 displays the signal and sideband regions for deuterons and antideuterons. The final correlation function, corrected for the sideband contributions, is determined using

$$C_\mathrm{signal}(k^*) = \frac{1}{\mathcal{P}} \cdot C_\mathrm{total}(k^*) - \frac{1}{(1-\mathcal{P})} \cdot C_\mathrm{sideband}(k^*)\,. \tag{4.10}$$

parameter	value(μ)	value(σ)
p_0	3.554	0.088
p_1	-1.25749	$1.192 \cdot 10^{-2}$
p_2	$-3.604 \cdot 10^{-1}$	$0.202 \cdot 10^{-2}$
p_3	$-1.003 \cdot 10^{-1}$	$1.230 \cdot 10^{-2}$
p_4	$-1.008 \cdot 10^{-2}$	$30.236 \cdot 10^{-4}$
p_5	-	$45.800 \cdot 10^{-5}$

TABLE 4.4: Fit parameters used for μ and σ as a function of transverse momentum.

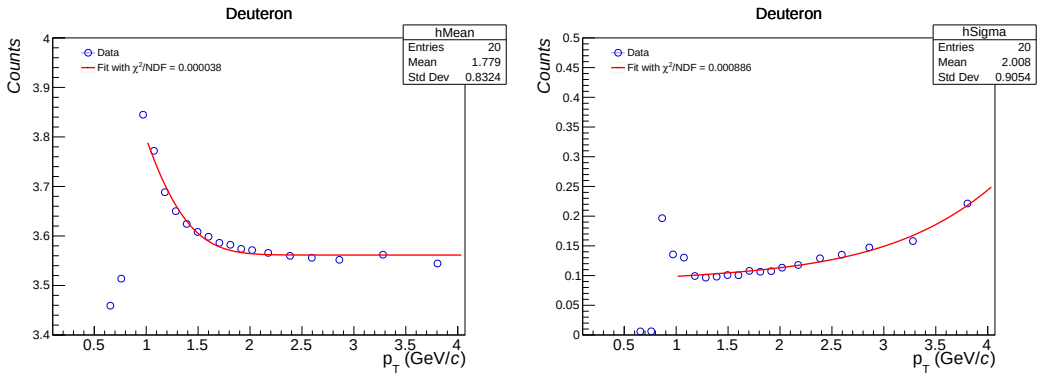

(a) μ parameter as a function of p_T.

(b) σ parameter as a function of p_T.

FIGURE 4.17: Evolution of the fit parameters μ and σ as a function of transverse momentum (see the text for further details).

The correlation C_{total} obtained in the signal region includes contributions from the underlying background in the sidebands. To isolate the signal contribution C_{signal} and account for the background, correlations C_{sideband} are evaluated in the sideband regions of the TOF m^2 distribution (shown in Fig. 4.18). These background correlations C_{sideband} are subtracted from C_{total} to obtain the sideband-corrected correlation function.

In this procedure, the p_T-weighted purity $\mathcal{P}$ of all p–d and $\overline{\text{p}}$–$\overline{\text{d}}$ pairs contributing to the correlation, as described in Eq. 4.6, is used to correct for the presence of background. To minimize bias from candidates that do not contribute to the femtoscopic signal, the p_T distributions of deuteron candidates, evaluated from 2-dimensional distributions of p_T versus k^* in p–d ($\overline{\text{p}}$–$\overline{\text{d}}$) pairs with $k^{<}200$ MeV/c, are used to extract $\mathcal{P}$. The purity values for deuterons in p–d pairs and antideuterons in $\overline{\text{p}}$–$\overline{\text{d}}$ pairs are found to be 66.6% and 57.1%, respectively.

The correlations of the lower and upper sidebands are defined based on their position relative to the signal region (see Fig. 4.18) and are shown in Fig. 4.19. To obtain the sideband-corrected correlation function C_{signal}, an average correlation from the sidebands is computed using the weighted mean, taking into account the contributions from the lower and upper sidebands weighted by the number of counts in each sideband. The weights w_i are determined by the statistical

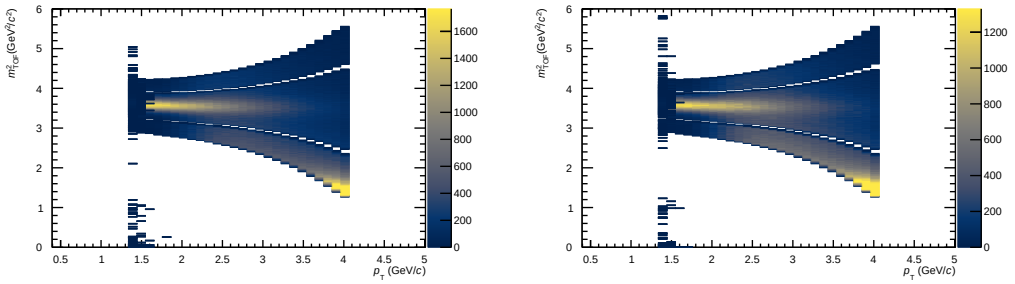

(a) Deuterons (b) Antideuterons

FIGURE 4.18: Signal and sideband regions for deuterons (a) and antideuterons (b) with $1.4 < p_{\mathrm{T}} < 4.05$ GeV/c.

uncertainties, as described by

$$x_{avg} \pm \sigma_{avg} = \frac{\sum_{i=1}^{i=nbins} w_i \cdot x_i}{\sum_{i=1}^{i=nbins} w_i} \pm \frac{1}{\sqrt{\sum_{i=1}^{i=nbins} w_i}} \qquad \text{and} \qquad w_i = \frac{1}{\sigma_i^2}. \tag{4.11}$$

After applying all the necessary corrections, the sideband-corrected correlation functions are shown in Fig. 4.19. Subsequently, the sideband-corrected correlation functions C_{signal} for p–d and $\overline{\mathrm{p}}$–$\overline{\mathrm{d}}$ in the p_{T} range $1.4 < p_{\mathrm{T}} < 4.05$ GeV/c are combined with the contributions from the high-purity sample ($0.5 < p_{\mathrm{T}} < 1.4$ GeV/c) and compared with the p–d correlations from the high-purity sample, as shown in Fig. 4.20. After the sideband correction, the final correlation function exhibits good

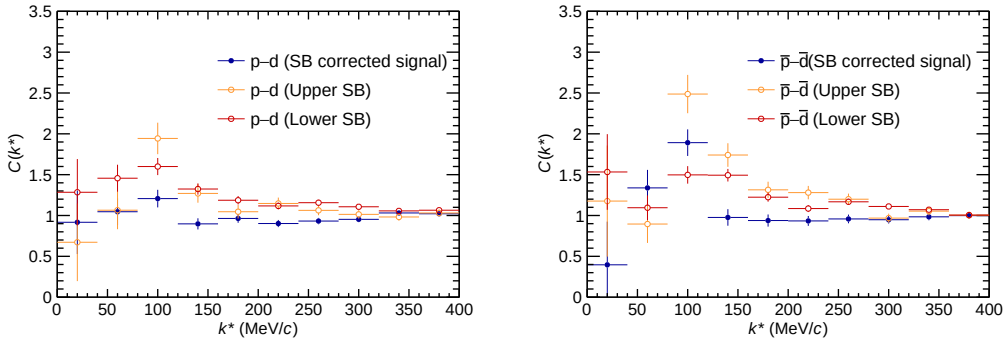

(a) p–d, signal and sideband (b) $\overline{\mathrm{p}}$–$\overline{\mathrm{d}}$, signal and sideband

FIGURE 4.19: Correlation functions of p–d and $\overline{\mathrm{p}}$–$\overline{\mathrm{d}}$ pairs for the lower sideband, the upper sideband, and the sideband-corrected signal.

agreement with the p–d correlation obtained from the high-purity sample in which the (anti)deuterons are selected only up to $p_{\mathrm{T}} < 1.4$ GeV/c. With the exception of the third bin, which shows a slightly higher value than the high-purity sample, all other bins are consistent within the error bars. The inflection in the third bin is also influenced by the choice of sidebands. It cannot be attributed to a signal, as the deuteron purity remains relatively low in the high-p_{T} sample.

Despite all the applied corrections, the increase in statistics is negligible. Therefore,

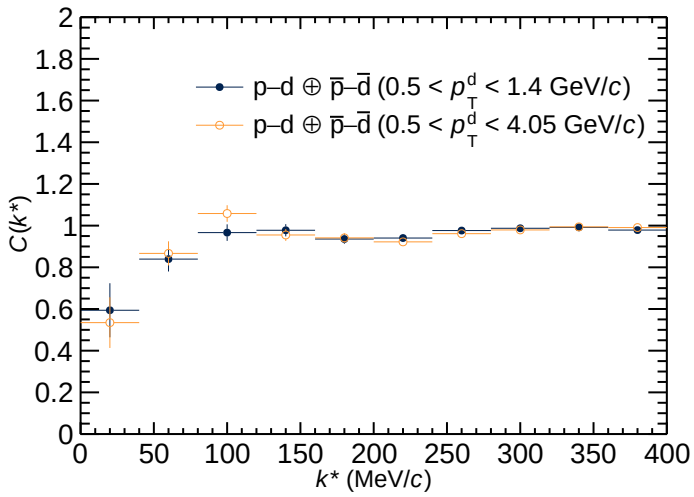

FIGURE 4.20: Comparison of the measured p–d $\oplus$ $\overline{\text{p}}$–$\overline{\text{d}}$ correlation obtained from deuteron (anti) candidates in the range $0.5 < p_{\text{T}} < 1.4$ GeV/c and the sideband-corrected p–d $\oplus$ $\overline{\text{p}}$–$\overline{\text{d}}$ correlation using (anti-)deuteron candidates in the full range $0.5 < p_{\text{T}} < 4.05$ GeV/c.

it has been decided to use the correlation obtained using the high-purity sample of deuterons as the final version of the correlation.

4.2.4 Systematic uncertainties

In general, the experimental setup can introduce uncertainties that are not solely due to limited statistics in the measurement but also arise from non-statistical biases. These biases can originate from various sources, such as the experimental setup, data collection procedures, or the modeling of theoretical curves and fitting to the data. Uncertainties stemming from such sources cannot be classified as purely statistical uncertainties but are regarded as systematic uncertainties. Additionally, it is important to note that systematic and statistical uncertainties are independent of each other, and the total uncertainties in the measurement are obtained by combining both sources using the following relation

$$\sigma_{\text{tot}} = \sqrt{\sigma_{\text{stat}}^2 + \sigma_{\text{sys}}^2}\,, \tag{4.12}$$

where σ_{stat} and σ_{sys} represent the statistical and systematic uncertainties, respectively. The calculation of σ_{stat} is relatively straightforward, as it is determined by the uncertainty associated with the statistical fluctuations in the data, which is directly related to the number of counts or events. However, the estimation of σ_{sys} relies on the specifics of the experimental setup and can vary from one experiment to another due to differences in apparatus and methodologies employed.

Systematic uncertainty of p–d correlation

The measured p–d correlation is affected by experimental conditions. In the case of the ALICE detector, the acceptance and efficiency of the detector setup have minimal impact on the measured correlations in femtoscopic analysis. Specifically, the effects stemming from detector efficiency are canceled when considering the ratio of $N_{\text{same}}(k^*)$ and $N_{\text{mixed}}(k^*)$. While the detector acceptance does influence

Selection criterion		Default	Variation
Proton candidates			
Min. p_{T}	(GeV/c)	0.5	0.4, 0.6
Max. $\lvert\eta\rvert$		0.8	0.77, 0.83
Particle Identification n_σ		3	2.5, 3.5
Min. n_{Cluster}		80	70, 90
Deuteron candidates			
Min. p_{T}	(GeV/c)	0.5	0.4, 0.6
Max. $\lvert\eta\rvert$		0.8	0.77, 0.83
Particle Identification n_σ		3	2.7, 3.3
Min. n_{Cluster}		80	70, 90
p–d *pairs*			
Close pair rejection $[\Delta\eta(\Delta\phi)]$		0.017	0.019, 0.015

TABLE 4.5: Variations in the selection criteria for proton and deuteron candidates are performed to evaluate systematic uncertainties.

both the source distributions and the correlations over a wide range, particularly the non-femtoscopic tails, the source is determined through experimental measurements of the pp correlation function, and these effects are accounted for in the determination of the source. A comprehensive examination of this effect is covered in prior studies [56]. Nonetheless, uncertainties stemming from variations in the selection criteria for candidate particles must be considered. The impact of slight modifications in the selection criteria for protons and deuterons on the extracted correlation function is quantified and incorporated into the systematic uncertainties.

The systematic uncertainties of the experimental data are assessed by randomly selecting 44 combinations of variations in the single particle selection criteria for protons and deuterons, each varying by up to 20% around their default values. All the variations applied to the selection criteria for particle candidates are listed in Tab. 4.5. Only variations that result in a pair yield modification of less than 10% in the range $0 < k^* < 200$ MeV/c are considered for the final set of variations.

To mitigate the impact of statistical fluctuations caused by the limited number of particle pairs at low k^*, systematic uncertainties are evaluated at k^* intervals of 40 MeV/c for the measured p–d correlation. For each variation, a criterion is set where the difference in maximum pair yield below $k^* < 400$ MeV/c is limited to 10% in order to select the final systematic variation. This criterion ensures a reasonably uniform distribution of systematic uncertainty across the range. Additionally, the systematic uncertainty is calculated bin by bin by taking the difference between the maximum and minimum values of correlation functions from all systematics

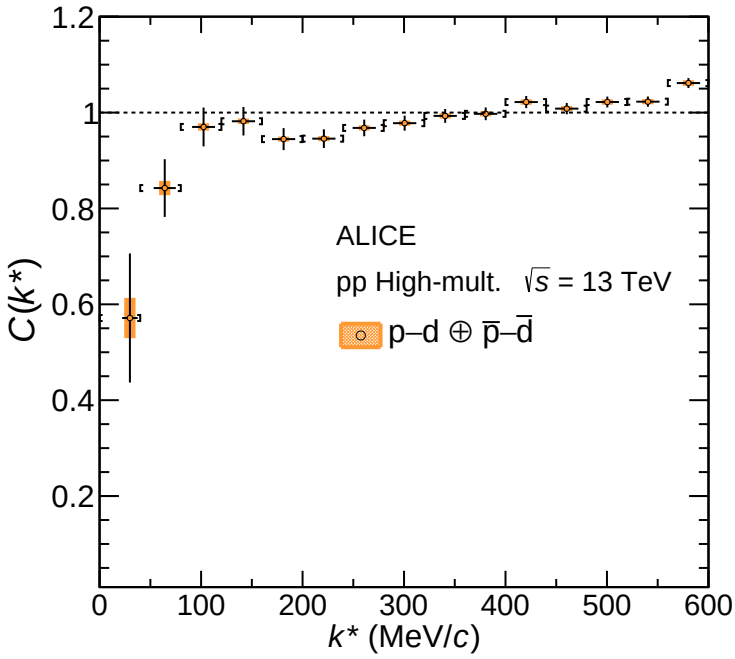

FIGURE 4.21: Experimental p–d $\oplus$ $\overline{\text{p}}$–$\overline{\text{d}}$ correlation function with systematic uncertainties.

variations and dividing by $\sqrt{12}$. To ensure a smooth representation of the systematic uncertainty across bins, the resulting uncertainty distribution is parameterized using an exponential function ($p_0 + e^{p_1 \cdot k^*}$, where p_0 and p_1 are parameters) and interpolated to obtain the final point-by-point uncertainties. The total systematic uncertainty is relatively small at the lowest k^* values, on the order of 5%, while it reaches approximately 1% for larger k^* values (> 100 MeV/c). The p–d correlation function, including systematic uncertainties, is presented in Fig. 4.21.

4.3 Modeling the total correlation function

As discussed earlier, the measured p–d correlation function primarily consists of the genuine signal from final-state interactions, as well as background contributions arising from residual correlations due to impurities, feed-down, and detector effects. In this work, the chosen approach is to address these effects by correcting the measured correlation function for momentum resolutions, as previously studied in the unfolding process described in Sec. 4.2.3. Additionally, all other relevant contributions to the modeled correlation function are incorporated through the decomposition method.

Decomposition of p–d correlation

The signal for final-state interaction in the measured p–d correlation is affected by two contributions: the misidentification of proton and deuteron candidates in the sample and the presence of proton candidates originating from weak decays. The former can be estimated and minimized by selecting candidates with nearly 100% purity. The latter requires estimation using DCA template fits, as discussed in Sec. 4.2.3. These effects are incorporated by modeling the total correlation function,

which is obtained as a weighted sum of all these contributions.

$$C_{\text{model}}(k^*) = 1 + \sum_i \lambda_{ij} \cdot (C_i(k^*) - 1), \tag{4.13}$$

where $C_i(k^*)$ represents the genuine correlations and contributions arising from various sources to the total measured correlation, and λ_{ij} are the weights assigned to determine the relative contributions. To determine the values of λ_{ij}, a data-driven approach proposed in Refs. [131, 203] is employed. These weights, λ_{ij}, are related to the properties of the single particle candidates, specifically the purity and fractions f_i of the proton and deuteron candidates. The relative weight parameter λ_{ij} for a pair of particles i, j is defined as follows:

$$\lambda_{ij} = \mathcal{P}_i \times f_i \otimes \mathcal{P}_j \times f_j, \tag{4.14}$$

where $\mathcal{P}_i$ and f_i represent the purity and fraction corresponding to the contribution of particle i, respectively. For p–d correlations, the following contributions need to be considered.

$$\begin{aligned}\{\text{p–d}\} = \text{p–d} + \text{p}_\Lambda\text{–d} + \text{p}_{\Sigma^+}\text{–d} + \tilde{\text{p}}\text{–d} + \text{p–}\tilde{\text{d}} + \text{p}_\Lambda\text{–}\tilde{\text{d}} \\ + \text{p}_{\Sigma^+}\text{–}\tilde{\text{d}} + \tilde{\text{p}}\text{–}\tilde{\text{d}} + \text{p}_M\text{–d} + \text{p}_x\text{–d}_M\,.\end{aligned}$$

Here, $\tilde{X}$ and X_{M} refer to misidentified particles and material particles as candidates X, respectively. Since the deuteron is a light nucleus and the decay sources of (anti-)deuterons such as (anti-)$^{\Lambda}_{3}$H are negligible or unknown, therefore the correlations of protons paired with deuterons from weak decays are assumed to be absent. Additionally, the Λ-d and Σ^+-d correlations are currently theoretically available but the effect is less than 1% and thus assumed to be flat. Therefore, it is assumed that the correlations of protons originating from the decay of Λ and Σ^+, when paired with deuterons, are flat. Also, the contributions from misidentifications and other residual correlation functions are also assumed to be flat. Thus, the number of contributions reduces to only two. The contributions of primary and feed-down particles are determined by the DCA template fits, as discussed in Sec. 4.2.3. To determine the values of λ_{ij} for the various contributions in Eq. 4.14, the p_{T}-weighted values of single particle purity $\mathcal{P}_i$ and fraction f_i are used. To minimize the bias from pairs that do not contribute to the final-state interaction, the p_{T} distribution of the candidates is extracted with a restriction on $k^* < 400$ MeV/c. All the p_{T}-weighted single-particle properties of (anti)protons and (anti-)deuterons are reported in Tab. 4.6. The calculated values of λ_{ij} for all contributions are listed in Tab. 4.7. The contribution to the genuine p–d correlation is 82%, while the total contribution from feed-downs, misidentifications, and material knock-out is 18% and assumed to be unity.

Genuine p–d correlation

By utilizing the measured p–d correlation, it becomes possible to study the genuine p–d interaction if the size of the source can be constrained through femtoscopy. The p–d correlation function is theoretically obtained using two different approaches, as described in Chap. 3.

The first approach is a simplistic one, which employs the Coulomb-corrected wavefunction for two point-like distinguishable protons and deuterons. The calculation is performed using scattering parameters for the p–d system based on the

Particle properties	p(%)	$\bar{\text{p}}$(%)	d(%)	$\bar{\text{d}}$(%)
Purity	98.18	97.93	100	100
Primary	85.38	85.89	95.07	100
From Λ decay	9.92	9.87	-	-
From Σ decay	4.25	4.23	-	
From Ξ^0 decay	-	-	-	-
From Ξ^- decay	-	-	-	-
Material	0.20	0.01	4.93	-

TABLE 4.6: Purity and fractions of p ($\bar{\text{p}}$) and d ($\bar{\text{d}}$).

Pair	λ_{ij}**(%)**		**Treatment**
p–d	82.0		Genuine
p_Λ–d	9.6	13.7	Feed-down (unity)
p_{Σ^+}–d	4.1		
$\tilde{\text{p}}$–d	1.7		
p–$\tilde{\text{d}}$	0.0		
p_Λ–$\tilde{\text{d}}$	0.0	1.7	Misidentification (unity)
p_{Σ^+}–$\tilde{\text{d}}$	0.0		
$\tilde{\text{p}}$–$\tilde{\text{d}}$	0.0		
p_M–d	0.2	2.6	Material knock-out (unity)
p_x–d_M	2.4		

TABLE 4.7: Weight parameters and treatment of the individual component of the p–d correlation function.

Lednický approximation. The second approach is theoretically more challenging, as it involves the three-body dynamics of the p–(p–n) system, which forms a p–d state. The source size for the p–d pairs is extracted using a data-driven approach, as discussed in Sec. 4.4.

The primary goal of this analysis is to examine whether different theoretical approaches can accurately describe the measured p–d correlation and determine if the considered theoretical p–d correlations can be distinguished given the available statistical precision of the data.

4.3.1 Baseline

In the ideal case, the modeled correlation function that incorporates all the relevant ingredients according to Eq. 4.13 is expected to be consistent with the data. However, femtoscopic measurements at ALICE can be affected by non-femtoscopic effects. In particular, in pp collisions, there is a minimal rise in tails at large $k^* > 200$ MeV/c, an unknown shape of residual correlations, and normalization of the correlation can lead to deviations. To account for these effects, the modeled correlation is multiplied by a polynomial baseline to correct for the aforementioned deviations [131].

$$C_{\text{fit}}(k^*) = C_{\text{non-femto}}(k^*) C_{\text{model}}(k^*)\,. \tag{4.15}$$

Parameter		Default	Variation
Femtoscopic fit range	(MeV/c)	700	680, 760
p–d source radius	(fm)	1.08	1.02, 1.14
NN source size	(fm)	1.43	1.27, 1.59
Systematic of data		1	No of var. 17

TABLE 4.8: Systematic variations of the parameters for the femtoscopic fit of the p–d correlation function. Details are explained in the text.

A polynomial of order 3 without the linear term $C_{\text{non-femto}}(k^*) = a + b \cdot k^{*2} + c \cdot k^{*3}$ has been chosen to model the non-femtoscopic background. The parameters a, b, and c are free fit parameters in the femtoscopic fit of $C_{\text{fit}}(k)$ to the data. This particular baseline function, motivated by the requirement of a flat baseline at $k^* = 0$ MeV/c, has been used in Ref. [205]. To obtain a more constrained baseline, the final fit has been performed up to $k^* = 700$ MeV/c. It is important to note that the baseline is determined using the theoretical correlation function obtained from full-fledged calculations using the HH method, as described in Chap. 3, considering both two- and three-body interactions with the AV18 and Urbana IX potentials, as shown in Fig. 3.13. The determined baseline serves as a background for all other calculations and is assumed to be common for all cases.

Systematic of the fit

Apart from the systematic uncertainties of the measured correlation function discussed in Sec. 4.2.4, the fit procedure of the modeled correlation described in Eq. 4.15 introduces additional uncertainties. To evaluate the systematic uncertainties associated with the femtoscopic fit, all correlation functions resulting from variations of the selection criteria are individually fitted. This involves modifying several input parameters of the fit.

Considering that the measured correlation exhibits a rising tail, a relatively large femtoscopic fit range is considered, as outlined in Tab. 4.8. The femtoscopic radius obtained from the p–p correlation function is used to model the p–d correlation function for the genuine interaction in the p–d system. It is varied according to its uncertainties. Furthermore, as discussed in the following section, the strong decays of resonances with a lifetime of approximately $c\tau \sim 1$ fm, which can produce protons, may influence the source size of p–d. Therefore, the total abundance of resonances is varied by 10%, resulting in a slight increase in the uncertainties on the source size. All sources of uncertainties are listed in Tab. 4.8. The uncertainties are computed as a 68% confidence interval around the central value in the final theoretical bands.

4.4 The source

According to the definition of correlation in femtoscopy, the size of the particle-emitting source must be constrained to study the interaction between a given pair of particles. One way to achieve this is by utilizing pairs of known interactions,

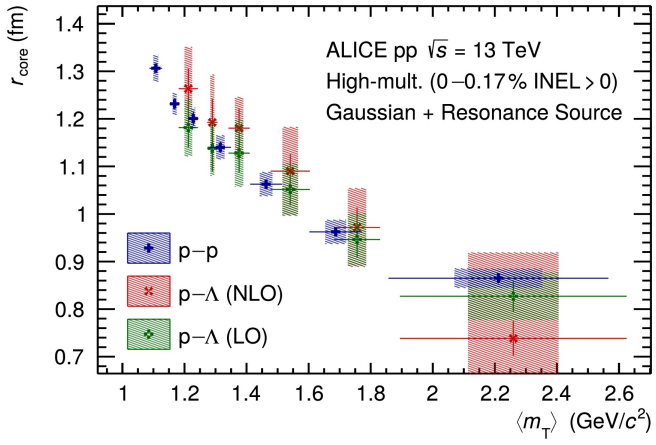

FIGURE 4.22: Femtoscopic source radius r_{core} as a function of $\langle m_{\text{T}} \rangle$ for the assumption of a Gaussian source with added resonances. The blue markers represent results from fitting the p–p correlation function with the strong AV18 potential [60], while the green (red) markers represent results from fitting the p–Λ correlation functions with the χEFT LO [206] (NLO [207]) potentials, respectively.

such as nucleon-nucleon (N-N) interactions. The baryon-baryon interaction, in particular, is well understood, making N-N pairs suitable candidates.

The investigation of the femtoscopic source in pp collisions at $\sqrt{s} = 13$ TeV is achieved by studying the source in p–p and p–Λ pairs, where the interactions are well understood [56]. The source is obtained by assuming a Gaussian distribution and performing fits to the femtoscopic correlation function in different transverse mass (m_{T}) regions of the p–p and p–Λ pairs. The transverse mass is defined as $m_T = \sqrt{k_{\text{T}}^2 + m^2}$, where k_{T} represents the pair's transverse momentum ($k_{\text{T}} = |p_{\text{T}_1} + p_{\text{T}_2}|/2$), and m is the average mass of the particle pair.

A scaling behavior of the source size has been observed for these systems, indicating a decrease in the measured source radii as the pair's transverse mass momentum (m_{T}) increases. It has also been demonstrated in Refs [56] that including all primordial protons and Λ particles, as well as those originating from strongly decaying resonances with short lifetimes ($c\tau \sim 1$ fm), in the analysis leads to corrections in the determination of the source size. After accounting for the effect of strongly decaying resonances, the source size for the Gaussian distribution is determined and referred to as r_{core}. The relationship between r_{core} and m_{T} is consistent for p–p and p–Λ pairs as shown in Figs. 4.22 and 4.23. This scaling with m_{T} holds true for all baryon-baryon pairs in pp collisions, suggesting that the same scaling can be assumed for p–d pairs. To interpolate the value of r_{core}, the behavior is parameterized as a polynomial of m_{T}, as suggested in Chapter 3 of the Ph.D. thesis by Andreas Mathis [59]

$$r_{\text{core}} = a \cdot m_{\text{T}}^{b} + c\,, \tag{4.16}$$

where the fit parameters are extracted as $a = 0.74^{+0.12}-0.05$ fm $(\text{GeV}/c^2)^{-b}$, $b = -1.85^{+0.54}-0.70$, and $c = 0.69^{+0.14}_{-0.019}$ fm. The source size for p–d pairs is obtained by using the m_{T} of the p–d pairs and Eq. 4.16. Further details on the source size for p–d pairs are provided in the following sections.

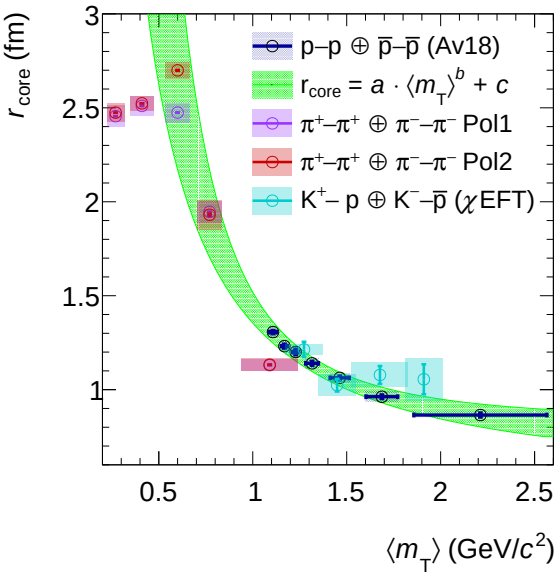

FIGURE 4.23: Figure provided by Maximilian Korwieser, preliminary results for femtoscopic source radius r_{core} as a function of $\langle m_T \rangle$ for the assumption of a Gaussian source with added resonances, for pp, π^+–π^+, and K^+–p.

4.4.1 Source for p–d pairs

For p–d pairs, the average transverse mass ($\langle m_T \rangle$) for all pairs below $k^* < 200$ MeV/c is $\langle m_T \rangle^{\text{p–d}} = 1.64$ GeV/c, correspondingly the extracted value of source size is $r_{\text{core}}^{\text{p–d}} = 0.99^{+0.05}_{-0.05}$ fm. However, approximately 64% of the total protons used to form p–d pairs are daughters of strongly decaying resonances with a lifetime of $c\tau \sim 1$ fm, as listed in Tab. 4.9, which leads to an effective increase in the source size. The impact of these resonances on the source size is evaluated by convolving the Gaussian source with an exponential distribution. The exponential tails are calculated using the kinematics of particle pairs in the event generator EPOS within the CATS framework [57]. While there are no deuterons in EPOS, the shape of the

resonances	$c\tau$(fm/c)	**fractions (%)**
Δ^{++}	1.64	21.87
Δ^{+}	1.64	14.60
Δ^{0}	1.64	7.20
$N(1440)^0$	0.56	0.91
$N(1520)^0$	1.64	1.75
$N(1680)^0$	1.52	1.15
$N(1535)^+$	1.31	1.02
$N(1440)^+$	0.56	0.91

TABLE 4.9: The relative contributions of short-lived resonances decaying into protons, according to the thermal model [208].

distribution is determined by kinematics rather than the interaction between particle pairs. Therefore, the Ξ^+ particle, whose mass is closer to that of the deuteron, is used as a proxy. The resulting source distribution for p–d can be fitted with an

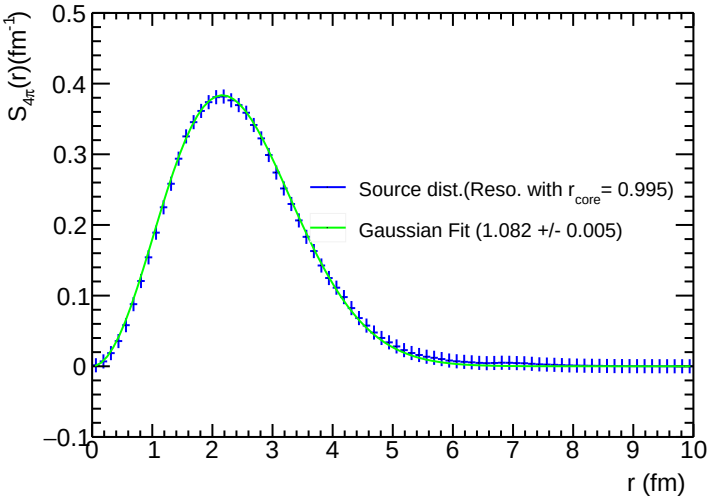

FIGURE 4.24: Source distributions for p–d pairs and their corresponding fits. The uncertainties shown in the figure are solely from the fit. However, considering the evaluation of a 10% yield variation of resonances, the final uncertainties in the source size determination are ± 0.06 fm.

effective Gaussian source radius of $r_{\text{eff}}^{\text{p–d}} = 1.08^{+0.06}_{-0.06}$ fm, as shown in Fig. 4.24. The extracted source size is used in the case of p–d system as an effective two-body system, where the distances represent the relative distance between the center-of-mass of the deuteron and proton.

4.4.2 Source for N–N pairs

The effective source size $r_{\text{eff}}^{\text{p–d}}$, discussed in Sec. 4.4.1, is suitable for two-body calculations such as the Lednický approach. However, as discussed in Chap. 3, the two-body source is not applicable in the case of three-body calculations, where distances represent the relative distances between the N-N pair. Specifically, theoretical calculations that start with an initial state proton-proton-nucleon (PPN) triplet, eventually forming a p–d system as proposed in Chap. 3, require the N-N source size $r^{\text{N–N}}$, which precisely represents the pairwise sources for the PPN triplet. To extract $r^{\text{N–N}}$, a relation is established between the average transverse momentum of the N-N pairs $k_{\text{T}}^{\text{N–N}}$ and the average transverse momentum $k_{\text{T}}^{\text{p–d}}$ of the p–d pairs. Protons and neutrons that participate in deuteron formation have an average transverse momentum that is half the transverse momentum of the deuteron, i.e., $\langle p_{\text{T}} \rangle^{\text{N}} = 1/2.0 \cdot \langle p_{\text{T}} \rangle^{\text{d}}$, where $\langle p_{\text{T}} \rangle^{\text{d}} = 0.9541^{+0.25}_{-0.25}$ GeV/c. The values of $\langle p_{\text{T}} \rangle$ for deuteron and protons are obtained by restricting $k^* < 400$ MeV/c, where a femtoscopic signal could be present. The average transverse momentum of protons that are paired with deuterons has different values, $\langle p_{\text{T}} \rangle^{\text{p}} = 0.72^{+0.18}_{-0.18}$ GeV/c. The difference between $\langle p_{\text{T}} \rangle^{\text{N}}$ and $\langle p_{\text{T}} \rangle^{\text{p}}$ gives rise to two possibilities of distances between

N-N pairs mentioned below.

$$k_{\mathrm{T}}^{\mathrm{N-p'}} = k_{\mathrm{T}}^{\mathrm{p-d}} - \frac{p_{\mathrm{T}}^{\mathrm{d}}}{4}, \tag{4.17}$$

$$k_{\mathrm{T}}^{\mathrm{N-N}} = k_{\mathrm{T}}^{\mathrm{p-d}} - \frac{p_{\mathrm{T}}^{\mathrm{p'}}}{2}, \tag{4.18}$$

where p′ and N represent the protons paired with the deuteron and the nucleon that forms the deuteron, respectively. Furthermore, using $m_T = \sqrt{k_{\mathrm{T}}^2 + m^2}$, the average transverse mass values of the N-N pairs are calculated using $\langle m_{\mathrm{T}} \rangle^{\mathrm{N-N}} = 1.12^{+0.04}_{-0.04}$ GeV/c and $\langle m_{\mathrm{T}} \rangle^{\mathrm{N-p'}} = 1.06^{+0.04}_{-0.04}$ GeV/c.

In the theoretical calculations, an average value of the source size is used for the Gaussian core is used $r_{\mathrm{core}}^{\mathrm{N-N}} = 1.35^{+0.14}_{-0.14}$ fm. Similarly, in the case of p–d, $r_{\mathrm{core}}^{\mathrm{N-N}}$ is enhanced by strongly decaying resonances that feed protons and neutrons as well. The Gaussian source is folded with an exponential distribution to account for this effect on the source size. The resulting source distribution for N-N pairs can be characterized by an effective Gaussian source radius equal to $r_{\mathrm{eff}}^{\mathrm{N-N}} = 1.43^{+0.16}_{-0.16}$ fm. This source size represents an average of distances between pp pairs and p-n pairs that form the p–d system. The femtoscopic radius $r_{\mathrm{eff}}^{\mathrm{N-N}}$ is used as an input for fitting the p–d correlation function predictions obtained from the HH method employing AV18+UIX potentials and the calculations based on the Pionless EFT at NLO.

4.5 Results and Discussion

To provide a physics interpretation of the measured p–d correlation, the results are compared with various theoretical calculations. Specifically, three-body calculations are performed using the HH formalism with AV18+UIX and NVIa+3N interaction potentials, as well as Pionless EFT at NLO. Additionally, a two-body calculation based on the Lednický approach is considered, assuming proton and deuteron as point-like distinguishable particles with asymptotic strong interaction between them. In the HH method, in addition to the full calculations, another calculation based on the Born approximation is considered by assuming no short-range strong interaction among three nucleons. The details of these models are discussed in Chap. 3. The results of these comparisons are presented in the following two subsections.

4.5.1 p–d as effective two-body system

The Lednický model has demonstrated reasonably good agreement with the data for $\mathrm{p}-\phi$, Λ–Λ $\Lambda-\Xi$, and $\mathrm{p}-\Sigma^0$ correlations [130, 209–211]. Therefore, it is natural to employ this model, assuming the deuteron as a point-like particle and treating the proton and deuteron as distinguishable particles. However, it has not yet been established whether deuterons (light nuclei) follow the same m_{T}-scaling as other baryon pairs in pp collisions at $\sqrt{s} = 13$ TeV. To establish a benchmark for m_{T} scaling and gain a better understanding of the final results of the p–d correlation using the two-body approach, a separate femtoscopic measurement was conducted within the ALICE collaboration, focusing on K^+–d particle pairs.

The K^+–d correlation measurement was performed by **Dr. Oton Vazquez Doce**[1]. As discussed in Chap. 3, the K^+–d system is relatively simple compared to the p–d system, involving non-identical particles, and the K–N interaction can be well described by the Lednický approach. The measured K^+–d correlation function is then fitted with theoretical K^+–d predictions, utilizing the source size obtained from m_T-scaling, to determine whether the K^+–d predictions accurately describe the measured K^+–d correlation function for the source size determined using m_T-scaling.

The theoretical predictions for K^+–d and p–d correlations are obtained using the Lednický approximation, considering both the Coulomb interaction and, if applicable, the strong interaction determined by the scattering parameters discussed in Chap. 3. As discussed in Sec. 4.4, the correlation function formula utilizes a Gaussian source distribution with an effective source size of $r_{\text{eff}}^{\text{p–d}} = 1.08^{+0.06}_{-0.06}$ fm for p–d pairs. For K^+–d pairs, a sum of two Gaussians is used to parameterize the source distribution, taking into account the contribution of broad resonances with significantly different decay times. The weighted average of the effective source size for K^+–d results in $r_{\text{eff}}^{K^+\text{–d}} = 1.41^{+0.03}_{-0.06}$. The final fits of the theoretical predictions to the data for K^+–d and p–d correlations are shown in Fig. 4.25. The measured

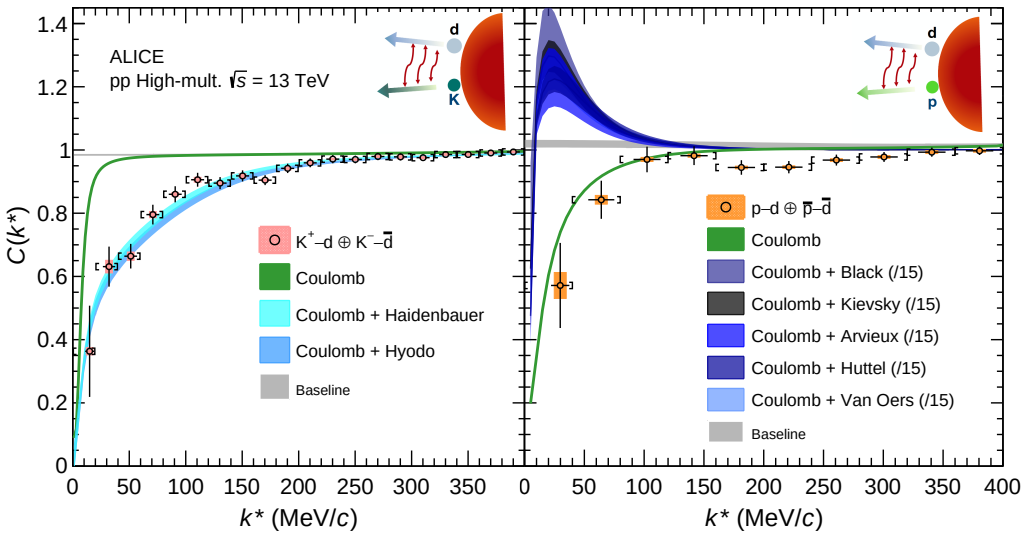

FIGURE 4.25: The final measured correlation functions K^+–d (left) and p–d (right). The data are shown by the black symbols, bars, and colored boxes representing the statistical and systematic uncertainties, respectively, and square brackets show the bin width of the measurement. Data are compared with theoretical correlation functions, shown by colored bands, obtained using the Lednický approximation. Bandwidths reflect uncertainties in the determination of the radius and residual contributions. In the case of p–d, the bands corresponding to the Coulomb + Strong interaction have been downscaled for values of $C(k)$ >1. See the text for details.

K^+–d and p–d correlation functions exhibit values below unity, indicating an

[1]Special thanks to Dr. Oton Vazquez Doce for providing K^+–d data for comparison purposes and for his invaluable contribution to the interpretation of the physics message

overall repulsive interaction. The predicted correlation functions, represented by the colored bands in Fig. 4.25, have been corrected to account for the feed-down of weak decays that feed to kaons and protons and for the residual background contributions. These corrections were applied using data-driven methods described in Sec. 4.3. The gray band near unity represents the residual background contribution. The width of the theoretical bands reflects the uncertainty propagation from experimental determinations, including source size, feed-down, and residual background. Additionally, the blue curves in Fig. 4.25 have been rescaled such that the difference between the theoretical expectation and unity is divided by 15 for positive values.

In the case of K^+–d , the measured data points lie below the prediction based on Coulomb-only interaction (indicated by the green line in Fig. 4.25), indicating the presence of a repulsive strong interaction which cannot be accounted for by the Coulomb-only interaction only. However, when the strong interaction is included using Lednický calculations using calculated scattering parameters from Prof. Hyodo and Prof. Haidenbauer of scattering parameters, an excellent agreement with the experimental correlation function is achieved within the uncertainties. This observation is particularly interesting considering that the K^+–d interaction is repulsive, as evidenced by the negative sign preceding the predicted scattering length. Since the scattering length of the K^+–d strong interaction is relatively small, around $1 - 2$ fm, the short-range structure of the interaction is expected to be repulsive in a monotonic nature for all distances. Consequently, only the asymptotic part of the strong interaction, calculated using the Lednický approach, is sufficient to describe the measured K^+–d correlation. Additionally, given that kaons are bosons while the proton and neutron that compose the deuteron are fermions, the Lednický approximation of treating the particles as point-like and distinguishable is sufficient. The properties of the deuteron as a light nucleus are effectively captured in the K^+–d scattering parameters. The agreement between the model and the data obtained for the small radius ($r_{\text{eff}}^{K^+\text{–d}} = 1.41^{+0.03}_{-0.06}$ fm) provides crucial information regarding the production of light (anti-)nuclei d($\overline{\text{d}}$), specifically demonstrating that (anti-)deuterons follow the same m_T-scaling as all other hadron pairs as shown in Fig. 4.23. This result plays a pivotal role in demonstrating the kinetic freeze-out phase of the system. It strongly supports the hypothesis that the correlated pairs of proton-neutron nucleons that form the deuteron are present at the early stages of the reaction.

The situation is quite different for the p–d system. In the Lednický approach, the theoretical correlation functions are calculated similarly as for the K^+–d system, treating protons and deuterons as distinguishable and point-like particles and considering both Coulomb and strong interactions. However, this approach leads to a significant discrepancy between the theoretical predictions and the experimental data. In the right panel of Fig. 4.25, one can observe a peak-like structure around $k^* \sim 20$ MeV/c when comparing the experimental p–d correlation with the five different blue curves.

The positive sign of the scattering parameters for p–d, as reported in Tab. 3.2, corresponds to a repulsive interaction for the quartet state ($S = 3/2$). However, for the doublet state ($S = 1/2$), the bound state ^{3}He emerges. As discussed in Chap. 3, these discrepancies can be attributed to several limitations of the Lednický

approximation in describing the p–d interaction. Firstly, the presence of the bound state and the fact that the p–d system is composed of three fermions. This raises the question of whether treating the deuteron as point-like and ignoring the internal structure, namely the nucleons, is valid. In particular, when the third proton is in close proximity to the deuteron, the antisymmetrization of the wavefunction cannot be correctly accounted for. The effective two-body approach becomes particularly vulnerable in such cases, as it no longer accurately represents the p–d system but instead a system of three nucleons.

Furthermore, the source size for p–d pairs is quite short, with $r_{\text{eff}}^{\text{p–d}} = 1.08^{+0.06}_{-0.06}$ fm. This implies that the treatment of p–d as an effective two-body system can not be appropriate. The close proximity of a proton to the deuteron brings the system into a regime where the effective two-body description breaks down.

Another important observation is that the theoretical p–d correlation function obtained with the Coulomb-only interaction (green curve in the right panel of Fig. 4.25) qualitatively resembles the shape of the experimental p–d correlation function, despite the significant scattering parameters reported in Tab. 3.2. This mismatch could be attributed to the inadequate treatment of the proper anti-symmetrization of the wavefunction, which describes the three-fermion system within the Lednický approximation, even when considering only the Coulomb interaction. Furthermore, the predictions for the p–d correlation function using the Coulomb interaction and those obtained by considering an effective two-body approach exhibit significant differences when compared to the results obtained by incorporating a proper three-body dynamics of the three nucleons, as illustrated in Fig. 3.10.

At this stage, it is evident that a comprehensive three-body calculation is necessary to interpret the p–d data accurately. This calculation should start from the three-nucleon system and asymptotically form the p–d state, taking into account the interactions among all three nucleons. By doing so, a more precise description of the p–d correlation can be obtained. A thorough study of the role of three-body dynamics in p–d systems has already been provided in Chap. 3. In the next subsection, the results of the comparison between predictions obtained from three-body calculations and the measured p–d correlation function are presented.

4.5.2 p–d as three-body system system

As discussed earlier, the calculation of the p–d correlation function assuming the proton-deuteron system as an effective two-body system using the Lednický formalism is inadequate to describe the p–d data. Therefore, a calculation incorporating the interactions and dynamics of the underlying p–(p–n) system is necessary. In this study, two distinct approaches are considered for the calculation of the p–d correlation function, taking into account the complete dynamics of the three nucleons. The first approach involves the PISA calculation based on the HH formalism, utilizing phenomenological potentials AV18 and UIX for 2N and 3N interactions, respectively, as well as for the benchmarking the calculations the NVIa+3N chiral potential was used. The second approach is based on the Pionless EFT at NLO, which provides a theoretical framework for describing low-energy nuclear physics without explicit pion degrees of freedom. The details of both the methods are described in Chap. 3.

The correlation functions from both methods are computed using Eq. 3.21, where the starting point of the calculation is the p–d wave function that accurately describes the three-body dynamics, considering the nuclear interaction represented by the underlying 2N+3N nuclear interaction. The formation of a deuteron occurs when the proton and neutron are well separated. In this formalism, the calculation of the three-body correlation function requires a source size for nucleon-nucleon pairs, denoted as $r_{\text{eff}}^{\text{N-N}}$ $1.43^{+0.16}_{-0.16}$ fm, which is determined using a data-driven approach as discussed in Sec. 4.4.2. This source size is then utilized to predict theoretical correlation functions for p–d.

Results using AV18 and UIX potentials

To study the microscopic behavior of the p–d system, the theoretical calculation employing the hyperspherical harmonics approach as illustrated in Chap. 3 is used in four different cases. The final results are shown in Figs. 4.26 and 4.27.

Firstly, two relatively simple cases are considered: (1) Coulomb-only interaction and (2) interaction considering AV18+UIX but performing the Born approximation of the p–d wave function. In the Born approximation, the correct antisymmetrization for the (pn)-p system is included, but the short-range contribution of the wave function is neglected. This calculation only accounts for the asymptotic part of the wave function, similar to the Lednický model, but it takes into consideration the microscopic structure of the p–d system. Fig. 4.26 illustrates how the orange band representing theoretical correlation function obtained from Born approximation compares to the experimental data, and the absolute value of $n\sigma$ panel demonstrates that this calculation is not accurate enough to reproduce the data, despite correctly accounting for antisymmetrization. Additionally, the green band in the same figure represents the full-fledged Coulomb-only calculation for the p–d system. The uncertainties on the bands are related to uncertainties on the source size $r_{\text{eff}}^{\text{N-N}}$ $1.43^{+0.16}_{-0.16}$ fm and the uncertainties from the baseline variations.
The second choice for the theoretical p–d correlation function is to include all possible interactions. The corresponding p–d wavefunctions have been obtained using the HH method, which takes into account all the relevant two- and three-body interactions in the p–(p–n) system, both in the short and asymptotic ranges. The nuclear interaction used in this method includes the AV18 plus the UIX and the Coulomb potential. These nuclear potentials accurately describe the three-body dynamics and are calibrated to p–d scattering observables [34, 173, 212]. Further details about the theoretical calculations can be found in Chap. 3.

The blue band in Fig. 4.27 represents calculations that consider the nuclear interaction (2N+3N) from AV18+UIX only in the $J^\pi = \frac{1}{2}^+, \frac{3}{2}^+$ partial waves relative to the p–d system. In these partial waves, the s-wave contributions dominate the small k^* region, as shown in Fig. 3.11. However, the nσ distribution for the blue band in the lower panel indicates that the calculation with even partial waves provides a moderate description of the data but fails to accurately reproduce the measured data in the small relative momentum region.
From Fig. 3.11, it is evident that for k^* larger than $\sim$ 60 MeV/c, the higher partial waves, in particular $J^\pi = 1/2^-$ and $J^\pi = 3/2^-$, start to dominate over the s-wave. Therefore, including more partial waves up to $J^\pi = \frac{7}{2}^-$ in the theoretical calculation improves the agreement between the calculation and the data, as demonstrated

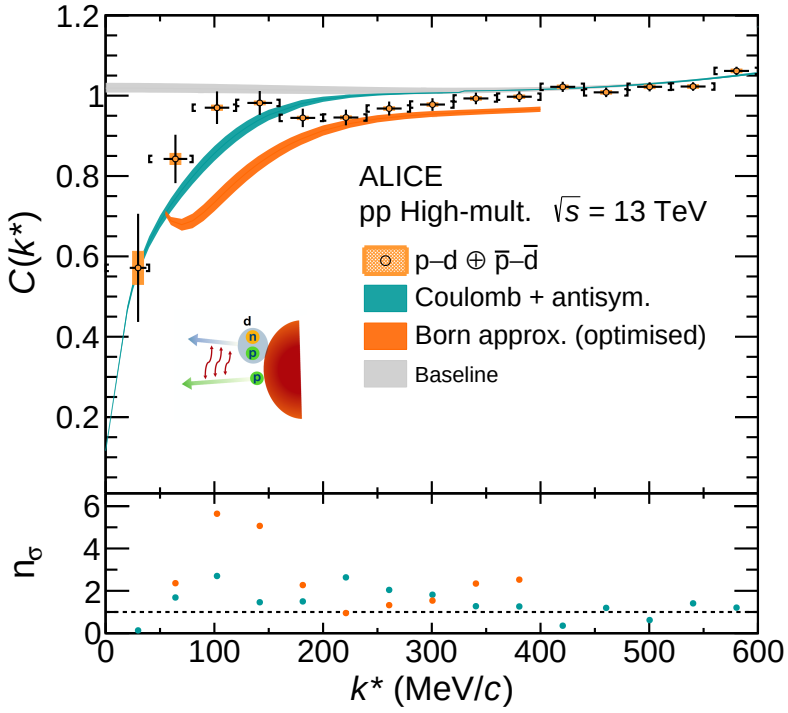

FIGURE 4.26: Measured p–d correlation function as a function of the p–d relative momentum k^*compared to three versions of a calculation of a three-body system. The experimental data are shown as circular symbols. The black vertical bars and orange boxes represent statistical and systematic uncertainties, and the square brackets show the bin width of the measurement. The non-femtoscopic background contributions are represented by the grey band of cubic baseline. The turquoise, and orange bands show the calculation obtained only with different theoretical calculations within the HH formalism. Details on the bands and calculations are discussed in the text. The lower panel shows the agreement between the theoretical calculations and the experimental data expressed in the absolute value of n_σ w.r.t to the measurement.

by the red curve in Fig. 4.27. In this case, the dominant contribution comes from the attractive p-wave, which brings the correlation function closer to the measured one. All of the three-body calculations are performed accounting for the deuteron breakup that opens at $k^* > 50$ MeV/c, which leads to a slight change in the slope of the correlation function as shown in the Fig. 3.13. However, the uncertainties of the measurement are large; therefore, any signature of such an effect is invisible. It is worth noting that the dip observed in the measured correlation function within the range $140 < k^* < 350$ MeV/c is accurately reproduced by the red band. In this k^* region, the short-range nuclear interaction becomes dominant, and its inclusion, through the incorporation of higher-order partial waves, successfully accounts for this behavior. The full calculation has been fitted to the experimental data by allowing for a multiplicative baseline (gray curve in Fig. 4.27) as a residual background. The fact that the baseline remains close to one suggests that there is little room for further modification due to a possible background contribution. The same background has been employed for the comparison of the other calculations. It can be observed that this calculation effectively reproduces the experimental data, as evidenced by the $n\sigma$ values for the red band consistently remaining close to or

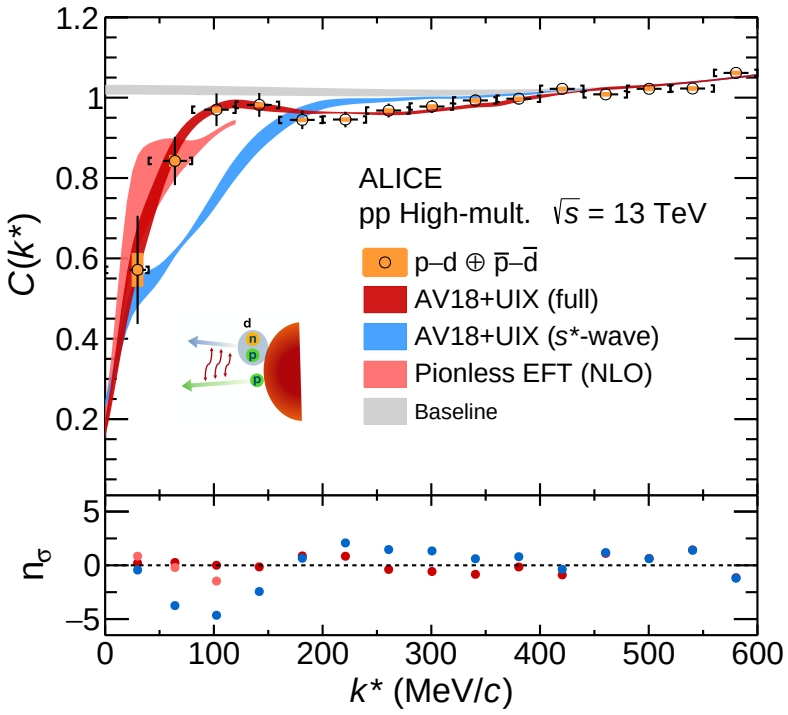

FIGURE 4.27: Measured p–d correlation function as a function of the p–d relative momentum k^* compared to three versions of a three-body system calculation. The measured p–d correlation function is the same as in Fig. 4.26. The non-femtoscopic background contributions are represented by the gray band with a cubic baseline. The red and blue bands correspond to calculations obtained using different theoretical calculations within the HH method, while the pink band represents the prediction from Pionless EFT at NLO. Details regarding the bands and calculations are discussed in the text. The lower panel illustrates the agreement between the theoretical calculations and the experimental data, expressed as the absolute value of n_σ with respect to the measurement.

below one throughout the entire energy range.

Results using χEFT potentials

In addition to the AV18+UIX potentials, the HH formalism can also be applied to NVIa+3N chiral potentials. It is interesting to compare the predicted p–d correlation function using NVIa+3N potentials, which are two- and three-nucleon potentials derived within Chiral EFT. The theoretical predictions, represented by red squared markers in Fig. 3.13, show very good agreement with the AV18+UIX calculations.

To further see the comparison of the predicted p–d correlation using the NVIa+3N potentials, a fitting procedure is performed using the same methodology as for AV18+UIX. The theoretical calculations are adjusted to fit the p–d data, and the results are shown by the pink band in Fig. 4.28. In the fitting process, the baseline (cubic without the linear term, same as in in the case of AV18+UIX) is left free and is represented by the grey band. The nσ values for the fit, indicated by the pink marker in the lower panel, consistently remain below or close to 1 for all values of k^*.

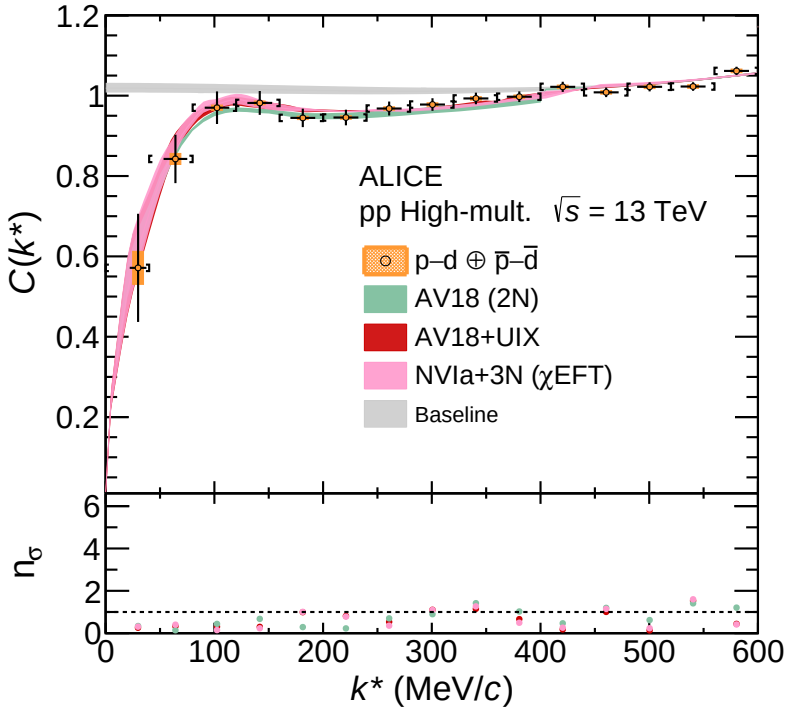

FIGURE 4.28: Comparison of the measured p–d correlation function as a function of the p–d relative momentum k^* with two versions of a three-body system calculation. The measured p–d correlation function is the same as in Fig. 4.26. The non-femtoscopic background contributions are represented by the gray band with a cubic baseline. The red, pistachio, and pink bands correspond to calculations obtained using HH formalism employing the AV18+UIX, AV18 (2N only) interaction, and χEFT NVIa+3N interaction, respectively. Details regarding the bands and calculations are discussed in the text. The lower panel illustrates the agreement between the theoretical calculations and the experimental data, expressed in nσ.

It is worth noting that the AV18+UIX potentials are realistic but phenomenological, while the NVIa+3N potentials are chiral potentials based on the symmetries of the QCD Lagrangian. Despite their different theoretical foundations, both sets of potentials provide an extremely good description of the measured p–d correlation function.

Effect of three-body force on p–d correlation

As discussed in Chap. 3, the effect of the three-body force on the p–d correlation function can be estimated by excluding the UIX potential in the HH formalism, effectively switching off the three-body force. The resulting p–d correlation function is found to be less sensitive to the three-body force, with an effect of approximately 3% for the chosen source size $r_{\text{eff}}^{\text{N-N}} = 1.43^{+0.16}_{-0.16}$ fm, as demonstrated in Fig. 3.14.

The predicted p–d correlation function without the three-body force has been used for comparison with the measurements, as shown by the pistachio-colored band in Fig. 4.28. From the figure, it can be observed that with the current statistics of the p–d correlation function, it is not possible to differentiate between the full calculation and the calculation without the three-body force.

Results from Pionless EFT

The Pionless EFT calculations, as discussed in Chap. 3, are based on a completely different theoretical framework aiming to describe the low-energy dynamics and interactions in the few nucleon systems without explicitly including pions as degrees of freedom. It employs a systematic expansion of the nuclear Lagrangian in terms of a small parameter related to the pion mass. This approach allows for a systematic and model-independent treatment of nuclear systems at low energies. In the context of p–d correlation, the Pionless EFT calculation has been performed at NLO in the EFT expansion.

It is important to note that the Pionless EFT approach is applicable only in the regime where momenta k^* are below the pion mass ($\sim$ 140 MeV). The theoretical predictions with a source size of $r_{\text{eff}}^{\text{N–N}} = 1.43^{+0.16}_{-0.16}$ fm are not fitted but rather compared using a multiplicative baseline, which is obtained by fitting the AV18+UIX predictions. The resulting p–d correlation function has been compared to the measured p–d correlation and is shown by the pink band in Fig. 4.27. In addition to the uncertainties shown in the band, the uncertainty arising from the truncation of the EFT expansion at NLO can be estimated to have a 10% effect, as discussed in Chap. 3. However, it should be noted that these uncertainties are not depicted in the band. Within the range of the applicability of this theory and considering the theoretical uncertainty associated with the method (related to the EFT expansion and variations in input parameters), a moderate agreement has been observed between the Pionless EFT calculation and the calculation using the AV18+UIX force, as well as with the measured correlation function.

4.5.3 Conclusions and remarks

The first-ever measured p–d correlation function with ALICE in pp collisions at $\sqrt{s} = 13$ TeV provides a unique indirect way to study the interaction in the system of three nucleons. The observed correlation indicates an overall repulsive strong interaction within the considered system. The measured p–d correlation function cannot be described by the effective two-body approach, which is determined from the baryon-baryon m_{T}-scaling in pp collisions at $\sqrt{s} = 13$ TeV. The fact that deuterons also follow the m_{T}-scaling, which is common for all baryon pairs in the pp collisions, is established by comparing the measured K^+–d correlation with the theoretical predictions obtained from the Lednický approach and employing the source size $1.41^{+0.03}_{-0.06}$ fm determined using the m_{T}-scaling.

The measured p–d correlation function provides valuable insights into the role of three-nucleon dynamics in the p–d system, especially at short distances. It is particularly sensitive to the proper treatment of the Pauli principle between the three nucleons and the short-range two-body interaction of the nucleons in the p–(p–n) system. Hence, relying solely on the Lednický model is inadequate to describe the p–d correlation function accurately. Furthermore, utilizing a microscopic Born-approximated wave function, which appropriately incorporates the antisymmetrization of the three nucleons but only captures the asymptotic features of the wave function, fails to accurately depict the observed data.

For the first time, it has been observed that an accurate description of the p–d correlation function can only be achieved through comprehensive three-body

calculations. These calculations consider the single nucleons as active degrees of freedom and properly account for the intricate dynamics of the three nucleons and their nuclear interactions in different partial waves. Two very different calculations based on the HH method and Pionless EFT at NLO have been tested, and compatible results were found. Despite utilizing different frameworks, both of these calculations incorporate the full three-body dynamics. In previous studies, similar measurements have been conducted [196–199]. The interpretation of the hadron-deuteron and deuteron-deuteron correlations in these studies relied on the Lednický calculation and a source radius value larger than that observed for other hadron-hadron pairs in the same collision system. It is important to note that the current study provides evidence that interpreting the p–d correlation function using any effective two-body calculation based solely on the asymptotic strong interaction is insufficient. Therefore, the misinterpretation of the data in these previous studies could have been due to the absence of accurate microscopic calculations specifically addressing the p–d system.

Furthermore, the comparison of the measured p–d correlation function with the one computed employing the full-fledged p–d calculation, which excludes genuine three-body interactions in the nuclear Hamiltonian, suggests that the current precision of the measurement is not sufficient to distinguish the contributions of the three-body force in the p–d correlation function. In the present inclusive p–d measurement, the effective source size is $r_{\text{eff}}^{\text{N-N}} = 1.43^{+0.16}_{-0.16}$ fm, and a precision below 3% is required to observe the effect of the three-nucleon interaction. This effect increases up to 4-5 percent when the calculation is carried out for $r_{\text{eff}}^{NN} = 1$ fm, as demonstrated in Fig. 3.14. Although the current measurement cannot provide such a small precision, there is a lot of room for improvement in statistics. Currently, the p–d correlation function has a total of 3850 pairs and antipairs below$k^* < 200$ MeV/c in 1 billion events. However, this statistic is expected to increase by over two orders of magnitude in Run 3 [213]. A preliminary estimate on the number of p–d pairs and antipairs below $k^* < 200$ MeV/c using the offline triggering system for the current data taken during Run 3 is $\sim 3.2 \times 10^5$ and for $\overline{\text{p}}$–$\overline{\text{d}}$ pairs, it is $\sim 3.1 \times 10^5$. These numbers are expected to increase by a factor of 2-3, resulting in 4 to 5 orders of magnitude more statistics. Such a large increase in statistics would enable for triggering of the pairs with large m_T values, allowing for the selection of small radii [56, 214]. Future measurements will provide an opportunity to study the effects of the three-nucleon interaction in the p–d correlation function.

To conclude, the studies on final state interactions using deuterons combined with other hadrons in pp collisions at the LHC offer a unique opportunity to investigate the strong interaction in three-body systems. This approach can be extended to systems such as Λ/Σ-d or Λ_c-d, enabling exploration of three-baryon systems in the strange and charm sectors.

Chapter 5

Light nuclei production studies

This chapter discusses the deuteron production in hadronic collisions via coalescence. In particular, the chapter has been divided into two sections: Sec. 5.1 is dedicated to the study of the coalescence mechanism based on the purely theoretical approach for (anti-)deuterons and (anti-)^{3}He. While Sec. 5.2 discusses the production of (anti-)deuterons within the coalescence approach using the Wigner formalism and different event generators. The findings of the studies in this chapter are summarised in the publications [76, 215].

5.1 Coalescence Model

As discussed in Sec. 1.8 the production yield of the light nuclei could also be described by the coalescence models. In the framework of coalescence, nucleons produced close in phase space during hadronic/nuclear collisions can coalesce into light nuclei [216, 217]. The coalescence process, where the light nuclei production is given by the probability that any A number of nucleons will coalesce into the nucleus of mass number $A = Z + N$, where Z and N are the numbers of protons and neutrons. The coalescence factor $\mathcal{B}_A$ is

$$E_A \frac{d^3N_A}{dp_A^3} = \mathcal{B}_A \left(E_{p,n} \frac{d^3N_{p,n}}{dp_{p,n}^3} \right)^A \Bigg|_{\vec{p}_p = \vec{p}_n = \frac{\vec{p}_A}{A}}, \tag{5.1}$$

where $p_{p,n}$ and $E_{p,n}$ are momenta and energies of the proton and neutron. In most experimental facilities, neutrons are not measured because of limitations in the reconstruction of neutron tracks. Therefore, experiments report relatively easily observable quantities such as $\mathcal{B}_2(p)$ the ratio of deuteron yield over the squared of unpolarised proton yield $p^0 \frac{dN}{d^3p}$ this ratio is also known as the coalescence factor for deuteron defined as

$$\mathcal{B}_2(p) = \frac{P_d^0 \frac{dN_d}{d^3P_d}}{\left(p^0 \frac{dN}{d^3p} \right)^2}, \tag{5.2}$$

where p^0 and P_d^0 are momenta of proton and deuteron. In a very simple case, neglecting the isospin of nucleons, the coalescence parameter can be given in the following expression

$$\mathcal{B}_A = \left(\frac{4\pi}{3} p_0^3 \right)^{A-1} \frac{m_A}{m_{\mathrm{p}}^{\mathrm{A}}}. \tag{5.3}$$

Here $\mathcal{B}_A$ is a function of the nucleus mass number, denoted by A, as well as the masses of the nucleus and proton, denoted by m_A and m_p, respectively. The parameter p_0 represents the maximum relative momentum at which coalescence can occur. In Chap. 1, it is discussed that the coalescence factor $\mathcal{B}_A$ in a simple coalescence approach is assumed to be independent of the momentum and size of the object relative to the length of homogeneity during particle emission. This simple picture works approximately well in small systems such as pp and p–Pb collisions [78, 95, 218–220]. For example, in Fig. 5.1, the calculated $\mathcal{B}'_2$ (red band), which is the multiplicity-

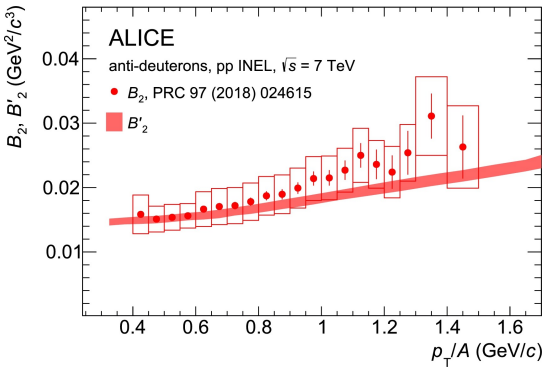

FIGURE 5.1: Comparison of coalescence factor $\mathcal{B}'_2$ obtained using the simple coalescence approach for of anti-deuterons as a function of the transverse momentum per nucleon p_T/A with the experimental data for $\mathcal{B}_2$ measured in inelastic pp collisions at $\sqrt{s} = 7$ TeV [95].

integrated value as a function of p_T is in agreement with the measured deuteron spectra (red boxes) in inelastic pp collisions at $\sqrt{s} = 7$ TeV [95]. However, the simple coalescence approach cannot describe the measured data when the size of the system is large. In particular, in Pb–Pb collisions the measured $\mathcal{B}_2$ [79] does not agree with simulations (green and red lines for two different tunes of the event generator) if we consider a simple coalescence approach in the AMPT event generator [221] as shown in Fig. 5.2. In the measured data, a strong decrease with centrality is observed for $\mathcal{B}_A$ [77, 79, 222, 223], cannot be explained by the simple coalescence scenario. The advanced coalescence models by [224, 225] consider this effect by using the source size and the relative momentum of the nucleons. In this section, the goal is to study advanced coalescence using a Wigner formalism approach to obtain the production probability of a nucleus. The overlap of the Wigner function with the phase-space distributions of the nucleons gives the latter.

5.1.1 Quantum mechanical treatment

In the coalescence formalism, nuclear clusters are often treated as point-like objects with no internal structure. Intuitively, this is not realistic; for example, the (anti-) deuteron has an rms radius of ∼2 fm, comparable to the size of the homogeneity radii in pp and Pb–Pb collisions. Therefore, proper inclusion of finite-size effects and the internal substructure of the cluster via the cluster wavefunction in the description of the coalescence process is required. In other words, the coalescence approach requires a quantum mechanical treatment.

In high-energy hadronic collisions, an excited state is produced. Such a high-excitation state (HXS) is extremely dynamic and at very high-temperature T∼156 MeV [13, 226]. Quantum mechanically, such an excited state can be characterized

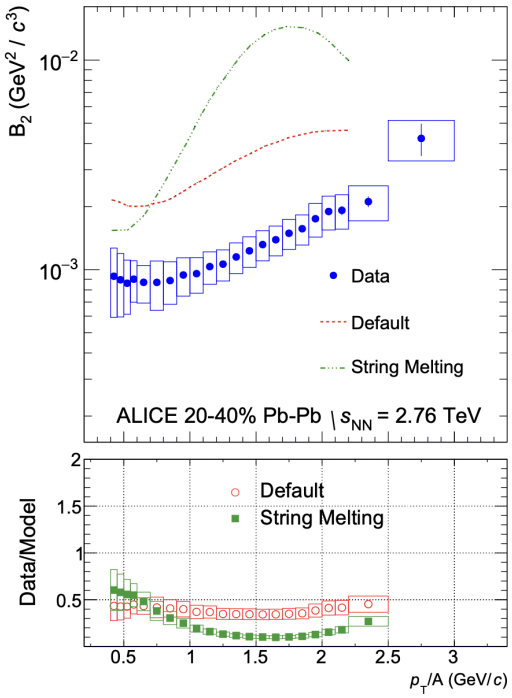

FIGURE 5.2: Comparison of coalescence factor $\mathcal{B}_2$ obtained using the simple coalescence in the simulation AMPT model [221] for deuterons as a function of the transverse momentum per nucleon p_T/A with the experimental data for $\mathcal{B}_2$ measured in inelastic Pb–Pb collisions at $\sqrt{s} = 2.76$ TeV [79].

by the density matrix $\hat{\rho}_{\mathrm{HXS}}$. The density matrix $\hat{\rho}_{\mathrm{HXS}}$ describes the quantum state of the strongly interacting system. In this case, it is a system of two nucleons, which includes all the information about the position and momentum of the two nucleons. According to quantum mechanics, a projection of a non-relativistic state such as light nuclei on $\hat{\rho}_{\mathrm{HXS}}$ allows one to calculate the probability density to find that non-relativistic state in the HXS. Since the binding energy of the light nuclei is $B_A \sim 2-3$ MeV for A = 2, 3 is much smaller than the temperature of hadronic collisions, the relative motion of the nucleons in the light nuclei is very small and non-relativistic quantum mechanics can describe their coalescence in a bound state. On the other hand, in hadronic collisions, the measured momenta of the light nuclei are few GeVs, and therefore the motion of light nuclei in the laboratory frame is relativistic. At first, the concept is applied to deuteron production since d as a proton-neutron bound state is the simplest light nuclei.

Deuteron formation in the density matrix formalism

In the laboratory frame, the deuteron as a two-particle bound state with momentum P_d is defined as $|\psi_d\rangle$. Here, the wavefunction ψ_d is written as the following expression

$$\psi_d(\vec{x}_n, \vec{x}_p) = e^{-\vec{P}_d \cdot \vec{X}} \phi_d(\vec{r}), \tag{5.4}$$

where $\vec{x}_n$ and $\vec{x}_p$ are the coordinates of the neutron and proton. $\vec{X} = (\vec{x}_n + \vec{x}_p)/2$ is the coordinate of the deuteron center-of-mass (COM) frame and $\vec{r} = \vec{x}_n - \vec{x}_p$ is the relative distance of the nucleons in the COM frame. $\phi_d(\vec{r})$ is the deuteron cluster wavefunction. Normalisation of $\phi_d(\vec{r})$ is performed with $\int d^3r|\phi_d(\vec{r})^2| = 1$.

The probability of deuteron production is then given by taking the projection of the deuteron state on the two-particle density matrix $\hat{\rho}_{\mathrm{HXS}}$

$$\begin{aligned}\frac{dN_d}{d^3P_d} &= (2\pi)^{-3} \left\langle \psi_{P_d} \left| \hat{\rho}_{\mathrm{HXS}} \right| \psi_{P_d} \right\rangle \\ &= \frac{S_d}{(2\pi)^3} \int d^3x_n \int d^3x_p \int d^3x'_n \int d^3x'_p \\ &\quad \psi^*_{P_d}\left(x'_n, x'_p\right) \psi_{P_d}\left(x_n, x_p\right) \rho_2\left(x'_n, x'_p; x_n, x_p; t_f\right) ,\end{aligned} \tag{5.5}$$

where the reduced density matrix of the proton-neutron state $\hat{\rho}_{\mathrm{HXS}}$ is given by $\rho_2(x'_n, x'_p; x_n, x_p; t_f)$. S_d is a normalization factor that accounts for the spin and isospin of the p-n state. In this formalism, t_f stands for the freeze-out[1] time of the collision fireball, and it is assumed to be well defined. The density matrix ρ_2 is specified for given t_f. In the collision fireball, the exact form of the two-nucleon density matrix ρ_2 is unknown. Therefore, it is assumed to be factorised in single-particle density matrices [226]

$$\rho_2\left(x'_n, x'_p; x_n, x_p; t_f\right) = \rho_n\left(x'_n, x_n, ; t_f\right) \rho_p\left(x'_p, x_p; t_f\right) . \tag{5.6}$$

The factorisation of ρ_2 into ρ_n and ρ_p implies that at the time of freeze-out the produced proton and neutron are uncorrelated. Factorisation of the density matrix can be avoided by using the Wigner function of the proton-neutron state from the event generator, as discussed in Sec. 5.1.1. However, to perform the analytic calculation of Eq. 5.5, the factorisation of ρ_2 as defined in Eq. 5.6. The single particle density matrix is given in [227, 228] and reads as

$$\rho_i\left(x, x'; t\right) = \int \frac{d^3k}{(2\pi)^3} e^{i\vec{k}(\vec{x}'-\vec{x})} f_i^W\left(\vec{k}, \frac{\vec{x}+\vec{x}'}{2}; t\right) , \tag{5.7}$$

where $i = n, p$ and f_i^W are the Wigner functions for the proton and neutron. Substituting ρ_2 in terms of ρ_n and ρ_p in Eq. 5.5, defining $\vec{R} = (\vec{x}_p + \vec{x}_n + \vec{x}'_p + \vec{x}'_n)/4$ as the COM coordinate of p and n, and $\vec{r} = (\vec{x}_p + \vec{x}'_p)/2 - (\vec{x}_n + \vec{x}'_n)/2$ as the classical relative coordinate between p and n results into the following relation

$$\begin{aligned}\frac{dN_d}{d^3P_d} =& \frac{S_d}{(2\pi)^3} \int d^3R \int \frac{d^3q}{(2\pi)^3} \int d^3r\, \mathcal{D}_d(\vec{q}, \vec{r}) \times \\ & f_n^W\left(\frac{\vec{P}_d}{2} + \vec{q}, \vec{R} + \frac{\vec{r}}{2}; t_f\right) f_p^W\left(\frac{\vec{P}_d}{2} - \vec{q}, \vec{R} - \frac{\vec{r}}{2}; t_f\right) .\end{aligned} \tag{5.8}$$

The term $\mathcal{D}_d(\vec{q}, \vec{r})$ is the Wigner transformation of the deuteron wavefunction and is defined as

$$\mathcal{D}_d(\vec{r}, \vec{q}) = \int d^3\xi\, e^{-i\,\vec{q}\cdot\vec{\xi}}\, \phi_d(\vec{r} + \vec{\xi}/2)\, \phi_d^*(\vec{r} - \vec{\xi}/2) . \tag{5.9}$$

[1] In the collision geometry, the freeze-out means all the produced particle momenta are well defined.

It is a quasi-probability distribution of the deuteron state, and hence the normalization is imposed as

$$\int d^3r \int \frac{d^3q}{(2\pi)^3}\mathcal{D}_d(\vec{r},\vec{q}) = \int d^3r|\phi_d(\vec{r})|^2 = 1$$
$$\int d^3q\mathcal{D}_d(\vec{r},\vec{q}) = (2\pi)^3|\phi_d(\vec{r})|^2\,. \tag{5.10}$$

As suggested in Ref. [13], a further simplification can be made in the evaluation of Eq. 5.8 by omitting the dependence on $\pm q$ in $f^W_{n,p}$. Such an approximation is expected to be valid up to a $\sim$10% accuracy for Pb-Pb collisions and has been studied by R. Scheibl et al. [226]. However, this approximation is not necessary when using an event generator and $\mathcal{D}_d(\vec{r},\vec{q})$ is properly treated. This is discussed in Sec. 5.1.1. A Fourier transform of $|\phi_d(\vec{r})|^2$ can be defined as

$$|\phi_d(\vec{r})|^2 = \int d^3k\,\frac{e^{i\vec{k}\cdot\vec{r}}}{(2\pi)^3}\mathcal{D}(\vec{k}) \implies \mathcal{D}(\vec{k}) = \int d^3r\,e^{-i\vec{k}\cdot\vec{r}}|\phi_d(\vec{r})|^2\,. \tag{5.11}$$

$\mathcal{D}(\vec{k})$ contains information on the substructure of d and the interaction among the nucleons. $\mathcal{D}(\vec{k})$ can be computed for different sets of wavefunctions. Substituting $\mathcal{D}(\vec{k})$ in Eq. 5.8 results in the following relation

$$\frac{dN_d}{d^3P_d} \approx \frac{S_d}{(2\pi)^6}\int d^3q\,\mathcal{D}(\vec{q})\int d^3R\int d^3r\,e^{i\vec{q}\cdot\vec{r}}f_n^W\left(\frac{\vec{P}_d}{2},\vec{R}+\frac{\vec{r}}{2};t_f\right)f_p^W\left(\frac{\vec{P}_d}{2},\vec{R}-\frac{\vec{r}}{2};t_f\right). \tag{5.12}$$

In Eq. 5.5, ρ_2 is projected onto the density matrix $|\psi_d\rangle\langle\psi_d|$ of an energy eigenstate $|\psi_d\rangle$, which represents the wavefunction of a free deuteron. This ensures the energy conservation. However, if we factorize ρ_2 into ρ_n and ρ_p, and replace the Wigner functions f_i^W of ρ_i in Eq. 5.12 with classical distribution functions of on-shell nucleons, it would violate energy conservation due to the binding energy of the deuteron [225]. In reality, two freely propagating nucleons cannot coalesce into a deuteron without the involvement of a third body. To address this issue, several attempts have been made to ensure energy conservation in the coalescence process by incorporating scattering with a third body [229]. The interaction of the neutron and proton with the third body causes one of the nucleons to become slightly off-shell. As a result, the slightly off-shell nucleon can combine with an on-shell nucleon to form a deuteron without violating energy conservation, as demonstrated in [226]. However, in the present study, the Wigner functions are not replaced by classical distributions, and thus Eq. 5.12 remains valid. Deuterons produced at the LHC are relativistic, so Eq. 5.12 needs to be Lorentz invariant, and a Lorentz factor γ_d can be multiplied to the left-hand side (LHS) of the equation. However, on the right-hand side, the computation becomes challenging for a relativistically expanding collision fireball, as different parts of the emission volume are relativistic with respect to each other, making the spatial integral $\int d^3R$ non-trivial [230]. Moreover, the exact freeze-out time t_f is not known, and the expanding collision geometry affects the common freeze-out surface as well as the common freeze-out temperature $t_f = t_f(\sim R)$.

Eq. 5.12 is valid only in the framework of a non-relativistic QM calculation of the Lorentz non-invariant quantity $\frac{dN_d}{d^3P_d}$. To evaluate a Lorentz-invariant deuteron

yield $\frac{dN_d}{d^3P_d}$, integration on the differential yield over the emission regions in an expanding fireball is required, as discussed in Ref. [13].

$$\frac{d}{d^3R}\left(\frac{dN_d}{d^3P_d}\right) \approx S_d \frac{d}{d^3R}\int d^3q \mathcal{D}(\vec{q})\mathcal{K}_2\left(\frac{\vec{P}_d}{2},\vec{q}\right), \tag{5.13}$$

Using $\mathcal{K}_2(P,q)$ function, which accounts for the case when proton and neutron are correlated

$$\mathcal{K}_2(P,q) = \frac{1}{(2\pi)^6}\int d^3R \int d^3r\, e^{i\vec{q}\cdot\vec{r}}\, f_1^W\left(\vec{P},\vec{R}+\frac{\vec{r}}{2};t_f\right) f_1^W\left(\vec{P},\vec{R}-\frac{\vec{r}}{2};t_f\right), \tag{5.14}$$

The differential yield gives the emission of deuterons per differential volume element d^3R. The definition of $\mathcal{B}_2$ still holds for yields in a volume element d^3R. To evaluate $\mathcal{B}_2$ from Eq. 5.2, one also needs to calculate the production yield $\left(p^0\frac{dN}{d^3p}\right)^2$ of two protons which are uncorrelated in the phase-space. The calculation of two proton yields will be discussed in the next Sec. 5.1.1.

Yields of correlated and uncorrelated protons pairs

The single-proton yield $p^0\frac{dN}{d^3p}$ can be easily calculated using the relation of the density matrix of HXS $\hat{\rho}_{\mathrm{HXS}}$ and the single-proton state $|\psi_p\rangle$.

$$\begin{aligned}\frac{dN}{d^3p} =& (2\pi)^{-3}\left\langle\psi_p\left|\hat{\rho}_{\mathrm{HXS}}\right|\psi_p\right\rangle \\ =& \frac{S_p}{(2\pi)^3}\int d^3x\int d^3x' \psi_p^*\left(x'\right)\psi_p\left(x\right)\rho_p\left(x';x,;t_f\right)\end{aligned} \tag{5.15}$$

Substituting the single-particle density matrix ρ_p from Eq. 5.7 into Eq. 5.15 gives

$$\frac{dN}{d^3p} = \frac{S_p}{(2\pi)^6}\int d^3k \int d^3x\int d^3x' \psi_p^*\left(x'\right)\psi_p\left(x\right) e^{i\vec{k}(\vec{x}'-\vec{x})} f_p^W\left(\vec{k},\frac{\vec{x}+\vec{x}'}{2};t_f\right). \tag{5.16}$$

Further simplification results in the following expression for the yield of a single particle

$$\frac{dN}{d^3p} = \frac{S_p}{(2\pi)^3}\int d^3x f_p^W\left(\vec{p},\vec{x};t_f\right). \tag{5.17}$$

Eventually, the product of yields of two protons is given by

$$\left(\frac{dN}{d^3p}\right)^2 = \frac{S_p^2}{(2\pi)^6}\int d^3x f_p^W\left(\vec{p},\vec{x};t_f\right)\int d^3x f_p^W\left(\vec{p},\vec{x};t_f\right) = S_p^2\cdot\mathcal{A}_2\left(p_p,p_p\right), \tag{5.18}$$

where function $\mathcal{A}_2\left(p_p,p_n\right)$ is defined as

$$\mathcal{A}_2\left(p_1,p_2\right) = \frac{1}{(2\pi)^6}\int d^3x f_1^W\left(\vec{p}_1,\vec{x};t_f\right)\int d^3x f_1^W\left(\vec{p}_2,\vec{x};t_f\right). \tag{5.19}$$

The Wigner function for protons f_p^W is not known, and therefore, it is not possible to calculate Eq. 5.18 analytically.

The process of coalescence is a final-state interaction and therefore, the two-particle yields can be related to the femtoscopic definition of correlation in the

experiments given as

$$C_2(P,q) = \frac{p_1^0 p_2^0 \frac{dN}{d^3p_1 d^3p_2}}{\left(p_1^0 \frac{dN}{d^3p_1}\right)\left(p_2^0 \frac{dN}{d^3p_2}\right)}. \tag{5.20}$$

The numerator $p_1^0 p_2^0 \frac{dN}{d^3p_1 d^3p_2}$ and denominator of Eq. 5.20 describe the yields of the protons which are correlated and uncorrelated respectively. The single particle yields in the denominator of Eq. 5.20 can be written by substituting from Eq. 5.18. The numerator is the yield of the correlated proton-proton pairs and can be computed in the same way as in the case of a single particle. As shown in Ref. [13], the correlated yield of two protons starting from a spin-symmetric wavefunction $|\psi(p_1,p_2)\rangle$ that describes the motion of two free-propagating protons

$$\psi^s_{\vec{p}_1,\vec{p}_2}(\vec{x}_1,\vec{x}_2) = \frac{1}{\sqrt{2}} e^{2i\vec{P}\cdot\vec{X}} \left(e^{i\vec{q}\cdot\vec{r}/2} - e^{-i\vec{q}\cdot\vec{r}/2}\right). \tag{5.21}$$

The total yield which is not Lorentz invariant, is then given by

$$\frac{dN^s}{d^3p_1 d^3p_2} = S_2^s \left(\mathcal{A}_2(p_1,p_2) - \mathcal{K}_2(P,q)\right), \tag{5.22}$$

where S_2^s is the spin factor for the symmetric state, $\vec{P} = (\vec{p}_1 + \vec{p}_2)/2$, $\vec{q} = \vec{p}_1 - \vec{p}_2$, $\mathcal{A}_2(p_1,p_2)$ is the uncorrelated part, and $\mathcal{K}_2(P,q)$ accounts for the quantum correlations between nucleons. Similar steps can be followed for the antisymmetric state with $S_2^a = S_2^s/3$. The total spin-unpolarised yield is given by

$$\frac{dN}{d^3p_1 d^3p_2} = (S_2^s + S_2^a)\mathcal{A}_2(p_1,p_2) + (S_2^a - S_2^s)\mathcal{K}_2(P,q), \tag{5.23}$$

$$= (S_2^s + S_2^a)\mathcal{A}_2(p_1,p_2)\left[1 + \frac{(S_2^a - S_2^s)\mathcal{K}_2(P,q)}{(S_2^s + S_2^a)\mathcal{A}_2(p_1,p_2)}\right]. \tag{5.24}$$

The factor $\mathcal{C}_2^{\rm PRF}(\vec{P},\vec{q}) \equiv \mathcal{K}_2/\mathcal{A}_2$ can be interpreted as a two proton correlation in phase-space [13], where the superscript PRF refers to the pair rest frame. Using uncorrelated and correlated yields of two protons from Eqs. 5.18 and 5.24 in Eq. 5.20 gives rise to the following relation.

$$C_2(P,q) = 1 - \frac{S_2^s - S_2^a}{S_2^s + S_2^a} \mathcal{C}^{\rm PRF}{}_2(P,q). \tag{5.25}$$

The single particle yield can be rewritten using $\mathcal{C}_2^{\rm PRF}$

$$\left(p^0 \frac{dN}{d^3p}\right)^2 = \frac{p_1^0 p_2^0 \frac{dN}{d^3p_1 d^3p_2}}{1 - \frac{S_2^s - S_2^a}{S_2^s + S_2^a}\mathcal{C}_2^{\rm PRF}(P,q)}. \tag{5.26}$$

The femtoscopic correlation can be then related to the $\mathcal{B}_2$ by substituting Eq. 5.26 into the Eq. 5.2

$$\mathcal{B}_2(p) = \frac{P_d^0 \frac{dN_d}{d^3P_d}}{p_1^0 p_2^0 \frac{dN}{d^3p_1 d^3p_2}} \times \left(1 - \frac{S_2^s - S_2^a}{S_2^s + S_2^a}\mathcal{C}_2^{\rm PRF}(P,q)\right). \tag{5.27}$$

Considering yield per unit of differential volume d^3R leads to Lorentz-invariant observable

$$\frac{d}{d^3R}\frac{dN}{d^3p_1 d^3p_2} = \frac{d}{d^3R}\left(d^3R\,(S_2^s + S_2^a)\mathcal{A}_2\,(p_1, p_2) + (S_2^a - S_2^s)\mathcal{K}_2(P, q)\right)\,. \tag{5.28}$$

Plugging in the differential yields for protons from Eq. 5.28 and for deuterons from Eq. 5.13 into Eq. 5.27 leads to the final results presented in Ref. [13]. The definition of $\mathcal{B}_2$ is then obtained as $\mathcal{C}_2^{\mathrm{PRF}}$

$$\mathcal{B}_2(p) \approx \frac{3}{2m}\int d^3q\mathcal{D}(\vec{q})\mathcal{C}_2^{\mathrm{PRF}}(\vec{p}, \vec{q})\,, \tag{5.29}$$

where, m is the proton mass $\mathcal{C}_2(\vec{P}, \vec{q}) \equiv \mathcal{C}_2^{\mathrm{PRF}}(\vec{P}, \vec{q}) \equiv \mathcal{A}_2/\mathcal{K}_2$ for the small relative momentum $\vec{q}$ of pairs of nucleons.

In this work, the definition of $\mathcal{C}_2^{\mathrm{PRF}}$ is obtained from a Gaussian source model [226]

$$\mathcal{C}_2^{\mathrm{PRF}} = e^{-R_\perp^2\vec{q}_\perp^2 - R_\parallel^2\vec{q}_l^2}\,. \tag{5.30}$$

Generally, for an extended region of homogeneity, the source size depends on two components: $R_\perp$ and $R_\parallel$ and momenta $\vec{q}_l$ and $\vec{q}_\perp$ are the components of $\vec{q}$ parallel to the beam axis and the transverse direction. However, for femtoscopic studies in small collision systems such as pp collisions, $R_\perp$ and $R_\parallel$ are assumed to be the same and equivalent to R which is known as the length of homogeneity. From now on, in this study $\mathcal{C}_2^{\mathrm{PRF}}$ is a Gaussian distribution defined as

$$\mathcal{C}_2^{\mathrm{PRF}} = e^{-R^2q^2}\,. \tag{5.31}$$

The final expression for $\mathcal{B}_2$ incorporating the source size R is given by

$$\mathcal{B}_2(R) \approx \frac{3}{2m}\int d^3q\mathcal{D}(\vec{q})e^{-R^2q^2}\,. \tag{5.32}$$

Unlike the simple coalescence model described by the Eq. 5.3. The coalescence factor in $\mathcal{B}_2$ in Eq. 5.32 depends on the source size R as well as the internal structure of the deuteron described by $\mathcal{D}(\vec{q})$. The dependence of $\mathcal{B}_2$ on deuteron wavefunction is discussed in the following section.

5.1.2 Role of deuteron wavefunction

The deuteron wavefunction $\phi_d(\vec{r})$ plays a crucial role in determining the coalescence factor $\mathcal{B}_2$ for deuteron. The Wigner density of the deuteron $\mathcal{D}(\vec{q})$ in Eq. 5.29 is defined as

$$\mathcal{D}(\vec{q}) = \int d^3r\, e^{-i\vec{q}\cdot\vec{r}}|\phi_d(\vec{r})|^2\,, \tag{5.33}$$

where $\phi_d(\vec{r})$ is the deuteron wavefunction. In this section, different predictions for $\mathcal{B}_2$ have been obtained as a function of the source radius R starting from Eq. 5.29 and using different hypotheses of $\phi_d(\vec{r})$.

Gaussian wavefunction

It is the simplest wavefunction of the deuteron that describes the internal structure of the deuteron as a spherical harmonic oscillator with the size parameter d = 3.2 fm

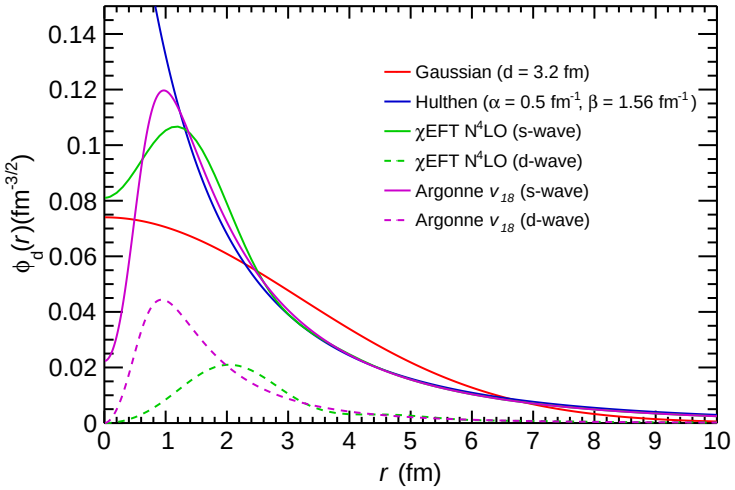

FIGURE 5.3: Deuteron wavefunctions using Gaussian(red), Hulthén potential (blue) [226], χEFT N^{4}LO s-wave and p-wave in solid and dashed green curves [32], from Argonne v_{18} NN potential [31], s-wave and p-wave in solid and dashed pink curves respectively.

($r \equiv |r|$) and has been commonly used in many works [13, 226, 231, 232]. The Gaussian wavefunction reads as

$$\phi_d(\vec{r}) = \frac{e^{-\frac{r^2}{2d^2}}}{(\pi d^2)^{3/4}}, \tag{5.34}$$

where $d = 3.2$ fm is the radius of the nucleus. The distribution as function of r is shown by the red curve in Fig. 5.3. The corresponding inverse Fourier transform of $\phi_d(\vec{r})$ is

$$\mathcal{D}(\vec{q}) = e^{-\frac{q^2 d^2}{4}}. \tag{5.35}$$

The expression for $\mathcal{B}_2$ as a function of the source radius R is obtained in the following

$$\begin{aligned}\mathcal{B}_2(R) =& \frac{6\pi}{m}\int dq\, q^2\, e^{-\frac{q^2d^2}{4}-R^2q^2} \\ =& \frac{3\pi^2}{2m\left[R^2+\left(\frac{d}{2}\right)^2\right]^{\frac{3}{2}}}.\end{aligned} \tag{5.36}$$

The coalescence factor $\mathcal{B}_2(R)$ using the Gaussian wavefunction as a function of R is shown in Fig. 5.4 (a), together with the other predictions for B_2. As shown in Ref. [13], Eq. 5.36 can also be generalized for a nuclear cluster with mass number A assuming that the nuclear cluster can be described by a wavefunction which is a product of Gaussians. This approach is rather simple, an exact calculation of $\mathcal{B}_A$ may require more sophisticated many-body wavefunctions calculated by solving using the many-body Schrödinger's equation. However, as a simple approach, one can use the nuclear cluster wavefunction as suggested in [13]. The internal wavefunction of the cluster can be used as a symmetric Gaussian function of the normalized Jacobi

coordinates $\vec{\xi}_n, n = 1, \ldots, A-1$

$$\phi_A\left(\vec{\xi}_1, \ldots, \vec{\xi}_{A-1}\right) = \frac{\exp\left(-\frac{\sum_{i=1}^{A-1}\vec{\xi}_i^2}{2d_A^2}\right)}{A^{\frac{3}{4}}\left(\pi d_A^2\right)^{\frac{3(A-1)}{4}}}, \tag{5.37}$$

where the Jacobi coordinate is defined as

$$\vec{\xi}_n = \frac{n}{\sqrt{n^2+n}}\left(\vec{r}_{n+1} - \frac{1}{n}\sum_{m=1}^{n}\vec{r}_m\right). \tag{5.38}$$

d_A is cluster size with A nucleons $d_A = r_{\text{rms}}\sqrt{\frac{2A}{3(A-1)}}$, r_i is the Cartesian coordinate of the i^{th} nucleon and r_{rms} the cluster rms charge radius. The coalescence parameter for a cluster of A nucleons and size d_A is then given as

$$\mathcal{B}_A(R) = \frac{2J_A+1}{2^A\sqrt{A}}\frac{1}{m^{A-1}}\left[\frac{2\pi}{R^2+(d_A/2)^2}\right]^{\frac{3}{2}(A-1)}, \tag{5.39}$$

where J_A is the total spin of the nucleus. For ^{3}He, $A = 3$ in Eq. 5.39 is used to calculate the theoretical prediction for B_3, shown in Fig. 5.4 (b).

Hulthén wavefunction

The second hypothesis used in this study is a Hulthén wavefunction. On the one hand, the choice of the Gaussian wavefunction is technically advantageous since the length of the vector $\vec{r}$ removes angular degrees of freedom and allows for a analytic evaluation, but it is an approximate wavefunction assuming d as a Harmonic Oscillator. The Hulthén wavefunction is obtained from the Hulthén potential which is very similar to the Yukawa theory of interaction among nucleons and is favoured by low-energy scattering experiments [233] and it provides a good description of the ground state of the deuteron.

$$\phi_d(r) = \sqrt{\frac{\alpha\beta(\alpha+\beta)}{2\pi(\alpha-\beta)^2}}\frac{e^{-\alpha r} - e^{-\beta r}}{r}, \tag{5.40}$$

where $\alpha = 0.2$ fm^{-1} and $\beta = 1.56$ fm^{-1} are parameters taken from Ref. [226]. The shape of the wavefunction is shown in the blue curve in Fig. 5.3. The analytical form of $\mathcal{D}(\vec{q})$ using this wavefunction is challenging as it has $|\vec{r}|$ in the exponents.

$$\mathcal{D}(\vec{q}) = \frac{2\alpha\beta(\alpha+\beta)}{(\alpha-\beta)^2}\frac{\left(\tan^{-1}\left(\frac{q}{\alpha}\right) - \tan^{-1}\left(\frac{q}{\beta}\right)\right)}{q}. \tag{5.41}$$

The corresponding expression for B_2 is given as

$$\begin{aligned}\mathcal{B}_2(R) =& \frac{12\pi\alpha\beta(\alpha+\beta)}{m(\alpha-\beta)^2}\int dq\, q\left(\tan^{-1}\left(\frac{q}{\alpha}\right) - \tan^{-1}\left(\frac{q}{\beta}\right)\right)e^{-R^2q^2} \\ =& \frac{3\pi^2}{R^2}\frac{\alpha\beta(\alpha+\beta)}{(\alpha-\beta)^2}\Big[e^{4\alpha^2R^2}\text{erfc}(2\alpha R) - 2e^{(\alpha+\beta)^2R^2}\text{erfc}((\alpha+\beta)R) \\ &+ e^{4\beta^2R^2}\text{erfc}(2\beta R)\Big],\end{aligned} \tag{5.42}$$

where erfc is the complementary error function. The coalescence factor $\mathcal{B}_2$ for this wavefunction is shown by the blue curve in Fig. 5.4 (a).

χEFT wavefunction

A more sophisticated deuteron wavefunction is obtained from calculations by χEFT (N^{4}LO). It is based on [32], and the normalisation is defined in [234]. A cutoff at $\Lambda_c = 500$ MeV is used. The deuteron wavefunction is

$$\psi_d(\vec{r}) = \frac{1}{\sqrt{4\pi}\, r} \left[u(r) \, + \, \frac{1}{\sqrt{8}}\, w(r)\, S_{12}(\hat{r}) \right] \chi_{1m} \,, \tag{5.43}$$

where $u(r)$ and $w(r)$ are radial wavefunctions, provided in numerical values. The values of $u(r)$ and $w(r)$ are shown in Fig. 5.3, $S_{12}(\hat{r}) = 3\vec{\sigma}_1 \cdot \vec{r}\, \vec{\sigma}_2 \cdot \vec{r} - \vec{\sigma}_1 \cdot \vec{\sigma}_2$ is the spin tensor, and χ_{1m} is a spinor. Furthermore, the deuteron substructure has been considered by defining $\vec{r}_1$ the proton coordinates, $\vec{r}_2$ the neutron coordinates, $\vec{r} = \frac{\vec{r}_1 - \vec{r}_2}{2}$, and $\vec{R} = \frac{\vec{r}_1 + \vec{r}_2}{2}$.
The spin averaged density for deuteron is

$$\begin{aligned} |\psi_d(\vec{r})|^2 \, &= \frac{1}{3} \sum_{m=0,\pm1} \psi_d(\vec{r}_1)^\dagger \psi_d(\vec{r}_2) \\ &= \frac{1}{4\pi\, r_1\, r_2} \Big\{ u(r_1)u(r_2) + \, w(r_1)w(r_2) \frac{1}{2} \left[3\, (\hat{r}_1 \cdot \hat{r}_2)^2 - 1 \right] \Big\} \,. \end{aligned} \tag{5.44}$$

Ignoring extension of the deuteron further simplifies Eq. 5.44 $\vec{r} = 0 \implies \vec{r}_1 = \vec{r}_2$. Such an assumption is required because of the way the framework is developed. As a further extension of this study, Eq. 5.44 has been treated explicitly in Sec. 5.1.1. The spin-averaged density of the deuteron can be expressed as

$$|\psi_d(r)|^2 = \frac{1}{4\pi\, r^2} \left[u^2(r) \, + \, w^2(r) \right] . \tag{5.45}$$

Using Eq. 5.29 and Eq. 5.33, the final results of $\mathcal{B}_2$ for χEFT have been obtained as

$$B_2(R) = \frac{6\pi}{m} \int_0^{\Lambda_c} dq \int_0^{\infty} dr\, q \, \left[u(r)^2 \, + \, w(r)^2 \right] \, \frac{\sin(qr)}{r}\, e^{-R^2 q^2} . \tag{5.46}$$

The χEFT wavefunction is given in numerical values, forcing Eq. 5.46 to have at most 1 numerical integration. However, $\int dq$ can still be performed, as $u(r)$ and $w(r)$ are independent of $\vec{q}$.

$$\begin{aligned} \mathcal{B}_2(R) = &\frac{3\pi}{mR^2} \int_0^{\infty} \frac{dr}{r} \, \left[u^2(r) \, + \, w^2(r) \right] \, \Big\{ e^{-\Lambda_c^2 R^2} \sin(\Lambda_c r) \\ &+ \, \frac{\sqrt{\pi} r}{4R}\, e^{-\frac{r^2}{4R^2}} \, \left[\mathrm{erf}\left(\frac{ir + 2R^2\Lambda_c}{2R} \right) \, - \, \mathrm{erf}\left(\frac{ir - 2R^2\Lambda_c}{2R} \right) \right] \Big\} \,. \end{aligned} \tag{5.47}$$

The final result of $\mathcal{B}_2$ using the χEFT wavefunctions as a function of source size is shown in the green curve in Fig. 5.4 (a).

Combination of two Gaussians

This particular Ansatz for the deuteron wavefunction does not originate from a theoretical calculation based on NN potential. However, it is obtained by fitting to the

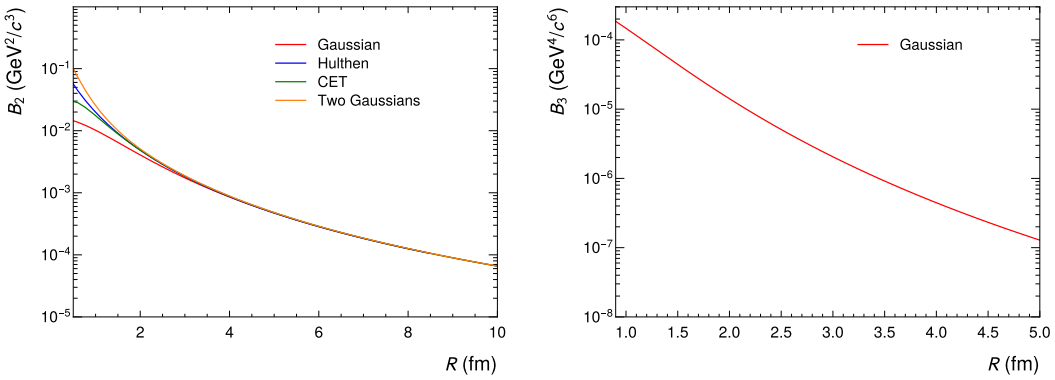

(a) (b)

FIGURE 5.4: Coalescence factor $\mathcal{B}_2$ (a) and $\mathcal{B}_3$(b) as a function of the source radius R for different wavefunctions (see text).

Hulthén wavefunction [235], sum of two Gaussians allows one to removes $\vec{r} \cdot \vec{\xi}$, the angle dependency in the Hulthén wavefunction. It is advantageous for the analytic calculations.

$$\phi_d(r) = \pi^{-3/4} \left[\frac{\Delta^{1/2}}{d_1^{3/2}} e^{-r^2/(2d_1^2)} + e^{i\alpha} \frac{(1-\Delta)^{1/2}}{d_2^{3/2}} e^{-r^2/(2d_2^2)} \right], \tag{5.48}$$

where α is the phase factor, $\Delta = 0.581$, $d_1 = 3.979$ fm and $d_2 = 0.890$ fm. The corresponding deuteron density is given by

$$|\phi_d(r)|^2 = \pi^{-3/2} \left[\frac{\Delta}{d_1^3} e^{-r^2/d_1^2} + \frac{1-\Delta}{d_2^3} e^{-r^2/d_2^2} \right]. \tag{5.49}$$

B_2 can be hence written as

$$\mathcal{B}_2(R) = \frac{24\pi^{5/2}}{m} \int_0^\infty dq \int_0^\infty dr \, |\phi_d(r)|^2 \, \sin(qr) \, r \, q \, e^{-R^2 q^2}, \tag{5.50}$$

and after integrating over q and r, one obtains

$$\mathcal{B}_2(R) = \frac{3\pi^{3/2}}{2mR^3} \left[\Delta \left(1 + \frac{d_1^2}{4R^2} \right)^{-3/2} + (1-\Delta) \left(1 + \frac{d_2^2}{4R^2} \right)^{-3/2} \right]. \tag{5.51}$$

This function is shown in Fig. 5.4 (a), together with the other predictions for B_2. Finally, all theoretical predictions for $\mathcal{B}_2$ as a function of the radius of the source R are shown in Fig. 5.4 (a). At large values of the source radius, they all show the same trend, which follows a volume term $\sim \frac{1}{R^3}$. In contrast, for small values of the source size, the different $\mathcal{B}_2$ predictions obtained using different deuteron wavefunctions differ significantly, with a maximum spread of around a factor 10. For ^{3}He, this study is limited to a Gaussian cluster wavefunction due to the lack of three-body wavefunctions and a density matrix formulation for $A = 3$. A prediction of $\mathcal{B}_3$ for ^{3}He is obtained using a Gaussian cluster wavefunction and is shown in Fig. 5.4 (b). A recent study by Ref. [232] used the density matrix of three nucleons to calculate $\mathcal{B}_3$ for ^{3}He, which could potentially be useful for predicting $\mathcal{B}_3$ for different wavefunctions.

Source size for nuclear coalescence

In order to obtain a theoretical prediction comparable to the measured $\mathcal{B}_A$, the calculation of the coalescence factor must be provided with the source size measured from the experiments. In the past few years, coalescence studies [13, 15, 231, 232, 235, 236] have used source size determined by the two-particle correlation measurements [56, 204] to predict $\mathcal{B}_A$ for $A = 2$ and 3. However, in all of these studies, the authors compared the prediction using a single m_{T}-integrated source size value with the measured $\mathcal{B}_A$. In this work, we perform a m_{T}-differential study of the coalescence parameter $\mathcal{B}_A$ for $A = 2$ and 3 using the source size. As discussed in Sec. 4.4, the source radius has been measured in HM pp collisions at $\sqrt{s} = 13$ TeV by ALICE using p–p and p–Λ correlations as a function of the mean transverse mass $\langle m_{\mathrm{T}} \rangle$ of the pair [56]. In Ref. [56], two different measured source radii as a function of $\langle m\mathrm{T} \rangle$ are reported, namely $r_{\mathrm{effective}}$ and r_{core}. The difference between the two is that r_{core} takes into account the contributions coming from the short-lived strong decay of resonances ($c\tau \sim 1$ fm) by subtracting them. Moreover, it has been shown in [56] that r_{core} is universal, as it describes p–p and p–Λ correlations simultaneously. Therefore, in this work, r_{core} is used. The difference between the values of r_{core} and r_0 is rather small: the corresponding $\mathcal{B}_2$ using $r_{\mathrm{effective}}$ is on average 10% smaller in the low p_{T}, as shown in the Fig. 5.5 $\mathcal{B}_2$ using r_0 and r_{core} for Hulthén wave function and for Gaussian wavefunction. During this study it was assumed that only primordial nucleons can participate in the light nuclei formation and therefore the values of r_{core} have been used as source size.

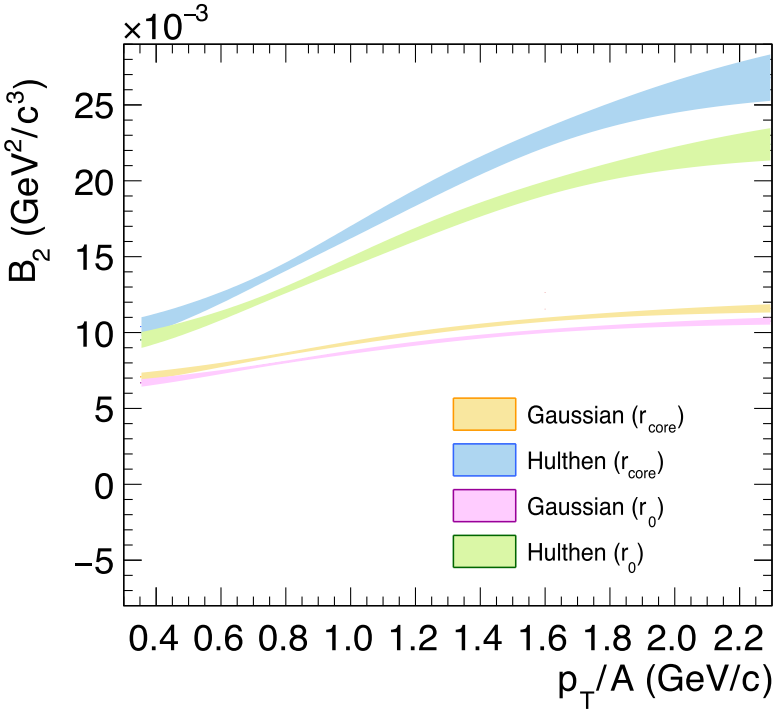

FIGURE 5.5: Comparison of theoretical predictions for the coalescence factor $\mathcal{B}_2$ as a function of p_{T}/A for (anti-)deuterons, considering the measured $r$core and r_0 from Ref. [56] as input source sizes for different wavefunctions: Gaussian (yellow and magenta) and Hulthén (blue and green).

To have a functional relation between $\langle m_{\mathrm{T}} \rangle$ and r_{core}, the data in [56] are parameterized using a function as $r_{\mathrm{source}}(\langle m_{\mathrm{T}} \rangle) = c_0 + \exp(c_1 + c_2 \langle m_{\mathrm{T}} \rangle)$, with c_i being free parameters, to map the transverse mass to the source radius. Since the measured yields of (anti-) d and (anti-) ^{3} He have been reported as functions of p_{T}/A for different high multiplicity intervals [76], a comparable $\mathcal{B}_A$ is then obtained as functions of p_{T} instead of m_{T}. To extract the values of $\mathcal{B}_2$ as a function of p_{T}, the value of p_{T} corresponding to m_{T} is taken from $m_{\mathrm{T}} = \sqrt{m_{\mathrm{p}}^2 + (p_{\mathrm{T}}/A)^2}$, where m_{p} is the mass of the proton. Furthermore, the rms radius of deuteron and ^{3}He [231] are used as input parameter in the Gaussian wavefunctions.

Finally, the predictions of $\mathcal{B}_A$ for deuteron and for ^{3}He have been compared with the data and are shown in the left and right panels of Fig. 5.12 respectively. For $\mathcal{B}_2$, only the HM I class corresponding to $\langle \mathrm{d}N_{\mathrm{ch}}/\mathrm{d}\eta \rangle_{|\eta_{\mathrm{lab}}|<0.5} = 35.8 \pm 0.5$, is considered. The multiplicity in this class is compatible with the multiplicity of pp events in which the femtoscopic study has been performed. The width of the bands represents the uncertainty propagated from the measurement of the source radius.

5.2 Coalescence as afterburner

In this section, we propose an alternate strategy to coalescence studies by introducing and analyzing in detail a coalescence afterburner. This new approach takes into account a realistic particle emission and space-momentum correlations of nucleons and allows for event-by-event simulation of deuterons and antideuterons in high-energy hadronic collisions. This study primarily focuses on pp collisions, as they are extremely relevant for the searches for antinuclei in cosmic rays as potential signatures for dark matter particles. We test and validate our model by analyzing deuteron production in high-multiplicity pp collisions at $\sqrt{s} = 13$ TeV, which is the only available data sample with measurements of deuteron yields and baryon source radius as a function of the deuteron kinematic properties [56, 76]. The size of the emitting source is a key ingredient in this study, enabling the development of a parameter-free model for deuteron production.

5.2.1 Wigner approach

The production of light nuclei can be studied using the Wigner formalism in event generators [237]. In this thesis, the coalescence framework has been extended to 4-dimensional space-time in order to incorporate the time component in the pair rest frame. The focus is solely on deuteron formation in coalescence considering several hypotheses for the deuteron wavefunction. Assuming the interactions between nucleon pairs and the surrounding particles are subdominant due to the low particle density and the ultrarelativistic motion of nucleons, wherein particles rapidly separate from each other, resulting in interactions primarily occurring at small relative momenta [49] and the Lorentz-invariant yield of deuterons with momentum $\vec{P}$ can be written as

$$\begin{aligned} \gamma \frac{\mathrm{d}N_{\mathrm{d}}}{\mathrm{d}^3P} = & \frac{S_{\mathrm{d}}}{(2\pi)^4} \int \mathrm{d}^4x_1 \int \mathrm{d}^4x_2 \int \mathrm{d}^4x_1' \int \mathrm{d}^4x_2' \\ & \times \Psi^*_{\mathrm{d},P}\left(x_1', x_2'\right) \Psi_{\mathrm{d},P}\left(x_1, x_2\right) \rho_{1,2}\left(x_1, x_2; x_1', x_2'\right) . \end{aligned} \tag{5.52}$$

Note that in this derivation, three vectors are represented with an arrow ($\vec{a}$), and four vectors are represented in italic (a). Here, $\Psi_{\mathrm{d},P}\left(x_1, x_2\right)$ is the bound-state Bethe-Salpeter amplitude that describes the deuteron [238], $\rho_{1,2}\left(x_1, x_2; x_1', x_2'\right)$ is the density matrix of the two nucleons that describes the dynamics and interaction of the two-nucleon state, γ is the Lorentz factor for the deuteron, and $S_\mathrm{d} = 3/8$ is a factor that takes into account the spin-isospin statistics of the two-nucleon state, which form a deuteron spin state ($S = 1$).

Similar to [13, 232], the two-nucleon density matrix is assumed to factorize into single-nucleon densities

$$\rho_{1,2}\left(x_1, x_2; x_1', x_2'\right) = \rho_1\left(x_1'; x_1\right)\rho_1\left(x_2'; x_2\right) , \tag{5.53}$$

where $\rho_1\left(x_1'; x_1\right)$ and $\rho_1\left(x_2'; x_2\right)$ are single nucleon density defined in terms of the Wigner function f_1^W [232]

$$\rho_1\left(x, x'\right) = \int \frac{\mathrm{d}^4k}{(2\pi)^4}\, e^{ik(x'-x)}\, f_1^W\left(k, \frac{x+x'}{2}\right) . \tag{5.54}$$

The deuteron Bethe-Salpeter amplitude can be defined as the product of the deuteron's motion and spread, expressed in the following relation

$$\Psi_\mathrm{d}\left(x_1, x_2\right) = e^{-iP\cdot r_\mathrm{d}}\,\varphi_\mathrm{d}(r) , \tag{5.55}$$

where r_d is the space-time position of the deuteron, P its four-momentum, and $\varphi_\mathrm{d}(r)$ is the deuteron spatio-temporal wavefunction. The coordinates can be transformed defining $c_{1,2} = \left(p_{1,2}\,P\right)/P^2$, where the pair total momentum is $P = p_1 + p_2 \equiv 2p$. In general, the dependence of the amplitude $\Psi_{\mathrm{d},P}$ on the pair total momentum and center of mass coordinate $r_\mathrm{d} = c_1x_1 + c_2x_2$ can be factored out from the dependence on the relative momentum $q = c_2p_1 - c_1p_2$ and relative position $r = x_1 - x_2$ [232]. Using the relative coordinates as defined above in Eq. 5.52 leads to the following expression for the deuteron yield

$$\begin{aligned}\gamma\,\frac{\mathrm{d}N_\mathrm{d}}{\mathrm{d}^3P} =& \frac{S_\mathrm{d}}{(2\pi)^4}\int \mathrm{d}^4r_\mathrm{d}\int\frac{\mathrm{d}^4q}{(2\pi)^4}\int \mathrm{d}^4r\,\tilde{\mathcal{D}}(q,r)\\ &\times f_1^W\left(P/2+q, r_\mathrm{d}+\frac{r}{2}\right) f_1^W\left(P/2-q, r_\mathrm{d}-\frac{r}{2}\right),\end{aligned} \tag{5.56}$$

where $\tilde{\mathcal{D}}(q,r)$ is the relativistic internal Wigner density of deuteron described by the interaction in p–n pair and is given as

$$\tilde{\mathcal{D}}(q,r) = \int \mathrm{d}^4\xi\, e^{iq\xi}\,\varphi_\mathrm{d}\left(r+\frac{\xi}{2}\right)\varphi_\mathrm{d}^*\left(r-\frac{\xi}{2}\right) . \tag{5.57}$$

From Sec. 5.1, it has been established that it is non-trivial to solve Eq. 5.5 analytically without factorizing ρ_2 into the single nucleon density matrices. However, the event generator can replace the two-nucleon density matrix with the corresponding two-body Wigner function [237], where the two-body Wigner function can be used as numerical output from the event generator. The two-body Wigner function is defined as

$$W_{np}\left(P/2+q, P/2-q, r, r_\mathrm{d}\right) = f_1^W\left(P/2+q, r_\mathrm{d}+\frac{r}{2}\right) f_1^W\left(P/2-q, r_\mathrm{d}-\frac{r}{2}\right) . \tag{5.58}$$

Using the smoothness and equal-time approximations, as done in [232], in the pair rest frame (PRF), one obtains $P = (M, \vec{0})$, $q = (0, \vec{q})$ and $r = (t^*, \vec{r}^*)$, and the Bethe-Salpeter amplitude becomes independent of time in the non-relativistic limit.

$$\Psi\left(q, r\right) \rightarrow \Psi\left(\vec{q}, \vec{r}^*\right). \tag{5.59}$$

Here, $t^* = t_1^* - t_2^*$ represents the relative time of appearance for the nucleons, where $t_{1,2}^*$ are the local times for individual nucleons in PRF. Due to the time independence of $\Psi\left(q, r\right)$, the integral over the four-momentum q becomes an integral over the momentum $\vec{q}$

$$\gamma \frac{\mathrm{d}N_\mathrm{d}}{\mathrm{d}^3P} = \frac{S_\mathrm{d}}{(2\pi)^7} \int \mathrm{d}^4r \int \mathrm{d}^4r_\mathrm{d} \int \mathrm{d}^3q\, \mathcal{D}(\vec{q}, \vec{r}) W_{np}\left(\vec{P}/2 + \vec{q}, \vec{P}/2 - \vec{q}, r, r_\mathrm{d}\right). \tag{5.60}$$

Accordingly, the deuteron Wigner density $\mathcal{D}(\vec{q}, \vec{r})$ is defined in a three-dimensional space. The time variable $r_\mathrm{d}^0 = t_f$ represents the time of kinetic freeze-out, i.e. the moment in which the mass momenta of the final-state particles are well defined[2]. To perform the integral over the time component, the space-time integral in Eq. 5.60 is separated and can be written as follows

$$\begin{aligned}\gamma \frac{\mathrm{d}N_\mathrm{d}}{\mathrm{d}^3P} =& \frac{S_\mathrm{d}}{(2\pi)^7} \int \mathrm{d}^3r \int \mathrm{d}^3r_\mathrm{d} \\ &\times \int dt^* \int dt_f \int \mathrm{d}^3q\, \mathcal{D}(\vec{q}, \vec{r})\, W_{np}\left(\vec{P}/2 + \vec{q}, \vec{P}/2 - \vec{q}, \vec{r}, \vec{r}_\mathrm{d}, t^*, t_f\right).\end{aligned} \tag{5.61}$$

As mentioned earlier, the value of t_f is fixed and the same for all particles. Consequently, the particle yield is constant at the time of chemical freeze-out. This allows us to omit the integration over t_f. Additionally, in this study, time equalization is performed using the PRF $2\pi\delta(t^* - t_\mathrm{eq})$, and by choosing $t_\mathrm{eq} = 0$, we have $t^* = 0$. Therefore, integrating over t^* in Eq. 5.61 eliminates the dependence on t^*, resulting in a genuine three-dimensional equation.[3]

$$\gamma \frac{\mathrm{d}N_\mathrm{d}}{\mathrm{d}^3P} = \frac{S_\mathrm{d}}{(2\pi)^6} \int \mathrm{d}^3r \int \mathrm{d}^3r_\mathrm{d} \int \mathrm{d}^3q\, \mathcal{D}(\vec{q}, \vec{r})\, W_{np}\left(\vec{P}/2 + \vec{q}, \vec{P}/2 - \vec{q}, \vec{r}, \vec{r_\mathrm{d}}\right), \tag{5.62}$$

where the Wigner function for the deuteron $\mathcal{D}_d(\vec{r}, \vec{q})$ is completely determined by the internal structure of the deuteron as defined in Eq. 5.9 and while other part W_np can be factorized assuming a factorization of space and momentum dependence of the proton–neutron [235].

$$W_{np} = H_{np}(\vec{r}_\mathrm{n}, \vec{r}_\mathrm{p})\, G_{np}(\vec{P}_d/2 + \vec{q}, \vec{P}_d/2 - \vec{q}). \tag{5.63}$$

By taking this step, the problem transitions from a purely quantum treatment to a semi-classical treatment. Additionally, spatial correlations in the emission of protons and neutrons are disregarded by a factorization of H_{np} as

$$H_{np}(\vec{r}_\mathrm{n}, \vec{r}_\mathrm{p}) = h(\vec{r}_\mathrm{n})\, h(\vec{r}_\mathrm{p}). \tag{5.64}$$

[2]In common practice, the particle yield is evaluated at the time of freeze-out t_f in a collision. In the context of light nuclei, this is a subtle assumption since at freeze-out, there are possible break-ups due to scattering in the phase space. However, despite this, the assumption seems to work well, as reported in [13].

[3]From here on, the theoretical framework is constructed in a three-dimensional space. All the vector quantities and their norms are represented with an arrow ($\vec{a}$) and in italic (a), respectively, unless specified otherwise.

Choosing a Gaussian Ansatz for $h(r)$ leads to

$$H_{np}(\vec{r},\vec{r}_d;r_0) = \frac{1}{(2\pi\, r_0)^3}\, \exp\left(-\frac{r^2+r_d^2}{4\, r_0^2}\right), \tag{5.65}$$

where r_0 is the size of the emission source of two nucleons. Possible space-momentum correlations at the hadron production point are considered in the source model, as discussed in [215].

For each pair of proton and neutron from the event generator to coalesce into a deuteron, a quasi-probability [4] $\mathcal{P}(r_0,q)$ is assigned which is a convolution of the spatial distribution of nucleons with the deuteron Wigner function.

$$\mathcal{P}(r_0,q) = \int d^3r_d \int d^3r\, H_{np}(\vec{r},\vec{r}_d;r_0)\; \mathcal{D}_d(\vec{r},\vec{q})\,. \tag{5.66}$$

Eqs. 5.65 and 5.66 are formulated assuming a Gaussian emission source for nucleons, where the mean value r_μ of the two-particle distance is related to the source size r_0 through the equation $r_\mu = \frac{4}{\sqrt{\pi}}\, r_0$. However, in event generators, the distribution of distances often exhibits a tail due to short-lived strongly decaying resonances, which is generally not Gaussian [56]. Therefore, to account for this, r_μ is evaluated from a fit to the distribution, and then the source size r_0 is determined using their relation $r_0 = \frac{\sqrt{\pi}}{4} r_\mu$.

Finally, the momentum distribution for d in Eq. 5.62 can be written as

$$\gamma \frac{d^3N_d}{dP_d^3} = \frac{S_d}{(2\pi)^6} \int d^3q\, \mathcal{P}(r_0,q) G_{np}(\vec{P}_d/2+\vec{q},\vec{P}_d/2-\vec{q}). \tag{5.67}$$

To predict deuteron spectra, two terms are required: $\mathcal{P}(r_0,q)$ and $G_{np}(\vec{P}_d/2+\vec{q},\vec{P}d/2-\vec{q})$. The former is determined theoretically and incorporates the internal structure of the deuteron via the deuteron wavefunction. Although the latter cannot be calculated exactly, it can be estimated using simulations where the space-momentum coordinates are known. In a sense, $G_{np}(\vec{P}_d/2+\vec{q},\vec{P}_d/2-\vec{q})$ represents a differential yield of the pair of nucleons in phase space.

5.2.2 Wigner density distributions for deuteron

The Wigner functions $\mathcal{D}d(\vec{r},\vec{q})$ for the deuteron are calculated using Eq. 5.9, where $\vec{r}$ and $\vec{q}$ are distance and relative momentum vectors respectively. In this study, four different wavefunctions, namely Gaussian, Hulthén, χEFT potentials at N^{4}LO, and Argonne $v18$ potential, are used to describe the internal structure of the deuteron. The two Gaussian wavefunctions (Ref. [235]) are disregarded as they are obtained by fitting to the Hulthén wavefunction. The corresponding Wigner densities for all considered wavefunctions are calculated in the following approach.

[4] Mathematically, this expression does not satisfy the condition of normalization to unity which is essential for a probability distribution, as $\mathcal{P}(r_0,q) \in [0,8]$. The values range from 0 to 8 because of the definition of the Wigner function, in particular, $\mathcal{D}_d(\vec{0},\vec{0}) = 8$, regardless of the choice of a normalized wavefunction.

Gaussian wavefunction

The Gaussian wavefunction for deuterons is defined in Eq. 5.34. It is the most simple definition of the wavefunction to evaluate $\mathcal{D}_d$ analytically.

$$\begin{aligned}\mathcal{D}_d(\vec{r},\vec{q}) &= \frac{1}{(\pi d^2)^{3/2}} \int d^3\xi\, e^{-i\vec{q}\cdot\vec{\xi}}\, e^{-\frac{|\vec{r}+\vec{\xi}/2|^2}{2d^2}}\, e^{-\frac{|\vec{r}-\vec{\xi}/2|^2}{2d^2}} \\ &= \frac{4}{\sqrt{\pi} d^3 q} \int d\xi\, \xi\, \sin(q\xi)\, e^{-\frac{4r^2+\xi^2}{4d^2}} \\ &= 8\, e^{-\frac{d^4q^2+r^2}{d^2}}.\end{aligned} \tag{5.68}$$

Subsequently, $\mathcal{P}(r_0, q)$ is calculated as

$$\mathcal{P}(r_0,q) = \left(\frac{d^2}{4r_0^2+d^2}\right)^{3/2} 8\, e^{-d^2q^2}. \tag{5.69}$$

The distribution of $\mathcal{P}(r_0, q)$, as shown in Fig. 5.6 reveals interesting characteristics. It is observed that the distribution of $\mathcal{P}(r_0, q)$ is significant for small relative momentum values ($q < 100$ MeV/c) and small source sizes ($r_0 < 2$ fm). This indicates that there is a higher probability of coalescence into deuterons for proton-neutron pairs with small relative momenta and close proximity (small source size).

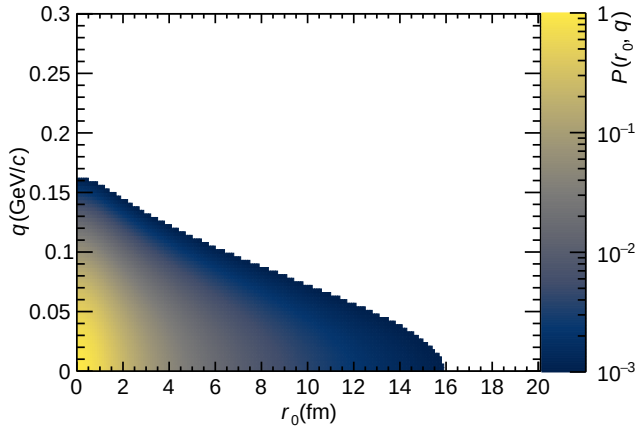

FIGURE 5.6: Deuteron formation probability ($\mathcal{P}(r_0, q)$) using $\mathcal{D}(\vec{r},\vec{q})$ for Gaussian wavefunction as a function of source size r_0 and relative momentum q of p-n pairs. For more details, see the text below.

Hulthén wavefunction

As discussed in Sec. 5.1, the Hulthén wavefunction is a suitable choice for describing the ground state of the deuteron, making it preferable over the Gaussian wavefunction. However, an exact calculation of $\mathcal{D}_d(\vec{r},\vec{q})$ is nontrivial due to the angles between the vectors $\vec{r}\cdot\vec{\xi}$ and $\vec{q}\cdot\vec{\xi}$. The wavefunction for the Hulthén potential is defined in Eq. 5.40. Calculating the Wigner density starting from the Fourier transform $\psi(\vec{k})$ is advantageous as it provides an elegant approach to handling the angles relative to the position vectors $\vec{r}$ and $\vec{q}$. The Fourier transform of Eq. 5.40 can be

expressed as follows

$$\psi(\vec{k}) = \frac{\sqrt{\alpha+\beta}}{\pi(\alpha-\beta)}\left(\frac{1}{k^2+\alpha^2}-\frac{1}{k^2+\beta^2}\right). \tag{5.70}$$

In Fourier space, Eq. 5.9 has the following form

$$\mathcal{D}(\vec{r},\vec{q}) \;=\; \int \mathrm{d}^3\xi \int \mathrm{d}^3k_1 \int \mathrm{d}^3k_2\, \psi^*(\vec{k}_2)\,\psi(\vec{k}_1)\, e^{-i\left[\vec{q}\cdot\vec{\xi}+\vec{k}_2\cdot(\vec{r}-\vec{\xi}/2)+\vec{k}_2\cdot(\vec{r}-\vec{\xi}/2)\right]}. \tag{5.71}$$

Here, $\vec{q}$ represents the relative momentum of the proton-neutron (p-n) pair. By making the substitutions $\vec{k}_2 = 2\vec{q}+\vec{k}_1$ and $\vec{k}1 = \vec{k}+\vec{q}$, and integrating over $\vec{\xi}$ and $\vec{k}2$, one can derive Eq. 5.72 as

$$\begin{aligned}\mathcal{D}(\vec{r},\vec{q}) \;&=\; 8\int \mathrm{d}^3k\, e^{2i\vec{r}\cdot\vec{k}}\,\psi^*(\vec{q}-\vec{k})\,\psi(\vec{q}+\vec{k})\\ &=\; \int \mathrm{d}^3k\, e^{i\vec{r}\cdot\vec{k}}\,\psi^*(\vec{q}-\vec{k}/2)\,\psi(\vec{q}+\vec{k}/2)\,.\end{aligned} \tag{5.72}$$

The integral depends on the angle θ between $\vec{r}$ and $\vec{k}$. To eliminate this angular dependence, an angular average over θ is performed using the weight factor $\sin(\theta)$[5]. With this simplification, the following expression for $\mathcal{D}_d(\vec{r},\vec{q})$ is obtained, which requires at most 1-dimensional integration

$$\begin{aligned}\mathcal{D}(\vec{r},\vec{q}) \;=&\frac{4(\alpha+\beta)^2}{\alpha\beta(\alpha-\beta)\pi qr}\int_0^\infty \mathrm{d}k\,\frac{\alpha^2\beta^2\sin(2kr)}{\alpha^2+\beta^2+2(k^2+q^2)}\\ &\times\left\{\frac{1}{k^2+q^2+\alpha^2}\ln\left[\frac{(k+q)^2+\alpha^2}{(k-q)^2+\alpha^2}\right]-\frac{1}{k^2+q^2+\beta^2}\ln\left[\frac{(k+q)^2+\beta^2}{(k-q)^2+\beta^2}\right]\right\}.\end{aligned} \tag{5.73}$$

The expression for $\mathcal{P}(r_0,q)$ becomes significantly more complicated, involving three 1-dimensional integrals as shown

$$\begin{aligned}\mathcal{P}(r_0,q) =&\frac{8\,\alpha^2\beta^2(\alpha+\beta)^2}{\pi^2\,q\,r_0^3\,\alpha\beta(\alpha-\beta)}\int_0^\infty\int_0^\infty\int_0^\infty dk\,dr\,dr_d\,r\,r_d^2\,\frac{\alpha^2\beta^2\sin(2kr)}{\alpha^2+\beta^2+2(k^2+q^2)}\\ &\times\exp\left(-\frac{r^2+r_d^2}{4\,r_0^2}\right)\left\{\frac{1}{k^2+q^2+\alpha^2}\ln\left[\frac{(k+q)^2+\alpha^2}{(k-q)^2+\alpha^2}\right]\right.\\ &\left.-\frac{1}{k^2+q^2+\beta^2}\ln\left[\frac{(k+q)^2+\beta^2}{(k-q)^2+\beta^2}\right]\right\}.\end{aligned} \tag{5.74}$$

Due to the complexity of these integrals, numerical evaluations are necessary to obtain the values of $\mathcal{P}(r_0,q)$. The final distribution of $\mathcal{P}(r_0,q)$ for the Hulthén wavefunction is shown in Fig. 5.7. It is worth noting that the distribution of $\mathcal{P}(r_0,q)$ exhibits a significant increase for small relative momentum q and small source size r_0. However, the spread of the distribution is still relatively larger than the width of the

[5]In physics, angular averaging refers to the process of averaging a physical quantity over all possible orientations or angles of a particular variable. This technique is commonly employed to eliminate the dependence on angular variables and obtain a simplified representation that captures the system's overall behavior or statistical properties. Angular averaging finds extensive application in various fields including scattering theory, cosmology, and statistical mechanics. By performing angular averaging, calculations can be simplified, angular dependencies can be removed, and averaged or statistically relevant quantities can be obtained, enabling a better description of the behavior of physical systems.

distribution for $\mathcal{P}(r_0, q)$ considering the Gaussian wavefunction. This observation suggests that the Hulthén wavefunction allows more proton-neutron (p-n) pairs to coalesce into deuterons.

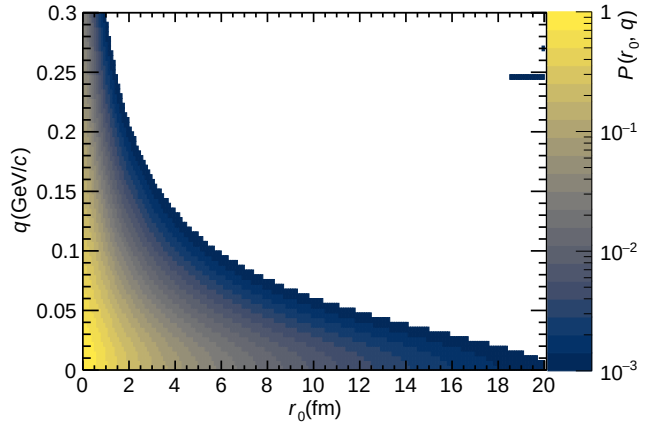

FIGURE 5.7: Deuteron formation probability ($\mathcal{P}(r_0, q)$) as a function of source size r_0 and relative momentum q of p-n pairs considering Hulthén wavefunction for d.

Argonne v_{18} wavefunction

As discussed in Chap 1.4.1, the Argonne v_{18} potential is a phenomenological NN potential that consists of an electromagnetic (EM) part, a one-pion exchange (OPE) part, and intermediate- and short-range terms. This potential has been directly fitted to the NN scattering database, low-energy NN scattering parameters, and the deuteron binding energy for the deuteron. With 40 adjustable parameters, it achieves a χ^2 per datum of 1.09 for 4301 pp and np data in the energy range of 0-350 MeV, constrained to nucleon-nucleon scattering measurements [31]. In this potential, the deuteron wavefunction takes the form mentioned in Eq. 5.43, where $S_{12}(\hat{r}) = 3, \vec{\sigma}_1 \cdot \vec{r}, , \vec{\sigma}_2 \cdot \vec{r} - \vec{\sigma}_1 \cdot \vec{\sigma}_2$ represents the spin tensor, χ_{1m} is a spinor, and $u(r)$ and $w(r)$ are the radial S and D wavefunctions, respectively.

We define $\vec{r}_1$ as the coordinates of the proton, $\vec{r}_2$ as the coordinates of the neutron, $\vec{r} = \frac{\vec{r}_1 - \vec{r}_2}{2}$, and $\vec{R} = \frac{\vec{r}_1 + \vec{r}_2}{2}$. The spin averaged density is given by Eq. 5.44, and the wavefunction is normalized as

$$\int \mathrm{d}^3 r \, |\psi_{\mathrm{d}}(\vec{r})|^2 = \int \mathrm{d}^3 r \, \frac{1}{4\pi r^2} \left[u^2(r) + w^2(r) \right] = 1 \,. \tag{5.75}$$

The contribution of the first addend in the integrand of Eq. 5.75 is dominant, as the first part of the integral is equal to 0.9424 [31]. The fact that the contribution of $|u(r)|^2$ is dominant resembles the predominant contribution of the s-wave in NN interaction. While the evaluation of the wavefunction from the Argonne v_{18} potential is only possible numerically, to obtain an analytical form of its Wigner density, the values of $u(r)/r$ and $w(r)/r$ are fitted with a suitable function, as mentioned below.

$$F(r) = \frac{N_1 a}{\pi(a^2 + r^2)} + \frac{N_2 b}{\pi(b^2 + (r - c)^2)} + N_3 e^{-\frac{r^2}{f}} \,, \tag{5.76}$$

where N_1, N_2, N_3, a, b, c, and f are fit parameters, the function $F(r)$ can describe both $u(r)/r$ and $w(r)/r$ individually. The fits to $u(r)/r$ and $w(r)/r$ are performed separately, resulting in two different sets of fit parameters for the S and D wave components, respectively, which are listed in Tab. 5.1. The fit function $F(r)$ provides a very good description of the shape of $u(r)/r$ in the range $0 < r < 15$ fm with a $\chi^2_{\text{ndf}} \sim 6.83 \times 10^{-8}$, and $w(r)/r$ with $\chi^2_{\text{ndf}} \sim 1.3 \times 10^{-10}$ in the same range. The Wigner density associated with $F(r)$ takes the form

$$\mathcal{D}(\vec{r},\vec{q}) = \frac{1}{8\pi}\sum_{i=1}^{6} T_i(r,q)\,. \tag{5.77}$$

The terms $T_i(r,q)$ involve at most two-dimensional integration, which can be numerically evaluated. The analytical forms of these terms are provided below:

$$\begin{aligned}
T_1 &= (2\pi f)^{3/2}\, N_3^2\, e^{-\frac{f^2q^2-4r^2}{2f}}\,,\\
T_2 &= \frac{16a^2N_1^2}{\pi qr}\int_0^\infty \mathrm{d}\xi\, \frac{\sin(q\xi)}{4a^2+4r^2+\xi^2}\,\ln\left[\frac{4a^2+(\xi+2r)^2}{4a^2+(\xi-2r)^2}\right]\,,\\
T_3 &= \frac{8aN_1N_3}{qr}\int_0^\infty \mathrm{d}\xi\, \sin(q\xi)\, e^{-\frac{2a^2+4r^2+\xi^2}{2f}}\\
&\quad\times\left[\mathrm{Ei}\left(\frac{4a^2+(2r+\xi)^2}{4f}\right)-\mathrm{Ei}\left(\frac{4a^2+(\xi-2r)^2}{4f}\right)\right]\,,\\
T_4 &= \frac{4bN_2N_3}{q}\int_0^\infty\int_{-1}^1 \mathrm{d}\xi\,\mathrm{d}\gamma\, \sin(q\xi)\,\xi\,\left(\frac{e^{-\frac{4r^2+4\gamma r\xi+\xi^2}{4f}}}{b^2+c^2-c\sqrt{4r^2-4\gamma r\xi+\xi^2}+r^2-\gamma r\xi+\frac{\xi^2}{4}}\right.\\
&\quad\left.+\,\frac{e^{-\frac{4r^2-4\gamma r\xi+\xi^2}{4f}}}{b^2+c^2-c\sqrt{4r^2+4\gamma r\xi+\xi^2}+r^2+\gamma r\xi+\frac{\xi^2}{4}}\right)\,,\\
T_5 &= \frac{4abN_1N_2}{\pi q}\int_0^\infty\int_{-1}^1 \mathrm{d}\xi\,\mathrm{d}\gamma\, \sin(q\xi)\,\xi\,\left[\frac{\left(a^2+r^2+\gamma r\xi+\frac{\xi^2}{4}\right)^{-1}}{b^2+\left(c-\frac{1}{2}\sqrt{4r(r-\gamma\xi)+\xi^2}\right)^2}\right.\\
&\quad\left.+\,\frac{\left(a^2+r^2-\gamma r\xi+\frac{\xi^2}{4}\right)^{-1}}{b^2+\left(c-\frac{1}{2}\sqrt{4r(r+\gamma\xi)+\xi^2}\right)^2}\right]\,,\\
T_6 &= \frac{4N_2^2b^2}{\pi q}\int_0^\infty\int_{-1}^1 \mathrm{d}\xi\,\mathrm{d}\gamma\, \sin(q\xi)\,\xi\,\left[\frac{1}{b^2+\left(c-\frac{1}{2}\sqrt{4r(r+\gamma\xi)+\xi^2}\right)^2}\right.\\
&\quad\left.\times\,\frac{1}{b^2+\left(c-\frac{1}{2}\sqrt{4r(r-\gamma\xi)+\xi^2}\right)^2}\right]\,,
\end{aligned} \tag{5.78}$$

where Ei is an exponential integral defined as $\mathrm{Ei}(x) = \int_x^\infty \mathrm{d}t\, e^{-t}/t$. The exact analytic form of $\mathcal{P}(r_0,q)$ using $\mathcal{D}(\vec{r},\vec{q})$ is challenging to obtain, requiring numerical integration. Fig. 5.8 illustrates the distribution of $\mathcal{P}(r_0,q)$ for the Argonne v_{18} wavefunction. Similar to the Gaussian and Hulth'en wavefunctions, this distribution favors higher coalescence probabilities for small q and r_0. However, the Argonne v_{18} distribution is narrower than the Hulthén distribution, limiting the phase space for

Fit parameters	$u(r)/r$	$w(r)/r$
N_1	0.81370516	-0.34242388
N_2	4.49712863	1.0973295
N_3	-0.68798139	-0.25201684
a	-10.82747628	4.33930564
b	1.68243617	1.28156015
c	-0.40957858	0.22952727
f	0.39633979	0.42620769

TABLE 5.1: Fit parameters for $F(r)$ extracted by performing a fit of $F(r)$ to the numerical values of $u(r)/r$ (2nd column) and $w(r)/r$ (3rd column) in the range $0 < r < 15$ fm.

coalescence. This emphasizes the importance of both small relative momenta and small relative distances for deuteron formation.

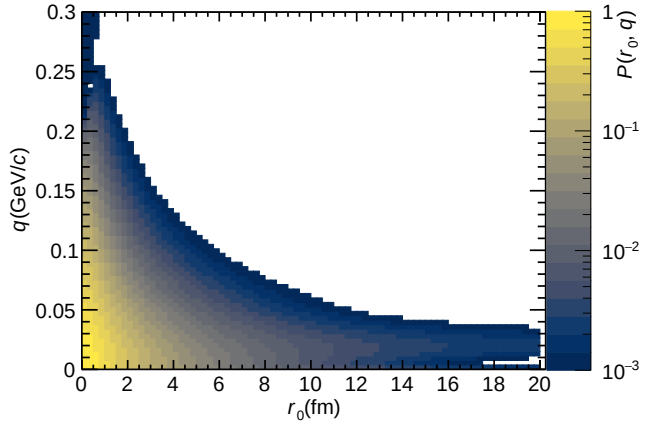

FIGURE 5.8: Deuteron formation probability ($\mathcal{P}(r_0, q)$) obtained as a function of source size r_0 and relative momentum q of p-n pairs and Argonne v_{18} wavefunction for d.

χEFT wavefunction

In Sec. 5.1.2, the importance of considering the χEFT (N^4LO) deuteron wavefunction for deuteron formation is discussed. The χEFT and Argonne v_{18} potentials, which are used to describe nucleon-nucleon interactions, are obtained through two different approaches. The χEFT potentials are based on chiral symmetry and derived from first principles, utilizing a systematic expansion of the chiral Lagrangian that describes the dynamics of nucleons in terms of momentum and pion mass. On the other hand, the Argonne v_{18} potential is a realistic phenomenological model. Therefore, it is intriguing to investigate the influence of these two distinct potentials on the prediction of the absolute yield of deuterons. The χEFT wavefunction of the deuteron also consists of two components, namely $u(r)$ and $w(r)$ representing the radial S and D waves, respectively, are numerical values. Therefore obtaining analytical expression for $\mathcal{D}(\vec{r}, \vec{q})$ necessitates fitting numerical values of wavefunction to analytical expressions. The analytic expression of the wavefunction is obtained with

Fit parameters	$u(r)/r$	$w(r)/r$
N_0	14.83063014	-
N_1	0.3644193	90.06036202
N_2	0.01876164	0.22901687
N_3	0.58780443	90.167747
a	2.95678555	-
b	7.03082423	-
c	2.85271022	-
r_0	2.65962623	-
α_1	0.86804832	1.75803721
α_2	-2.99220936	2.55621569
α_3	2.51249685	1.7664106
β_1	1.81024872	2.07489033
β_2	12.77230151	4.11299107
β_3	0.95031591	2.0759802

TABLE 5.2: Fit parameters for $\mathcal{F}(r)$ extracted by performing a fit of $F(r)$ to the numerical values of $u(r)/r$ (2nd column) and $w(r)/r$ (3rd column) in the range $0 < r < 15$ fm.

with the following fit function

$$\mathcal{F}(r) = \frac{N_0}{\left(a^2r^2 - r_0^2\right)^2 b^{-1} + c^2 r_0^2} + + \sum_{i=1}^{3} \frac{N_i \alpha_i}{\pi(r-\beta_i)^2 + \alpha_i^2}\,, \tag{5.79}$$

where the fit parameters are denoted by N_0, N_i, α_i, β_i, a, b, c, and r_0. For $w(r)/r$, only the second term of $\mathcal{F}(r)$ is used, as it adequately captures the numerical values. Separate fits are performed for $u(r)/r$ and $w(r)/r$, resulting in two sets of fit parameters provided in Tab. 5.2. The fits describe the distributions of $u(r)/r$ and $w(r)/r$ with χ^2_{ndf} values of 3.31×10^{-8} and 3.23×10^{-3} for $u(r)/r$ and $w(r)/r$, respectively, within the range of $0 < r < 15$ fm. The Wigner density associated with $F(r)$ can be expressed as follows

$$\mathcal{D}(\vec{r},\vec{q}) = \frac{1}{2q\pi^2} \int_0^\infty \int_{-1}^{1} \mathrm{d}\zeta\, \mathrm{d}\gamma\, \sin(q\zeta)\, \zeta\, \left(\kappa_0 + \kappa_1 + \kappa_2 + \kappa_3\right)\,, \tag{5.80}$$

where the terms κ_0, κ_1, κ_2, and κ_3 are defined as

$$\kappa_0 = \frac{4bN_0^2}{\left[\left(4r_0^2 - a^2\left(\zeta^2 + 4r^2 + 4\gamma\zeta r\right)\right)^2 + 4bc^2r_0^2\right]\left[\left(4r_0^2 - a^2\left(\zeta^2 + 4r^2 - 4\gamma\zeta r\right)\right)^2 + 4bc^2r_0^2\right]}\,, \tag{5.81}$$

$$\kappa_1 = \sum_{i=1}^{3} \frac{4\alpha_i^2 N_i^2}{\left[\left(2\beta_i - \sqrt{\zeta^2 + 4r^2 - 4\gamma\zeta r}\right)^2 + 4\alpha_i^2\right]\left[\left(2\beta_i - \sqrt{\zeta^2 + 4r^2 + 4\gamma\zeta r}\right)^2 + 4\alpha_i^2\right]}\,, \tag{5.82}$$

$$\kappa_2 = \sum_{\substack{i=1 \\ i\neq j}}^{3}\sum_{j=1}^{3} 8N_iN_j\alpha_i\alpha_j \times \times \left\{ \frac{1}{\left[\left(2\beta_i - \sqrt{\zeta^2+4r^2-4\gamma\zeta r}\right)^2 + 4\alpha_i^2\right]\left[\left(2\beta_j - \sqrt{\zeta^2+4r^2+4\gamma\zeta r}\right)^2 + 4\alpha_j^2\right]} + \frac{1}{\left[\left(2\beta_i - \sqrt{\zeta^2+4r^2+4\gamma\zeta r}\right)^2 + 4\alpha_i^2\right]\left[\left(2\beta_j - \sqrt{\zeta^2+4r^2-4\gamma\zeta r}\right)^2 + 4\alpha_j^2\right]} \right\}, \tag{5.83}$$

$$\kappa_3 = \sum_{i=1}^{3} 4\,\pi N_0\, N_i\alpha_i \times \left\{ \frac{4b}{\left[\left(2\beta_i - \sqrt{\zeta^2+4r^2-4\gamma\zeta r}\right)^2 + 4\alpha_i^2\right]\left[\left(4r_0^2 - a^2\left(\zeta^2+4r^2+4\gamma\zeta r\right)\right)^2 + 4bc^2r_0^2\right]} + \left[\frac{1}{\left(2\beta_i - \sqrt{\zeta^2+4r^2+4\gamma\zeta r}\right)^2 + 4\alpha_i^2} \frac{4b}{\left(4r_0^2 - a^2\left(\zeta^2+4r^2-4\gamma\zeta r\right)\right)^2 + 4bc^2r_0^2} \right] \right\}. \tag{5.84}$$

Similar to the case of Argonne v_{18}, in this case as well, obtaining an exact analytic form for $\mathcal{P}(r_0, q)$ using $\mathcal{D}(\vec{r}, \vec{q})$ is not easy. All the integrals in Eq. 5.80 are performed numerically. The obtained $\mathcal{P}(r_0, q)$, using the deuteron wavefunction from χEFT (N^{4}LO), is shown in Fig. 5.9 has maximum at small r_0 and small q.

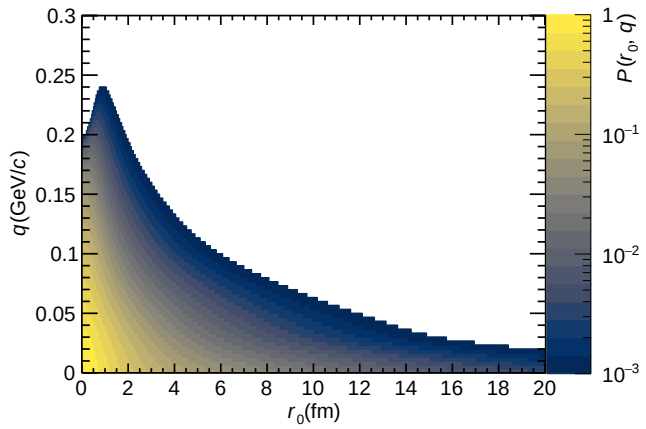

FIGURE 5.9: Deuteron formation probability ($\mathcal{P}(r_0, q)$) as a function of source size r_0 and relative momentum q of p-n pairs and χEFT N^{4}LO wavefunction for deuteron.

5.2.3 Source for nucleon production

As mentioned in Sec. 5.1, the function $\mathcal{P}(r_0, q)$ provides the probability of deuteron formation for pairs of protons and neutrons with appropriate spin configurations. However, before the deuteron formation occurs, the pair of p-n must be produced. Ideally, one could use nucleons produced from collision experiments for this purpose. However, due to

various limitations, such as the non-reconstruction of neutron tracks in many experiments and the challenge of accurately tagging tracks to extract the particle positions, using real data is currently not feasible. Therefore, p-n pairs from simulations are employed as an alternative to study the production of deuterons

In simulations, particularly with PYTHIA and EPOS, it is possible to obtain the coordinates of the particles. However, this comes at a cost. Simulations cannot capture all the experimental effects on events as seen in collision experiments. Specifically, the source geometry is not well known in simulations, and the source itself plays an important role in determining $\mathcal{P}(r_0, q)$. To address this issue, simulations are tuned to reproduce the data.

In this study, for the pp events, two Monte Carlo event generators are used: EPOS 3.117 [122] and PYTHIA 8.3 [239] with the Monash 2013 tune configuration.

The simulations using EPOS were performed by **Maximilian Horst**, while another simulation using PYTHIA 8.3 was conducted by **Shushanta Tripathy**. In both simulations, to account for realistic particle emission and correlations among particles, the emitting source is constrained to the measurements of the baryon-emitting source [56], as discussed in Sec. 5.1.2.

The fundamental difference between the EPOS and PYTHIA event generators is that EPOS 3 [122] is a hybrid Monte Carlo event generator where the reaction volume is divided into the 'core' and 'corona'. The two separate reaction volumes are defined by the local density and transverse momentum of the string segments. The core volume represents a thermalized bulk of matter that evolves according to 3+1D viscous hydrodynamics and then hadronizes using a Cooper-Frye mechanism [240, 241]. On the other hand, the particles in the corona originate from string fragmentation.

In contrast, PYTHIA 8.3 [239] is an event generator that includes parton scatterings and is complemented by parton showers incorporating initial- and final-state radiation through the leading-logarithm approximation. The hadronization in PYTHIA 8.3 is modeled using the Lund string fragmentation model [242]. The Monash 2013 tune [243] is used in this study because it provides a better description of minimum-bias events in pp collisions at LHC energies. Additionally, this tune incorporates a multiparton interaction-based color-reconnection scheme. In this scheme, the strings between partons can be ordered to reduce the total string length. The events in the Monash 2013 tune consist of particles originating from multiparton interactions as well as from beam remnants. This particular aspect of the PYTHIA Monash 2013 tune is crucial for simulating the experimental effects observed in collisions.

To be used in the coalescence afterburner, the nucleon-emitting source must be modeled to account for particle multiplicity, the potential contribution of feed-down from strongly decaying resonances, and the phase-space correlations among the particles of interest in the events. The MC simulations are tuned to reproduce the measured average charged-particle multiplicity density at midrapidity. Specifically, when comparing with the deuteron spectra in [76], the multiplicity class referred to as *HM I* is considered in which the mean multiplicity is $\langle dN_{\rm ch}/d\eta \rangle_{|\eta|<0.5} = 35.8 \pm 0.5$ [76]. Therefore, the events in EPOS and PYTHIA are triggered to reproduce the multiplicity in the data from ALICE [76]. This type of selection often rejects the simulated events; for EPOS 3, the acceptance of events is approximately 10^{-2}. However, in the case of PYTHIA 8.3, the acceptance factor is even lower$\sim \times 10^{-5}$.

In addition to the multiplicity distribution, event generators also need to consider the contribution of strongly decaying resonances that produce protons and neutrons, which can subsequently participate in the formation of a deuteron. Short-lived resonances that decay into nucleons effectively increase the source size [56]. However, the native EPOS3 and PYTHIA event generators fail to reproduce the $m_{\rm T}$-scaling behavior of the source size,

as depicted by the orange and green curves in Fig. 5.10.

To achieve agreement with the measured m_{T}-scaling, the following procedure is employed: first, the equal-time approximation in the PRF is performed. Then, the obtained values of the source are adjusted on an event-by-event basis. This adjustment ensures that the final outcomes accurately reproduce the measured m_{T} values, as depicted by the red and blue curves in Fig. 5.10. Further details regarding this process will be discussed in the following text.

The equal-time of emissions in the PRF is necessary to determine the distance between emitted pairs of nucleons. This process is performed at the particle level in each event where the particle coordinates are accessible. The term "equal time of emission" refers to the synchronization of emission times for particles involved in collisions. Since the particles are paired, one particle only observes the other particle at the moment of its emission. Consequently, while the second particle is emitted from the strong decay Δt time after the first one, the first particle needs to travel a distance of $c\Delta t$ with the resonance. Once the daughter of the resonance becomes visible to the primordial particle, the relative distance between them is calculated. For instance, consider the scenario where a primordial neutron is paired with a proton, which is the daughter particle from a strongly decaying resonance with a characteristic decay length ($c\tau \sim 1$ fm). In this case, the neutron is propagated along its momentum in the phase space until the proton emerges from the resonance. Subsequently, the distance between the daughter proton and the neutron is calculated. Further details and additional information can be found in [215].

The source size from the native event generators, denoted as r_0^{native}, is obtained by taking the mean value r_μ^{native} of the $d_{\mathrm{pn}}^{\mathrm{native}}$ distribution, following the relation $r_0^{\mathrm{native}} = (\sqrt{\pi}/4), r_\mu^{\mathrm{native}}$. However, as mentioned earlier, neither of the native event generators accurately reproduces the m_{T} scaling observed in the data measured by ALICE. Therefore, a scaling procedure is required to tune the event generators. This involves introducing an additional m_{T}-scaling factor $\mathcal{S}(m_{\mathrm{T}}) = r_0^{\mathrm{ALICE}}/r_0^{\mathrm{native}}$, which is used to correct the proton-neutron distance as $d_{\mathrm{pn}}^{\mathrm{scaled}} = \mathcal{S}(m_{\mathrm{T}}), d_{\mathrm{pn}}^{\mathrm{native}}$. After applying this scaling, the event generators successfully reproduce the source size r_0 as a function of m_{T}, as depicted by the red and blue curves for EPOS 3 and PYTHIA 8.3 in Fig. 5.10.

5.2.4 (Anti-)deuteron production in the event generators

To obtain the momentum spectra of (anti-)deuterons using EPOS 3 and PYTHIA 8.3, we utilized the modeled source size, as well as the momentum spectra of protons and neutrons simulated with EPOS 3 and PYTHIA 8.3. The Wigner function formalism from Sect 5.2.2 was employed in this process. To ensure a realistic particle emission in the event generators, the momentum spectra of protons and neutrons were reweighted to match the proton measurement by ALICE [56]. These reweighted spectra are represented by the red (EPOS 3) and yellow bands (PYTHIA 8.3) in Fig. 5.11. Since protons and neutrons belong to the same isospin doublet, we assume they have similar momentum spectra.

The next steps involve event-by-event coalescence using the generated protons and neutrons and the statistical rejection method described in Sec. 5.2.2. In the first step, nucleons are selected, and in the second step, the source size r_0 is extracted for each selected pair of nucleons using the method discussed in Sec. 5.2.3. By combining the source size r_0 of the nucleons with the relative momentum $\vec{q}$, the coalescence probability $\mathcal{P}\left(\frac{\sqrt{\pi}}{4}, d_{\mathrm{pn}}^{scaled}, q\right)$ for a single proton-neutron pair is calculated using the distributions shown in Figs. 5.6, 5.7, 5.8, and 5.9.

Finally, the produced spectra of (anti-)deuterons are used to calculate the average deuteron and antideuteron spectra. These averaged spectra are obtained using EPOS 3 and PYTHIA 8.3 and are presented in Fig. 5.13.

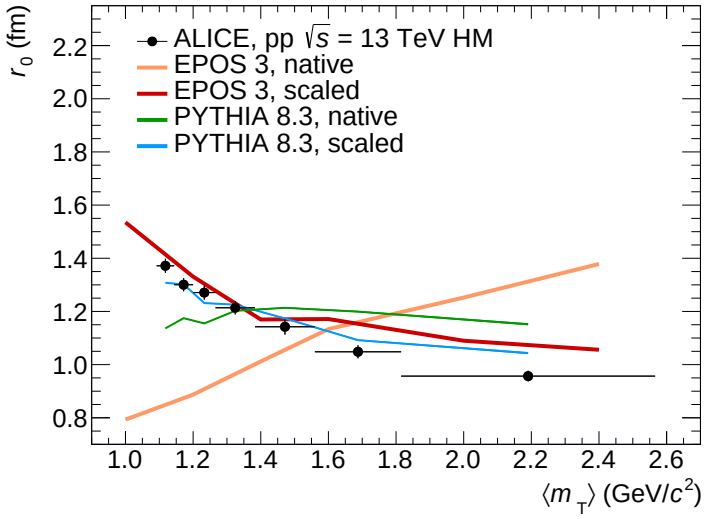

FIGURE 5.10: Comparison between the source size r_0 measured by ALICE [56], the native ones for EPOS 3 (orange) and PYTHIA 8.3 (green) and those obtained after the source modeling (in red and blue for EPOS 3 and PYTHIA 8.3, respectively), as a function of the average transverse mass $\langle m_T \rangle$ of the proton-proton (antiproton-antiproton) pair. For the ALICE data, statistical and systematic uncertainties are summed in quadrature and shown as vertical bars, while for EPOS 3 and PYTHIA 8.3 uncertainties are negligible.

5.2.5 Coalescence factor of deuteron from event generator

One can use the predicted yield by the event generators to calculate the deuteron formation probability, the coalescence factor $\mathcal{B}_A$, an invariant quantity that can be accessed experimentally. From the event generators, the $\mathcal{B}_2$ for different wavefunction hypotheses are obtained in green (Hulthén), blue (Argonne v_{18}), and red (Gaussian), the solid bands obtained using the EPOS 3 and the shaded bands are obtained using PYTHIA 8.3 and are shown in Fig. 5.15.

5.3 Results

The final results of the studies on the coalescence model performed in Sec. 5.1 and the studies on the parameter-free coalescence model based on EPOS 3 and PYTHIA 8.3 in Sec. 5.2 are presented in Sec. 5.3.1 and 5.3.2.

5.3.1 $\mathcal{B}_A$ for deuteron and ^{3}He

The study of $\mathcal{B}_A$ using the coalescence model in a transverse momentum p_T of deuteron and p_T of ^{3}He are shown in Fig. 5.12. The colored bands represent the uncertainty propagated from the measurement of the source radius. In the case of $\mathcal{B}_2$ as presented in Fig. 5.12 (a), the calculated $\mathcal{B}_2$ using the Gaussian wavefunction provides the best description of the data as depicted by the orange band, even though the Hulthén wavefunction is favored by low-energy scattering experiments [233][6], off blue band obtained using Hulthén wavefunction shows agreement between the calculated $\mathcal{B}_2$ and the data within factor 2. The pistachio band computed using the two Gaussians wavefunction shows the worst agreement between the data and the calculation. The calculated $\mathcal{B}_2$ using the deuteron wavefunctions from the N^{4}LO χEFT which is by far the most precise theoretical calculation, is significantly

[6]Reminder: although the Hulthén wavefunction is considered better than the Gaussian wave function, it is important to note that AV18 and χEFT wavefunctions are even better choices as they provide the best description of NN scattering observables with a χ^2/datum$\sim$ 1.

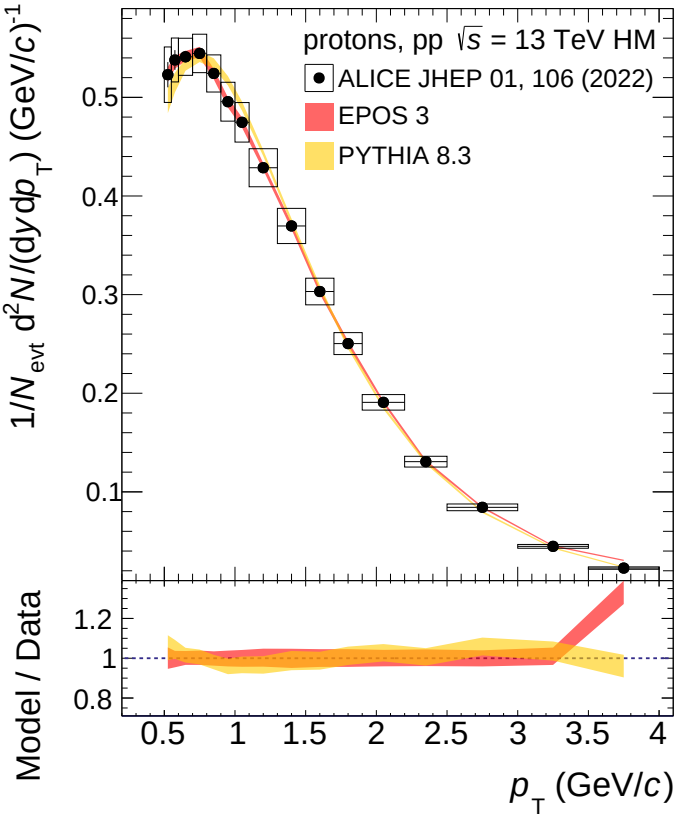

FIGURE 5.11: The proton spectra compared with the measured spectra of proton in pp collisions by ALICE [56]. The upper panel shows proton spectra simulated by EPOS 3 and PYTHIA 8.3, compared with the measured proton spectra in pp collisions by ALICE [56]. In the lower panel, the data-to-model ratios are shown [215].

larger than the measurement, as represented by the grey band. The fact that χEFT deviates by factor two indicates the limits of the coalescence approach used for this calculation.

For ^{3}He, the coalescence prediction $\mathcal{B}_3$ using a wavefunction for the ^{3}He cluster as a product of Gaussians is above the data by almost a factor of 2 except for the last p_T interval, which is consistent with the measured B_3 within the uncertainties as shown in Fig. 5.12 (b).

5.3.2 Deuteron yield

The studies utilizing the coalescence model which properly accounts for the space-momentum correlation of nucleons within the event generators EPOS3 and PYTHIA 8.3, demonstrate deuteron spectra that exhibit significantly improved agreement with the data, as depicted in Fig. 5.13. The solid and shaded bands represent the deuteron spectra obtained with EPOS 3 and PYTHIA 8.3, respectively. The ALICE data in pp collision at $\sqrt{s} = 13$ TeV are depicted by the black boxes and bars. The red, green, and blue bands correspond to the spectra obtained using a simple Gaussian wavefunction, Hulthén wavefunction, and the wavefunction derived from the most accurate phenomenological potential Argonne v_{18}, along with simulations from the EPOS 3 and PYTHIA 8.3 event generators. Irrespective of the event generator employed, the results obtained using the Argonne v_{18} wavefunction exhibit excellent agreement with the data measured by ALICE. The uncertainty band around the model calculations incorporates statistical uncertainties from the simulations and systematic uncertainties, estimated to be approximately 6%. To evaluate these uncertainties, the source size in the model is varied by $\pm$7% based on the uncertainties reported in [56].

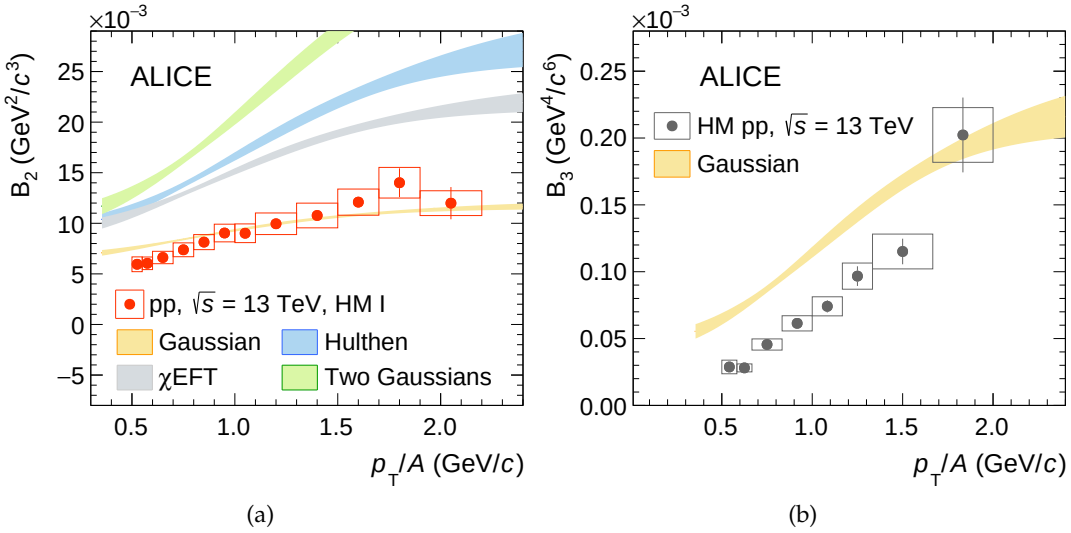

FIGURE 5.12: Comparison between measurements and theoretical predictions for the coalescence factor $\mathcal{B}_2$ for (anti-)deuterons (a) and $\mathcal{B}_3$ for (anti-)^{3}He (b) as a function of p_T/A [76]. Vertical bars and boxes represent statistical and systematic uncertainties, respectively. Theoretical predictions are obtained using different wavefunctions to describe nuclei: Gaussian (yellow), Hulthén (blue), χEFT (gray) and two Gaussians (green).

The final systematic uncertainty is calculated by comparing the relative deviation in the final spectra between the default source size and the varied one. Additionally, the primordial fractions of nucleons are varied by $\pm$10%. Finally, the total systematic uncertainty in the model is determined as the quadrature sum of the systematic uncertainties from all sources. As for the Hulthén and Argonne v_{18} wavefunctions, the χEFT wavefunction is also computed for the first time in this work, with the detailed information provided in Sec. 5.2.2. On the one hand, the Argonne v_{18} potential incorporates central, tensor, and spin-orbit interactions to construct the core part of the interaction. On the other hand, the χEFT NN potential is systematically derived from the underlying theory of QCD and involves a perturbative expansion in powers of a small parameter associated with the pion mass. The χEFT two-body interactions are computed using Feynman diagrams that include pions and nucleons. The leading-order (LO) two-body interactions solely rely on one-pion exchange, while higher-order (NLO, NNLO, etc.) interactions involve multiple pion exchanges and nucleon self-interactions. Nevertheless, the predicted deuteron yields obtained from both the Argonne v_{18} potential and χEFT are in agreement, as presented by the blue and orange bands in Fig. 5.14. In addition to the deuteron spectra presented in Fig. 5.13, the extended studies on the coalescence model using EPOS 3 and PYTHIA 8.3 also involve the determination of the coalescence factor $\mathcal{B}_2$, as illustrated in Fig. 5.15. This figure compares the measured $\mathcal{B}_2$ as a function of p_T/A by ALICE [76] (depicted by black boxes and lines) with the results obtained using EPOS 3 and PYTHIA 8.3 (represented by solid and shaded bands). The solid and shaded bands, colored red, green, and blue, correspond to the predictions obtained using Gaussian, Hulthén, and Argonne v_{18} wavefunctions for EPOS 3 and PYTHIA 8.3, respectively. In this study, for $\mathcal{B}_2$ as well, the Argonne v_{18} wavefunction provides the best description of the data, in agreement with both event generators. The calculation utilizing the Gaussian wavefunction underestimates the data, while the Hulthén wavefunction calculation overestimates it. Furthermore, in the case of EPOS, the statistics are larger than PYTHIA 8.3, resulting in smaller uncertainty bands on the curves for EPOS 3.

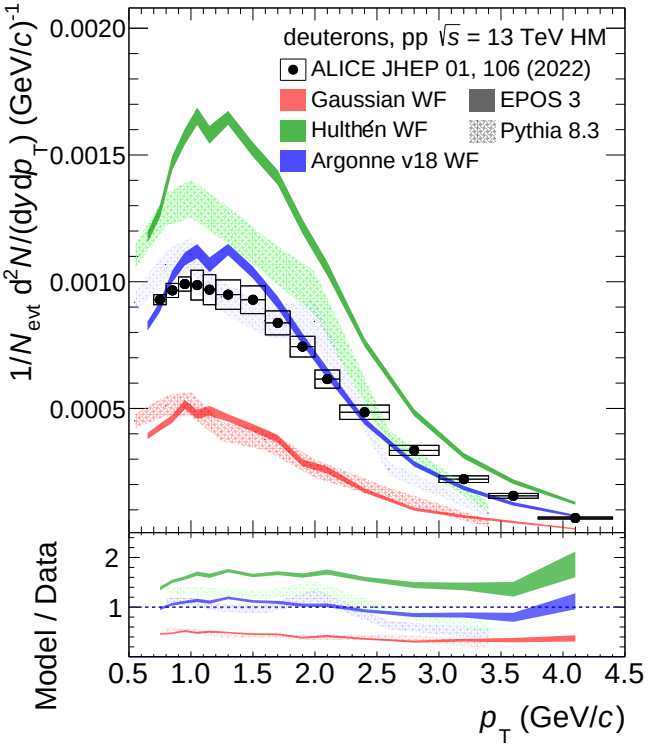

FIGURE 5.13: The upper panel shows an average of deuteron and anti-deuteron spectra obtained performing the coalescence of proton-neutron pairs in EPOS 3 and PYTHIA 8.3, and different hypotheses for the deuteron wavefunction, compared with the measured spectra of the deuteron in pp collisions by ALICE [56]. The width of the bands represents the statistical uncertainty of the models. The systematic uncertainty of the spectra (6%) is not shown. In the lower panel, the data-to-model ratios are shown [215].

5.4 Discussion

In coalescence calculations, determining the absolute yield of the particles is challenging due to the limited knowledge of the density matrix for the two-particle system. However, it is still possible to construct a probability of nuclei formation $\mathcal{B}_A$ by leveraging the correlations present in the coalescence factors [13]. The coalescence factors $\mathcal{B}_2$ for (anti)deuterons and $\mathcal{B}_3$ for (anti)helions, as shown in Fig. 5.12, are crucial for understanding the formation mechanism of nuclei. These factors provide insights into the role of interactions among constituent nucleons in the process of nucleon coalescence, which leads to the formation of (anti)deuterons and (anti)helions. The dependence of these factors on p_T/A offers valuable insights into the underlying dynamics and mechanisms involved in the formation of these composite particles.

In the simple coalescence scenario, the coalescence factor $\mathcal{B}_A$ was calculated assuming no correlation between nucleons [216, 217]. However, in a realistic scenario, nucleons interact with each other, resulting in quantum correlations among the nucleons that form light nuclei. This introduces a dependence of $\mathcal{B}_A$ on the source size and the interaction among the nucleons [226]. Following this idea, recent coalescence calculations have utilized the source size measured by experiments and the internal wave function of deuteron [13, 231, 232] to predict $\mathcal{B}_A$. However, the predicted values of $\mathcal{B}_A$ in these studies use the integrated value of the source size over transverse mass (m_T). The extension of the calculations to a more realistic deuteron wavefunction incorporating the p_T-dependent source size allows for the differential study of the coalescence parameter $\mathcal{B}_A$, revealing a

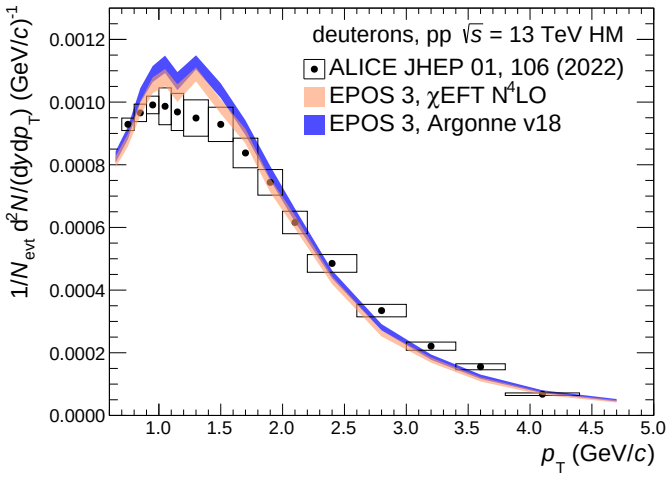

FIGURE 5.14: Deuteron spectra obtained with EPOS 3, comparing two wavefunction hypotheses, i.e. Argonne v_{18} and χEFT [215]. Predictions are compared with the corresponding ALICE measurement [56].

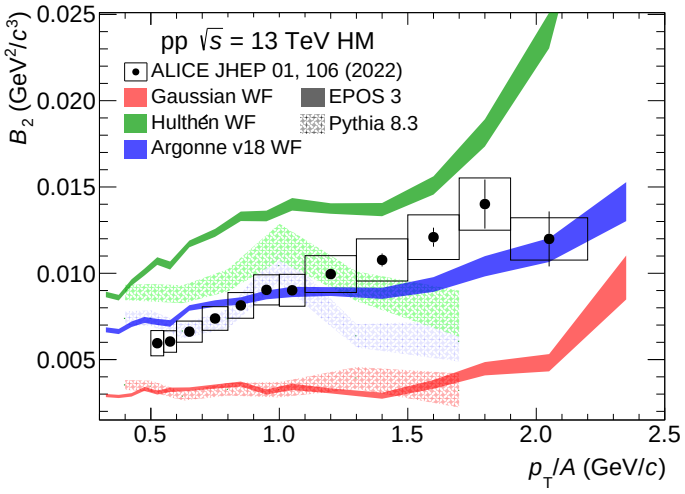

FIGURE 5.15: Comparison of the coalescence parameter $\mathcal{B}_2$ obtained from the coalescence of proton-neutron pairs simulated using EPOS 3 and PYTHIA 8.3 event generators, considering different hypotheses for the deuteron wavefunction [215]. The final results are compared with the measurement by ALICE [56].

clear increase in both $\mathcal{B}_2$ and $\mathcal{B}_3$ with increasing p_T/A. This observed behavior of $\mathcal{B}_2$ and $\mathcal{B}_3$ is consistent with measurements from ALICE [56] and well captured by the predictions of the coalescence model using different wavefunctions.

In the case of (anti)deuterons, various wavefunctions have been employed, including single and double Gaussian [235], Hulthén [226], and a function obtained from χEFT N^{4}LO with a cutoff at 500 MeV [32]. Fig. 5.12 shows that the prediction using the Gaussian wavefunction provides the best agreement with the data. However, the Gaussian wavefunction, which describes the internal structure of the deuteron as a spherical harmonic oscillator with a size parameter $d = 3.2$ fm, is expected to deviate from the data due to its simplicity. On the other hand, the wavefunction from the Hulthén potential and the χEFT wavefunction show poor agreement with the data, deviating by a factor of 2.

To predict the coalescence factor $\mathcal{B}_3$ for (anti-)^{3}He, the calculation currently relies on a Gaussian wavefunction using the method developed in Ref. [13]. However, the general recipe used for $\mathcal{B}_2$ cannot be directly extended to $\mathcal{B}_3$ calculation, as it requires new *ab initio* calculations using a three-particle density matrix. The coalescence prediction of $\mathcal{B}_3$ using a Gaussian wavefunction for ^{3}He consistently overestimates the data by almost a factor of 2, except for the last p_{T} interval, which is consistent with the measured $\mathcal{B}_3$ within the uncertainties, see Fig. 5.12 (b).

The study of the coalescence mechanism as an afterburner, based on a state-of-the-art Wigner function formalism, successfully reproduces the (anti)deuteron spectra measured by ALICE in pp collisions at $\sqrt{s} = 13$ TeV, collected with a high-multiplicity trigger. One of the key features of this study is that it combines event generators and an improved theoretical calculation based on the Wigner approach to provide the absolute yield of deuterons as a function of transverse momentum while preserving the space-momentum correlation of nucleons. This achievement has not been attained by the theoretical developments in coalescence models or by the direct manipulation of the emitting source provided by event generators such as EPOS 3 and PYTHIA 8.3. In this study, the measured source size [56] is used as a constraint, enabling a parameter-free prediction of the (anti)deuteron spectra. The Gaussian wavefunction is an overly simplistic approximation for the internal structure of the deuteron when considering coalescence studies. The predicted yield using the Gaussian wavefunction deviates from the measured data by approximately a factor of 1/2. The yield predicted using Hulthén wavefunction tends to overshoot the data, possibly because of its similarity to the Yukawa potential. The Hulthén potential exhibits Coulomb-like behavior for small distances (r) and exponentially decays to zero as r increases. However, it lacks an infinitely repulsive region. Consequently, the wavefunction shows a monotonically increasing trend for small r, resulting in a high coalescence probability $\mathcal{P}(r_0, q)$ at short distances. This high probability leads to an overshoot in the deuteron spectra. Although the Argonne v_{18} and χEFT are distinct approaches, the deuteron wavefunctions obtained from these approaches exhibit minimal differences, except for very short ranges. Specifically, the χEFT deuteron wavefunction displays less repulsion than the one derived from the Argonne v_{18} potential. Nonetheless, the predicted deuteron yields using both Argonne v_{18} and χEFT are compatible, suggesting that the production of the deuteron remains unaffected by extremely short-range interactions, as illustrated in Fig. 5.14.

Furthermore, it becomes evident that Gaussian and Hulthén wavefunctions are less accurate compared to χEFT and Argonne v_{18} deuteron wavefunction for studying deuteron production. Therefore, their use for this purpose is discouraged.

In Fig. 5.13, it is natural to question the significant difference in the predicted deuteron spectra obtained using the Hulthén and Argonne v_{18} potentials, despite having the same wavefunctions in the asymptotic region. The explanation lies in the shape of the wavefunctions. According to quantum mechanics, the deuteron wavefunction in the asymptotic region ($r \gtrsim 1.5$ fm) is determined by solving the Schrödinger equation with an interaction potential that accurately reproduces the deuteron binding energy ($E_{\mathrm{B}} \sim 2.2$ MeV). As both potentials yield the correct binding energy, the wavefunctions calculated using the Hulthén and Argonne v_{18} potentials exhibit remarkable similarity in the asymptotic region, as depicted in Fig. 5.3. However, as mentioned earlier, the Hulthén and Argonne v_{18} potentials significantly differ in the short-range regime ($r \lesssim 1.5$ fm), resulting in distinctly different computed wavefunctions. The Argonne v_{18} potential incorporates a strong repulsive core, leading to the wavefunction vanishing as $r \to 0$ fm. The notable discrepancy in the predicted yields between calculations using these two wavefunctions indicates the sensitivity of the production mechanism of light nuclei to the short-range strong interaction between nucleons and is observed for the first time. Furthermore, since the predicted yields from the Argonne v_{18} potential and χEFT exhibit remarkable similarity, and the two wavefunctions are relatively similar, the same argument for difference between Hulthén and χEFT potentials holds. Conducting further investigations with different interaction

potentials and expanding the studies to systems with $A > 2$ could contribute to a deeper understanding of the formation mechanism of light nuclei.

From Fig. 5.15 and Fig. 5.12 (a), it is noteworthy that the prediction of $\mathcal{B}_2$ using the purely theoretical approach yields a better description of the data when utilizing a Gaussian wavefunction rather than the χEFT wavefunction. Conversely, the prediction of $\mathcal{B}_2$ using the coalescence mechanism as an afterburner, based on a state-of-the-art Wigner function formalism with the Argonne $v18$ potential, EPOS 3, and PYTHIA 8.3, exhibits excellent agreement with the measured data by ALICE. This observation is intriguing given the similarity between the deuteron wavefunctions derived from the Argonne $v18$ potential and χEFT, leading to the conclusion that the space-momentum correlation in the purely theoretical approach for calculating $\mathcal{B}_2$ cannot be disregarded.

In conclusion, the studies in Sec. 5.1 show the importance of considering the quantum-mechanical properties of nucleons in the formation of nuclei and the necessity of including a realistic source function when applying the Wigner formalism to calculate the coalescence probability. The state-of-the-art coalescence model successfully describes the d/p and ^{3}He/p ratios observed in the ALICE experiment. For the first time, a differential study of the coalescence model as a function of the transverse mass of protons has been conducted using the measured yields of (anti)nuclei and the source size determined with high precision femtoscopic measurements [56]. Although the current theoretical approach offers a valuable means to study the coalescence mechanism in a differential manner, it has some limitations. The fact that the deuteron wavefunction derived from χEFT and Hulthén wavefunctions fail to provide a satisfactory description of the data, indicating the need for improvement in the theoretical framework of $\mathcal{B}_A$ calculations. Moreover, the calculation of $\mathcal{B}_2$ in this study, assumes no space-momentum correlations, as the relative momentum between the nucleons ($\vec{q} = (\vec{p}_{\mathrm{p}} - \vec{p}_{\mathrm{n}})/2$) has been neglected in the Wigner function of the proton-neutron state. This approximation is expected to be accurate to within $\sim$10% for Pb-Pb collisions. In pp collisions, no further studies related to this approximation have been conducted, and since the source size is small, it would be interesting to investigate the effect of such an approximation. Additionally, the calculation cannot be directly extended to cases where $A \geq 3$ with different wavefunctions, as it would require repeating the entire derivation for the three-or-more particle density matrix within the coalescence model. Nevertheless, such an extension could provide further insights into whether the formation of ^{3}He can be accurately described by coalescence.

Furthermore, the coalescence model developed in Sec. 5.2, based on the Wigner approach, along with event generators utilizing the Argonne v_{18} wavefunction, provides an excellent description of the measured deuteron yield. This demonstrates that the coalescence model developed in this study can accurately predict deuteron yields without requiring any free parameters. Moreover, this study emphasizes the importance of simultaneously measuring proton production spectra and the size of the emitting source at different collision energies. This allows for accurate predictions of light nucleus yields. The developed model can also be used for other energies, enabling the generation of realistic spectra of antinuclei resulting from cosmic ray collisions. This, in turn, facilitates reliable predictions of (anti)deuteron production yields at various energies and multiplicities, providing crucial estimates of antideuterons produced in collisions between cosmic rays and the interstellar medium. Such predictions are crucial in the quest for dark matter annihilation through the detection of antinuclei in the final state.

Chapter 6

Summary and outlook

This thesis comprehensively summarizes the two main topics investigated during the Ph.D. research. Firstly, it delves into the study of strong interactions in three-body systems, specifically focusing on the proton-deuteron system. The investigation encompasses both theoretical analysis and the measurement of momentum correlations. Secondly, the thesis emphasizes the study of light (anti-)nuclei formation in hadron-hadron collisions.

The first part of this thesis focuses on the role of three-nucleon dynamics and their interactions in the proton-deuteron system. This is achieved by analyzing the femtoscopic proton-deuteron correlation function in pp collisions at $\sqrt{s} = 13$ TeV at LHC. The study demonstrates the feasibility of investigating interactions in three-particle systems by examining the momentum correlation between hadron and deuteron pairs. Specifically, the p–d correlation function was analyzed in pp collisions, where the emitted particles are in close proximity, with distances equal to or shorter than 1 fm. This distance is smaller than the average distance observed in conventional nuclei. The production of hadrons at such small distances offers a unique opportunity to explore three-body systems like p–d or three hadron triplets, allowing for studying interactions at extremely short distances. Using the analysis of K^+–d pairs and m_T-scaling relation, which is common for all baryon-baryon pairs in pp collisions at $\sqrt{s} = 13$ TeV, it was established that deuterons follow the same m_T-scaling relation for the emission source. The K^+–d correlation function was obtained assuming effective two-body interaction in the Lednický approach.

The measured p–d correlation functions exhibit a prominent signal at small relative momenta, indicating the presence of a repulsive strong interaction. Two theoretical approaches were employed to interpret this signal: treating p–d as an effective two-body system and considering p–d as an ensemble of three nucleons. Upon accurate determination of the p–d source size from the m_T scaling, which is $r_{\text{eff}}^{\text{p–d}} = 1.08^{+0.06}_{-0.06}$ fm, it became apparent that effective two-body calculations are incapable of describing the measured p–d correlation function. This limitation arises from several factors, including constraints on the model and the inherent nature of the system, which involves three indistinguishable particles. In such a system, the formation and breakup of the deuteron at short distances can lead to possible rearrangements, rendering the effective two-body model inadequate. As a result, relying solely on the Lednický model proves insufficient for accurately describing the p–d correlation function. Furthermore, employing a Born-approximated wavefunction, which properly accounts for the antisymmetrization of the three nucleons but only considers the asymptotic features of the wave function, fails to reproduce the experimental data. This indicates that additional dynamics beyond just asymptotic strong interaction are necessary to adequately describe the interaction when all nucleons are in close proximity.

To accurately describe the measured p–d correlation function, a novel approach was employed for the first time. This approach involved obtaining a comprehensive p–d wavefunction using two separate methods: the Hyperspherical approach, which utilized realistic phenomenological potentials AV18+UIX and solved the Schrödinger equation, and the Pionless EFT approach, which was based on the effective Lagrangian of three-nucleon

dynamics without explicit pions and involved solving the Fadeev equations. These approaches considered the three-body dynamics induced by the strong interaction among the three nucleons.

In addition to the full three-body wavefunction, the calculation also required extending the two-body source to a three-body source, as discussed in Refs. [153, 156, 244]. This extension was motivated by previous works where the starting point was the single particle source, and pairwise two-particle relative distances were utilized. Remarkably, both calculations yielded consistent results, further validating the obtained p–d wavefunction and its ability to describe the measured p–d correlation function.

The measured p–d correlation function exhibits sensitivity to the inclusion of partial waves within the correlation function. The calculated correlation function using the HH method and AV18+UIX interactions only in the $J^\pi = \frac{1}{2}^+, \frac{3}{2}^+$ partial waves relative to the p–d system, which are dominated by the s wave contributions. While this calculation moderately describes the data, it falls short in accurately capturing the behavior observed at small relative momenta. However, the agreement between the calculated correlation function and the measured data improves when additional partial waves, specifically up to $J^\pi = \frac{7}{2}^-$, are included in the calculation. In this extended calculation, the contributions from p-waves become dominant, leading to a better agreement with the experimental results with the n_σ remaining consistently close to or below one across the entire range of energies.

In addition, this measurement also aimed to investigate the impact of genuine three-body forces by excluding the UIX potential from the HH approach. The theoretical calculation predicts that the effect of the 3N interaction on the source size, with two nucleons at $r_{\text{eff}}^{\text{NN}} = 1.4$ fm, is at most 3%. However, this effect increases to 5% for a smaller source size with $r_{\text{eff}}^{\text{NN}} = 1$ fm. It is important to note that the current p–d correlation function comprises only 3850 pairs below $k^* < 200$ MeV/c. Consequently, the precision of the current measurement lacks the required sensitivity to distinguish contributions originating from genuine three-body interaction terms present in the nuclear Hamiltonian. Therefore, while calculations incorporating the full three-body dynamics yield compatible results, further advancements in measurement precision are necessary to achieve a more precise understanding of the specific contributions and interactions arising from the genuine three-body terms in the nuclear Hamiltonian.

Nonetheless, the anticipated significant improvement in statistics during Run 3 offers promising prospects for conducting more precise studies. Based on the offline trigger for Run 3, a preliminary estimate suggests a substantial increase in the pair statistics. The total number of p–d pairs below $k^* < 200$ MeV/c in the current data taken during Run 3 is $\sim 3.2 \times 10^5$, while for $\overline{\text{p}}$–$\overline{\text{d}}$ pairs, it is $\sim 3.1 \times 10^5$. These numbers are expected to increase by a factor of 2-3, resulting in 4 to 5 orders of magnitude more statistics. This increased statistical significance will enhance the precision of the measurements to 1-2%. With such an increase in the statistics, studying the p–d correlation m_{T} differentially will be possible, enabling investigations at smaller source sizes of $\sim$ 1 fm. This enhanced precision will provide a unique tool to unravel the contributions stemming from genuine three-body interactions and facilitate a more comprehensive investigation of their effects in the p–d system.

The thesis work demonstrated that deuteron-hadron correlation measurements exhibit sensitivity to the three-body dynamics at short distances. This sensitivity opens up opportunities to study combinations of strange or charm hadrons with deuterons. It allows for investigations into the spin-isospin dependence of the strong interaction in these systems.

In the pursuit of studying the strong interaction in three-body systems through Femtoscopy at ALICE, I am excited to mention an intriguing study conducted by my colleague Laura Šerkšytė. She measured three-particle correlations that go beyond the scope of effective two-body correlations involving a deuteron and a hadron. Instead, the study

directly measured the correlation of a system consisting of three unbound particles. Laura Šerkšytė investigated the femtoscopic correlations of p–p–p and p–p–Λ in pp collisions at $\sqrt{s} = 13$ TeV [158]. The analysis revealed that the measured correlation functions were influenced by both two-body and three-body effects, as well as the quantum statistics, Coulomb interactions, and strong interaction. Kubo's cumulant method was employed to study the genuine three-body effects, enabling the separation of correlations induced solely by two interacting particles in a triplet.

The correlation functions and corresponding cumulants were measured for p–p–p and p–p–Λ triplets in pp collisions at $\sqrt{s} = 13$ TeV, utilizing the high-multiplicity data sample recorded by ALICE during Run 2. The analysis revealed that the hadrons were emitted at average relative distances of approximately 1 fm in this collision system, making it a unique experimental setup that allowed exploring three-body interactions at scales smaller than typical inter-particle distances in nuclei. This scenario can be analogously understood as a high-density environment.

Remarkably, both p–p–p and p–p–Λ cumulants exhibited nonzero signals, indicating the presence of genuine three-body effects. Although the data for p–p–p and p–p–Λ correlations in Run 2 were limited, ongoing studies focus on dedicated triggers for p–p–p and p–p–Λ in Run 3. The statistics are expected to increase by orders of magnitude, as extensively discussed in Laura's PhD thesis [159]. With the increased statistics and the complete theoretical development of three-body correlation functions, the ultimate goal of studying the contribution of genuine three-body forces in the system of three hadrons can be achieved in the foreseeable time.

In the second part of this thesis, the production of light (anti-)nuclei, specifically (anti-)deuteron and (anti-)^{3}He, in proton-proton collisions, was investigated. The study employed the Coalescence model in two different approaches.

Firstly, a theoretical approach was employed, focusing on the main observable of the Coalescence factor $\mathcal{B}_A$. This approach used different internal wavefunctions for the deuteron, while a Gaussian wavefunction was used for ^{3}He. The source size for the emission of the nucleons that form light (anti-)nuclei were employed from the fetoscopic source measurement in proton-proton collisions at$\sqrt{s} = 13$ TeV. A significant increase in the calculated coalescence factors $\mathcal{B}_2$ and $\mathcal{B}_3$ was observed as a function of transverse momentum per nucleon (p_{T}/A). The uncertainties in the theoretical predictions are solely arising due to the uncertainties in the determination of source size from the femtoscopic p–p correlations. In the case of deuterons, the prediction using a Gaussian wavefunction for the deuteron is found to be in good agreement with the experimental results obtained by the ALICE collaboration. However, the calculations employing a more accurate wavefunction for the deuteron derived from χEFT (N^{4}LO), which is based on the fundamental symmetries of QCD and describes nucleon-nucleon scattering data with $\chi^2/\mathrm{ndf} \sim 1$, qualitatively reproduced the shape but overestimated the mean values of the data by a factor of approximately 2. Similarly, predictions using the deuteron wavefunctions from the Hulthén potential and a sum of two Gaussians fitted to the Hulthén wavefunction also resulted in an overestimation of the data by a factor of approximately 2. The discrepancy between the more precise wavefunction derived from χEFT and the experimental data suggests the need for further refinement in the theoretical development of the calculation of $\mathcal{B}_A$ by taking into account the space-momentum correlation in the Wigner function of the two-nucleons. In the case of ^{3}He, $\mathcal{B}_3$ consistently overshoots the measurements across all transverse momentum per nucleon ranges. However, using the Gaussian wave function for ^{3}He is rather an oversimplification. It would be interesting to explore different wavefunctions for ^{3}He based on calculations based on the three-body potentials in the Fadeev Equations or the Hyper Spherical harmonics for $A = 3$ approach, which involve the three-body dynamics of the nucleons that form ^{3}He. To investigate different wavefunction hypotheses for ^{3}He, the density matrix formalism needs to be developed for three particles, which can be pursued in future studies.

Secondly, the Coalescence model was employed as an afterburner, incorporating the Wigner formalism and utilizing two different Monte Carlo event generators, namely EPOS 3.117 and PYTHIA 8.3. The emission source size measured in proton-proton collisions was also taken into account. Currently, this model is developed only for the production of (anti-)deuterons productions. The predicted yield successfully reproduces the measured (anti-)deuteron yield in proton-proton collisions at a center-of-mass energy of 13 TeV, collected with a high-multiplicity trigger. An essential aspect of this study is preserving the space-momentum correlation of nucleons, which is achieved by directly adjusting the emitting source provided by the event generators considering the measured source. The constraint to the measured source size allows for a parameter-free prediction of the (anti-)deuteron spectra.

In this study, four different internal wavefunctions of the deuteron have been utilized to calculate the probability of deuteron formation. These wavefunctions include a simple Gaussian, the Hulth'en, the Argonne v_{18}, and the one derived from χEFT (N^{4}LO) calculations. Notably, this is the first instance where coalescence studies have incorporated the Hulth'en, Argonne v_{18}, and χEFT (N^{4}LO) wavefunctions. Among these wavefunctions, both the Argonne v_{18} and χEFT wavefunctions, which are based on a realistic representation of nucleon-nucleon interactions, demonstrate the strongest agreement with the deuteron spectra measured by ALICE. Surprisingly, the predictions obtained from calculations using the Argonne v_{18} and χEFT (N^{4}LO) wavefunctions exhibit exceptional consistency and successfully reproduce the spectra. This finding indicates that the production of the deuteron remains unaffected by extremely short-range interactions, where the wavefunctions from the two approaches differ. Moreover, the excellent agreement between the data and predictions demonstrates that the current state-of-the-art model can accurately predict deuteron spectra by providing correct proton spectra and source sizes as input, without requiring any free parameters.

Additionally, this study highlights the importance of simultaneously measuring the proton production spectra and the size of the emitting source for various collision energies. Such measurements would enable the prediction of (anti-)deuteron production yields for different energies and multiplicities, facilitating a reliable estimation of antideuterons produced in the collisions of cosmic rays with the interstellar medium. This estimation is particularly significant for the search for dark-matter annihilation, where antinuclei are present in the final state.

In the future, it would be beneficial to expand this study to include $A = 3$, where ^{3}He is of great importance. Investigating ^{3}He would provide a more comprehensive understanding of 2N and 3N interactions and composite particle formation in high-energy collisions. Additionally, it would contribute to the study of (anti-)^{3}He produced in cosmic ray collisions with the interstellar medium, which plays a crucial role in the search for dark-matter annihilation with antinuclei as the final products.

In conclusion, the work presented in this thesis marks the beginning of a new era in the study of interactions in many-body systems using Femtoscopy. The findings and methodologies discussed here lay the groundwork for investigating various systems, including those involving strange and charm hadrons, which exhibit bound or unbound ensembles of hadrons. These systems provide the ultimate stage for studying the strong interaction. I eagerly anticipate the upcoming Run 3 and Run 4, where measurements of hadron-deuteron, deuteron-deuteron, and multi-hadron correlations will be conducted. These measurements are crucial for obtaining an accurate equation of state at large densities and, subsequently, advancing our understanding of neutron stars. Future experiments hold great promise for further unraveling the intricacies of the strong interaction in complex many-body systems.

Appendix A

Relevant Publications

- ALICE Collaboration. (2022). Production of light (anti)nuclei in pp collisions at $\sqrt{s} =$ 13 TeV, J. High Energ. Phys., 106 (2022)
- M. Mahlein, L. Barioglio, F. Bellini, L. Fabbietti, C. Pinto, B. Singh, and S. Tripathy. (2023) Novel parameter-free coalescence model for deuteron production, arXiv preprint arXiv:2302.12696 (Submitted to EPJC)
- M. Viviani, S. König, A. Kievsky, L. E. Marcucci, B. Singh, and O. Vázquez Doce. (2023). Role of three-body dynamics in nucleon-deuteron correlation functions, arXiv preprint arXiv:2306.02478 (Submitted to Phys. Rev. C.)
- ALICE Collaboration (2023). Exploring the strong interaction of three-body systems at the LHC, the manuscript is currently under collaboration review rounds.

Appendix B

Details of p–d analysis

B.1 DCA fits of protons

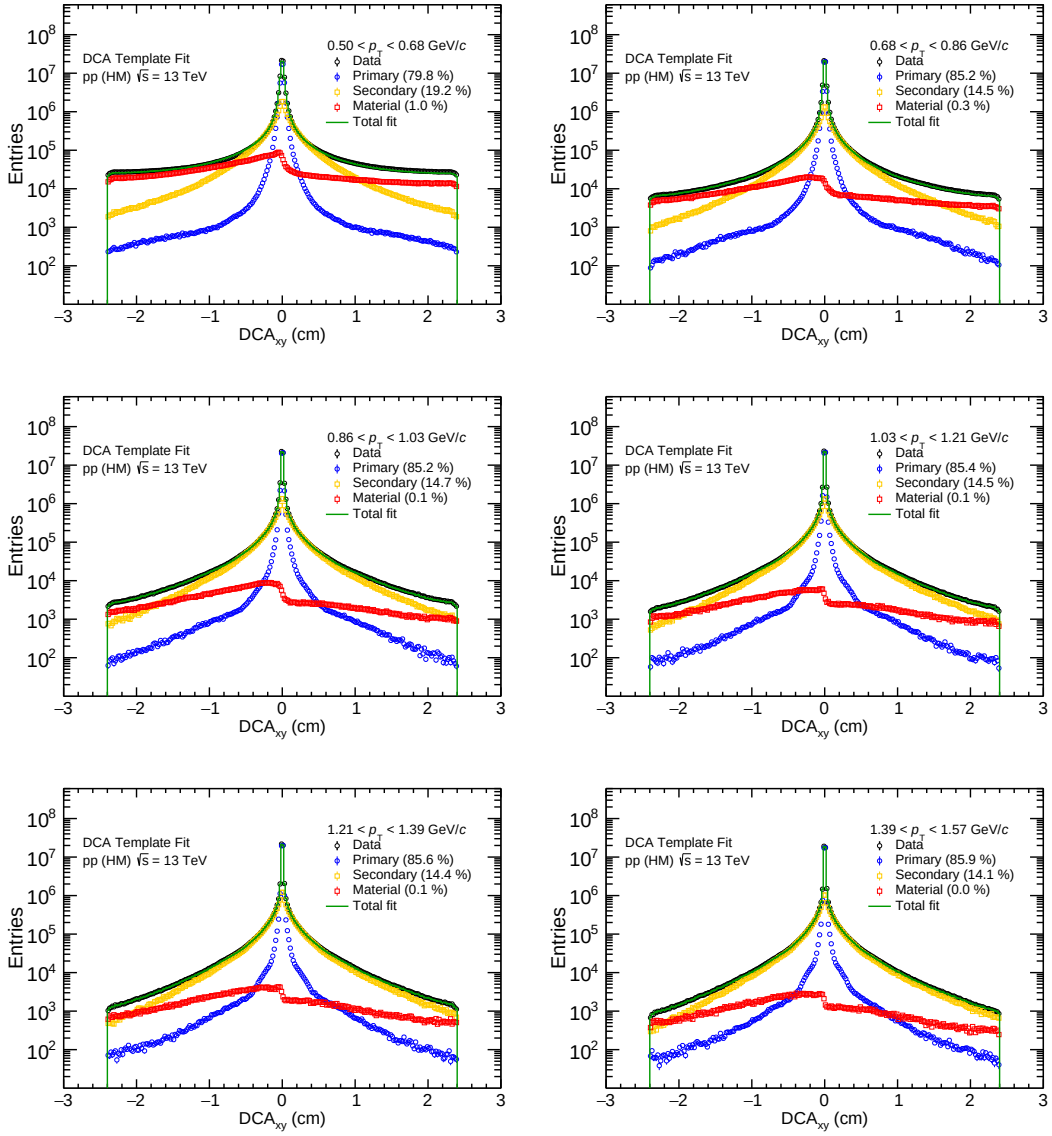

FIGURE B.1: Template fit for the DCA_{xy} distribution for protons in $0.5 < p_{\mathrm{T}} < 1.57\,\mathrm{GeV}/c$.

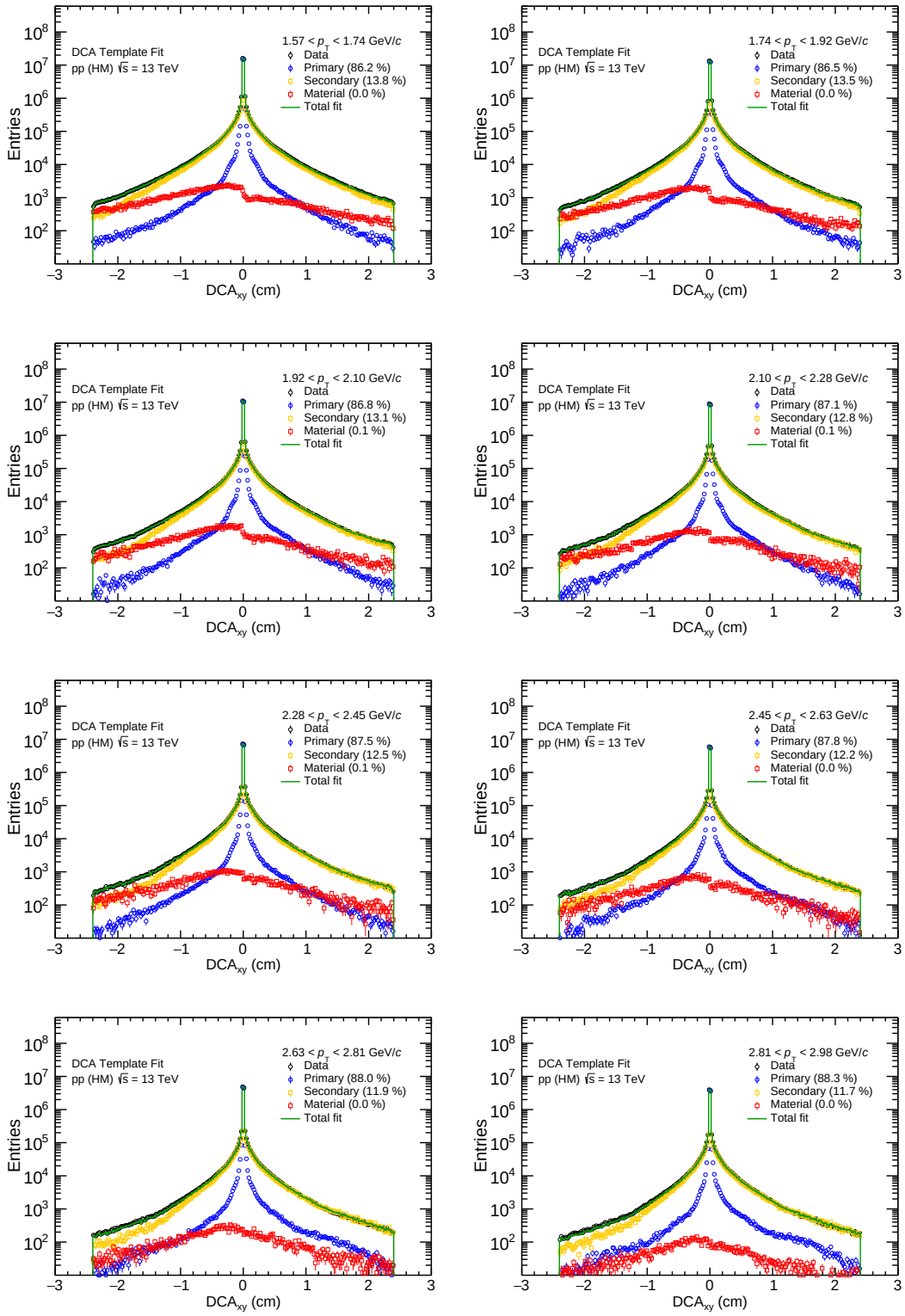

FIGURE B.2: Template fit for the DCA_{xy} distribution for protons in $1.57 < p_{\mathrm{T}} < 2.98\,\mathrm{GeV}/c$.

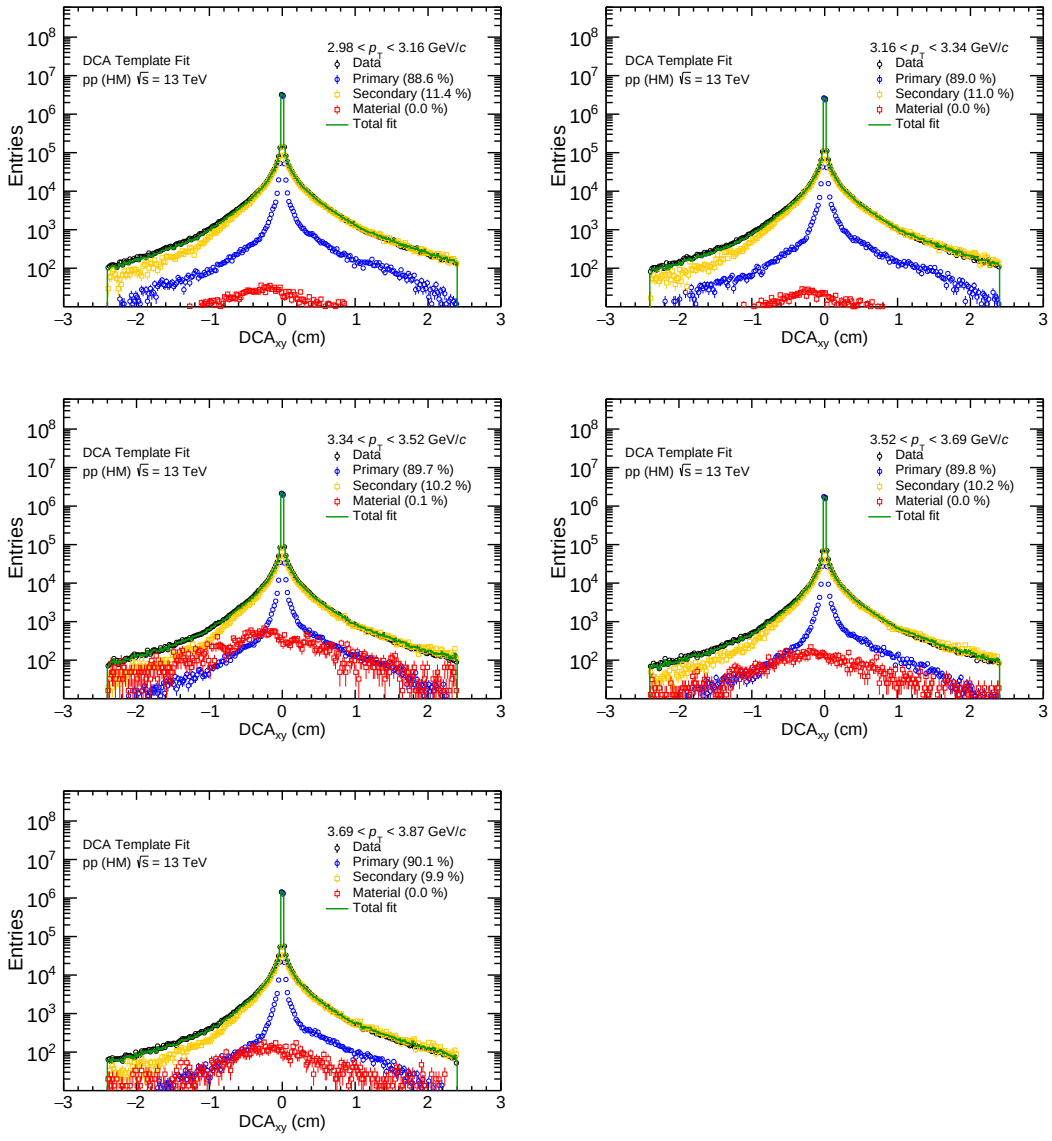

FIGURE B.3: Template fit for the DCA_{xy} distribution for protons in $2.98 < p_T < 4.05\,GeV/c$.

B.2 DCA fits for antiprotons

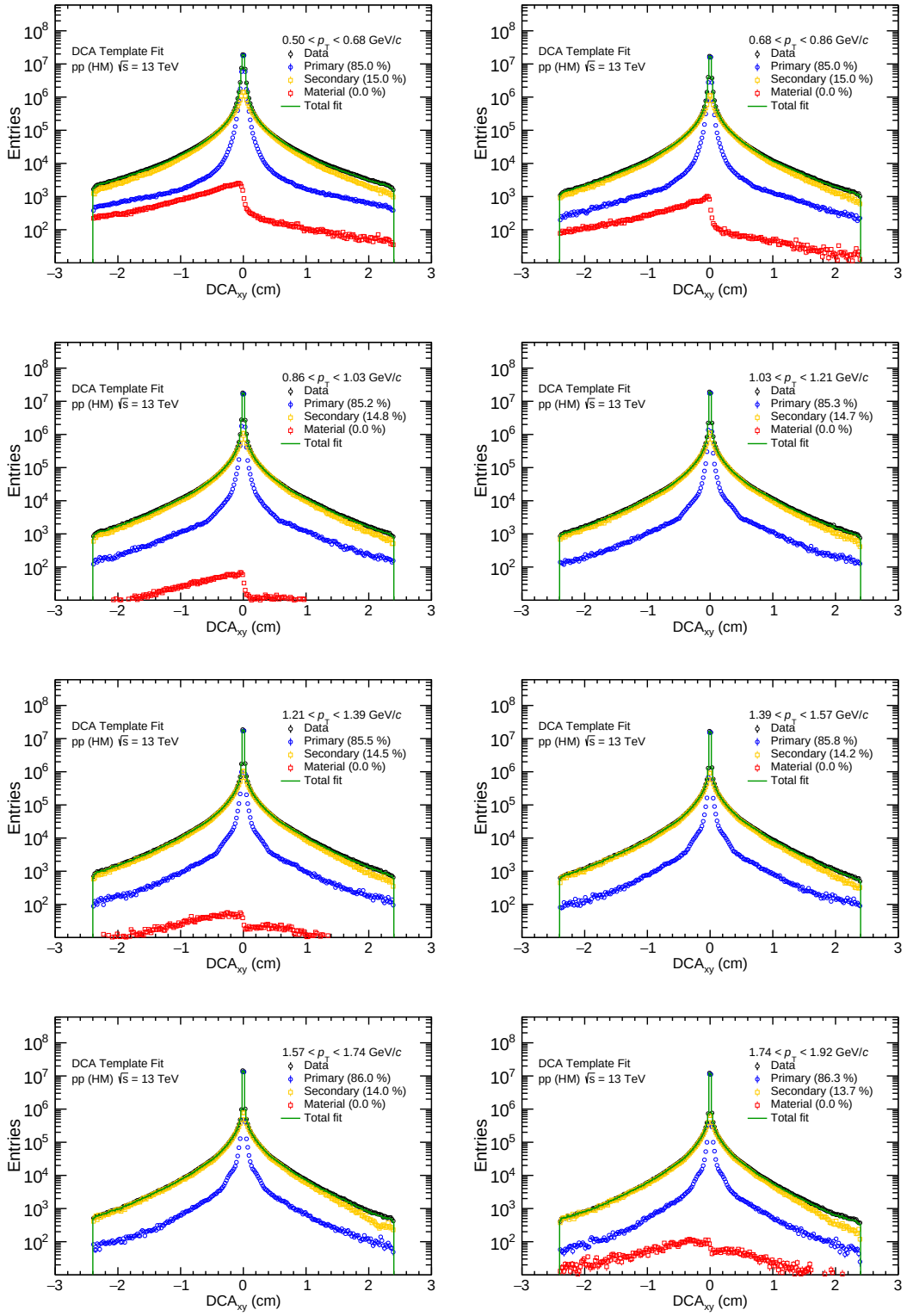

FIGURE B.4: Template fit for the DCA_{xy} distribution for antiprotons in $0.5 < p_{\mathrm{T}} < 1.92\ \mathrm{GeV}/c$.

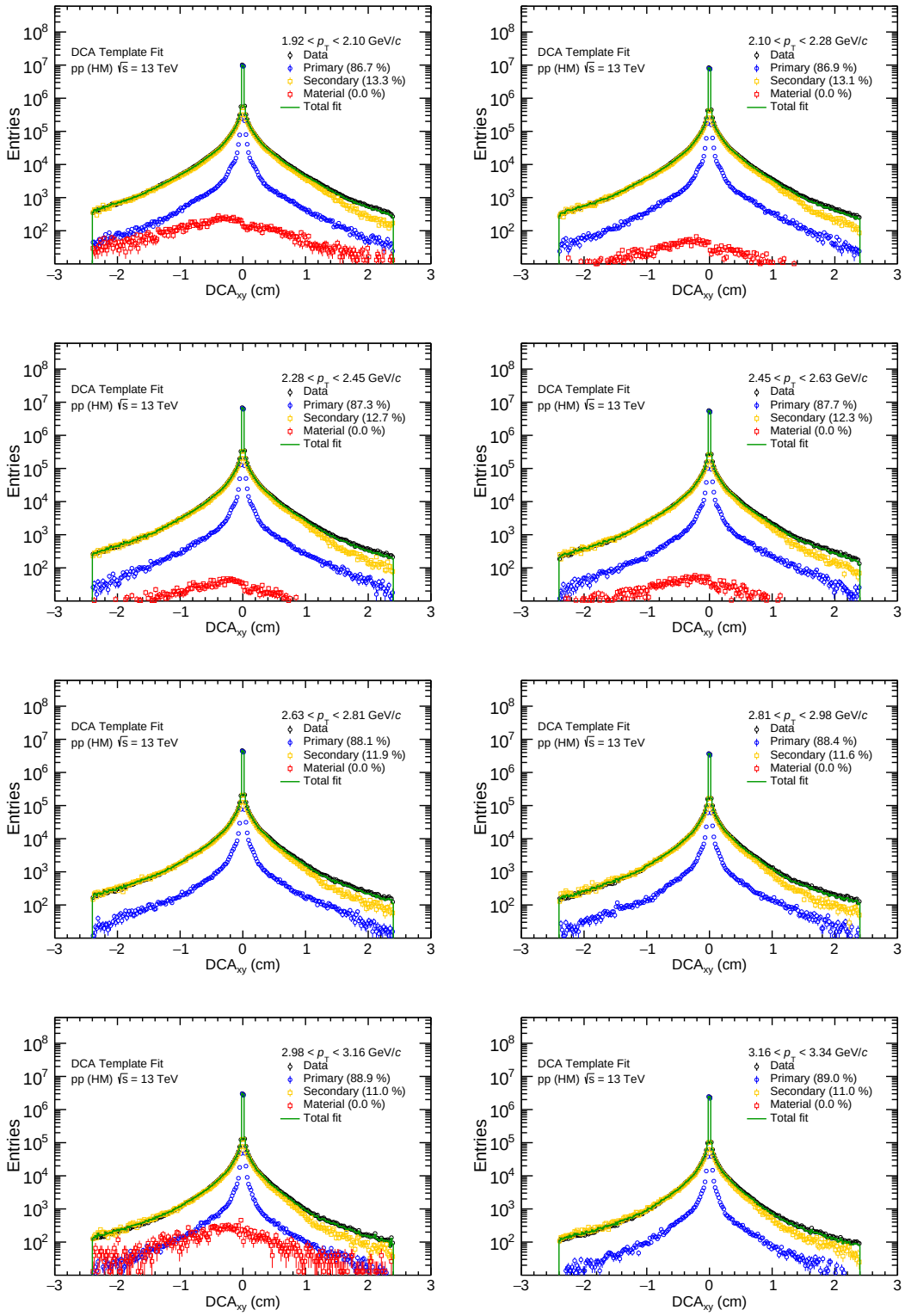

FIGURE B.5: Template fit for the DCA$_{xy}$ distribution for antiprotons in $1.92 < p_{\mathrm{T}} < 3.34\,\mathrm{GeV}/c$.

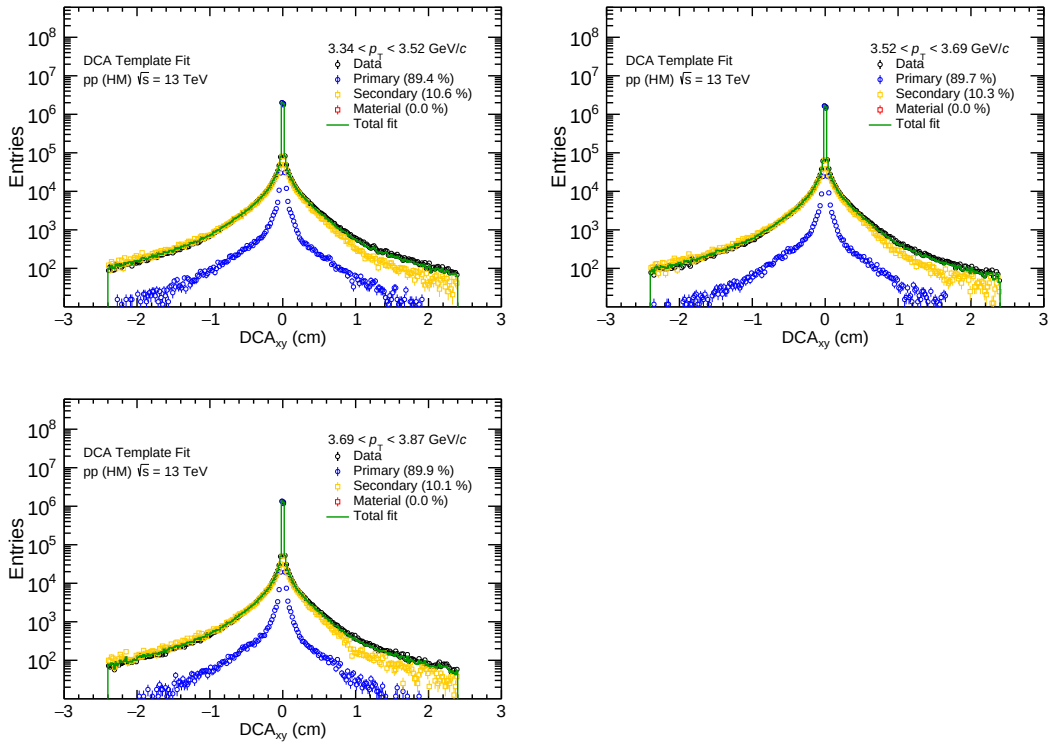

FIGURE B.6: Template fit for the DCA_{xy} distribution for antiprotons in $3.34 < p_{\mathrm{T}} < 4.05\ \mathrm{GeV}/c$.

B.3 TOF mass squared fits for deuterons

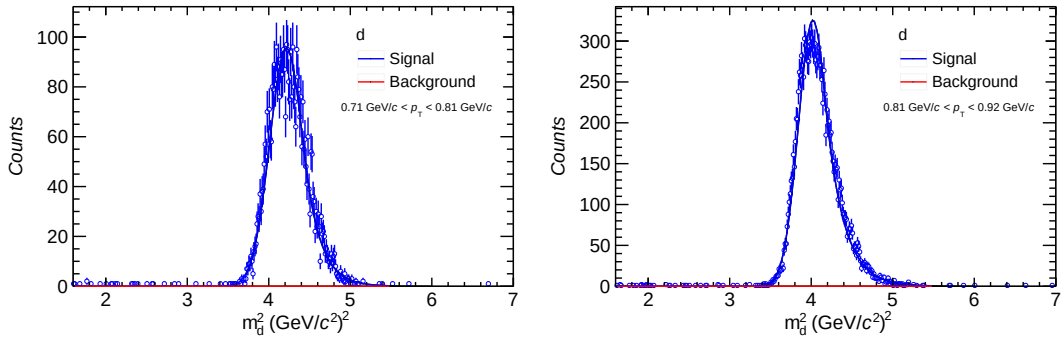

FIGURE B.7: Figures for m^2_{TOF} fits for deuterons in slices of p_{T} in $0.7 < p_{\mathrm{T}} < 0.92\ \mathrm{GeV}/c$.

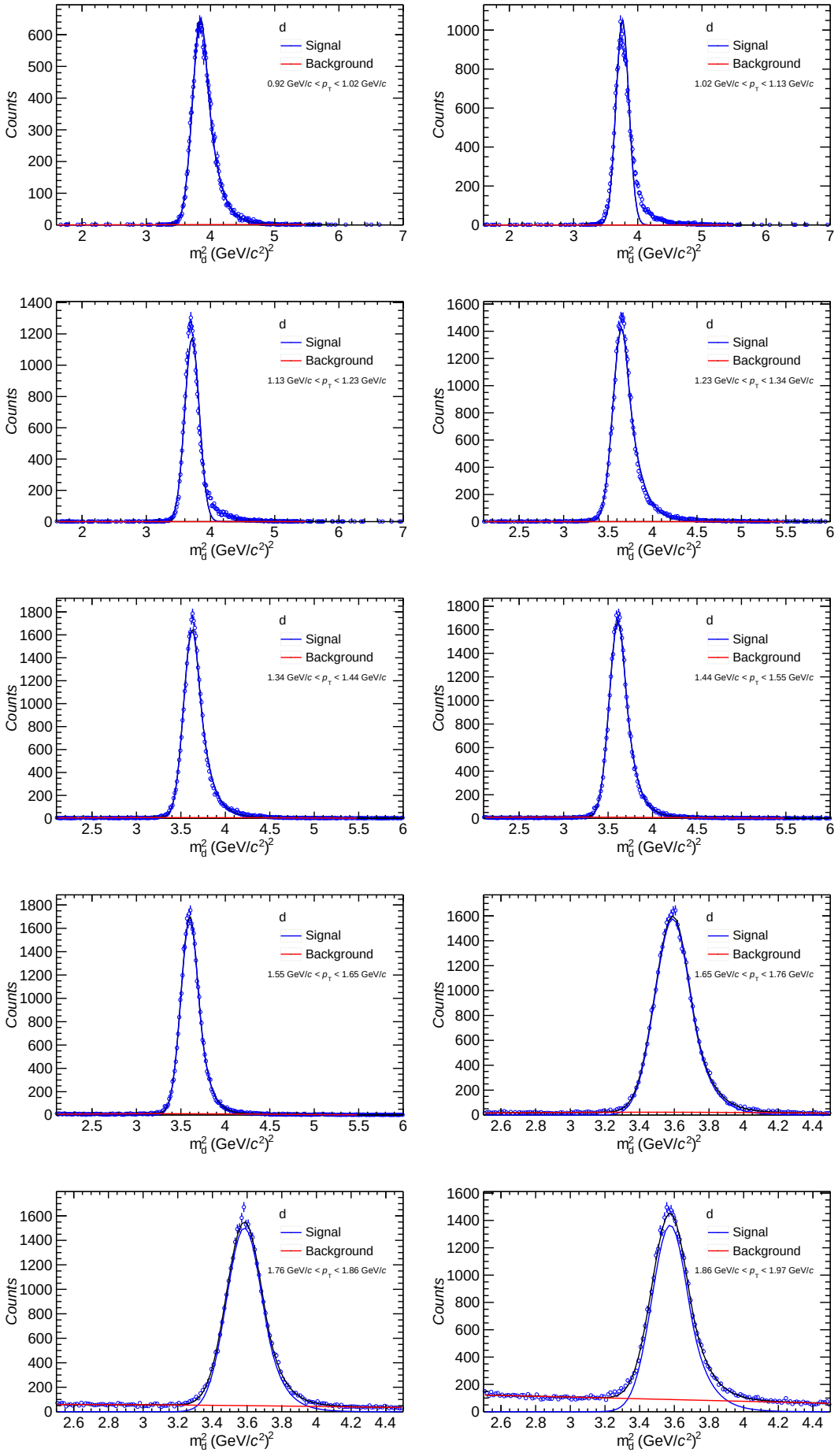

FIGURE B.8: Figures for m^2_{TOF} fits for deuterons in slices of p_{T} in $0.92 < p_{\mathrm{T}} < 1.97\,\mathrm{GeV}/c$.

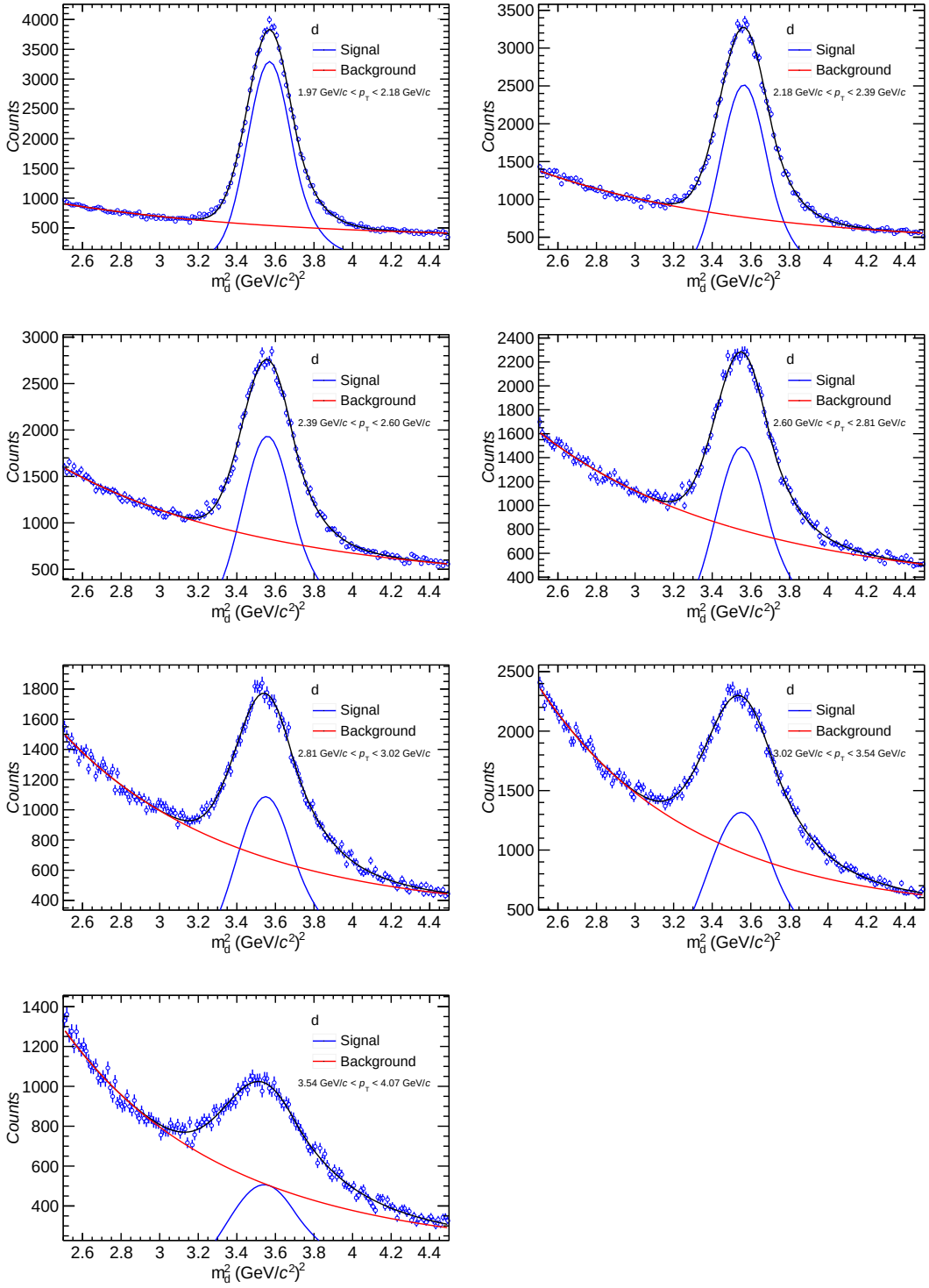

FIGURE B.9: Figures for m^2_{TOF} fits for deuterons in slices of p_{T} in $1.97 < p_{\mathrm{T}} < 4.05\,\mathrm{GeV}/c$.

B.4 TOF mass squared fits for antideuterons

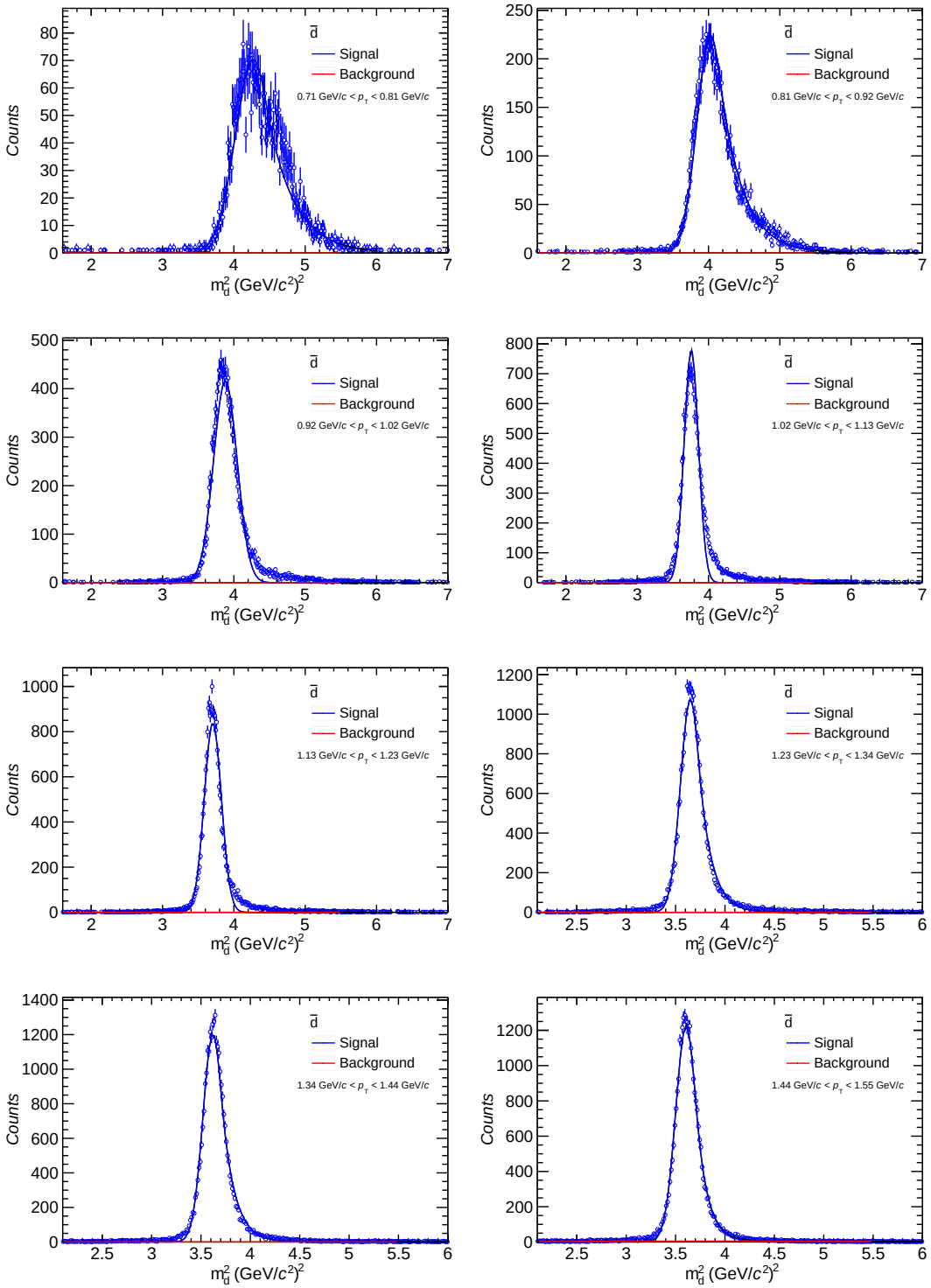

FIGURE B.10: Figures for m^2_{TOF} fits for antideuterons in slices of p_{T} in $0.7 < p_{\mathrm{T}} < 1.57$ GeV/c.

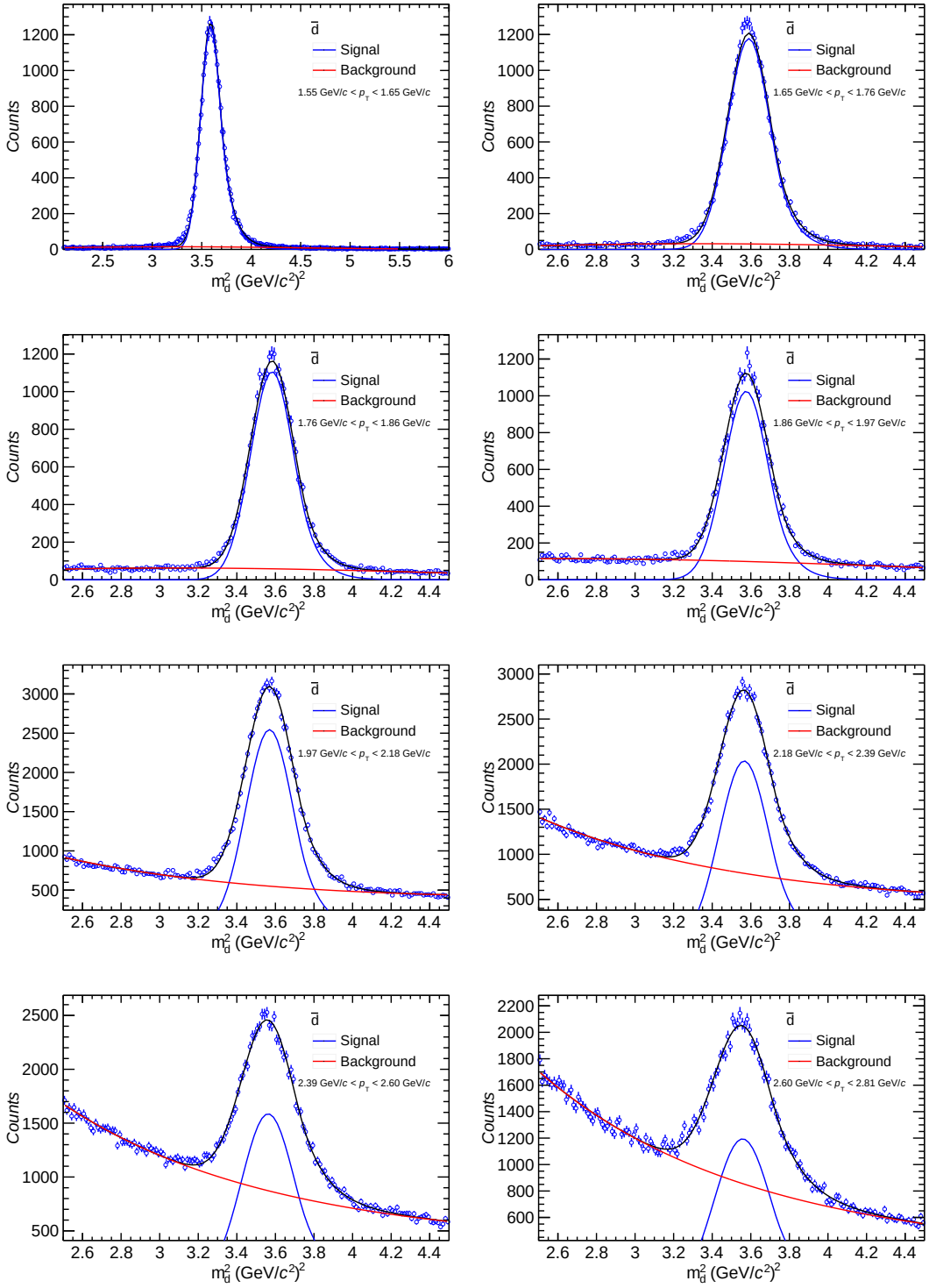

FIGURE B.11: Figures for m^2_{TOF} fits for antideuterons in slices of p_{T} in $1.56 < p_{\mathrm{T}} < 2.81\ \mathrm{GeV}/c$.

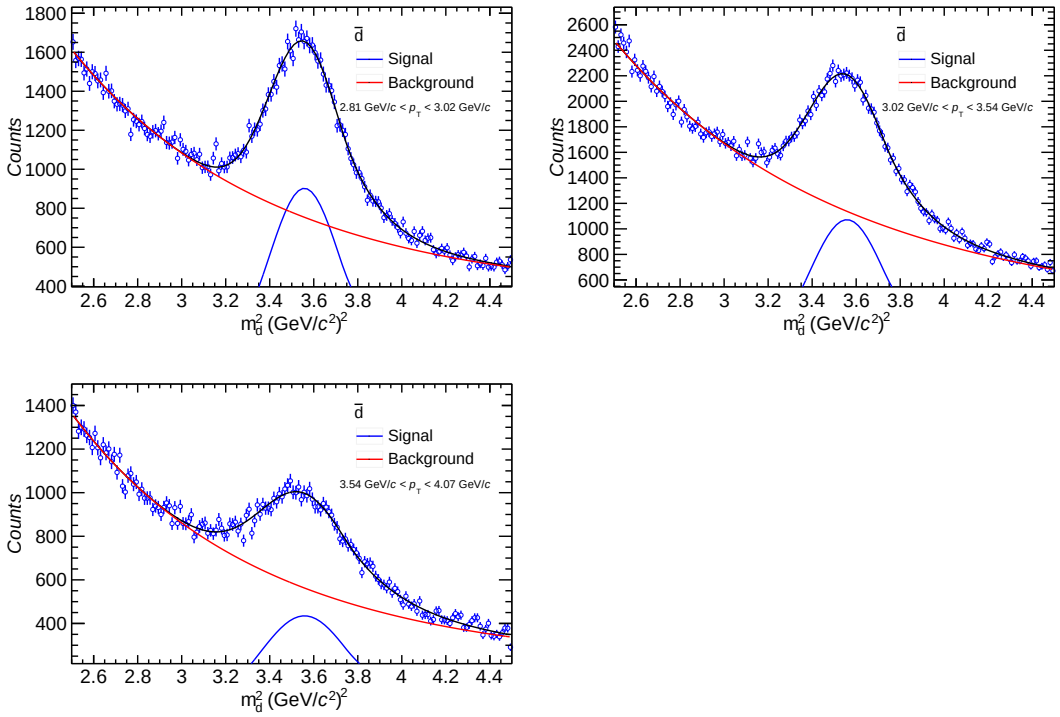

FIGURE B.12: Figures for m^2_{TOF} fits for antideuterons in slices of p_{T} in $2.81 < p_{\mathrm{T}} < 4.05\,\mathrm{GeV}/c$.

B.5 DCA template fits for deuterons

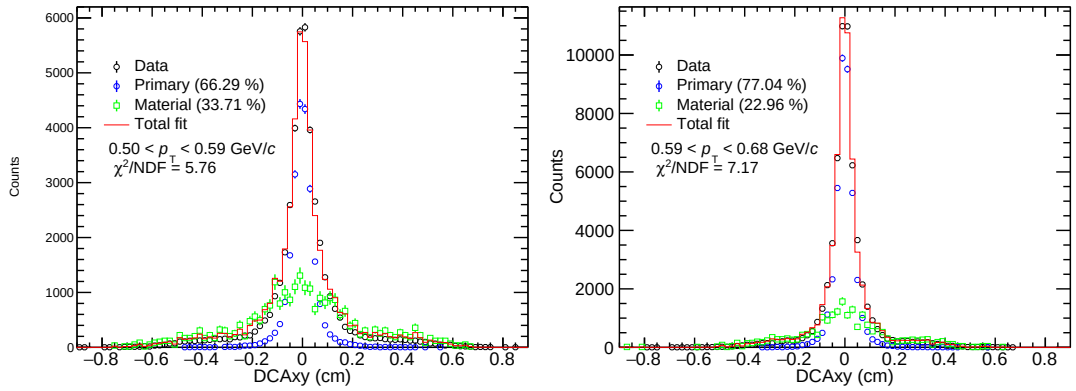

FIGURE B.13: Figures for DCA fits for deuterons in slices of p_{T} in $0.5 < p_{\mathrm{T}} < 0.68\,\mathrm{GeV}/c$.

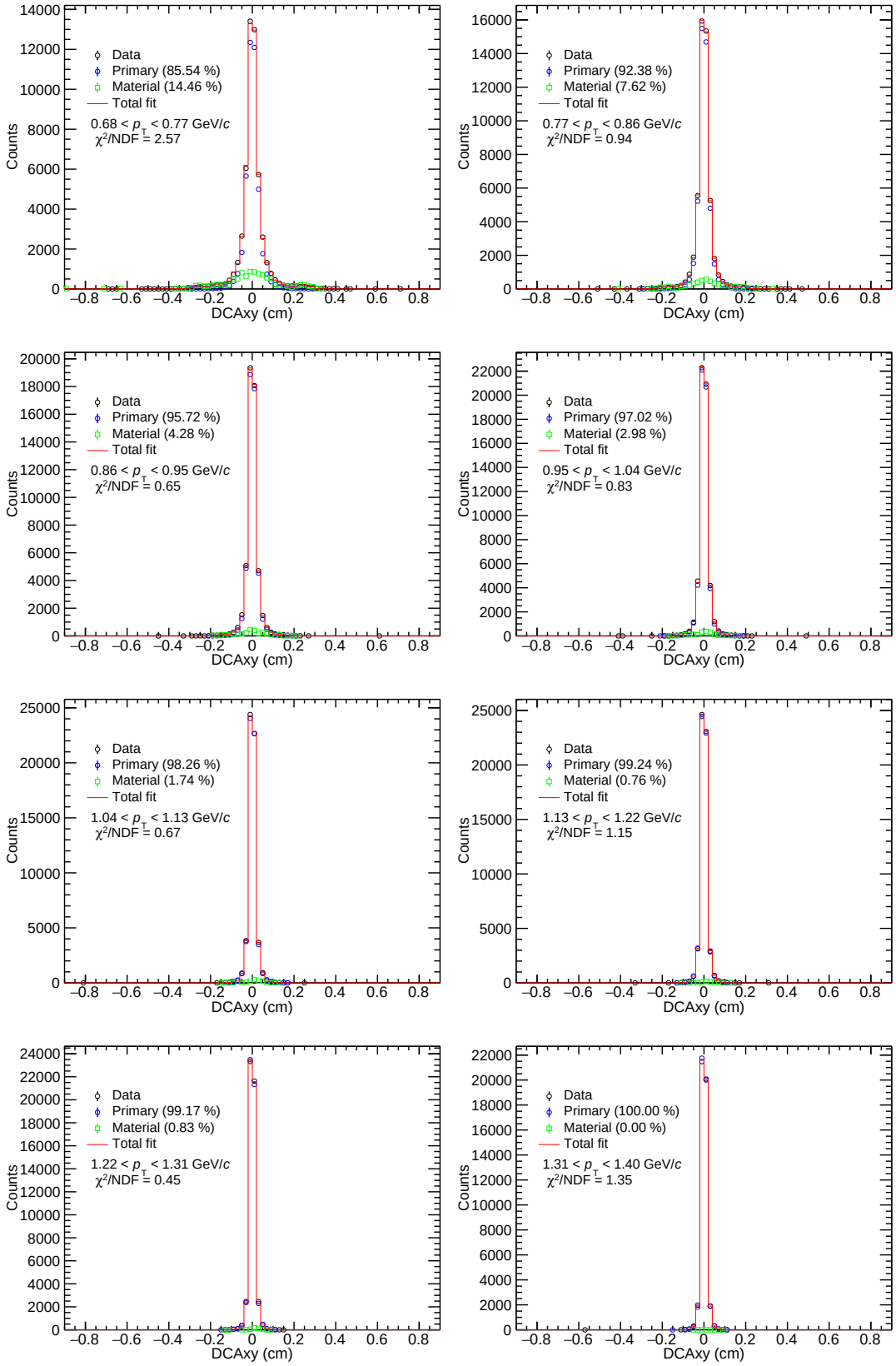

FIGURE B.14: Figures for DCA fits for deuterons in slices of p_T in $0.68 < p_T < 1.4\,\mathrm{GeV}/c$.

Bibliography

[1] A. Akmal, V. R. Pandharipande, and D. G. Ravenhall. The Equation of state of nucleon matter and neutron star structure. *Phys. Rev. C*, 58:1804–1828, 1998. doi: 10.1103/PhysRevC.58.1804. 2, 75

[2] J. M. Lattimer. Neutron Stars and the Nuclear Matter Equation of State. *Ann. Rev. Nucl. Part. Sci.*, 71:433–464, 2021. doi: 10.1146/annurev-nucl-102419-124827.

[3] C. Drischler, J.W. Holt, and C. Wellenhofer. Chiral effective field theory and the high-density nuclear equation of state. *Annual Review of Nuclear and Particle Science*, 71(1): 403–432, 2021. doi: 10.1146/annurev-nucl-102419-041903. URL `https://doi.org/10.1146/annurev-nucl-102419-041903`. 2

[4] Anton Andronic, Peter Braun-Munzinger, Krzysztof Redlich, and Johanna Stachel. Decoding the phase structure of QCD via particle production at high energy. *Nature*, 561:321–330, 2018. doi: 10.1038/s41586-018-0491-6. 2, 24

[5] A. Andronic, P. Braun-Munzinger, J. Stachel, and H. Stöcker. Production of light nuclei, hypernuclei and their antiparticles in relativistic nuclear collisions. *Phys. Lett.*, B697:203–207, 2011. doi: 10.1016/j.physletb.2011.01.053.

[6] F. Becattini, Eduardo Grossi, Marcus Bleicher, Jan Steinheimer, and Reinhard Stock. Centrality dependence of hadronization and chemical freeze-out conditions in heavy ion collisions at $\sqrt{s_{NN}}$ = 2.76 TeV. *Phys. Rev.*, C90:054907, 2014. doi: 10.1103/PhysRevC.90.054907.

[7] Volodymyr Vovchenko and Horst Stöcker. Examination of the sensitivity of the thermal fits to heavy-ion hadron yield data to the modeling of the eigenvolume interactions. *Phys. Rev.*, C95:044904, 2017. doi: 10.1103/PhysRevC.95.044904.

[8] Natasha Sharma, Jean Cleymans, Boris Hippolyte, and Masimba Paradza. A Comparison of p-p, p-Pb, Pb-Pb Collisions in the Thermal Model: Multiplicity Dependence of Thermal Parameters. *Phys. Rev.*, C99:044914, 2019. doi: 10.1103/PhysRevC.99.044914. 2, 24

[9] Tim Neidig, Kai Gallmeister, Carsten Greiner, Marcus Bleicher, and Volodymyr Vovchenko. Towards solving the puzzle of high temperature light (anti)-nuclei production in ultra-relativistic heavy ion collisions. *Phys. Lett. B*, 827:136891, 2022. doi: 10.1016/j.physletb.2022.136891. 2

[10] S. T. Butler and C. A. Pearson. Deuterons from High-Energy Proton Bombardment of Matter. *Phys. Rev.*, 129:836–842, 1963. doi: 10.1103/PhysRev.129.836. 27

[11] Joseph I. Kapusta. Mechanisms for deuteron production in relativistic nuclear collisions. *Phys. Rev. C*, 21:1301–1310, 1980. doi: 10.1103/PhysRevC.21.1301. 28

[12] Rudiger Scheibl and Ulrich W. Heinz. Coalescence and flow in ultrarelativistic heavy ion collisions. *Phys. Rev.*, C59:1585–1602, 1999. doi: 10.1103/PhysRevC.59.1585. 2, 76

[13] Kfir Blum and Masahiro Takimoto. Nuclear coalescence from correlation functions. *Phys. Rev. C*, 99:044913, Apr 2019. doi: 10.1103/PhysRevC.99.044913. URL `https://link.aps.org/doi/10.1103/PhysRevC.99.044913`. 114, 117, 118, 119, 120, 121, 125, 127, 128, 142, 144

[14] Kai-Jia Sun, Che Ming Ko, and Benjamin Dönigus. Suppression of light nuclei production in collisions of small systems at the Large Hadron Collider. *Phys. Lett. B*, 792: 132–137, 2019. doi: 10.1016/j.physletb.2019.03.033.

[15] M. Kachelrieß, S. Ostapchenko, and J. Tjemsland. Revisiting cosmic ray antinuclei fluxes with a new coalescence model. *JCAP*, 08:048, 2020. doi: 10.1088/1475-7516/2020/08/048. 125

[16] Shreyasi Acharya et al. Hypertriton Production in p-Pb Collisions at $\sqrt{s_{NN}}$=5.02 TeV. *Phys. Rev. Lett.*, 128(25):252003, 2022. doi: 10.1103/PhysRevLett.128.252003. 2, 76

[17] David Griffiths.
Introduction to Elementary Particles.
Wiley-VCH, 2008. ISBN 978-3-527-40601-2. 3, 4

[18] Wikipedia.
Standard Model
`https://en.wikipedia.org/wiki/Standard_Model`
Accessed: 3rd Dec 2020, 2020. 3

[19] David J. Gross and Frank Wilczek. Ultraviolet behavior of non-abelian gauge theories. *Phys. Rev. Lett.*, 30:1343–1346, Jun 1973. doi: 10.1103/PhysRevLett.30.1343. URL `https://link.aps.org/doi/10.1103/PhysRevLett.30.1343`. 4

[20] Steven Weinberg. Non-abelian gauge theories of the strong interactions. *Phys. Rev. Lett.*, 31:494–497, Aug 1973. doi: 10.1103/PhysRevLett.31.494. URL `https://link.aps.org/doi/10.1103/PhysRevLett.31.494`.

[21] H. Fritzsch, M. Gell-Mann, and H. Leutwyler. Advantages of the color octet gluon picture. *Physics Letters B*, 47(4):365–368, 1973. ISSN 0370-2693. doi: https://doi.org/10.1016/0370-2693(73)90625-4. URL `https://www.sciencedirect.com/science/article/pii/0370269373906254`. 4

[22] Michiel Botje Lecures (Nikhef, Science Park, Amsterdam).
Lecture notes Particle Physics II, Asymptotic Freedom
`https://www.nikhef.nl/~h24/qcdcourse/section-6.pdf`
Accessed: 3rd Dec 2020, 2013. 6

[23] Peter W. Higgs. Broken symmetries and the masses of gauge bosons. *Phys. Rev. Lett.*, 13:508–509, Oct 1964. doi: 10.1103/PhysRevLett.13.508. URL `https://link.aps.org/doi/10.1103/PhysRevLett.13.508`. 6

[24] PDG. Review of particle physics. *Phys. Rev. D*, 98:030001, Aug 2018. doi: 10.1103/PhysRevD.98.030001. URL `https://link.aps.org/doi/10.1103/PhysRevD.98.030001`. 7

[25] R. Rapp, J. Wambach, and H. van Hees. The chiral restoration transition of qcd and low mass dileptons: Datasheet from landolt-börnstein - group i elementary particles, nuclei and atoms · volume 23: "relativistic heavy ion physics" in springermaterials (https://doi.org/10.1007/978-3-642-01539-7_6), 2010. URL `https://materials.springer.com/lb/docs/sm_lbs_978-3-642-01539-7_6`. 7

[26] S. Klimt, M. Lutz, and W. Weise. Chiral phase transition in the su(3) nambu and jona-lasinio model. *Physics Letters B*, 249(3):386–390, 1990. ISSN 0370-2693. doi: https://doi.org/10.1016/0370-2693(90)91003-T. URL `https://www.sciencedirect.com/science/article/pii/037026939091003T`. 7

[27] W Glöckle. *The quantum mechanical few-body problem*. Texts and monographs in physics. Springer, Berlin, 1983. doi: 10.1007/978-3-642-82081-6. URL `https://cds.cern.ch/record/99109`. 8

[28] A. M. Mukhamedzhanov, V. Eremenko, and A. I. Sattarov. Generalized faddeev equations in the alt-grassberger-sandhas form for deuteron stripping with explicit inclusion of target excitations and coulomb interaction. *Phys. Rev. C*, 86:034001, Sep 2012. doi: 10.1103/PhysRevC.86.034001. URL https://link.aps.org/doi/10.1103/PhysRevC.86.034001. 8

[29] V. G. J. Stoks, R. A. M. Klomp, C. P. F. Terheggen, and J. J. de Swart. Construction of high-quality nn potential models. *Phys. Rev. C*, 49:2950–2962, Jun 1994. doi: 10.1103/PhysRevC.49.2950. URL https://link.aps.org/doi/10.1103/PhysRevC.49.2950. 9

[30] R. Machleidt, F. Sammarruca, and Y. Song. Nonlocal nature of the nuclear force and its impact on nuclear structure. *Phys. Rev. C*, 53:R1483–R1487, Apr 1996. doi: 10.1103/PhysRevC.53.R1483. URL https://link.aps.org/doi/10.1103/PhysRevC.53.R1483. 9

[31] R. B. Wiringa, V. G. J. Stoks, and R. Schiavilla. Accurate nucleon-nucleon potential with charge-independence breaking. *Phys. Rev. C*, 51:38–51, 1995. doi: 10.1103/PhysRevC.51.38. 9, 75, 121, 132

[32] D. R. Entem, R. Machleidt, and Y. Nosyk. High-quality two-nucleon potentials up to fifth order of the chiral expansion. *Phys. Rev. C*, 96(2):024004, 2017. doi: 10.1103/PhysRevC.96.024004. 9, 121, 123, 143

[33] D. R. Entem and R. Machleidt. Accurate charge-dependent nucleon-nucleon potential at fourth order of chiral perturbation theory. *Phys. Rev. C*, 68:041001, Oct 2003. doi: 10.1103/PhysRevC.68.041001. URL https://link.aps.org/doi/10.1103/PhysRevC.68.041001. 9

[34] A. Kievsky, M. Viviani, and L. E. Marcucci. $n-d$ scattering including electromagnetic forces. *Phys. Rev. C*, 69:014002, Jan 2004. doi: 10.1103/PhysRevC.69.014002. URL https://link.aps.org/doi/10.1103/PhysRevC.69.014002. 10, 107

[35] Kimiko Sekiguchi. Experimental approach to three-nucleon forces via few-nucleon scattering. *Few-Body Systems*, 60, Aug 2019. doi: 10.1007/s00601-019-1523-y. URL https://doi.org/10.1007/s00601-019-1523-y. 10, 11

[36] H. Witała, A. Nogga, H. Kamada, W. Glöckle, J. Golak, and R. Skibiński. Modern nuclear force predictions for the neutron-deuteron scattering lengths. *Phys. Rev. C*, 68:034002, Sep 2003. doi: 10.1103/PhysRevC.68.034002. URL https://link.aps.org/doi/10.1103/PhysRevC.68.034002. 10

[37] Steven C. Pieper, V. R. Pandharipande, R. B. Wiringa, and J. Carlson. Realistic models of pion-exchange three-nucleon interactions. *Phys. Rev. C*, 64:014001, Jun 2001. doi: 10.1103/PhysRevC.64.014001. URL https://link.aps.org/doi/10.1103/PhysRevC.64.014001. 10

[38] Alessandro Lovato, Omar Benhar, Stefano Fantoni, Alexey Yu. Illarionov, and Kevin E. Schmidt. Density-dependent nucleon-nucleon interaction from three-nucleon forces. *Phys. Rev. C*, 83:054003, May 2011. doi: 10.1103/PhysRevC.83.054003. URL https://link.aps.org/doi/10.1103/PhysRevC.83.054003. 11

[39] Jun-ichi Fujita and Hironari Miyazawa. Pion Theory of Three-Body Forces. *Progress of Theoretical Physics*, 17(3):360–365, 03 1957. ISSN 0033-068X. doi: 10.1143/PTP.17.360. URL https://doi.org/10.1143/PTP.17.360. 10

[40] B. S. Pudliner, V. R. Pandharipande, J. Carlson, and R. B. Wiringa. Quantum monte carlo calculations of $A \leq 6$ nuclei. *Phys. Rev. Lett.*, 74:4396–4399, May 1995. doi: 10.1103/PhysRevLett.74.4396. URL https://link.aps.org/doi/10.1103/PhysRevLett.74.4396. 12

[41] E. Epelbaum, A. Nogga, W. Glöckle, H. Kamada, Ulf-G. Meißner, and H. Witała. Three-nucleon forces from chiral effective field theory. *Phys. Rev. C*, 66:064001, Dec 2002. doi: 10.1103/PhysRevC.66.064001. URL https://link.aps.org/doi/10.1103/PhysRevC.66.064001. 12

[42] V. Bernard, E. Epelbaum, H. Krebs, and Ulf-G. Meißner. Subleading contributions to the chiral three-nucleon force: Long-range terms. *Phys. Rev. C*, 77:064004, 2008.

[43] V. Bernard, E. Epelbaum, H. Krebs, and Ulf-G. Meißner. Subleading contributions to the chiral three-nucleon force. II. short-range terms and relativistic corrections. *Phys. Rev. C*, 84:054001, Nov 2011. doi: 10.1103/PhysRevC.84.054001. URL https://link.aps.org/doi/10.1103/PhysRevC.84.054001.

[44] H. Krebs, A. Gasparyan, and E. Epelbaum. Chiral three-nucleon force at n4lo: Longest-range contributions. *Physical Review C*, 85(5):054006, May 2012. 12

[45] A. Kievsky, M. Viviani, L. Girlanda, and L. E. Marcucci. Comparative study of three-nucleon force models in $a = 3, 4$ systems. *Phys. Rev. C*, 81:044003, Apr 2010. doi: 10.1103/PhysRevC.81.044003. URL https://link.aps.org/doi/10.1103/PhysRevC.81.044003. 13

[46] R. Hanbury Brown and R.Q. Twiss.
A Test of a new type of stellar interferometer on Sirius.
Nature, 178:1046–1048, 1956. doi: 10.1038/1781046a0. 13

[47] Gerson Goldhaber, William B. Fowler, Sulamith Goldhaber, T. F. Hoang, Theodore E. Kalogeropoulos, and Wilson M. Powell. Pion-pion correlations in antiproton annihilation events. *Phys. Rev. Lett.*, 3:181–183, Aug 1959. doi: 10.1103/PhysRevLett.3.181. URL https://link.aps.org/doi/10.1103/PhysRevLett.3.181. 13

[48] Gerson Goldhaber, Sulamith Goldhaber, Won-Yong Lee, and Abraham Pais.
Influence of Bose-Einstein statistics on the anti-proton proton annihilation process.
Phys. Rev., 120:300–312, 1960. doi: 10.1103/PhysRev.120.300. 13

[49] Michael Annan Lisa, Scott Pratt, Ron Soltz, and Urs Wiedemann.
FEMTOSCOPY IN RELATIVISTIC HEAVY ION COLLISIONS: Two Decades of Progress.
Annual Review of Nuclear and Particle Science, 55(1):357–402, 2005. doi: 10.1146/annurev.nucl.55.090704.151533. 13, 14, 16, 126

[50] Ulrich Heinz and Barbara V. Jacak. Two-particle correlations in relativistic heavy-ion collisions. *Annual Review of Nuclear and Particle Science*, 49(1):529–579, 1999. doi: 10.1146/annurev.nucl.49.1.529. URL https://doi.org/10.1146/annurev.nucl.49.1.529. 13

[51] Richard Lednicky.
Finite-size effects on two-particle production in continuous and discrete spectrum.
Phys. Part. Nucl., 40:307–352, 2009. doi: 10.1134/S1063779609030034. 14, 15, 18, 19, 47, 48, 77

[52] Steven E. Koonin. Proton pictures of high-energy nuclear collisions. *Physics Letters B*, 70(1):43–47, 1977. ISSN 0370-2693. doi: https://doi.org/10.1016/0370-2693(77)90340-9. URL https://www.sciencedirect.com/science/article/pii/0370269377903409. 15

[53] ALICE Collaboration.
Femtoscopy of pp collisions at $\sqrt{s} = 0.9$ and 7 TeV at the LHC with two-pion Bose-Einstein correlations.
Phys. Rev. D, 84:112004, 2011. doi: 10.1103/PhysRevD.84.112004. 16

[54] ALICE Collaboration.
Two-pion femtoscopy in p-Pb collisions at $\sqrt{s_{\mathrm{NN}}} = 5.02$ TeV.
Phys. Rev. C, 91:034906, 2015. doi: 10.1103/PhysRevC.91.034906. 16

[55] S. Acharya et al. Kaon femtoscopy in pb-pb collisions at $\sqrt{s_{\mathrm{NN}}}$ = 2.76 tev. *Physical Review C*, 96(6):064613, 2017. 16

[56] ALICE Collaboration.
Search for a common baryon source in high-multiplicity pp collisions at the LHC.
Physics Letters B, 811:135849, 2020. doi: 10.1016/j.physletb.2020.135849. 16, 42, 51, 78, 95, 100, 112, 125, 126, 129, 137, 138, 139, 140, 142, 143, 144, 145

[57] D.L. Mihaylov, V. Mantovani Sarti, O.W. Arnold, L. Fabbietti, B. Hohlweger, and A.M. Mathis.
A femtoscopic Correlation Analysis Tool using the Schrödinger equation (CATS).
Eur. Phys. J. C, 78(5):394, 2018. doi: 10.1140/epjc/s10052-018-5859-0. 16, 17, 42, 101

[58] Dimitar Lubomirov Mihaylov. Analysis techniques for femtoscopy and correlation studies in small collision systems and their applications to the investigation of p–Λ and $\Lambda - \Lambda$ interactions with ALICE. *PhD thesis, Technical University of Munich*, 2021. 17, 86

[59] Andreas Mathis.
First Measurement of the Proton–Σ^0 Interaction via the Femtoscopy Method.
PhD thesis, Technical University of Munich, 2020. 18, 87, 100

[60] Robert B. Wiringa, V.G.J. Stoks, and R. Schiavilla.
An Accurate nucleon-nucleon potential with charge independence breaking.
Phys. Rev. C, 51:38–51, 1995. doi: 10.1103/PhysRevC.51.38. 17, 42, 43, 100

[61] R. Lednicky and V.L. Lyuboshits.
Final State Interaction Effect on Pairing Correlations Between Particles with Small Relative Momenta.
Sov. J. Nucl. Phys., 35:770, 1982. 18, 48

[62] G. Gamow. Expanding universe and the origin of elements. *Phys. Rev.*, 70:572–573, Oct 1946. doi: 10.1103/PhysRev.70.572.2. URL `https://link.aps.org/doi/10.1103/PhysRev.70.572.2`. 20

[63] R. A. Alpher, H. Bethe, and G. Gamow. The origin of chemical elements. *Phys. Rev.*, 73: 803–804, Apr 1948. doi: 10.1103/PhysRev.73.803. URL `https://link.aps.org/doi/10.1103/PhysRev.73.803`. 20

[64] John Ellis. From little bangs to the big bang. *Journal of Physics: Conference Series*, 50(1): 8, nov 2006. doi: 10.1088/1742-6596/50/1/002. URL `https://dx.doi.org/10.1088/1742-6596/50/1/002`. 20

[65] Jordi José and Christian Iliadis. Nuclear astrophysics: the unfinished quest for the origin of the elements. *Reports on Progress in Physics*, 74(9):096901, aug 2011. doi: 10.1088/0034-4885/74/9/096901. URL `https://dx.doi.org/10.1088/0034-4885/74/9/096901`. 20

[66] Alinka Lépine-Szily and Pierre Descouvemont. Nuclear astrophysics: nucleosynthesis in the universe. *International Journal of Astrobiology*, 11(4):243–250, 2012. doi: 10.1017/S1473550412000158. 20

[67] John C. Mather et al. Measurement of the Cosmic Microwave Background spectrum by the COBE FIRAS instrument. *Astrophys. J.*, 420:439–444, 1994. doi: 10.1086/173574. 21

[68] Amol Upadhye, Steven S. Gubser, and Justin Khoury. Unveiling chameleon fields in tests of the gravitational inverse-square law. *Phys. Rev. D*, 74:104024, Nov 2006. doi: 10.1103/PhysRevD.74.104024. URL `https://link.aps.org/doi/10.1103/PhysRevD.74.104024`. 21

[69] Rajeev S. Bhalerao. Relativistic heavy-ion collisions, 2014. 21

[70] Wit Busza, Krishna Rajagopal, and Wilke van der Schee.
Heavy Ion Collisions: The Big Picture, and the Big Questions.
Ann. Rev. Nucl. Part. Sci., 68:339–376, 2018. doi: 10.1146/annurev-nucl-101917-020852. 21

[71] V. T. Cocconi, T. Fazzini, G. Fidecaro, M. Legros, N. H. Lipman, and A. W. Merrison. Mass Analysis of the Secondary Particles Produced by the 25-Gev Proton Beam of the Cern Proton Synchrotron. *Phys. Rev. Lett.*, 5:19–21, 1960. doi: 10.1103/PhysRevLett.5.19. 24, 75

[72] S. Nagamiya. Experimental overview. *Nucl. Phys. A*, 544:5C–26C, 1992. doi: 10.1016/0375-9474(92)90562-X. 24, 75

[73] C. Adler et al. Anti-deuteron and anti-He-3 production in s(NN)**(1/2) = 130-GeV Au+Au collisions. *Phys. Rev. Lett.*, 87:262301, 2001. doi: 10.1103/PhysRevLett.87.262301. [Erratum: Phys.Rev.Lett. 87, 279902 (2001)]. 24, 75

[74] S. S. Adler et al. Deuteron and antideuteron production in Au + Au collisions at s(NN)**(1/2) = 200-GeV. *Phys. Rev. Lett.*, 94:122302, 2005. doi: 10.1103/PhysRevLett.94.122302.

[75] H. Agakishiev et al. Observation of the antimatter helium-4 nucleus. *Nature*, 473:353, 2011. doi: 10.1038/nature10079. [Erratum: Nature 475, 412 (2011)]. 75

[76] S. Acharya and Others. Production of light (anti)nuclei in pp collisions at $\sqrt{s} = 13$ TeV. *Journal of High Energy Physics*, 2022(1):106, 2022. doi: 10.1007/JHEP01(2022)106. URL `https://doi.org/10.1007/JHEP01(2022)106`. 28, 113, 126, 137, 141

[77] Jaroslav Adam et al. Production of light nuclei and anti-nuclei in pp and Pb-Pb collisions at energies available at the CERN Large Hadron Collider. *Phys. Rev. C*, 93(2):024917, 2016. doi: 10.1103/PhysRevC.93.024917. 28, 75, 114

[78] S. Acharya et al. (Anti-)deuteron production in pp collisions at $\sqrt{s} = 13$ TeV. *Eur. Phys. J. C*, 80(9):889, 2020. doi: 10.1140/epjc/s10052-020-8256-4. 114

[79] Shreyasi Acharya et al. Measurement of deuteron spectra and elliptic flow in Pb-Pb collisions at $\sqrt{s_{\rm NN}}$ = 2.76 TeV at the LHC. *Eur. Phys. J.*, C77(10):658, 2017. doi: 10.1140/epjc/s10052-017-5222-x. 24, 75, 114, 115

[80] L. Adamczyk et al. Measurement of elliptic flow of light nuclei at $\sqrt{s_{NN}} = 200$, 62.4, 39, 27, 19.6, 11.5, and 7.7 GeV at the BNL Relativistic Heavy Ion Collider. *Phys. Rev. C*, 94(3):034908, 2016. doi: 10.1103/PhysRevC.94.034908. 24, 75

[81] J. Adam et al. Beam-energy dependence of the directed flow of deuterons in Au+Au collisions. *Phys. Rev. C*, 102(4):044906, 2020. doi: 10.1103/PhysRevC.102.044906.

[82] Shreyasi Acharya et al. Measurement of the (anti-)3He elliptic flow in Pb–Pb collisions at sNN=5.02TeV. *Phys. Lett. B*, 805:135414, 2020. doi: 10.1016/j.physletb.2020.135414. 24, 75

[83] Shreyasi Acharya et al. First measurement of antideuteron number fluctuations at energies available at the Large Hadron Collider. *submitted to Phys. Rev. Lett.*, 4 2022. 24, 75

[84] E.G. Kessler, Jr, M.S. Dewey, R.D. Deslattes, A. Henins, H.G. Börner, M. Jentschel, C. Doll, and H. Lehmann. The deuteron binding energy and the neutron mass. *Physics Letters A*, 255(4):221–229, 1999. ISSN 0375-9601. doi: https://doi.org/10.1016/S0375-9601(99)00078-X. URL https://www.sciencedirect.com/science/article/pii/S037596019900078X. 24

[85] C. Van Der Leun and C. Alderliesten. The deuteron binding energy. *Nuclear Physics A*, 380(2):261–269, 1982. ISSN 0375-9474. doi: https://doi.org/10.1016/0375-9474(82)90105-1. URL https://www.sciencedirect.com/science/article/pii/0375947482901051. 24

[86] Peter Braun-Munzinger, Benjamin Dönigus, and Nicole Löher. ALICE investigates 'snowballs in hell'. *CERN Courier*, 55(7):26–30, 2015. URL https://cds.cern.ch/record/2232490. 24

[87] Mary K. Gaillard, Paul D. Grannis, and Frank J. Sciulli. The standard model of particle physics. *Rev. Mod. Phys.*, 71:S96–S111, Mar 1999. doi: 10.1103/RevModPhys.71.S96. URL https://link.aps.org/doi/10.1103/RevModPhys.71.S96. 24

[88] J. Cleymans, S. Kabana, I. Kraus, H. Oeschler, K. Redlich, and N. Sharma. Antimatter production in proton-proton and heavy-ion collisions at ultrarelativistic energies. *Phys. Rev.*, C84:054916, 2011. doi: 10.1103/PhysRevC.84.054916. 24

[89] Volodymyr Vovchenko, Benjamin Dönigus, and Horst Stoecker. Canonical statistical model analysis of p-p , p -Pb, and Pb-Pb collisions at energies available at the CERN Large Hadron Collider. *Phys. Rev. C*, 100(5):054906, 2019. doi: 10.1103/PhysRevC.100.054906. 24

[90] Peter Braun-Munzinger, Volker Koch, Thomas Schäfer, and Johanna Stachel. Properties of hot and dense matter from relativistic heavy ion collisions. *Physics Reports*, 621:76–126, 2016. ISSN 0370-1573. doi: https://doi.org/10.1016/j.physrep.2015.12.003. URL https://www.sciencedirect.com/science/article/pii/S0370157315005013. Memorial Volume in Honor of Gerald E. Brown. 25

[91] S. Acharya et. al. Production of ^{4}he and $\overline{^4\mathrm{He}}$ in pb–pb collisions at snn=2.76tev at the lhc. *Nuclear Physics A*, 971:1–20, 2018. ISSN 0375-9474. doi: https://doi.org/10.1016/j.nuclphysa.2017.12.004. URL https://www.sciencedirect.com/science/article/pii/S0375947417304839. 26, 27

[92] J. Cleymans, K. Redlich, and E. Suhonen. Canonical description of strangeness conservation and particle production. *Z. Phys. C*, 51:137–141, 1991. doi: 10.1007/BF01579571. 26

[93] A. Andronic, F. Beutler, P. Braun-Munzinger, K. Redlich, and J. Stachel. Thermal description of hadron production in e+e- collisions revisited. *Phys. Lett. B*, 675:312–318, 2009. doi: 10.1016/j.physletb.2009.04.024. 26

[94] Becattini et al. A comparative analysis of statistical hadron production. *The European Physical Journal C*, 66:377–386, 2010. doi: 10.1140/epjc/s10052-010-1265-y. 26

[95] Shreyasi Acharya et al. Multiplicity dependence of (anti-)deuteron production in pp collisions at $\sqrt{s} = 7$ TeV. *Phys. Lett.*, B794:50–63, 2019. doi: 10.1016/j.physletb.2019.05.028. 28, 114

[96] Lyndon Evans and Philip Bryant. Lhc machine. *Journal of Instrumentation*, 3(08):S08001, aug 2008. doi: 10.1088/1748-0221/3/08/S08001. URL https://dx.doi.org/10.1088/1748-0221/3/08/S08001. 29

[97] Esma Mobs. The CERN accelerator complex - August 2018. Complexe des accélérateurs du CERN - Août 2018. 2018. URL https://cds.cern.ch/record/2636343. General Photo. 30

[98] The ATLAS Collaboration. The atlas experiment at the cern large hadron collider. *Journal of Instrumentation*, 3(08):S08003, aug 2008. doi: 10.1088/1748-0221/3/08/S08003. URL https://dx.doi.org/10.1088/1748-0221/3/08/S08003. 29

[99] The CMS Collaboration. The cms experiment at the cern lhc. *Journal of Instrumentation*, 3(08):S08004, aug 2008. doi: 10.1088/1748-0221/3/08/S08004. URL https://dx.doi.org/10.1088/1748-0221/3/08/S08004. 30

[100] The LHCb Collaboration. The lhcb detector at the lhc. *Journal of Instrumentation*, 3(08): S08005, aug 2008. doi: 10.1088/1748-0221/3/08/S08005. URL https://dx.doi.org/10.1088/1748-0221/3/08/S08005. 30

[101] The TOTEM Collaboration. The totem experiment at the cern large hadron collider. *Journal of Instrumentation*, 3(08):S08007, aug 2008. doi: 10.1088/1748-0221/3/08/S08007. URL https://dx.doi.org/10.1088/1748-0221/3/08/S08007. 30

[102] ALICE Collaboration.
ALICE: Physics performance report, volume I.
J. Phys. G, 30:1517–1763, 2004. doi: 10.1088/0954-3899/30/11/001. 31, 39

[103] ALICE Collaboration.
ALICE: Physics performance report, volume II.
J. Phys. G, 32:1295–2040, 2006. doi: 10.1088/0954-3899/32/10/001.

[104] ALICE Collaboration.
Performance of the ALICE Experiment at the CERN LHC.
Int. J. Mod. Phys. A, 29:1430044, 2014. doi: 10.1142/S0217751X14300440. 31, 32, 37, 39, 78

[105] and F Carminati, P Foka, P Giubellino, A Morsch, G Paic, J-P Revol, K Safarík, Y Schutz, and U A Wiedemann (editors). Alice: Physics performance report, volume i. *Journal of Physics G: Nuclear and Particle Physics*, 30(11):1517, oct 2004. doi: 10.1088/0954-3899/30/11/001. URL https://dx.doi.org/10.1088/0954-3899/30/11/001. 31

[106] ALICE Collaboration.
The ALICE experiment at the CERN LHC.
JINST, 3:S08002, 2008. doi: 10.1088/1748-0221/3/08/S08002. 31, 79

[107] Arturo Tauro.
3D ALICE Schematics of ALICE during RUN2 and after the upgrade, for RUN3. 2017. 32

[108] ALICE collaboration. Alignment of the alice inner tracking system with cosmic-ray tracks. *Journal of Instrumentation*, 5(03):P03003, mar 2010. doi: 10.1088/1748-0221/5/03/P03003. URL https://dx.doi.org/10.1088/1748-0221/5/03/P03003. 34

[109] J. Alme et al.
The ALICE TPC, a large 3-dimensional tracking device with fast readout for ultra-high multiplicity events.
Nucl. Instrum. Meth. A, 622:316–367, 2010. doi: 10.1016/j.nima.2010.04.042. 33, 35

[110] B Abelev et al. Upgrade of the ALICE Experiment: Letter Of Intent. *J. Phys. G*, 41: 087001, 2014. doi: 10.1088/0954-3899/41/8/087001. 34

[111] ALICE Collaboration.
Real-time data processing in the ALICE High Level Trigger at the LHC.
Comput. Phys. Commun., 242:25–48, 2019. doi: 10.1016/j.cpc.2019.04.011. 35

[112] H. Bethe. Zur Theorie des Durchgangs schneller Korpuskularstrahlen durch Materie. *Annalen der Physik*, 397:325., 1930. doi: 10.1002/andp.19303970303. 35

[113] F. Carnesecchi. Performance of the alice time-of-flight detector at the lhc. *Journal of Instrumentation*, 14(06):C06023, jun 2019. doi: 10.1088/1748-0221/14/06/C06023. URL https://dx.doi.org/10.1088/1748-0221/14/06/C06023. 36

[114] R. Brun and F. Rademakers.
ROOT: An object oriented data analysis framework.
Nucl. Instrum. Meth. A, 389:81–86, 1997. doi: 10.1016/S0168-9002(97)00048-X. 38

[115] R. Frühwirth. Application of kalman filtering to track and vertex fitting. *Nuclear Instruments and Methods in Physics Research Section A: Accelerators, Spectrometers, Detectors and Associated Equipment*, 262(2):444–450, 1987. ISSN 0168-9002. doi: https://doi.org/10.1016/0168-9002(87)90887-4. URL https://www.sciencedirect.com/science/article/pii/0168900287908874. 38

[116] Torbjorn Sjostrand, Stephen Mrenna, and Peter Z. Skands.
PYTHIA 6.4 Physics and Manual.
JHEP, 05:026, 2006. doi: 10.1088/1126-6708/2006/05/026. 40

[117] Peter Z. Skands. Tuning monte carlo generators: The perugia tunes. *Phys. Rev. D*, 82:074018, Oct 2010. doi: 10.1103/PhysRevD.82.074018. URL https://link.aps.org/doi/10.1103/PhysRevD.82.074018.

[118] Skands P., Carrazza S., and Rojo J. Tuning pythia 8.1: the monash 2013 tune. *The European Physical Journal C*, 74:1434–6052, Oct 2014. doi: 10.1140/epjc/s10052-014-3024-y. URL https://doi.org/10.1140/epjc/s10052-014-3024-y.

[119] Torbjörn Sjöstrand, Stefan Ask, Jesper R. Christiansen, Richard Corke, Nishita Desai, Philip Ilten, Stephen Mrenna, Stefan Prestel, Christine O. Rasmussen, and Peter Z. Skands. An introduction to pythia 8.2. *Computer Physics Communications*, 191:159–177, 2015. doi: https://doi.org/10.1016/j.cpc.2015.01.024. URL https://www.sciencedirect.com/science/article/pii/S0010465515000442. 40, 79

[120] S. Roesler, R. Engel, and J. Ranft. The monte carlo event generator dpmjet-iii. In Andreas Kling, Fernando J. C. Barão, Masayuki Nakagawa, Luis Távora, and Pedro Vaz, editors, *Advanced Monte Carlo for Radiation Physics, Particle Transport Simulation and Applications*, pages 1033–1038, Berlin, Heidelberg, 2001. Springer Berlin Heidelberg. ISBN 978-3-642-18211-2. 40

[121] Xin-Nian Wang and Miklos Gyulassy. hijing: A monte carlo model for multiple jet production in pp, pA, and AA collisions. *Phys. Rev. D*, 44:3501–3516, Dec 1991. doi: 10.1103/PhysRevD.44.3501. URL https://link.aps.org/doi/10.1103/PhysRevD.44.3501. 40

[122] K. Werner, B. Guiot, Iu. Karpenko, and T. Pierog. Analysing radial flow features in p-Pb and p-p collisions at several TeV by studying identified particle production in EPOS3. *Phys. Rev. C*, 89(6):064903, 2014. doi: 10.1103/PhysRevC.89.064903. 40, 137

[123] K. Werner, Iu. Karpenko, T. Pierog, M. Bleicher, and K. Mikhailov. Event-by-Event Simulation of the Three-Dimensional Hydrodynamic Evolution from Flux Tube Initial Conditions in Ultrarelativistic Heavy Ion Collisions. *Phys. Rev. C*, 82:044904, 2010. doi: 10.1103/PhysRevC.82.044904.

[124] H. J. Drescher, M. Hladik, S. Ostapchenko, T. Pierog, and K. Werner. Parton based Gribov-Regge theory. *Phys. Rept.*, 350:93–289, 2001. doi: 10.1016/S0370-1573(00)00122-8. 40

[125] R. Brun, F. Bruyant, M. Maire, A. C. McPherson, and P. Zanarini. GEANT3. *Nuclear Instruments and Methods in Physics Research Section A: Accelerators, Spectrometers, Detectors and Associated Equipment*, 9 1987. 40

[126] GEANT4 Collaboration. Recent developments in geant4. *Nuclear Instruments and Methods in Physics Research Section A: Accelerators, Spectrometers, Detectors and Associated Equipment*, 835:186–225, 2016. ISSN 0168-9002. doi: https://doi.org/10.1016/j.nima.2016.06.125. URL https://www.sciencedirect.com/science/article/pii/S0168900216306957. 40, 79

[127] R Brun, R Hagelberg, M Hansroul, and J C Lassalle. *Simulation program for particle physics experiments, GEANT: user guide and reference manual*. CERN, Geneva, 1978. URL https://cds.cern.ch/record/118715. 40

[128] M. Hoffmann, J. W. Durso, K. Holinde, B. C. Pearce, and J. Speth. Role of correlated two pion exchange in K + N scattering. *Nucl. Phys. A*, 593:341–361, 1995. doi: 10.1016/0375-9474(95)00320-Z. 42, 43

[129] J. Haidenbauer, G. Krein, Ulf-G. Meissner, and L. Tolos. DN interaction from meson exchange. *Eur. Phys. J. A*, 47:18, 2011. doi: 10.1140/epja/i2011-11018-3. 42

[130] ALICE Collaboration.
Investigation of the p-Σ^0 interaction via femtoscopy in pp collisions.
Phys. Lett. B, 805:135419, 2020. doi: 10.1016/j.physletb.2020.135419. 42, 78, 87, 103

[131] ALICE Collaboration.
p-p, p-Λ and Λ-Λ correlations studied via femtoscopy in pp reactions at $\sqrt{s}$ = 7 TeV.
Phys. Rev. C, 99(2):024001, 2019. doi: 10.1103/PhysRevC.99.024001. 42, 79, 87, 97, 98

[132] T. C. Black, H. J. Karwowski, E. J. Ludwig, A. Kievsky, S. Rosati, and M. Viviani. Determination of proton-deuteron scattering lengths. *Phys. Lett. B*, 471:103–107, 1999. doi: 10.1016/S0370-2693(99)01366-0.
https://doi.org/10.1016/S0370-2693(99)01366-0. 43, 44, 45, 50

[133] J. Arvieux. Phase-shift analysis of elastic proton-deuteron scattering cross sections and ^{3}He excited states. *Nucl. Phys. A*, 221:253–268, 1974. doi: 10.1016/0375-9474(74)90317-0.
https://doi.org/10.1016/0375-9474(74)90317-0. 45, 46, 48, 50

[134] E. Huttel, W. Arnold, H. Baumgart, H. Berg, and G. Clausnitzer. Phase-shift analysis of pd elastic scattering below break-up threshold. *Nucl. Phys. A*, 406:443–455, 1983. doi: 10.1016/0375-9474(83)90369-X.
https://doi.org/10.1016/0375-9474(83)90369-X. 45, 50

[135] A. Kievsky, S. Rosati, M. Viviani, C. R. Brune, H. J. Karwowski, E. J. Ludwig, and M. H. Wood. The Three nucleon system near the N - d threshold. *Phys. Lett. B*, 406:292–296, 1997. doi: 10.1016/S0370-2693(97)00691-6.
https://doi.org/10.1016/S0370-2693(97)00691-6. 43, 44, 45, 50

[136] A Sibirtsev, J Haidenbauer, S Krewald, and Ulf-G Meißner. Kaon-deuteron scattering at low energies. *Journal of Physics G: Nuclear and Particle Physics*, 32(11):R395, oct 2006. doi: 10.1088/0954-3899/32/11/R02. URL https://dx.doi.org/10.1088/0954-3899/32/11/R02. 43

[137] W. T. H. Van Oers and K. W. Brockman. Phase-shift analysis of elastic nucleon-deuteron scattering. *Nucl. Phys. A*, 92:561–583, 1967. doi: 10.1016/0375-9474(67)90633-1.
https://doi.org/10.1016/0375-9474(67)90633-1. 44, 45, 50

[138] L. D. Knutson, L. O. Lamm, and J. E. McAninch. Determination of the phase shifts for p-d elastic scattering at e_p=3 mev. *Phys. Rev. Lett.*, 71:3762–3765, Dec 1993. doi: 10.1103/PhysRevLett.71.3762. URL https://link.aps.org/doi/10.1103/PhysRevLett.71.3762. 44

[139] R. Sherr, J. M. Blair, H. R. Kratz, C. L. Bailey, and R. F. Taschek. Scattering of protons by deuterons. *Phys. Rev.*, 72:662–672, Oct 1947. doi: 10.1103/PhysRev.72.662. URL https://link.aps.org/doi/10.1103/PhysRev.72.662.

[140] C.R Brune, W.H Geist, H.J Karwowski, E.J Ludwig, K.D Veal, M.H Wood, A Kievsky, S Rosati, and M Viviani. Possible three-nucleon force effects in d–p scattering at low energies. *Physics Letters B*, 428(1):13–17, 1998. ISSN 0370-2693. doi: https://doi.org/10.1016/S0370-2693(98)00370-0. URL https://www.sciencedirect.com/science/article/pii/S0370269398003700.

[141] E. Huttel, W. Arnold, H. Berg, H.H. Krause, J. Ulbricht, and G. Clausnitzer. Differential cross sections and analyzing powers for pd elastic scattering below 1.0 mev. *Nuclear Physics A*, 406(3):435–442, 1983. ISSN 0375-9474. doi: https://doi.org/10.1016/0375-9474(83)90368-8. URL https://www.sciencedirect.com/science/article/pii/0375947483903688.

[142] T.B. Clegg, H.J. Karwowski, S.K. Lemieux, R.W. Sayer, E.R. Crosson, W.M. Hooke, C.R. Howell, H.W. Lewis, A.W. Lovette, H.J. Pfutzner, K.A. Sweeton, and W.S. Wilburn. A new atomic beam polarized ion source for the triangle universities nuclear laboratory: overview, operating experience, and performance. *Nuclear Instruments and Methods in Physics Research Section A: Accelerators, Spectrometers, Detectors and Associated Equipment*, 357(2):200–211, 1995. ISSN 0168-9002. doi: https://doi.org/10.1016/0168-9002(94)01078-1. URL https://www.sciencedirect.com/science/article/pii/0168900294010781. 44

[143] W. Cameron et al. K+ p Elastic Scattering from 130-MeV/c to 755-MeV/c. *Nucl. Phys. B*, 78:93–109, 1974. doi: 10.1016/0550-3213(74)90117-5. 44

[144] R. W. Bland, M. G. Bowler, J. L. Brown, J. A. Kadyk, G. Goldhaber, S. Goldhaber, V. H. Seeger, and G. H. Trilling. The k-plus p interaction from 864 to 1585 mev/c - cross sections and mass distributions. *Nucl. Phys. B*, 13:595–621, 1969. doi: 10.1016/0550-3213(69)90194-1. 44

[145] R. G. Glasser, G. A. Snow, D. Trevvett, R. A. Burnstein, C. Fu, R. Petri, G. Rosenblatt, and H. A. Rubin. Low Momentum K+ d Scattering. *Phys. Rev. D*, 15:1200–1214, 1977. doi: 10.1103/PhysRevD.15.1200. 44

[146] Takashi Takaki. Optical potential approach to K^+d scattering at low energies. *Phys. Rev. C*, 81:055204, May 2010. doi: 10.1103/PhysRevC.81.055204. URL https://link.aps.org/doi/10.1103/PhysRevC.81.055204. 45

[147] S.S. Kamalov, E. Oset, and A. Ramos. Chiral unitary approach to the k–deuteron scattering length. *Nuclear Physics A*, 690(4):494–508, 2001. ISSN 0375-9474. doi: https://doi.org/10.1016/S0375-9474(00)00709-0. URL https://www.sciencedirect.com/science/article/pii/S0375947400007090. 45

[148] Johann Haidenbaur. K^+–d scattering parameters extracted by fitting the effective range formula to K^+–d elastic scattering cross-section. *Provided in private communication*. 45

[149] Tetsuo Hyodo. K^+–d scattering parameters calculated using fixed-center-approach and using the kn scattering parameter. *Provided in private communication*. 45

[150] R. S. Christian and J. L. Gammel. Elastic scattering of protons and neutrons by deuterons. *Phys. Rev.*, 91:100–121, Jul 1953. doi: 10.1103/PhysRev.91.100. URL https://link.aps.org/doi/10.1103/PhysRev.91.100. 46

[151] A. Kievsky, S. Rosati, W. Tornow, and M. Viviani. Critical comparison of experimental data and theoretical predictions for n-d scattering below the breakup threshold. *Nuclear Physics A*, 607(4):402–424, 1996. ISSN 0375-9474. doi: https://doi.org/10.1016/0375-9474(96)00240-0. URL https://www.sciencedirect.com/science/article/pii/0375947496002400. 46

[152] Sebastian König and H.-W. Hammer. Precision calculation of the quartet-channel $p-d$ scattering length. *Phys. Rev. C*, 90:034005, Sep 2014. doi: 10.1103/PhysRevC.90.034005. URL https://link.aps.org/doi/10.1103/PhysRevC.90.034005. 46

[153] Stanislaw Mrówczyński and Patrycja Słoń. Hadron–Deuteron Correlations and Production of Light Nuclei in Relativistic Heavy-ion Collisions. *Acta Phys. Polon. B*, 51(8): 1739–1755, 2020. doi: 10.5506/APhysPolB.51.1739. 47, 76, 148

[154] Sebastian König, Dean Lee, and H. W. Hammer. Causality constraints for charged particles. *J. Phys. G*, 40:045106, 2013. doi: 10.1088/0954-3899/40/4/045106. 49

[155] M. Viviani, S. König, A. Kievsky, L. E. Marcucci, B. Singh, and O. Vázquez Doce. Role of three-body dynamics in nucleon-deuteron correlation functions. *Submitted to PRC*, 2023. URL https://doi.org/10.48550/arXiv.2306.02478. 51, 60, 61, 62, 63, 65, 66, 67, 69, 70, 71

[156] Stanislaw Mrowczynski. Production of light nuclei at colliders – coalescence vs. thermal model. *Eur. Phys. J. ST*, 229(22-23):3559–3583, 2020. doi: 10.1140/epjst/e2020-000067-0. 51, 53, 148

[157] R. Del Grande, L. Šerkšnytė, L. Fabbietti, et al. A method to remove lower order contributions in multi-particle femtoscopic correlation functions. *Eur. Phys. J. C*, 82 (244):1–10, 2022. doi: 10.1140/epjc/s10052-022-10209-z. 52

[158] ALICE Collaboration. Towards the understanding of the genuine three-body interaction for p−p−p and p−p−Λ. 6 2022. 52, 149

[159] Laura Šerkšnytė. can be found under
Novel technique to access the strong interaction in three-body systems and Re-evaluated cosmic ray antinuclei fluxes.
PhD thesis, Technical University of Munich, 2023. 53, 149

[160] A. Kievsky, S. Rosati, M. Viviani, L. E. Marcucci, and L. Girlanda. A High-precision variational approach to three- and four-nucleon bound and zero-energy scattering states. *J. Phys. G*, 35:063101, 2008. doi: 10.1088/0954-3899/35/6/063101. 54, 56, 57, 58, 59, 60

[161] L. E. Marcucci, J. Dohet-Eraly, L. Girlanda, A. Gnech, A. Kievsky, and M. Viviani. The Hyperspherical Harmonics method: a tool for testing and improving nuclear interaction models. *Front. in Phys.*, 8:69, 2020. doi: 10.3389/fphy.2020.00069. 54, 55, 56, 59, 60

[162] B. S. Pudliner, V. R. Pandharipande, J. Carlson, and R. B. Wiringa. Quantum monte carlo calculations of $A \leq 6$ nuclei. *Phys. Rev. Lett.*, 74:4396–4399, May 1995. doi: 10.1103/PhysRevLett.74.4396. URL https://link.aps.org/doi/10.1103/PhysRevLett.74.4396. 56

[163] M. Piarulli, L. Girlanda, R. Schiavilla, R. Navarro Pérez, J. E. Amaro, and E. Ruiz Arriola. Minimally nonlocal nucleon-nucleon potentials with chiral two-pion exchange including Δ resonances. *Phys. Rev. C*, 91(2):024003, 2015. doi: 10.1103/PhysRevC.91.024003. 56

[164] A. Baroni et al. Local chiral interactions, the tritium Gamow-Teller matrix element, and the three-nucleon contact term. *Phys. Rev. C*, 98(4):044003, 2018. doi: 10.1103/PhysRevC.98.044003. 56

[165] L. D. Faddeev. *Mathematical Aspects of the Three-Body Problems in the Quantum Scattering Theory*. D. Davey and Company, New York, 1965. Translated from Russian, the Israel Program for Scientific translations, Jerusalem. 56

[166] W. Glöckle, H. Witała, D. Hüber, H. Kamada, and J. Golak. The three-nucleon continuum: achievements, challenges and applications. *Physics Reports*, 274(3):107–285, 1996. ISSN 0370-1573. doi: https://doi.org/10.1016/0370-1573(95)00085-2. URL https://www.sciencedirect.com/science/article/pii/0370157395000852. 56

[167] Nogga, Kamada, and Glockle. Modern nuclear force predictions for the alpha particle. *Physical review letters*, 85 5:944–7, 2000. 56

[168] A. Deltuva, R. Machleidt, and P. U. Sauer. Realistic two-baryon potential coupling two-nucleon and nucleon-Δ-isobar states: Fit and applications to three-nucleon system. *Phys. Rev. C*, 68:024005, Aug 2003. doi: 10.1103/PhysRevC.68.024005. URL https://link.aps.org/doi/10.1103/PhysRevC.68.024005.

[169] A. Deltuva, A. C. Fonseca, and P. U. Sauer. Momentum-space treatment of the coulomb interaction in three-nucleon reactions with two protons. *Phys. Rev. C*, 71:054005, May 2005. doi: 10.1103/PhysRevC.71.054005. URL https://link.aps.org/doi/10.1103/PhysRevC.71.054005. 56

[170] W. Kohn. Variational methods in nuclear collision problems. *Phys. Rev.*, 74:1763–1772, Dec 1948. doi: 10.1103/PhysRev.74.1763. URL https://link.aps.org/doi/10.1103/PhysRev.74.1763. 56

[171] Steven C. Pieper, K. Varga, and R. B. Wiringa. Quantum monte carlo calculations of $a = 9, 10$ nuclei. *Phys. Rev. C*, 66:044310, Oct 2002. doi: 10.1103/PhysRevC.66.044310. URL https://link.aps.org/doi/10.1103/PhysRevC.66.044310. 56

[172] M. Kamimura. Nonadiabatic coupled-rearrangement-channel approach to muonic molecules. *Phys. Rev. A*, 38:621–624, Jul 1988. doi: 10.1103/PhysRevA.38.621. URL https://link.aps.org/doi/10.1103/PhysRevA.38.621. 56

[173] A. Kievsky, M. Viviani, and S. Rosati. Polarization observables in p - d scattering below 30-MeV. *Phys. Rev. C*, 64:024002, 2001. doi: 10.1103/PhysRevC.64.024002. 60, 62, 107

[174] A. Kievsky, M. Viviani, and L. E. Marcucci. $n-d$ scattering including electromagnetic forces. *Phys. Rev. C*, 69:014002, Jan 2004. doi: 10.1103/PhysRevC.69.014002. URL https://link.aps.org/doi/10.1103/PhysRevC.69.014002. 60

[175] A. Kievsky, J.L. Friar, G.L. Payne, S. Rosati, and M. Viviani. Phase shifts and mixing parameters for low-energy proton-deuteron scattering. *Phys. Rev. C*, 63:064004, 2001. 62

[176] H.-W. Hammer, S. König, and U. van Kolck. Nuclear effective field theory: status and perspectives. *Rev. Mod. Phys.*, 92(2):025004, 2020. doi: 10.1103/RevModPhys.92.025004. 65

[177] H. A. Bethe. Theory of the effective range in nuclear scattering. *Phys. Rev.*, 76(1):38–50, 1949. doi: 10.1103/PhysRev.76.38. 65

[178] P. F. Bedaque, H.-W. Hammer, and U. van Kolck. Renormalization of the three-body system with short-range interactions. *Phys. Rev. Lett.*, 82:463–467, 1999. doi: 10.1103/PhysRevLett.82.463. 65

[179] Paulo F. Bedaque, H.-W. Hammer, and U. van Kolck. Effective theory of the triton. *Nucl. Phys. A*, 676:357–370, 2000. doi: 10.1016/S0375-9474(00)00205-0. 65

[180] Jared Vanasse, David A. Egolf, John Kerin, Sebastian König, and Roxanne P. Springer. 3He and pd Scattering to Next-to-Leading Order in Pionless Effective Field Theory. *Phys. Rev. C*, 89(6):064003, 2014. doi: 10.1103/PhysRevC.89.064003. 66, 68, 69

[181] Sebastian König and H.-W. Hammer. Low-energy p-d scattering and He-3 in pionless EFT. *Phys. Rev. C*, 83:064001, 2011. doi: 10.1103/PhysRevC.83.064001. 66, 67

[182] Frank Tabakin and K. T. R. Davies. Smooth Velocity-Dependent Potential and Nuclear Matter. *Phys. Rev.*, 150(3):793–800, 1966. doi: 10.1103/PhysRev.150.793. 67

[183] Sebastian König. Energies and radii of light nuclei around unitarity. *Eur. Phys. J. A*, 56 (4):113, 2020. doi: 10.1140/epja/s10050-020-00098-9. 68

[184] Sebastian König, Harald W. Grießhammer, and H. W. Hammer. The proton-deuteron system in pionless EFT revisited. *J. Phys. G*, 42:045101, 2015. doi: 10.1088/0954-3899/42/4/045101. 68, 69

[185] Shung-ichi Ando and Michael C. Birse. Effective field theory of 3He. *J. Phys. G*, 37: 105108, 2010. doi: 10.1088/0954-3899/37/10/105108.

[186] Sebastian Koenig and H. W. Hammer. Low-energy p-d scattering and He-3 in pionless EFT. *Phys. Rev. C*, 83:064001, 2011. doi: 10.1103/PhysRevC.83.064001.

[187] Sebastian König, Harald W. Grießhammer, H.-W. Hammer, and U. van Kolck. Effective theory of 3H and 3He. *J. Phys. G*, 43(5):055106, 2016. doi: 10.1088/0954-3899/43/5/055106.

[188] J. Kirscher and D. Gazit. The Coulomb interaction in Helium-3: Interplay of strong short-range and weak long-range potentials. *Phys. Lett. B*, 755:253–260, 2016. doi: 10.1016/j.physletb.2016.02.011. 69

[189] Hans-Werner Hammer, Andreas Nogga, and Achim Schwenk. Three-body forces: From cold atoms to nuclei. *Rev. Mod. Phys.*, 85:197, 2013. doi: 10.1103/RevModPhys.85.197. 75

[190] M. Baldo, G. F. Burgio, and I. Bombaci. Microscopic nuclear equation of state with three-body forces and neutron star structure. 7 1996. 75

[191] M. H. Wood, C. R. Brune, B. M. Fisher, H. J. Karwowski, D. S. Leonard, E. J. Ludwig, A. Kievsky, S. Rosati, and M. Viviani. Low-energy $p-d$ scattering: High-precision data, comparisons with theory, and phase-shift analyses. *Phys. Rev. C*, 65:034002, Feb 2002. doi: 10.1103/PhysRevC.65.034002. URL `https://link.aps.org/doi/10.1103/PhysRevC.65.034002`. 75

[192] Evgeny Epelbaum, Hermann Krebs, and Patrick Reinert. High-precision nuclear forces from chiral EFT: State-of-the-art, challenges and outlook. *Front. in Phys.*, 8:98, 2020. doi: 10.3389/fphy.2020.00098. 75

[193] Evgeny Epelbaum, Hans-Werner Hammer, and Ulf-G. Meissner. Modern Theory of Nuclear Forces. *Rev. Mod. Phys.*, 81:1773–1825, 2009. doi: 10.1103/RevModPhys.81.1773. 75

[194] E. Epelbaum et al. Few- and many-nucleon systems with semilocal coordinate-space regularized chiral two- and three-body forces. *Phys. Rev. C*, 99(2):024313, 2019. doi: 10.1103/PhysRevC.99.024313. 75

[195] Shreyasi Acharya et al. Production of deuterons, tritons, ^{3}He nuclei and their antinuclei in pp collisions at $\sqrt{s}$ = 0.9, 2.76 and 7 TeV. *Phys. Rev.*, C97(2):024615, 2018. doi: 10.1103/PhysRevC.97.024615. 75

[196] C. B. Chitwood et al. Final-State Interactions between Noncompound Light Particles for O-16-Induced Reactions on Au-197 at EA=25 MeV. *Phys. Rev. Lett.*, 54:302–305, 1985. doi: 10.1103/PhysRevLett.54.302. 76, 112

[197] J. Pochodzalla, C. K. Gelbke, C. B. Chitwood, D. J. Fields, W. G. Lynch, M. B. Tsang, and W. A. Friedman. External Coulomb distortion of proton-deuteron final-state interactions for induced reactions on Au at E / A = 35 MeV. *Phys. Lett. B*, 175:275–278, 1986. doi: 10.1016/0370-2693(86)90855-5. 76

[198] Josef Pochodzalla et al. Two-particle correlations at small relative momenta for induced40 reactions on Au-197 at E/A=60 MeV. *Phys. Rev. C*, 35:1695–1719, 1987. doi: 10.1103/PhysRevC.35.1695. 76

[199] Correlations of neutral and charged particles in 40Ar- 58Ni reaction at 77 MeV/u. Eur. Phys. J. A 32, 55–59 (2007). *Eur. Phys. J. A.*, 32:55–59, 2007. doi: https://doi.org/10.1140/epja/i2006-10279-1. 76, 77, 112

[200] S. Acharya et al. Unveiling the strong interaction among hadrons at the LHC. *Nature*, 588(7837):232–238, 2020. doi: 10.1038/s41586-020-3001-6. 78

[201] ALICE Collaboration.
Insight into particle production mechanisms via angular correlations of identified particles in pp collisions at $\sqrt{s} = 7$ TeV.
Eur. Phys. J. C, 77(8):569, 2017. doi: 10.1140/epjc/s10052-017-5129-6. [Erratum: Eur.Phys.J.C 79, 998 (2019)]. 78

[202] Acharya and Others. Production of deuterons, tritons, ^{3}He nuclei, and their antinuclei in pp collisions at $\sqrt{s} = 0.9$, 2.76, and 7 tev. *Phys. Rev. C*, 97:024615, Feb 2018. doi: 10.1103/PhysRevC.97.024615. URL `https://link.aps.org/doi/10.1103/PhysRevC.97.024615`. 83

[203] Oliver Arnold.
Study of the hyperon-nucleon interaction via femtoscopy in elementary systems with HADES and ALICE.
PhD thesis, Technical University of Munich, 2017. 87, 97

[204] J. et al Adam. One-dimensional pion, kaon, and proton femtoscopy in pb-pb collisions at $\sqrt{s_{NN}} = 2.76$ tev. *Phys. Rev. C*, 92:054908, Nov 2015. doi: 10.1103/PhysRevC.92.054908. URL `https://link.aps.org/doi/10.1103/PhysRevC.92.054908`. 87, 125

[205] ALICE Collaboration. Exploring the nΛ–nΣ coupled system with high precision correlation techniques at the lhc. *Physics Letters B*, 833:137272, 2022. ISSN 0370-2693. doi: https://doi.org/10.1016/j.physletb.2022.137272. URL `https://www.sciencedirect.com/science/article/pii/S0370269322004063`. 88, 99

[206] Henk Polinder, Johann Haidenbauer, and Ulf-G. Meissner.
Hyperon-nucleon interactions: A Chiral effective field theory approach.
Nucl. Phys. A, 779:244–266, 2006. doi: 10.1016/j.nuclphysa.2006.09.006. 100

[207] J. Haidenbauer, U.-G. Meißner, and A. Nogga.
Hyperon–nucleon interaction within chiral effective field theory revisited.
Eur. Phys. J. A, 56(3):91, 2020. doi: 10.1140/epja/s10050-020-00100-4. 100

[208] Volodymyr Vovchenko and Horst Stoecker.
Thermal-FIST: A package for heavy-ion collisions and hadronic equation of state.
Comput. Phys. Commun., 244:295–310, 2019. doi: 10.1016/j.cpc.2019.06.024. 101

[209] ALICE Collaboration. Experimental evidence for an attractive $p-\phi$ interaction. *Phys. Rev. Lett.*, 127:172301, Oct 2021. doi: 10.1103/PhysRevLett.127.172301. URL `https://link.aps.org/doi/10.1103/PhysRevLett.127.172301`. 103

[210] ALICE Collaboration.
Study of the Λ-Λ interaction with femtoscopy correlations in pp and p-Pb collisions at the LHC.
Phys. Lett. B, 797:134822, 2019. doi: 10.1016/j.physletb.2019.134822.

[211] First measurement of the Λ–Ξ interaction in proton–proton collisions at the lhc. *Physics Letters B*, page 137223, 2022. ISSN 0370-2693. doi: https://doi.org/10.1016/j.physletb.2022.137223. URL `https://www.sciencedirect.com/science/article/pii/S0370269322003574`. 103

[212] A. Deltuva, A. C. Fonseca, A. Kievsky, S. Rosati, P. U. Sauer, and M. Viviani. Benchmark calculation for proton-deuteron elastic scattering observables including Coulomb. *Phys. Rev. C*, 71:064003, 2005. doi: 10.1103/PhysRevC.71.064003. 107

[213] Z. Citron et al. Report from Working Group 5: Future physics opportunities for high-density QCD at the LHC with heavy-ion and proton beams. *CERN Yellow Rep. Monogr.*, 7:1159–1410, 2019. doi: 10.23731/CYRM-2019-007.1159. 112

[214] Dimitar Mihaylov and Jaime González González. Novel model for particle emission in small collision systems. 5 2023. 112

[215] M. Mahlein, L. Barioglio, F. Bellini, L. Fabbietti, C. Pinto, B. Singh, and S. Tripathy. Novel parameter-free coalescence model for deuteron production, 2023. URL `https://arxiv.org/abs/2302.12696`. 113, 129, 138, 140, 142, 143

[216] S. T. Butler and C. A. Pearson. Deuterons from high-energy proton bombardment of matter. *Phys. Rev.*, 129:836–842, Jan 1963. doi: 10.1103/PhysRev.129.836. URL `https://link.aps.org/doi/10.1103/PhysRev.129.836`. 113, 142

[217] Joseph I. Kapusta. Mechanisms for deuteron production in relativistic nuclear collisions. *Phys. Rev. C*, 21:1301–1310, Apr 1980. doi: 10.1103/PhysRevC.21.1301. URL `https://link.aps.org/doi/10.1103/PhysRevC.21.1301`. 113, 142

[218] S. et al. Acharya. Production of deuterons, tritons, ^{3}He nuclei, and their antinuclei in pp collisions at $\sqrt{s} = 0.9$, 2.76, and 7 tev. *Phys. Rev. C*, 97:024615, Feb 2018. doi: 10.1103/PhysRevC.97.024615. URL `https://link.aps.org/doi/10.1103/PhysRevC.97.024615`. 114

[219] Shreyasi Acharya et al. Multiplicity dependence of light (anti-)nuclei production in p-Pb collisions at $\sqrt{s_{\rm NN}}$ = 5.02 TeV. *Phys. Lett. B*, 800:135043, 2020. doi: 10.1016/j.physletb.2019.135043.

[220] Shreyasi Acharya et al. Production of (anti-)^{3}He and (anti-)^{3}H in p-Pb collisions at $\sqrt{s_{\rm NN}}$ = 5.02 TeV. *Phys. Rev.*, C101(4):044906, 2020. doi: 10.1103/PhysRevC.101.044906. 114

[221] Zi-Wei Lin, Che Ming Ko, Bao-An Li, Bin Zhang, and Subrata Pal. Multiphase transport model for relativistic heavy ion collisions. *Phys. Rev. C*, 72:064901, Dec 2005. doi: 10.1103/PhysRevC.72.064901. URL `https://link.aps.org/doi/10.1103/PhysRevC.72.064901`. 114, 115

[222] Shreyasi Acharya et al. Production of ^{4}He and $^4\overline{\rm He}$ in Pb-Pb collisions at $\sqrt{s_{\rm NN}}$ = 2.76 TeV at the LHC. *Nucl. Phys.*, A971:1–20, 2018. doi: 10.1016/j.nuclphysa.2017.12.004. 114

[223] Jaroslav Adam et al. $^3_\Lambda$H and $^3_\Lambda\overline{\rm H}$ production in Pb-Pb collisions at $\sqrt{s_{\rm NN}} = 2.76$ TeV. *Phys. Lett.*, B754:360–372, 2016. doi: 10.1016/j.physletb.2016.01.040. 114

[224] J. L. Nagle, B. S. Kumar, D. Kusnezov, H. Sorge, and R. Mattiello. Coalescence of deuterons in relativistic heavy ion collisions. *Phys. Rev. C*, 53:367–376, Jan 1996. doi: 10.1103/PhysRevC.53.367. URL `https://link.aps.org/doi/10.1103/PhysRevC.53.367`. 114

[225] Carl B. Dover, Ulrich Heinz, Ekkard Schnedermann, and József Zimányi. Covariant coalescence model for relativistically expanding systems. *Phys. Rev. C*, 44:1636–1654, Oct 1991. doi: 10.1103/PhysRevC.44.1636. URL `https://link.aps.org/doi/10.1103/PhysRevC.44.1636`. 114, 117

[226] Rüdiger Scheibl and Ulrich Heinz. Coalescence and flow in ultrarelativistic heavy ion collisions. *Phys. Rev. C*, 59:1585–1602, Mar 1999. doi: 10.1103/PhysRevC.59.1585. URL `https://link.aps.org/doi/10.1103/PhysRevC.59.1585`. 114, 116, 117, 120, 121, 122, 142, 143

[227] E. Wigner. On the quantum correction for thermodynamic equilibrium. *Phys. Rev.*, 40: 749–759, Jun 1932. doi: 10.1103/PhysRev.40.749. URL https://link.aps.org/doi/10.1103/PhysRev.40.749. 116

[228] R.P. Feynman. Statistical mechanics: a set of lectures. *Phys. Rev. C*, 59:1585–1602, 1972. URL https://cmc.marmot.org/Record/.b12304189. 116

[229] P. Danielewicz and P. Schuck. Formulation of particle correlation and cluster production in heavy-ion-induced reactions. *Physics Letters B*, 274(3):268–274, 1992. ISSN 0370-2693. doi: https://doi.org/10.1016/0370-2693(92)91985-I. URL https://www.sciencedirect.com/science/article/pii/037026939291985I. 117

[230] Fred Cooper and Graham Frye. Single-particle distribution in the hydrodynamic and statistical thermodynamic models of multiparticle production. *Phys. Rev. D*, 10:186–189, Jul 1974. doi: 10.1103/PhysRevD.10.186. URL https://link.aps.org/doi/10.1103/PhysRevD.10.186. 117

[231] Francesca Bellini and Alexander P. Kalweit. Testing production scenarios for (anti-)(hyper-)nuclei and exotica at energies available at the cern large hadron collider. *Phys. Rev. C*, 99:054905, May 2019. doi: 10.1103/PhysRevC.99.054905. URL https://link.aps.org/doi/10.1103/PhysRevC.99.054905. 121, 125, 126, 142

[232] Francesca Bellini, Kfir Blum, Alexander Phillip Kalweit, and Maximiliano Puccio. Examination of coalescence as the origin of nuclei in hadronic collisions. *Phys. Rev. C*, 103:014907, Jan 2021. doi: 10.1103/PhysRevC.103.014907. URL https://link.aps.org/doi/10.1103/PhysRevC.103.014907. 121, 124, 125, 127, 128, 142

[233] R J N Phillips. The two-nucleon interaction. *Reports on Progress in Physics*, 22(1):562–634, jan 1959. doi: 10.1088/0034-4885/22/1/314. URL https://doi.org/10.1088/0034-4885/22/1/314. 122, 139

[234] R. Machleidt. The High precision, charge dependent Bonn nucleon-nucleon potential (CD-Bonn). *Phys. Rev. C*, 63:024001, 2001. doi: 10.1103/PhysRevC.63.024001. 123

[235] M. Kachelrieß, S. Ostapchenko, and J. Tjemsland. Alternative coalescence model for deuteron, tritium, helium-3 and their antinuclei. *Eur. Phys. J. A*, 56(1):4, 2020. doi: 10.1140/epja/s10050-019-00007-9. 124, 125, 128, 129, 143

[236] Yuuka Kanakubo, Yasuki Tachibana, and Tetsufumi Hirano.
Unified description of hadron yield ratios from dynamical core-corona initialization.
Phys. Rev. C, 101(2):024912, 2020. doi: 10.1103/PhysRevC.101.024912. 125

[237] M. Kachelriess, S. Ostapchenko, and J. Tjemsland. On nuclear coalescence in small interacting systems. *Eur. Phys. J. A*, 57(5):167, 2021. doi: 10.1140/epja/s10050-021-00469-w. 126, 127

[238] Hans A. Bethe, Frederic de Hoffmann, and Freeman J. Dyson. Mesons and Fields. Volume II: Mesons. *Physics Today*, 8(6):27–27, 06 1955. ISSN 0031-9228. doi: 10.1063/1.3062050. URL https://doi.org/10.1063/1.3062050. 127

[239] Torbjörn Sjöstrand, Stefan Ask, Jesper R. Christiansen, Richard Corke, Nishita Desai, Philip Ilten, Stephen Mrenna, Stefan Prestel, Christine O. Rasmussen, and Peter Z. Skands. An introduction to PYTHIA 8.2. *Comput. Phys. Commun.*, 191:159–177, 2015. doi: 10.1016/j.cpc.2015.01.024. 137

[240] Fred Cooper and Graham Frye. Comment on the Single Particle Distribution in the Hydrodynamic and Statistical Thermodynamic Models of Multiparticle Production. *Phys. Rev. D*, 10:186, 1974. doi: 10.1103/PhysRevD.10.186. 137

[241] Fred Cooper, Graham Frye, and Edmond Schonberg. Landau's hydrodynamic model of particle production and electron-positron annihilation into hadrons. *Phys. Rev. D*, 11:192–213, Jan 1975. doi: 10.1103/PhysRevD.11.192. 137

[242] Bo Andersson, G. Gustafson, G. Ingelman, and T. Sjostrand. Parton Fragmentation and String Dynamics. *Phys. Rept.*, 97:31–145, 1983. doi: 10.1016/0370-1573(83)90080-7. 137

[243] Peter Skands, Stefano Carrazza, and Juan Rojo. Tuning PYTHIA 8.1: the Monash 2013 Tune. *Eur. Phys. J. C*, 74(8):3024, 2014. doi: 10.1140/epjc/s10052-014-3024-y. 137

[244] Stanisław Mrówczyński and Patrycja Słoń. Deuteron-deuteron correlation function in nucleus-nucleus collisions. *Phys. Rev. C*, 104(2):024909, 2021. doi: 10.1103/PhysRevC.104.024909. 148